Development and application of techniques in solid-state NMR

Nesbitt, Geoffrey John

Development and Application of Techniques in Solid-state NMR

by

Geoffrey John Nesbitt
(Collingwood College)
B.Sc. (Hons), University of Guelph (1980)
M.Phil. (Science), University of Concordia (1983)

A thesis submitted for the degree of
Doctor of Philosophy
of the University of Durham
December 1986

MEMORANDUM

The research and work presented in this thesis has been carried out in the School of Chemical Sciences of the University of East Anglia between October 1983 and September 1984, and in the Department of Chemistry at the University of Durham between October 1985 and October 1986. The time adjoining these two years was an intercalation period where the author was employed by the University of Durham as an experimental research officer. It is the original work of the author unless stated otherwise. None of this work has been submitted for any other degree.

Development and Application of Techniques in Solid-state NMR

by

Geoffrey John Nesbitt

ABSTRACT

The purpose of this thesis is to describe research into the extension and development of methods in solid state NMR, and their application to chemical systems where, for various reasons, analysis was difficult, incomplete, or impossible by other spectroscopic techniques. In particular silicon-29, sodium-23, fluorine-19 and proton nuclei have been used as molecular probes in inorganic silicates, macrocyclic polyether crown complexes and fluoropolymer chemical systems.

The sodium-23 chemical shift and lineshape have been shown to be sensitive to coordination and local symmetry. The cross-polarization experiment has also been applied to the sodium-23 nucleus, and shown to exhibit the same steric selectivity which has been observed in carbon-13 and silicon-29 experiments.

A probe has been configured at 4.7 Tesla to perform proton and fluorine-19 CRAMPS experiments. Multiple pulse sequences and CRAMPS experiments have been used to investigate the molecular motions and chemical environments of the systems investigated.

Conclusions are drawn upon the results which support the utility of these methods in application to difficult solid state systems.

Acknowledgements

A learning environment is a very precious commodity. I have been fortunate, during the course of this research, in knowing two inspiring academic communities in Norwich and in Durham. The communities themselves were composed of people who gave generously of their time, and expertise, much to my benefit. I hope that I have used you graciously, well, and with the respect that I have intended.

Foremost I humbly thank my learned advisor, Professor R.K Harris, for stimulating these environments, and providing the freedom that I might grow in them. I would also like to thank Dr.s: B. Say, A. Root, R. Yeung and A. Kenwright; P. Belton, S. Tanner, K. Wright; I.J. Cox, P. Stephenson; I. Appleyard, P. Reams, A. Royston; and the Durham Cowboys (P. Jackson, L. Merwin, P. Wilkes and junior members) for what can best be described as 'illuminating discussions', philosophical and other wise.

I would like to thank Dr. L. Dent-Glasser (University of Aberdeen), John Fuller (The British Museum: Natural History), Dr.s P. Belton and S. Tanner (The Food Research Institute), Dr. E. Smith and P. Garner-Gray (Unilever Research), and Dr.G. Hays (Shell Laboratorium, Amsterdam), for the kind donation of chemical systems, as referenced in Chapter Three.

Anyone reading this thesis will recognize that the multidisciplinary nature of the research described within required the application of wide ranging skills and expertise. Well, don't look at me sunshine! These investigations have benefitted from the technical assistance of M. Higham, Dr. E.J. Ross, T. Caygill, S. Atkinson, and the infamous Thomas Argument. This manuscript was typed with considerable enthusiasm and duress by Shirley Stewart, and the figures profit from the steady hand of Elizabeth Wood.

Dr. Angelika Sebald has suffered enormously with the burden of my friendship through the course of preparing this tome, and her critical comments on the text have much improved the contents. Without the support and love of my family I would not have managed the confidence to finish. Words will never adequately describe how much those letters have meant.

I acknowledge and thank the Committee of Vice Chancellors and Principals of the Universities of the United Kingdom for an award under the ORS scheme, and Unilever Research for a case award for one year.

Lastly, Horace Walpole (Fourth Earl of Orford) once said: "Life is tragic to those who feel, comic to those who think". For what it's worth, I hope that this thesis provokes a laugh or two.

to ruth

The following abbreviations and symbols have been used:

B_o = static magnetic field
B_1 = applied magnetic field
CP = Cross Polarization
CRAMPS = Combined Rotation And Multiple Pulse Sequences
circumflex = ^ indicates a quantum mechanical operator
EFG = Electric Field Gradient
FID = Free Induction Decay
FT = Fourier Transform
FTIR = Fourier Transform Infrared spectroscopy
h = Planck's constant/2π
$\mathcal{H}$ = Hamiltonian operator; subscript indicates nature of operator
MAR = Magic Angle Rotation
MPS = Multiple Pulse Sequence || Multiple Pulse decoupling Sequence
N_α, N_β = spin populations in α and β spin states
NMR = Nuclear Magnetic Resonance
NQR = Nuclear Quadrupole Resonance
Operators = quantum mechanical operators are
ppm = parts per million
rf = radio frequency
SPE = Single Pulse experiment
SP = Single Pulse decoupled Experiment
T = Temperature
Tensors = all doubly underlined
tp = pulse width

ν = frequency of irradiating rf field

VASS = Variable Angle Sample Spinning

Vectors = are underlined

ω_o = $\nu.2\pi$ radians $\sec^{-1}$

INDEX PAGE

CHAPTER FIVE: QUADRUPOLAR NUCLEI: ^{23}Na SINGLE AND DOUBLE METHODS DEVELOPMENT. 88

CHAPTER SIX: APPLICATIONS OF NMR METHODS TO THE STUDY OF CHEMICAL SYSTEMS IN THE SOLID STATE

REFERENCES

CHAPTER ONE

INTRODUCTION

"The game is afoot".
S. Holmes

INTRODUCTION

Currently there exist a large array of spectroscopic techniques which may be used to investigate chemical systems in the solid state. Of these, magnetic resonance methods are useful because crystallographic, chemical, and magnetic equivalence describe different properties of a solid. Other criteria such as spectroscopic interference, chemical impurities, or sample matrix may select NMR as the method of preference. The ultimate utility of solid state NMR is demonstrated when these relationships can be exploited, allowing the measurement of data not accessible by other analytical methods.

The purpose of this thesis is to describe research where magnetic resonance methods have been extended, and applied to chemical systems where, for various reasons, analysis was difficult, incomplete, or impossible by other spectroscopic techniques.

In order to fully comprehend the nature of the interactions responsible for the data observed, it is necessary to consider the theoretical derivation of magnetic resonance phenomena. Chapter two describes the NMR experiment, and those interactions which govern the magnetic behaviour of nuclei in solids.

Chapter three documents the experimental details of the investigations performed during the course of this research. Hardware and software are described briefly and the chemical systems studied are listed. This chapter includes a description of an NMR probe configured to perform the CRAMPS experiment in application to the systems of interest in this research.

In Chapters Four and Five the basic theory covered in Chapter two is extended to include rigorous descriptions of the CRAMPS experiment and quadrupolar nuclei, respectively. In both chapters examples of experimental calibration and verification are demonstrated in application to well charaterized chemical systems. The purpose of both chapters is to document the capabilities of the different experiments in known compounds.

Chapter six demonstrates the application of the magnetic resonance methods described in the previous chapters to difficult or novel chemical systems. Corroboration with other spectroscopic methods is used where possible, and the complementary nature of techniques noted. A variety of systems have been studied demonstrating the versatile nature of magnetic resonance methods when applied to solid state problems. Conclusions are made upon the discussion of the data presented for each chemical system.

Finally, general conclusions are drawn upon the merit and nature of the data generated as a result of the experiments described in this thesis. Suggestions of future investigations are made in light of the data published here.

CHAPTER TWO

THEORY

"The whole of science is nothing more than the refinement of everyday thinking".

A. Einstein

2.1 General Theory of Nuclear Magnetic Resonance (NMR)

The magnetic resonance experiment is possible because nuclei exhibit the property of spin. Given a positive charge, and an appropriate mass, a nucleus will possess a detectable magnetic moment.[1] When placed in a magnetic field, $\underline{B}_o$, the magnetic moment, $\underline{\mu}$, is subjected to a torque which is a consequence of the field acting upon the spin angular momentum (colinear with $\underline{\mu}$). The result of this action will be the precession of $\underline{\mu}$ about the axis defined by the direction of the magnetic field in a laboratory coordinate system. Any nucleus with non zero spin, $\underline{I}$, will exhibit a quantization of its spin axis orientation into 2I+1 levels. The energies of the allowed levels, relative to that in zero magnetic field, can be described by

$$E = \frac{-h}{2\Pi} \gamma \, M_I \underline{B}_o \qquad (2.1)$$

where M_I is the magnetic quantum number, which is bound by the selection rule governing magnetic dipole transitions such that

$$\Delta M_I = \pm 1; \quad M_I = I, I-1, \ldots -I+1, -I \qquad (2.2)$$

Magnetic resonance can occur when an external radio frequency field, $\underline{B}_1$, is applied to the magnetized spin ensemble, such that the Bohr frequency condition is satisfied.

$$|\hbar\underline{\omega}_o| = \Delta E = |\hbar\gamma\underline{B}_o| \qquad (2.3)$$

Figure 2.1 illustrates both the classical and quantum mechanical representation of the resonance condition. From this representation several obvious deductions can be made with regard to the detection of an NMR signal.

The two possible orientations of the nuclear spin define a high (β), and a low (α) energy state for any possible positive γ. If both states have equal populations, then in any transition ($\alpha \rightarrow \beta$ or $\beta \rightarrow \alpha$) there would be no net change of energy, and no signal to measure. However, at thermal equilibrium, the population distribution of nuclei between the two states can be described by a Boltzmann distribution

$$\frac{N_\beta}{N_\alpha} = \exp\left(\frac{-h\nu}{kT}\right) \qquad (2.4)$$

$$\simeq 1 - \frac{h\nu}{kT} \ *$$

giving $N_\alpha > N_\beta$, meaning net absorption can occur at the resonance condition, and produce the corresponding signal.

Examination of equation 2.4 shows a thermal equilibrium relationship between the spin populations of the two states. Obviously the excitation and detection of a signal will affect this distribution. Relaxation mechanisms return the spin system to thermal equilibrium

---

* Truncation of the exponential expansion is justified since $\frac{\Delta E}{kT} << 1$

Figure 2.1 : Resonance Condition for Nuclei with $I=1/2$

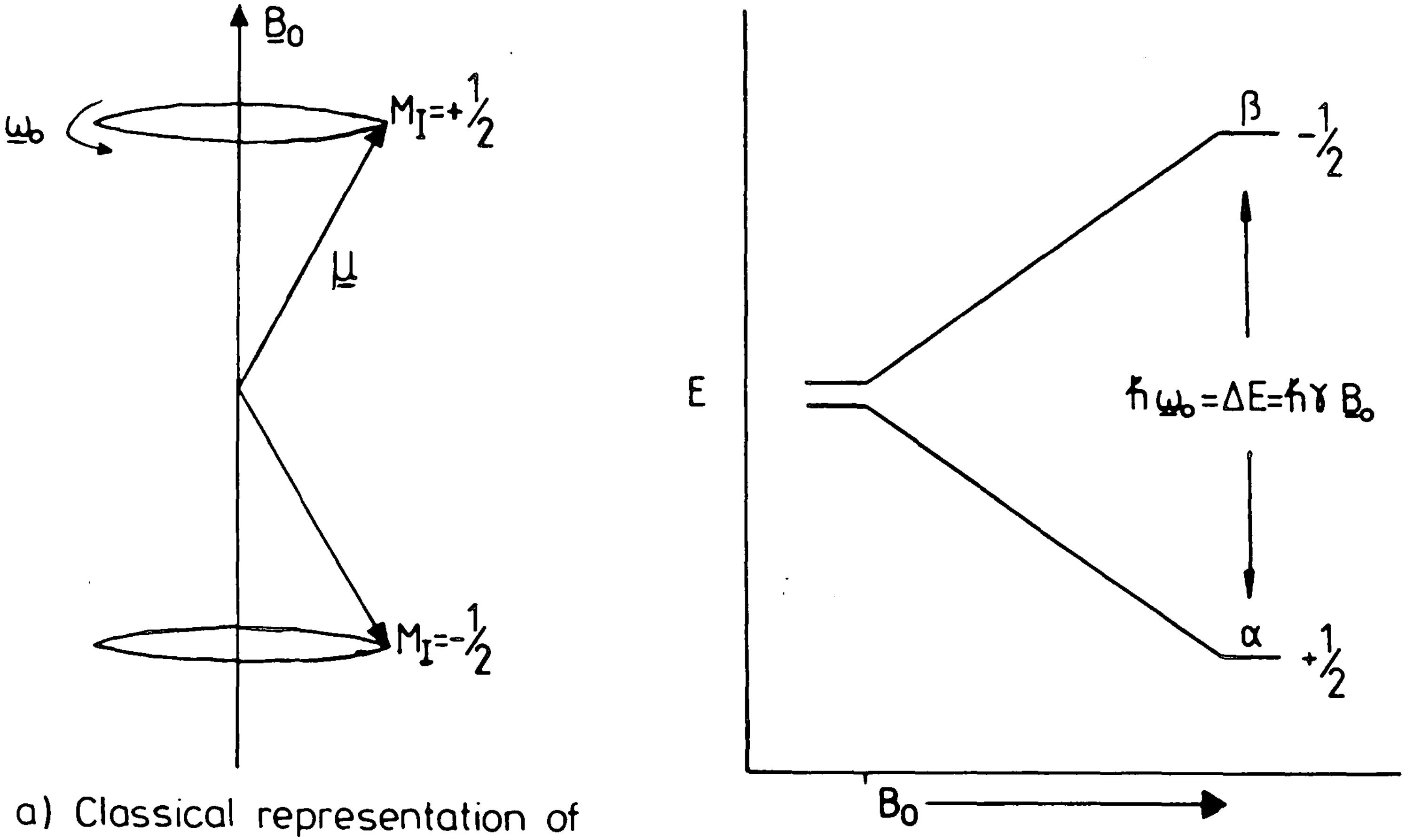

a) Classical representation of $\underline{\mu}$ interaction with $\underline{B}_0$

b) Quantum Mechanical representation of quantized spin states via contact with the lattice.[2] Without this contact saturation would occur, and where equal populations exist in the two possible states no signal may be observed.

There are many mechanisms of spin relaxation, varying in degree of importance depending upon the characteristics of the sample, and these will be discussed in detail in later chapters where appropriate. Fundamental to all relaxation mechanisms is the presence of an internal magnetic field at the nuclear site. A relaxation transition may be induced only if the frequency of this local field is equal to the resonance frequency of the nucleus to be relaxed. The local field is supplied by the thermal motion of the lattice. Relaxation phenomena can then be treated as a statistical problem, evaluating the probability of nuclear spin flip occuring as a result of coupling between the spin and the lattice. Relaxation via a nuclear transition must be energy conserving with the lattice, and is usually described as a time constant over which a transition is expected

Figure 2.2 demonstrates the response of magnetization to a $\frac{\pi}{2}$ pulse, and subsequent relaxation via the transverse (T_2) and longitudinal (T_1) exponential decay times. This figure allows an intuitive grasp of the phenomenological equations which Bloch[3] developed to describe the rate of magnetization decay.

Figure 2.2 : Effect of $\pi/2$ pulse and relaxation on magnetization in Rotating frame.

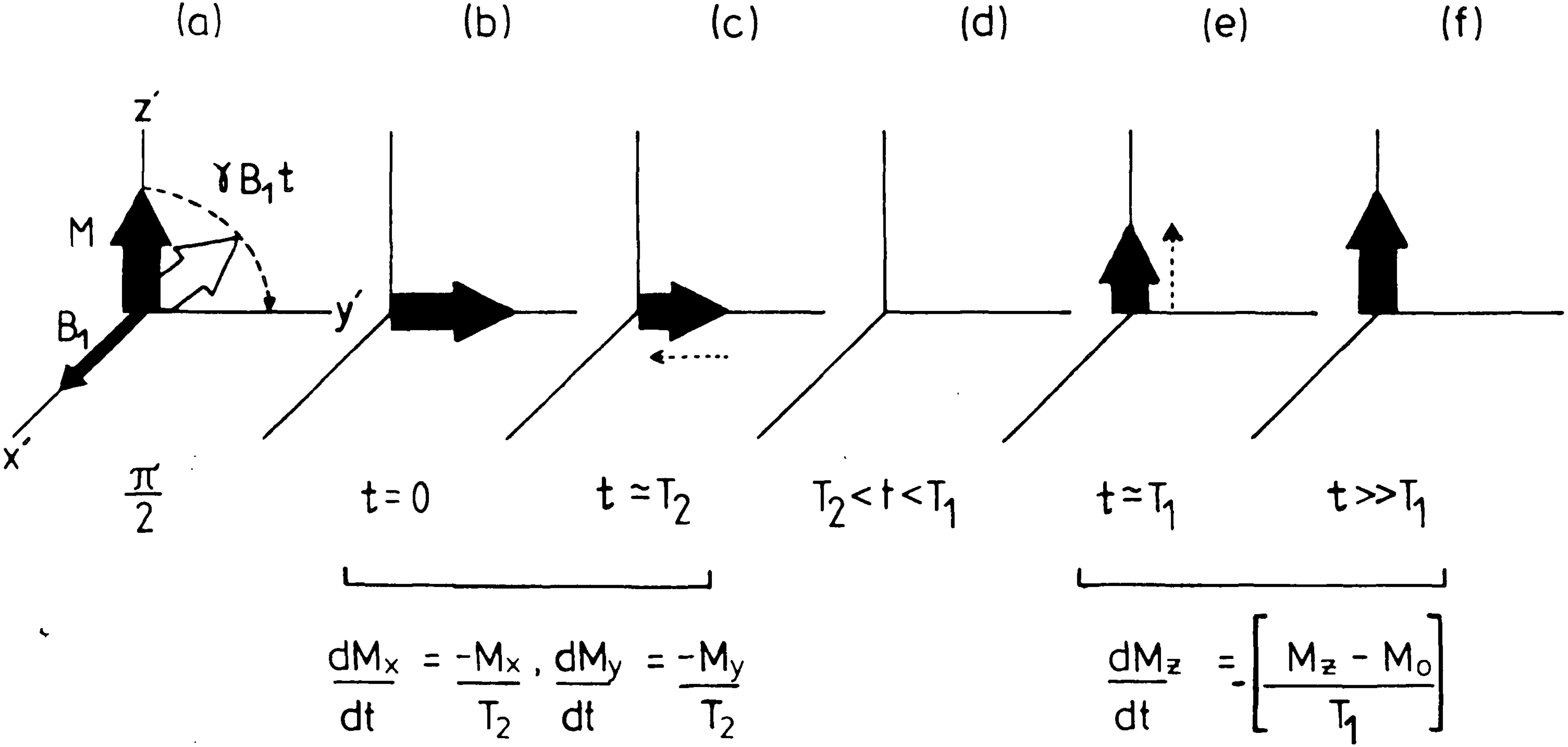

Further examination of equation 2.3 shows a linear relationship between $\underline{\omega}_o$, the angular frequency of radiation absorbed by the nuclei from $\underline{B}_1$, and γ, in a constant field. This means that in order to maintain the resonance condition, the study of higher γ nuclei is done at a higher frequency of $\underline{\omega}_o$ given a constant field, $\underline{B}_o$. There are certain advantages in using the highest value of $\underline{B}_o$ possible, but this can oppose other constraints caused by the correspondingly high $\underline{\omega}_o$ required. This will be discussed in further detail in Chapter Four.

The final 'general' deduction which will be made from Figure 2.1 concerns shielding of the nucleus. The fundamental reason why magnetic resonance is useful in the investigation of chemical problems is because the resonant frequency at which equation 2.3 is fulfilled is a unique solution, which is diagnostic of the electronic environment of the nucleus. The equation modelling the resonance condition must then be modified to allow for the perturbation of the nuclear shielding, resulting in an explicit equation for a 'nucleus A' such that

$$\underline{\omega}_A = \gamma_A \underline{B}_o (1-\underline{\sigma}_A) \qquad (2.5)$$

The measurement of separate signals for nuclei in chemically different environments first demonstrated this relationship.[4]

The theory stated thus far has been general to all nuclear magnetic resonance. Ultimately this thesis is concerned with the application of magnetic resonance techniques to the study of the solid state. The theory of spin interactions in solids will now be considered.

2.2 Nuclear Magnetic Resonance applied to the Solid State

Isotropy in a solid means literally that all directions are equivalent. For our purposes, the degree of anisotropy present in a solid is determined by the motional averaging acting on the state, within the time scale of the NMR experiment. This is highly dependent upon the nature of the material.

In a solution state the response of a material's properties to perturbation is usually linear and isotropic, and may be adequately described using scalar quantities. At the other extreme, most crystals are anisotropic, showing limited symmetry. Under these criteria the reponse to external forces depends upon the magnitude and orientation of the perturbing field. In such restricted symmetry the set of all directions is reduced to a closed group of transformations which operate on the physical properties to describe the system response. The coefficients of this sub-group obey the transformation properties of a tensor. In polycrystalline and amorphous materials some isotropic behaviour is recovered such that on the scale of some macroscopic interactions the material appears homogeneous. However, some anisotropic properties are preserved, and it is the investigation of these contributions with which we are concerned.

In order to properly describe the interaction between energy and matter, there are two kinds of symmetry which must be understood. There is an inherent symmetry of the perturbing force, a quantity which can be rigorously defined and controlled in the experiment. There are also the symmetries concerned with space and time which represent the specific anisotropy of the material in which the interaction is studied. It is the derivation of both these relationships to which we now turn our attention.

2.3 Basic Nuclear Spin Interactions

The nuclear spin Hamiltonian can be described using several terms which represent all the physically different interactions of the nuclear spins. Figure 2.3 illustrates the communication possible between a nuclear spin and its environment,[5] and several general comments can be made concerning these relationships. Beginning with the static applied field, assumed constant in space, the magnitude of the interactions decreases as sphere boundaries are crossed. The spin Hamiltonians can be separated between external and internal fields on the basis of this distinction. Further subdivision can be made using the nature of the interaction to distinguish the form of the Hamiltonian, shown in Table 2.1. Each form will be discussed in turn using a self-consistent notation.

Table 2.1: Differentiation of Hamiltonians.

TERM	DESCRIPTION	MAGNITUDE	COUPLING
$h\mathscr{H}=h\mathscr{H}_Z$	Zeeman	ext	Single Nuclear Spin
+ $h\mathscr{H}_{RF}$	radiofrequency	ext	
+ $h\mathscr{H}_{SR}$	spin rotation	int	
+ $h\mathscr{H}_{CS}$	chemical shielding	"	Nuclear spin to e^-
+ $h\mathscr{H}_Q$	quadrupolar	"	
+ $h\mathscr{H}_J$	indirect	"	Nuclear spin to Nuclear spin
+ $h\mathscr{H}_D$	dipolar	"	

Figure 2.3: Spin Interactions

Hamiltonian	Mechanism
$\hbar\mathcal{H} = \hbar\mathcal{H}_{ext} + \hbar\mathcal{H}_{int}$	
$\hbar\mathcal{H}_{ext} = \hbar\mathcal{H}_{o} + \hbar\mathcal{H}_{rf}$	1
$\hbar\mathcal{H}_{int} = \hbar\mathcal{H}_{D} + \hbar\mathcal{H}_{CS} + \hbar\mathcal{H}_{Q} + \hbar\mathcal{H}_{J} + \hbar\mathcal{H}_{SR} + \hbar\mathcal{H}_{L}$	2-7
where	
$\hbar\mathcal{H}_{D} = \frac{\hbar^2\gamma^2}{r^3}\left[(1-3\cos^2\beta)(\hat{I}_Z.\hat{S}_Z - \frac{1}{4}(\hat{I}_+\hat{S}_- + \hat{I}_-\hat{S}_+))\right]$	2
$\hbar\mathcal{H}_{CS} = \hbar\frac{1}{3}\,\mathrm{Tr}\underline{\sigma} + \frac{1}{3}\sum_{j=1}^{3}(3\cos^2\beta-1)\sigma_{jj}$	3,6
$\hbar\mathcal{H}_{Q} = \hbar\frac{e^2qQ}{4I(2I-1)}\left[(3\cos^2\beta-1).(3\hat{I}_Z^2-I(I-1))\right]$	3,6
$\hbar\mathcal{H}_{J}$ = indirect spin-spin coupling	3
$\hbar\mathcal{H}_{SR}$ = spin rotation	3
$\hbar\mathcal{H}_{L}$ = relaxation mechanisms	3,4,5,7

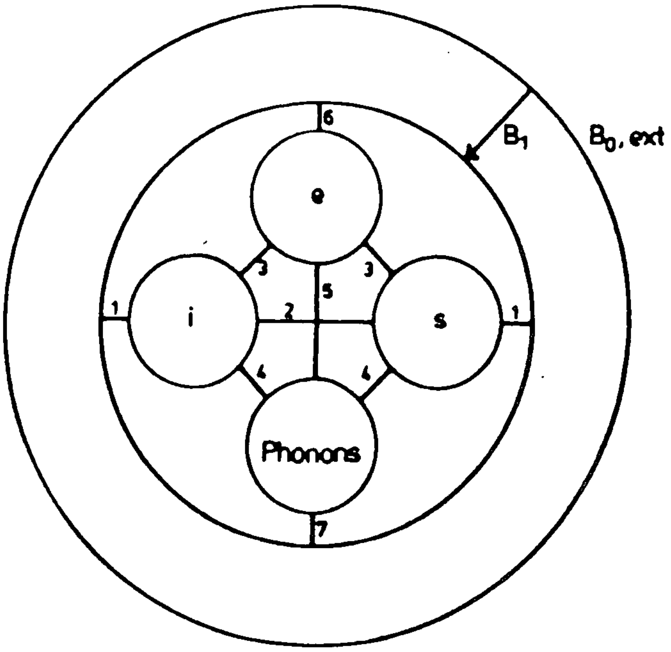

2.3.1.1 The Zeeman Hamiltonian: $\mathscr{H}_Z$

The Hamiltonian for the nuclear spin-magnetic field (Zeeman) interaction can be written from equation 2.1 as

$$h\mathscr{H}_Z = h\gamma\hat{\underline{I}}\ \underline{B}_o = -h\underline{\omega}_o\ \hat{\underline{I}} \qquad (2.6)$$

For an ensemble of nuclear spins (where ι runs over all nuclei) this may be rewritten as

$$h\mathscr{H}_Z = -h\sum_{\iota}\underline{\omega}_o{}^{\iota}\hat{\underline{I}}_Z{}^{\iota} \qquad (2.7)$$

2.3.1.2 The Radio frequency Hamiltonian: $\mathscr{H}_{RF}$

The perturbing radio frequency (rf) field is conventionally applied normal to the static field and it is assumed here to be aligned parallel to the x axis. The Hamiltonian would be of the form

$$h\mathscr{H}_{RF} = h\ \gamma\ \hat{\underline{I}}_X\ \underline{B}_1\cos(\omega t+\phi) \qquad (2.8)$$

where the form of $\underline{B}_1$ allows for the modulation of amplitude ($\underline{B}_1$), frequency (ωt) and phase (ϕ) of the perturbing field. The action on an ensemble of spins can be written

$$h\mathscr{H}_{RF} = -h\underline{B}_1\cos(\omega t+\phi)\sum_{\iota}\gamma^{\iota}\hat{\underline{I}}_x^{\iota} \qquad (2.9)$$

This will be discussed in greater detail when considering the nutation of spins by multiple pulse methods.

2.3.2 The Internal Spin Hamiltonians:

For the purposes of this thesis, particular attention has been given to the form and behaviour of the chemical shielding, quadrupolar, and dipolar spin Hamiltonians.

2.3.2.1 The Spin-Rotation Hamiltonian: $\mathcal{H}_{SR}$

The spin-rotation Hamiltonian describes any coupling between nuclear spins and the magnetic moment associated with the angular momentum of a molecule. The relationship over 'ι' spins in a molecule 'm' with the magnetic moment of the angular momentum J^m is

$$h\mathcal{H}_{SR} = h \sum_{m} \sum_{\iota} \hat{\underline{I}}^{\iota} . \underline{\underline{C}}^{\iota,m} . \underline{J}^{m} \qquad (2.10)$$

where $\underline{\underline{C}}^{\iota,m}$ is a tensor relating the contribution of the dot product shown. This interaction is usually small and will not be discussed further in this thesis.

2.3.2.2 The Chemical Shielding Hamiltonian: $\mathcal{H}_{CS}$

The coupling of a spin $\underline{I}$ with the magnetic field $\underline{B}_o$ (in this case restricted to the static field) can be described using the shielding tensor $\underline{\underline{\sigma}}$ such that

$$h\mathcal{H}_{CS} = h \sum_{\iota} \gamma^{\iota} \, \hat{\underline{I}}^{\iota} . \underline{\underline{\sigma}}^{\iota} . \underline{B}_o \qquad (2.11)$$

The shielding tensor has no restrictions upon its symmetry and explicitly describes the orientation of a spin relative to a set of axes.

Since it is common to measure $\underline{\sigma}_{ZZ}$,[6] equation 2.11 can be rewritten[8,7]

$$\hbar\mathcal{H}_{CS} = \hbar \sum_{\iota} \gamma^{\iota} \cdot \underline{\underline{\sigma}}^{i}{}_{ZZ} \cdot \underline{B}_{o} \qquad (2.12)$$

The principal axes can be chosen such that under an orthogonal transformation there are discrete Euler angles[9] (α,β,γ) describing the rotation matrix which diagonalizes the chemical shielding tensor. By definition the solution of the matrix will be its trace, in this case the isotropic chemical shift, given by

$$|\underline{\sigma}| = R(\alpha,\beta,\gamma) . \begin{bmatrix} \sigma_{XX} & o & o \\ o & \sigma_{YY} & o \\ o & o & \sigma_{ZZ} \end{bmatrix} . R^{-1}(\alpha,\beta,\gamma)$$

$$= \frac{1}{3} \left[\sigma_{XX}+\sigma_{YY}+\sigma_{ZZ}\right]$$

$$= \frac{1}{3} T_{r}\underline{\sigma} \qquad (2.13)$$

2.3.2.3 The Quadrupolar Interaction: $\mathcal{H}_Q$

The interaction between a nuclear spin I and its electric field gradient tensor $\underline{\underline{V}}$ can be written in the general form

$$\hbar\mathcal{H}_{Q} = \hbar \; \underline{\hat{I}} . \underline{\underline{V}} . \underline{\hat{I}} \qquad (2.14)$$

Principal axes can be chosen so that V(X,Y,Z) is symmetric $(V_{XY}=V_{YX})$ and traceless $(V_{XX}+V_{YY}+V_{ZZ}=0)$.

Expansion of the quadrupolar Hamiltonian by carrying through the matrix multiplication produces

$$\begin{aligned} h\mathcal{H}_Q &= h \quad V_{XX}\hat{I}_X^2 + V_{YY}\hat{I}_Y^2 + V_{ZZ}\hat{I}_Z^2 \\ &+ V_{XY}(\hat{I}_X\hat{I}_Y + \hat{I}_Y\hat{I}_X) \\ &+ V_{YZ}(\hat{I}_Y\hat{I}_Z + \hat{I}_Z\hat{I}_Y) \\ &+ V_{ZX}(\hat{I}_Z\hat{I}_X + \hat{I}_X\hat{I}_Z) \end{aligned} \qquad (2.15)$$

Note that the spin vectors are not symmetric ($\hat{I}_{XY} \neq \hat{I}_{YX}$) and obey the identity

$$\hat{I}_X^2 + \hat{I}_Y^2 + \hat{I}_Z^2 = I(I+1)$$

This combined with the traceless property of the EFG allows equation 2.15 to be written[10]

$$\begin{aligned} h\mathcal{H}_Q &= h \quad V_{ZZ} \left[3\hat{I}_Z^2 - I(I+1)\right] + (V_{XX} - V_{YY}) \cdot (\hat{I}_X^2 - \hat{I}_Y^2) \\ &+ V_{XY} \; (\hat{I}_X\hat{I}_Y + \hat{I}_Y\hat{I}_X) \\ &+ V_{YZ} \; (\hat{I}_Y\hat{I}_Z + \hat{I}_Z\hat{I}_Y) \\ &+ V_{ZX} \; (\hat{I}_Z\hat{I}_X + \hat{I}_X\hat{I}_Z) \end{aligned} \qquad (2.16)$$

This equation is valid for any axes, and we can now choose principal axes to symmetrise $\underline{\underline{V}}$ so that

$$V_{XZ} = V_{YZ} = V_{XY} = 0$$

and $$|V_{ZZ}| \geq |V_{XX}| \geq |V_{YY}|$$

and define $$eq = V_{ZZ} \text{ and } \eta = \frac{\left[V_{XX} - V_{YY}\right]}{V_{ZZ}}$$

which after an orthogonal (diagonalizing) transformation puts the quadrupolar Hamiltonian in the form[11]

$$h\mathcal{H}_Q = \frac{he^2qQ}{4I(2I-1)}\left[3\hat{I}_Z^2 - I(I+1) + \frac{1}{2}\,\eta(\hat{I}_X^2+\hat{I}_Y^2)\right] \quad (2.17)$$

where

Q is the quadrupole moment

eq is the field gradient $\left[= V_{ZZ} = \frac{\partial^2 V}{\partial Z^2}\right]$

η is the asymmetry parameter $\left[= \frac{V_{XX}-V_{YY}}{V_{ZZ}}\right]$

Close examination of equation 2.17 yields some intuitive observations. For a spin I=0, the matrices $\hat{\underline{I}}_X$, $\hat{\underline{I}}_Y$, $\hat{\underline{I}}_Z$ are all zero, hence, as one would expect, there can be no quadrupolar interaction. For a spin $I = \frac{1}{2}$ we know from the properties of the Pauli spin[12] matrices that

$$\hat{I}_X^2 = \hat{I}_Y^2 = \hat{I}_Z^2 = \frac{1}{3}I(I+1)$$

and

$$\hat{I}_X\hat{I}_Y = -\hat{I}_Y\hat{I}_X$$

where upon substitution, $\mathcal{H}_Q$ once again goes to zero. Further, the asymmetry parameter defines the nature of quadrupolar coupling, and it can be seen that in a cubic environment the EFG at the nuclear site would go to zero ($V_{XX} = V_{YY} = V_{ZZ} = 0$) and the coupling term vanishes.

2.3.2.4 The Indirect Spin-Spin Coupling Interaction: $\mathcal{H}_J$

The coupling between two nuclei (ι,k) (like or unlike) via their associated electrons can be described by a second rank tensor $\underline{\underline{J}}$ such that[13]

$$h\mathcal{H}_j = h \sum_{\iota<k}' \hat{\underline{I}}_\iota \cdot \underline{\underline{J}}_{\iota k} \cdot \hat{\underline{I}}_k \qquad (2.18)$$

As you would expect the magnitude of indirect spin-spin coupling generally increases with the mass of the nuclei involved. The nuclei studied in this thesis are usually of low enough mass that this term may be neglected.

2.3.2.5 The Dipole-Dipole Interaction: $\mathcal{H}_D$

The interaction between two nuclear dipoles (again, like or unlike) can be described classically using the magnetic moment, $\underline{\mu}$, as an example, in the following manner:

$$E = \frac{1}{r_{IS}^3}\, \underline{\mu}_1 \cdot \underline{\mu}_2 - 3 \left[\frac{(\underline{\mu}_I \cdot \underline{r}')\ (\underline{\mu}_S \cdot \underline{r}')}{r_{IS}^2} \right] \frac{\mu_o}{4\pi} \qquad (2.19)$$

where $\underline{r}'$ is the internuclear vector common to the dipoles and $\underline{r}_{IS}$ is the internuclear distance. The magnetic moment can be written as the product of the nuclear spin operator ($\hat{\underline{I}}$) and magnetogyric ratio (γ) associated with each nucleus, giving[14]

$$h\mathcal{H}_D = \frac{h^2 \gamma_I \gamma_S}{r_{IS}^3} \left[\hat{\underline{I}}_I \cdot \hat{\underline{I}}_S - 3 \frac{\left[\hat{\underline{I}}_I \cdot \underline{r}'\right]\ \left[\hat{\underline{I}}_S \cdot \underline{r}'\right]}{r_{IS}^2} \right] \frac{\mu_o}{4\pi} \qquad (2.20)$$

If the internuclear vector $\underline{r}'$ is expressed in terms of polar coordinates, θ and ϕ, describing the positions of the two dipoles, where the Z axis is parallel to the applied static field, the transforming coordinates look like

$$
\begin{aligned}
X &= r\sin\theta\cos\phi \\
Y &= r\sin\theta\sin\phi \\
Z &= r\cos\theta
\end{aligned}
\qquad (2.21)
$$

such that,

$$
\hbar\mathcal{H}_D = \hbar^2\frac{\gamma_I\gamma_S}{r^3_{IS}}\left[\underline{\hat{I}}_I\underline{\hat{I}}_S - 3\left[\hat{I}_{IZ}\cos\theta+\sin\theta(\hat{I}_{IZ}\cos\phi+\hat{I}_{IY}\sin\phi)\right]\right.
$$

$$
\left.\left[\hat{I}_{SZ}\cos\theta+\sin\theta(\hat{I}_{SX}\cos\phi+\hat{I}_{SY}\sin\phi\right]\right]\frac{\mu_o}{4\pi}
$$

When the trigonometric terms are defined using Euler's notation ($e^{\iota\phi}=\cos\theta+\iota\sin\theta$) and gathered in the manner first proposed by Van Vleck[15] equation 2.20 becomes

$$
\hbar\mathcal{H}_D = \hbar^2\frac{\gamma_I\gamma_S}{r^3}\,(A+B+C+D+E+F) \qquad (2.22)
$$

where

$$
A = \hat{I}_{IZ}\hat{I}_{SZ}(1-3\cos^2\theta) \qquad (2.22a)
$$

$$
B = -\frac{1}{4}(1-3\cos^2\theta)\left[(\hat{I}_{IX}-\iota\hat{I}_{IY})\cdot(\hat{I}_{SX}+\iota\hat{I}_{SY}) + \right.
$$

$$
\left.(\hat{I}_{IX}+\iota\hat{I}_{IY})\cdot(\hat{I}_{SX}-\iota\hat{I}_{SY})\right] \qquad (2.22b)
$$

$$C = -\frac{3}{2}\sin\theta\cos\theta e^{-\iota\phi}\left[(\hat{I}_{IX}+\iota\hat{I}_{IY})\hat{I}_{SZ} + (\hat{I}_{SX}+\iota\hat{I}_{SY})\hat{I}_{IZ}\right] \quad (2.22c)$$

$$D = -\frac{3}{2}\sin\theta\cos\theta e^{\iota\phi}\left[(\hat{I}_{IX}-\iota\hat{I}_{IY})\hat{I}_{SZ} + (\hat{I}_{SX}-\iota\hat{I}_{SY})\hat{I}_{IZ}\right] \quad (2.22d)$$

$$E = -\frac{3}{4}\sin^{-2}\theta e^{-2\iota\Phi}\left[(\hat{I}_{IX}+\iota\hat{I}_{IY})\cdot(\hat{I}_{SX}+\iota\hat{I}_{SY})\right] \quad (2.22e)$$

$$F = -\frac{3}{4}\sin^{-2}\theta e^{2\iota\Phi}\left[(\hat{I}_{IX}-\iota\hat{I}_{IY})\cdot(\hat{I}_{SX}-\iota\hat{I}_{SY})\right] \quad (2.22f)$$

The convenience of this notation can be exploited to qualitatively differentiate between the sources of contributions to the dipolar line shape.[16] It is important to realise that equation 2.22 describes all contributions possible by the selection rules which define the allowed transitions according to the magnetic quantum number M.

Term A causes no change in M_I or M_S and contributes in first order to commute with $\mathcal{H}_Z$. This is the case for like or unlike spins.

Term B describes a simultaneous change of two neighbouring dipoles, in opposing directions. For like spins energy is conserved allowing contributions to $\mathcal{H}_Z$. For unlike spins there is a net change in ΔM, which disallows contribution to the truncated Hamiltonian.

Terms C and D (D is the conjugate of C) alter one spin state only and terms E and F (F is the conjugate of E) raise or lower both spin states, such that none can contribute in first order.

The resultant secular Hamiltonians can be written for like spins

$$\hbar\mathcal{H}_D = \frac{\hbar^2 \frac{1}{2} \gamma^2}{r^3} \quad (1-3\cos^2\theta)(3\hat{I}_{IZ}\hat{I}_{SZ}-\hat{\underline{I}}_I \cdot \hat{\underline{I}}_S) \quad (2.23)$$

and for unlike spins

$$\hbar\mathcal{H}_D = \hbar^2 \frac{\gamma_I\gamma_S}{r^3} \; (1-3\cos^2\theta)(\hat{I}_{IZ}\hat{I}_{SZ}) \qquad (2.24)$$

2.4 The Rotation Manipulation

The high resolution features normally observed in solution state NMR are a result of rapid molecular tumbling, which averages the internal nuclear spin interactions to their isotropic values. The key to this averaging lies in the time dependent nature of the motions in a non-viscous liquid, relative to the NMR experimental time frame.

The interactions dominating a solid state spectrum do so because their contribution is time dependent in the effective Hamiltonian. Haeberlen[13] has pointed out that by using discriminating methods, the different dominating internal Hamiltonians can be selectively averaged, leaving other contributions of interest untouched. This is the essence of most methods in high resolution solid state NMR, and there are a variety of techniques with which it can be accomplished, according to their selectivity, as shown in Table 2.2. In this thesis the coherent averaging techniques of Magic Angle Rotation (MAR)[17,18] and Multiple Pulse Sequences (MPS)[19] will be used extensively. For this reason these two methods and their action on the internal Hamiltonians characterized by the chemical shielding, dipolar, and quadrupolar interactions will be discussed in detail.

Table 2.2: Spin manipulations

MANIPULATION	ACTION	EXAMPLE
Dilution	C.A. in coordinate space	matrix isolation[36,37]
Melting	I.A. in coordinate space	variable temperature[35]
Polarization	C.A. in coordinate space	artificial polarization[34]
Spin Locking	I.A. in spin space	broad band decoupling[21,22]
Sample Rotation	C.A. in coordinate space	MAR[17] and VASS[18]
Spin Rotation	C.A. in spin space	MPS[19]

C.A. = coherent averaging

I.A. = incoherent averaging

The fundamental principal common to all the methods listed in Table 2.5 is the manipulation of rotations which act upon the internal Hamiltonians. All three Hamiltonians of interest can be treated similarly and generally in the application of a rotation transformation which converts the coordinate axes system from a laboratory to a rotating frame of reference. However, the final form of each Hamiltonian contributes differently to the effective Hamiltonian under the two different methods (MAR & MPS) and for this reason each interaction will be discussed separately.

2.4.1 Dipolar Hamiltonian under Rotation

The truncated dipolar Hamiltonian for unlike spins has already been stated in equation 2.23 as

$$\hbar\mathcal{H}_D = \sum \hbar^2 \frac{\gamma_\iota \ \gamma_S}{r_{IS}^3} \quad (3\cos^2\theta_{IS}-1)(3\hat{I}_{IZ}\hat{I}_{SZ} - \underline{\hat{I}}_I \cdot \underline{\hat{I}}_S) \qquad (2.23)$$

Rotation of the internuclear vector $\underline{r}_{IS}$ in $\underline{B}_o$, may be performed by application of a rotation transformation which relates the axes in the new frame of reference to θ_{IS}.[18] This can be represented by the equation

$$\cos\theta_{IS} = \cos\beta\cos\beta'_{IS} + \sin\beta\sin\beta'_{IS}\cos(\omega_r t+\phi_{IS}) \qquad (2.25)$$

where β is the angle around which the sample rotates relative to $\underline{B}_{oZ}$ (the laboratory frame) and β'_{IS} is the angle between the intermolecular vector $\underline{r}_{IS}$ and the axis of rotation.

Substitution of equation 2.25 into 2.23 yields[18]

$$\hbar\mathcal{H}_D(t) = \sum_{I<S} \hbar^2 \frac{\gamma_I\gamma_S}{r_{IS}^3} (3\hat{I}_{IZ}\hat{I}_{SZ} - \underline{\hat{I}}_I\cdot\underline{\hat{I}}_S)$$

$$\frac{1}{2}\left[(3\cos^2\beta-1)(3\cos^2\beta'_{IS}-1)\right.$$

$$+ \frac{3}{2}\sin 2\beta\sin 2\beta'_{IS}\cos(\omega_r t+\phi_{IS})$$

$$\left.+ \frac{3}{2}\sin^2\beta\sin^2\beta'_{IS}\cos 2(\omega_r t+\phi_{IS})\right] \qquad (2.26)$$

Examination of equation 2.26 shows that:

1. At $\beta = \beta'_{IS} = \arccos\left[\frac{1}{\sqrt{3}}\right] = 54^o44'08''$ the term $\frac{1}{2}(3\cos^2\beta-1)$ goes to zero. This means that $\mathcal{H}_D$ secular vanishes.

2. The last two 'time dependent' terms produce rotational echoes[20] at ω_r and $2\omega_r$.

3. Truncation of the Hamiltonian will also take place if a rotation in 'spin-space' is performed upon the Hamiltonian. At this point it is sufficient to note that through the first term in equation 2.26 it can be seen that manipulation of the spin isochromats can also cause the secular Hamiltonian to become time dependent, and vanish in the rotating frame. $(\langle 3\hat{I}_{IZ}(t)\hat{I}_{SZ}(t) - \underline{I}_I\underline{I}_S\rangle = 0)$. This is accomplished through the use of symmetrised pulse sequences[13,21,22,23] and will be discussed in further detail in Chapter 4.

2.4.2 The Chemical Shielding Hamiltonian under Rotation

The Hamiltonian describing the chemical shielding interaction has been written as

$$h\mathcal{H}_{CS} = \sum_{\iota} h\gamma_{\iota} \cdot \hat{\underline{I}}_{\iota} \; \underline{\underline{\sigma}}_{\iota ZZ} \cdot \underline{B}_{o} \qquad (2.12)$$

Under a rotation equivalent to that shown for the dipolar Hamiltonian, the relationship between the principal axes of $\underline{\sigma}$ and the angle β to $\underline{B}_o$ around which the rotation is performed, can be written[13]

$$h\mathcal{H}_{CS} = h\underline{\omega}_{o} \cdot \hat{\underline{I}}_{o} \left[\sigma + \delta \left[\frac{3\cos^{2}\beta - 1}{2} + \frac{\eta \sin^{2}\beta \cos^{2}\phi}{2} \right] \right] \qquad (2.27)$$

where $\delta = \sigma_3 - \sigma_{iso}$ (anisotropy)

$\eta = \dfrac{\sigma_2 - \sigma_1}{\delta}$ (asymmetry)

At $\beta = 54.7^{o}$ the second term again goes to zero giving

$$h\mathcal{H}_{CS} = h\underline{\omega}_{o}\hat{\underline{I}}_{o}\sigma \qquad (2.28)$$

Immediately upon sample spinning the anisotropic powder pattern degenerates to an isotropic resonance with echoes at ω_r, $2\omega_r$, ... The frequency of rotation dictates the effective contribution of these terms when measured against the limit of the anisotropy experienced by the nucleus. The intensities of the echo manifold are related to the moments of the shielding tensors, and can be used to find their value.[24,25]

There is no mechanism in which a spin space rotation can act upon the shielding anisotropy, and this will be discussed further with regard to the Combined Rotation and Multiple Pulse Spectra (CRAMPS) experiment.

2.4.3. The Quadrupolar Hamiltonian under Rotation

The Hamiltonian describing the quadrupolar interaction can be written

$$h\mathcal{H}_Q = h\,\frac{e^2qQ}{4I(2I-1)}\left[3\hat{I}_Z^2-I(I+1)+\frac{1}{2}\eta(\hat{I}_X{}^2+\hat{I}_Y^2)\right] \qquad (2.17)$$

Under a coordinate transformation where the principal axes system is defined in terms of a polar coordinate rotation about $\underline{B}_o$, equation 2.20 takes the form[26]

$$\begin{aligned}
h\mathcal{H}_Q &= h\,\frac{e^2qQ}{4I(2I-1)}\\
&V_{ZZ}\left[\frac{1}{2}(\cos^2\beta-1).(3\hat{I}_Z^2-I(I+1))\right.\\
&\left.+\frac{3}{4}(\hat{I}_+\hat{I}_Z+\hat{I}_Z\hat{I}_+)\sin2\beta e^{-\iota\psi}+\frac{3}{4}\hat{I}_+^2\sin^2\beta e^{-2\iota\psi}\right]\\
&+(V_{XX}-V_{YY})\left[-\frac{1}{2}(3\hat{I}_Z^2-\hat{I}^2)\sin^2\beta\cos2\phi\right.\\
&+\frac{1}{2}(\hat{I}_Z\hat{I}_++\hat{I}_+\hat{I}_Z)(\iota\sin\beta\sin2\phi e^{-\iota\psi}+\frac{1}{2}\sin2\beta\cos2\phi e^{-\iota\psi}\\
&\left.-\frac{1}{2}\hat{I}_+^2\left[\frac{1}{2}(1+\cos^2\beta)\cos2\phi e^{-2\iota\psi}+\cos\beta\sin2\phi e^{-2\iota\psi}\right]\right]
\end{aligned}$$

where β, ϕ, ψ are the Euler angles of the rotation transformation, relative to the laboratory frame.

Under rapid rotation at the'magic angle' the first-order quadrupolar effect averages to zero when the rotational frequency is large relative to the nuclear quadrupole frequency $\underline{\omega}_Q$.[27] This is a rare condition, met for nuclei possessing small quadrupolar moments (i.e. cesium, lithium) or the special case of isotropic crystalline state[28] since

$$\underline{\omega}_Q = \frac{\hbar^{-1}3e^2qQ}{2I(2I-1)} \qquad (2.30)$$

The truncated internal Hamiltonian can be written

$$\hbar\mathcal{H}_Q = \frac{\hbar e^2qQ}{4I(2I-1)}\left[\frac{1}{2}(\cos^2\beta-1).(3\hat{I}_Z^2-I(I+1))\right] \qquad (2.31)$$

in its simplest form, omitting the second order terms.

It is necessary, at this point, to realise that the magnitude of the quadrupolar frequency forces conditions upon the nature of the quadrupolar Hamiltonian contribution to the effective Hamiltonian. Depending upon this magnitude, the Zeeman field no longer defines the major resonance absorption, and is subjected to the following constraints:

1. $|\underline{\omega}_Q|>>|\underline{\omega}_Z|$ In this case pure quadrupole resonance will be observed, and the Zeeman splitting may be treated as a perturbation upon the quadrupole field.[29]

2. $|\underline{\omega}_Q|<<|\underline{\omega}_Z|$ As mentioned previously, this is the case for nuclei with very small quadrupolar moments or cubic symmetry. An important consequence for the

latter condition is that for nuclei with $I = n+\frac{1}{2}$ where n is an integer, the central transition is unaffected to first order by $\underline{\omega}_Q$.[30] This means that the Hamiltonian may be treated in the same manner as that for a spin $\frac{1}{2}$ nucleus, and the quadrupolar broadening of the central transition will be averaged by a rotation in coordinate space, through the $(3\cos^2\beta-1)$ term of equation 3.31. This will be discussed further in Chapter Five, with experimental confirmation.

The third and last condition is really just an extended case of the 'strong field' consideration. As the quadrupolar frequency increases, the magnitude of its perturbation on the Zeeman resonance grows, until finally the problem can only be properly evaluated when both internal Hamiltonians are solved simultaneously.

3. $|\underline{\omega}_Q| \simeq |\underline{\omega}_Z|$ This is by far the most interesting and involved condition from an NMR perspective. The contribution of the quadrupolar Hamiltonian is a function of $\underline{\omega}_Q$, and η, which effectively describe the orientation of the EFG about $\underline{B}_o$. Where $\underline{\omega}_Q$ is large the quantization of the spin order is no longer along the Z axis due to the perturbing effect of the quadrupole coupling. This causes significant mixing of the energy levels. It has been shown that the central transition $(\frac{1}{2},-\frac{1}{2})$ is not broadened by quadrupolar effects to first order[31] and there have been studies examining the effect of variable angle rotations as a function of η.[28,32] Generally it is very difficult to examine the case where $\underline{\omega}_Q$ is

anything but very small, since, as $\underline{\omega}_Q$ approaches $\underline{\omega}_Z$ in magnitude the frequency shifts are of such a large order it becomes experimentally impossible to observe anything but the central transition.[29]

This subject will be discussed in further detail in Chapter Five, but in conclusion, examination of equation 2.31 shows that it is possible to affect the quadrupolar contribution through rotations in both coordinate and spin space; the first via the $(3\cos^2\beta-1)$ term, and the latter through MPS methods. To date there has only been one report of the latter method operating on the second order contributions.[33]

2.5 The Cross-Polarization Manipulation

The polarization transfer experiment is an important technique in the investigation of rare spin systems. This method can give significant sensitivity enhancement[38], and when combined with heteronuclear decoupling[39], and rotation in coordinate space[7], can demonstrate spectral editing properties based upon the efficiency and rate of polarization transfer at a rare nucleus site.[40] These mechanisms will be discussed here in sufficient rigour to allow unambiguous interpretation of the data to be presented in this thesis.

The cross-polarization (cp) experiment basically works on the principle of spin order transfer occuring between an abundant(I) and dilute(S) spin system.[41] The spin system, in the presence of perturbing fields, may be described by

$$\hbar\mathcal{H} = \hbar\mathcal{H}_Z + \hbar\mathcal{H}_{II} + \hbar\mathcal{H}_{SS} + \hbar\mathcal{H}_{IS} + \hbar\mathcal{H}_{1I} + \hbar\mathcal{H}_{1S} \qquad (2.32)$$

where

$$\hbar\mathcal{H}_Z = -\hbar\sum_{\iota} \underline{\omega}_o^{\iota}\ \underline{\hat{I}}_{oZ}{}^{\iota} \qquad (2.7)$$

$$\hbar\mathcal{H}_{II} = \hbar^2\ \frac{\frac{1}{2}\gamma_I^2}{r^3} \sum_{i<j}^{N_I}\sum (1-3\cos^2\theta)(3\hat{I}_{iZ}\hat{I}_{jZ}-\underline{\hat{I}}_i\underline{\hat{I}}_j) \qquad (2.23)$$

$$\hbar\mathcal{H}_{SS} = \hbar^2\ \frac{\frac{1}{2}\gamma_S^2}{r^3} \sum_{m<n}^{N_S}\sum (1-3\cos^2\theta)(3\hat{S}_{mZ}\hat{S}_{nZ}-\underline{\hat{S}}_m\underline{\hat{S}}_n)$$

$$h\mathcal{H}_{IS} = h^2 \frac{\gamma_I\gamma_S}{r^3} \sum_{\iota=1} \sum_{m=1} (1-3\cos^2\theta)(\hat{I}_Z\hat{S}_Z) \qquad (2.24)$$

$$h\mathcal{H}_{1I} = -h\ \underline{B}_1\cos(\omega t+\phi) \sum_{\iota} \gamma^{\iota}\hat{\underline{I}}_X^{\ \iota} \qquad (2.9)$$

$$h\mathcal{H}_{1S} = -h\ \underline{B}_1\cos(\omega t+\phi) \sum_{\iota} \gamma^{\iota}\hat{\underline{S}}_X^{\iota}$$

If we consider this Hamiltonian in a doubly rotating frame, both perturbing fields are stationary and all the contributions become time independent by the transformation

$$\mathcal{H}_{rot} = R\ \mathcal{H}_{lab}R^{-1}$$

where

$$R = \exp\left[-\iota t(\underline{\omega}_{oI}\hat{I}_Z + \underline{\omega}_{oS}\hat{S}_Z)\right] \qquad (2.33)$$

This is necessary since we wish to evaluate the Hamiltonian in an environment (set of axes) where the secular dependence of all internal Hamiltonians can be considered while under the influence of the perturbing fields. Figure 2.4 illustrates a classical (2.4a) and thermodynamic (2.4b) picture of the preparation of the spin systems thus far.

It is now possible to consider the two spin systems as Zeeman reservoirs which communicate through the dipolar coupling. If the abundant spins (I) are given a high degree of spin order (thermodynamically cold) and the dilute spins (S) are brought into thermodynamic contact, polarization transfer will occur. Eventually an equilibrium will be established in a time T_{IS}. This will occur at a maximum rate when the Hartmann-Hahn condition is satisfied such that

Figure 2.4 : The Cross - Polarization Sequence

a) Radio - frequency Spin-Locking

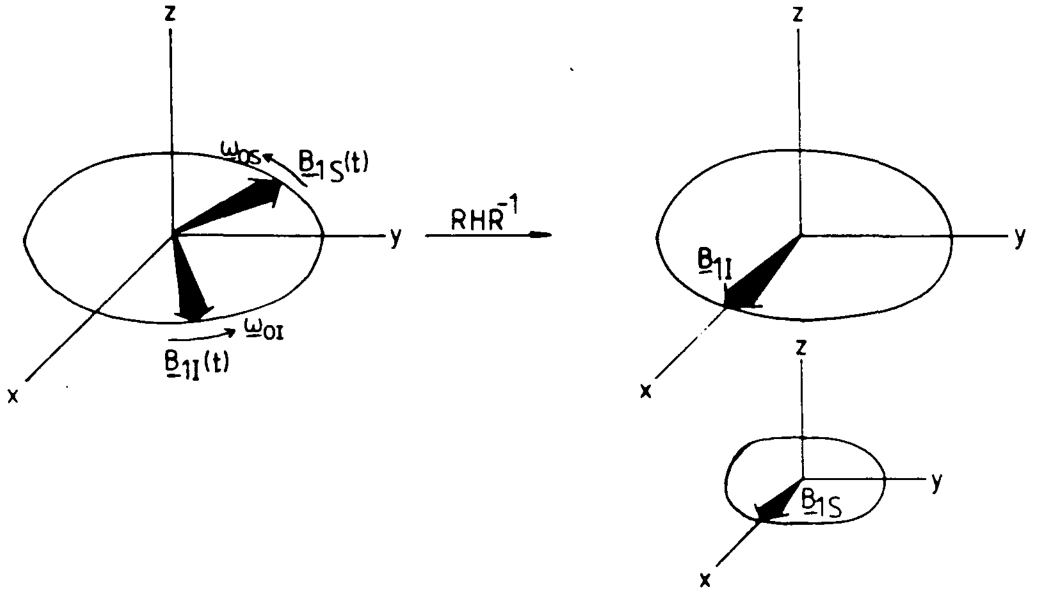

b) Thermodynamic response

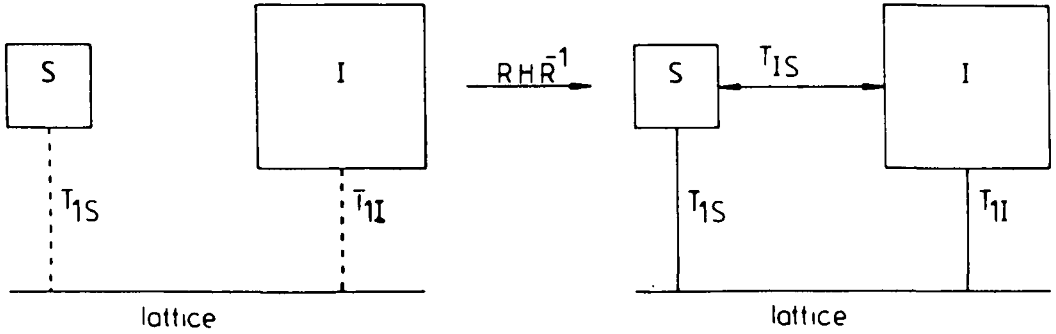

$$\gamma_I \underline{B}_{1I} = \gamma_S \underline{B}_{1S} \qquad (2.34)$$

The dilute spin system may now be observed directly, and will exhibit a magnetization enhancement which is proportional to the ratio of the γ's involved.

A further advantage of using the abundant spin reservoir as a polarization source, is that the relevant relaxation mechanisms controlling the experiment are wholly dependent upon the abundant nuclei. This is usually a distinct advantage since, because of the scarcity of the dilute nuclei, the T_1 and $T_{1\rho}$ values tend to be long.

In order for any mechanism to cause spin relaxation at a nuclear site, it must be able to produce an oscillating magnetic field of a frequency which is in resonance with that of the nucleus which is to be relaxed. The correlation time, τ_c, has been defined to characterise the average time in which a relaxation transition might be induced at a nucleus. From Figure 2.5 it can be seen that the T_1 is going to be proportional to the correlation time in the region where $\omega_L\tau_c$<<1. In the solid state this is not always the case. The question of which side of the minimum point in Figure 2.5 ($\omega_L\tau_c = 1$) the measurements are made on is an important one, since it reverses the conclusion concerning the relative mobility of the nuclear site.[42]

Figure 2.5 : Effect of Molecular Motion on Relaxation

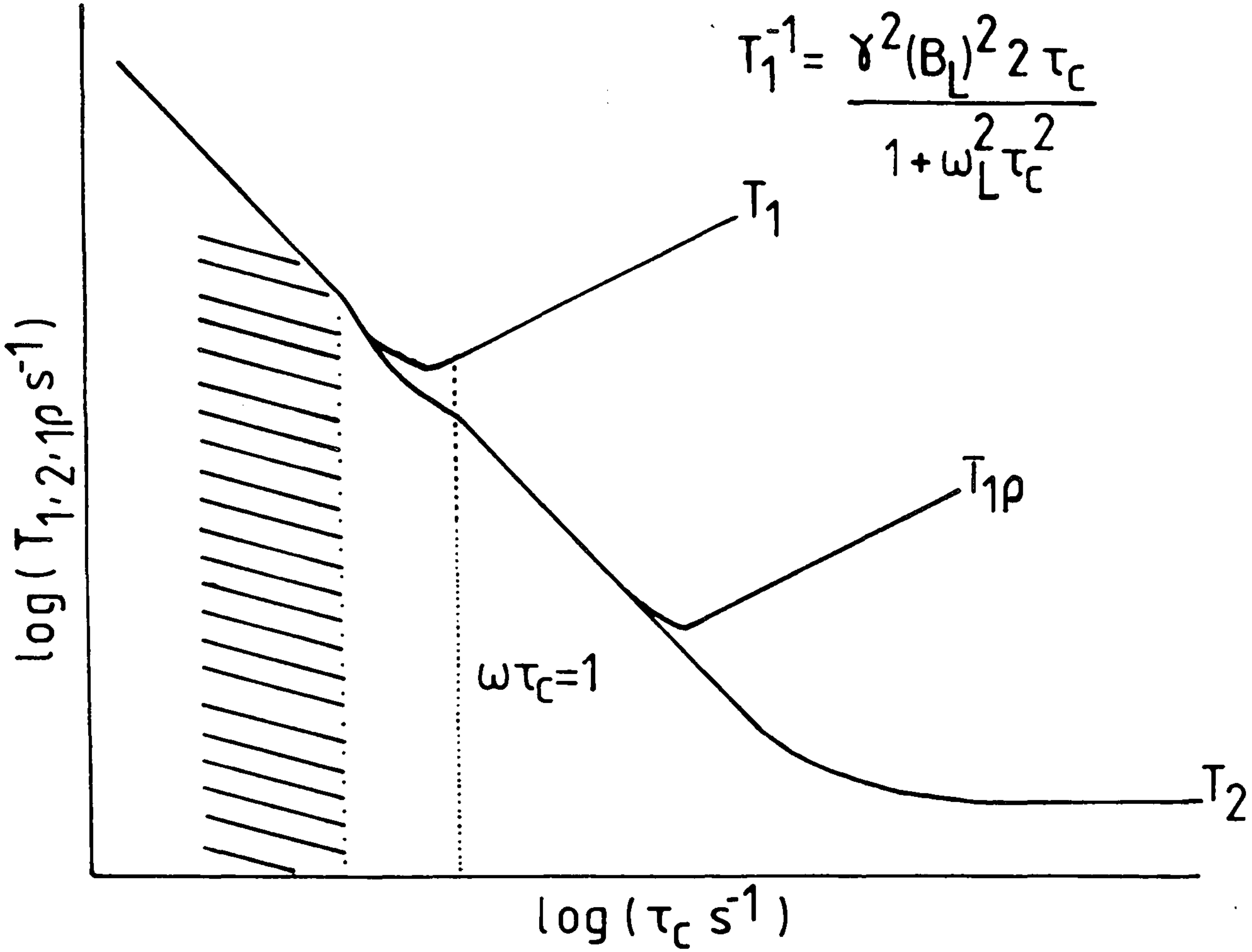

2.5.1 Spin Dynamics of the CP Experiment

In order to properly understand the nuances of the CP experiment it is necessary to consider the spin dynamics in further depth.[43]

If we reconsider equation 2.35 we see that it can be rewritten

$$h\mathcal{H}_{eff} = h\mathcal{H}_{ZI}(t) + h\mathcal{H}_{ZS}(t) + h\mathcal{H}_{II} + h\mathcal{H}_{SS} + h\mathcal{H}_{1S} \qquad (2.35)$$

where $\mathcal{H}_{ZI}$ and $\mathcal{H}_{ZS}$ are the Zeeman energies of the abundant and dilute spin systems, respectively. In the doubly rotating frame we can write a truncated Hamiltonian as

$$h\mathcal{H}_{rot} = -\gamma_I h\left[\frac{\left[\underline{B}_o+\underline{\omega}_I\right]}{\gamma_I}\hat{I}_Z+\underline{B}_{1I}\hat{I}_X\right]$$

$$-\gamma_S h\left[\frac{\left[\underline{B}_o+\underline{\omega}_S\right]}{\gamma_S}\hat{S}_Z+\underline{B}_{1S}\hat{S}_X\right] \qquad (2.36)$$

$$+ \quad h\mathcal{H}_{II} + h\mathcal{H}_{SS} + h\mathcal{H}_{IS}$$

$$+ \quad \text{time dependent terms.}$$

The secular terms commute with the static Zeeman interaction and are of the usual form (equation 2.32) where $\mathcal{H}_{IS}$ represents the energy conserving flip flop term between unlike spins.

The Zeeman terms $\mathcal{H}_{ZI}$ and $\mathcal{H}_{ZS}$ commute with each other, and cannot exchange energy directly. However, as long as $\underline{B}_{1I} = 0$, $\mathcal{H}_{ZI}$ will not commute with $\mathcal{H}_{IS}$, and coupling may occur between these terms. Similarly, so long as $\underline{B}_{1S} = 0$, $\mathcal{H}_{ZS}$ may couple with $\mathcal{H}_{IS}$, and now the polarization transfer pathway is obvious. The cross-relaxation time T_{IS} will depend upon several parameters:

1. Degree of match between energy levels.
2. Heat capacity of reservoirs (thermodynamic)
3. Strength of coupling (through non-commutation properties of terms).

The nature of the cross-relaxation mechanism has been investigated in some depth in order to quantify the magnitude and character of contributions to this term.[41,44,45] Further consideration has been given to the nature of T_{IS} under static[38] and MAR[40] conditions, and the effect on the Hartman-Hahn mismatch. Equation 2.32 exhibits a dependency of the dipolar coupling terms for unlike spins on β. Naively, one would expect a suppressed cross-relaxation to occur at $54^{o}44'$, and this has been experimentally confirmed.[38]

The subject of cross-polarization and the effect of cross-relaxation will be discussed again with experimental evidence in later chapters.

CHAPTER THREE

EXPERIMENTAL

"Everybody wants to peel their own banana"
Young's Principle on emergent Individuation

3.1 The Spectrometer Systems

The spectrometer which was used for the majority of the investigations performed in this thesis is a Bruker CXP-200 NMR spectrometer equiped with a 4.7 Tesla widebore (89.5 mm) magnet. The instrument is double channel and 'multinuclear' over a wide range of operating frequencies. The relevant properties of the nuclei studied in this thesis are shown in Table 3.1.

Table 3.1 Operating Criteria for Relevant Nuclei

	Spin	Natural Abundance%	Sensitivity (relative to proton)	Frequency (MHz)
^{1}H	$\frac{1}{2}$	100	1.0	200.13
^{19}F	$\frac{1}{2}$	100	0.8	188.276
^{13}C	$\frac{1}{2}$	1.11	1.7 E-4	50.322
^{23}Na	$\frac{3}{2}$	100	9.2 E-2	52.938
^{27}Al	$\frac{5}{2}$	100	0.2	52.147
^{29}Si	$\frac{1}{2}$	4.7	3.7 E-4	39.747
^{79}Br	$\frac{3}{2}$	50.5	4.0 E-2	50.155
^{127}I	$\frac{5}{2}$	100	9.5 E-2	40.047

The CXP spectrometer is equipped for solution and solid state NMR research and we list here briefly those features relevant to the investigations in this thesis;

- fast digitation (spectral widths ≙ 1 E 6 Hz)
- broadband tunable low frequency channel (4 to 95 MHz ~800 W)
- switchable high frequency channel (188/200 MHz ~ 800 W)
- two broadband high resolution MAR (Andrew-Beams type) solids probes covering 30-80 MHz between them
- two broadband high resolution MAR (double bearing) solids probes covering 20-90 MHz
- one purpose built probe for the CRAMPS experiment to be described in section 3.2
- one high power high frequency solids probe.

The details of this spectrometer construction are well known[1] and transparent to most aspects of the experiments performed throughout the course of these investigations, except where noted.

For the purposes of verification or alternatively because of the complementary nature of techniques, several other spectroscopic instruments were used to obtain data presented in this thesis. These instruments are listed here with any pertinent operating notes.

The Fourier Transform Infra-red spectra were obtained using a Nicolet 60 SX airbearing FTIR Spectrometer equiped with Marrick Praying Mantis diffuse reflectance accessory which was accomodated within the purging chamber. Background subtraction was used on all runs, a null file having been run using KBr. All experiments were run under

N_2(g) to eliminate CO(g) and H_2O(g) interference.

All powder diffraction data were run on a Philips PW1130 spectrometer equiped with a 3 kilowatt generator, PW1050 goniometer head and using Co Kα radiation source. The samples were finely ground and loosely presented on double sided tape mounted on a glass slide.

All solution state NMR data were recorded on a Bruker AC-250 spectrometer equiped with a 5.8 Tesla narrow bore magnet. Samples were run locked to an internal deuterated solvent. Degassing was not considered necessary.

Some samples were run at higher field in order to check true linewidth or quadrupolar effects. Where this was the case, the spectra were obtained using a Varian VXR-300 configured with a 7.0 Tesla narrow bore magnet. A double bearing probe system designed by Doty was used which allowed MAR of between three and four kilohertz. High power decoupling was limited to ~200 watts on this spectrometer, corresponding to a decoupling field of approximately 30 kHz.

3.2 Configuration of a Probe to Perform CRAMPS Experiments

The basic design criteria which are important in the configuration of an NMR spectrometer have been well documented in the literature.[2,3] With respect to research into solids, using NMR methods, additional constraints are placed upon the spectrometer, especially with regard to delivering a very <u>intense</u> (high wattage), <u>short</u> (ca 2-5 μs) and <u>coherent</u> (homogeneous and phased) pulse to the sample. The capabilities of the CXP spectrometer are such that, for most purposes, all components can be treated as completely adequate to this task. This is not the case however, when considering the CRAMPS experiment, for the simple reason that this technique is extreme in its sensitivity and demands upon all three criteria mentioned above. Specifically, the probe used in these investigations warrants a great deal of attention, and it is the detail of the experience gained in the successful configuration of a CRAMPS probe which comprise this section.

3.2.1 Criteria and Design

Essentially there are two separate and serious questions to be answered which seem to approach each other from opposite directions. They are: 1. what is the best way to present the sample to the rf? and 2. what is the best way to present the rf to the sample? These are not the same question and find their answers in different constraints, although they form a summation such that if either answer fails, the experiment fails also.

The first question can be considered by defining the experimental conditions in more detail. The investigations will study proton and fluorine nuclei in a variety of solid matrices. By definition the sample must be spun stably and rapidly, and for the experiments of interest, about the 'magic angle'. Given these criteria it is possible to make deductions about the optimum sample delivery system. The size of sample need not be large since both the proton and fluorine nuclei are abundant and very sensitive to the NMR experiment. This will also help on the rf side since it lessens the area over which an homogeneous rf field must be assured. The shape of the sample should be round in order to provide an electrically 'soft' appearance to the pulse.[4] The rotors must also be transparent to the experiment such that no background signal is present. Additionally the rotors should spin stably at high speeds (ca 3-4 kHz), and accommodate a variety of sample types.

The details of spinner design and construction have been considered in the literature.[5] Given the materials available and the expertise of the machine shop resident in this university, the design chosen was a double bearing system, shown in Figure 3.1. These rotors were machined from two polymers to allow for background free operation for two different nuclei. The rotors intended for the proton CRAMPS experiments were made from KEL-F-281 and the rotors for use in the fluorine-19 investigations were machined from an acetal polymer, Delrin. The mass of the sample relative to that of the rotor was small (ca 16 mm^3) which made these rotors extremely stable in their spinning speed. The use of a double bearing system helped to assure a constant angle orientation over a variety of spinning speeds.

Figure 3.1

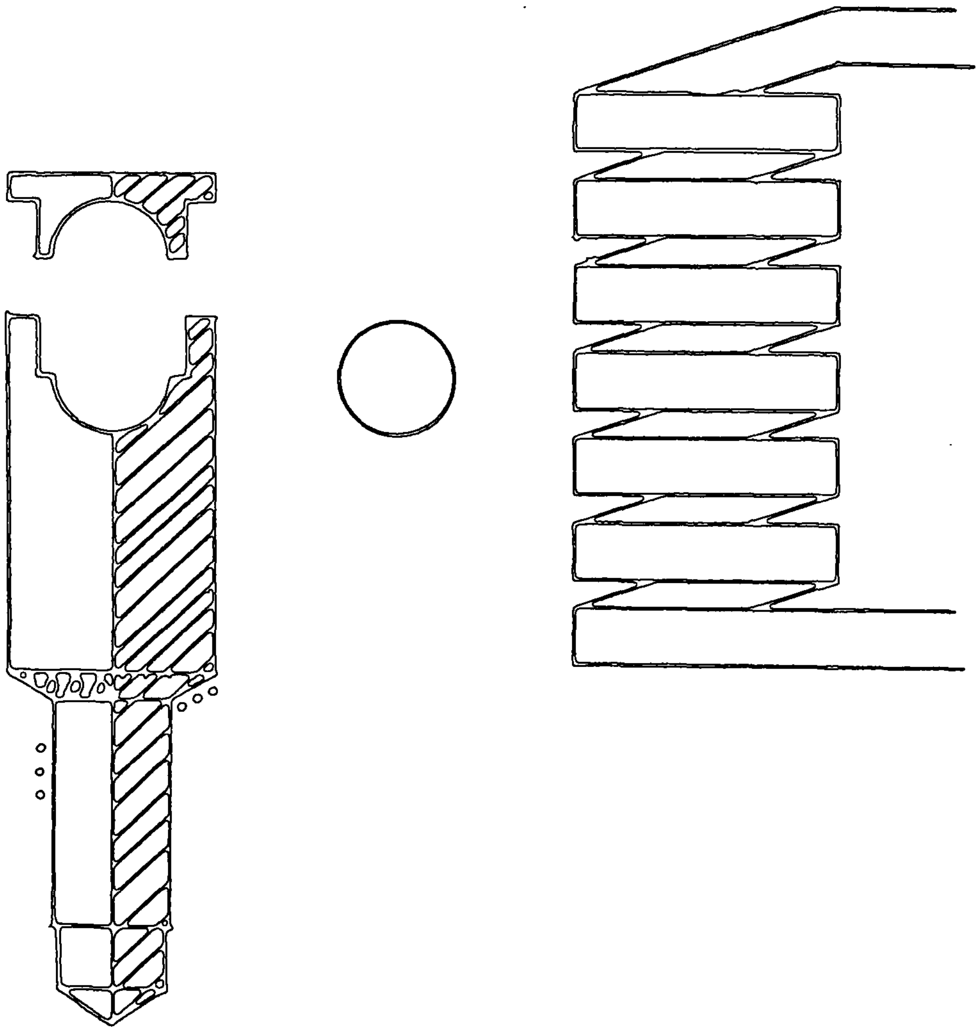

Figure 3.2

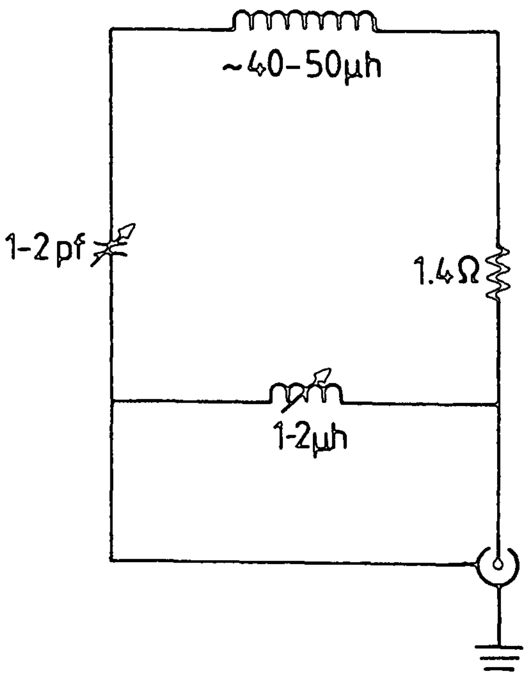

The dimensions of the rotor were adjusted to deliver the sample sphere in the middle of the sample coil where the most homogeneous rf field would be.

The second question, concerning the presentation of the rf field, requires much more complicated considerations. The rf field in the coil must be intense, highly homogeneous, and fall off quickly after the pulse in order to allow observation of quickly decaying signals. The design should be such that probe tuning and shielding remains fixed between experiments and yet versatile enough to accommodate a variety of samples which may or may not be electrically transparent (i.e. ionic compounds, electrically lossy samples).

A number of different strategies have been documented in the literature to meet these criteria, ranging from low power, high Q circuits[6] to high power, low Q circuits[7]. The system chosen for these investigations uses a single series resonant coil for both transmitting the rf pulse and detecting the NMR signal. As shown in Figure 3.2 the coil is inductively matched to earth and capacitively tuned to resonance. The matching load is set to the nominal 50 Ω load requirement of the transmitter and receiver. This circuit is set up with a low 'Q', conveniently spoiled by a bundle(ca. 4) of $\frac{1}{4}$ watt, 5.6 ohm resistors sitting in front of the coil.

The coil inductance depends upon the diameter and the number of turns in the coil according to the formula[3];

$$L = n^2 a^2/(9a + 10b) \qquad (3.1)$$

where n = number of turns in coil

a = diameter of coil (inches)

b = length of coil (inches)

Given that the 'Q' of a system is defined[3] as

$$Q = \frac{\omega_o L}{R}$$

where L = inductance (μhenries)

R = resistance (ohms)

ω_o = resonant frequency (MHz)

it is possible to make an educated guess of the quality factor 'Q', of a circuit given the coil dimensions.[8] An optimum valve of 23 has been calculated,[9] and it is in this neighbourhood that it is wished to operate. It will be assumed that the bundle of resistors in the circuit efficiently "spoils" the Q of the resonant coil and determines the effective resistance in the circuit. For a coil of 5 turns with diameter 7 mm and length 18 mm there will be an inductance of approximately 46 μhenries. Since the tuning capacitor is an air dielectric 'pfenig' type, it is reasonable to assume a perfect Q value, so this component may be ignored. This gives a Q of approximately 30 at 200 MHz, which is a reasonable "ball park figure" given the number of assumptions made through the course of this calculation. The circuit shown in Figure 3.2 gives a band width of approximately 5-6 MHz, which is too narrow to allow retuning between the operating frequency of ^{1}H and ^{19}F nuclei.

Accordingly the resonant coil must be changed to allow for the 12 MHz frequency shift. A dual channel probe is currently under construction which may circumvent this problem.

Figure 3.3 shows the final products of these design considerations. Two spinning stators are shown; the aluminium rig, in place in the probe, was designed for experiments involving very low levels of protons. Generally it was much more troublesome in its spinning behaviour and electrical matching than the polymer stator shown on the right of the Figure. Below right are shown the Kel-F and Delrin rotors, and below them the matching inductor and bundle of non-magnetic resistors. The flat wire coil was found to be superior to round wire coils in homogeneity and power handling capabilities in all circumstances. The flat wire was rolled flat on a rolling mill from 18 and 20 gauge tinned copper or copper wire. The surface was then treated to remove any aberrations before final winding and shaping.

The final product shown in Figure 3.3 was found to perform adequately for a variety of MPS experiments and over a diverse range of sample matrices. Documentation of the behaviour of this probe will be discussed in Chapter 4.

Figure 3.3: Proton and Fluorine-19 CRAMPS Probe

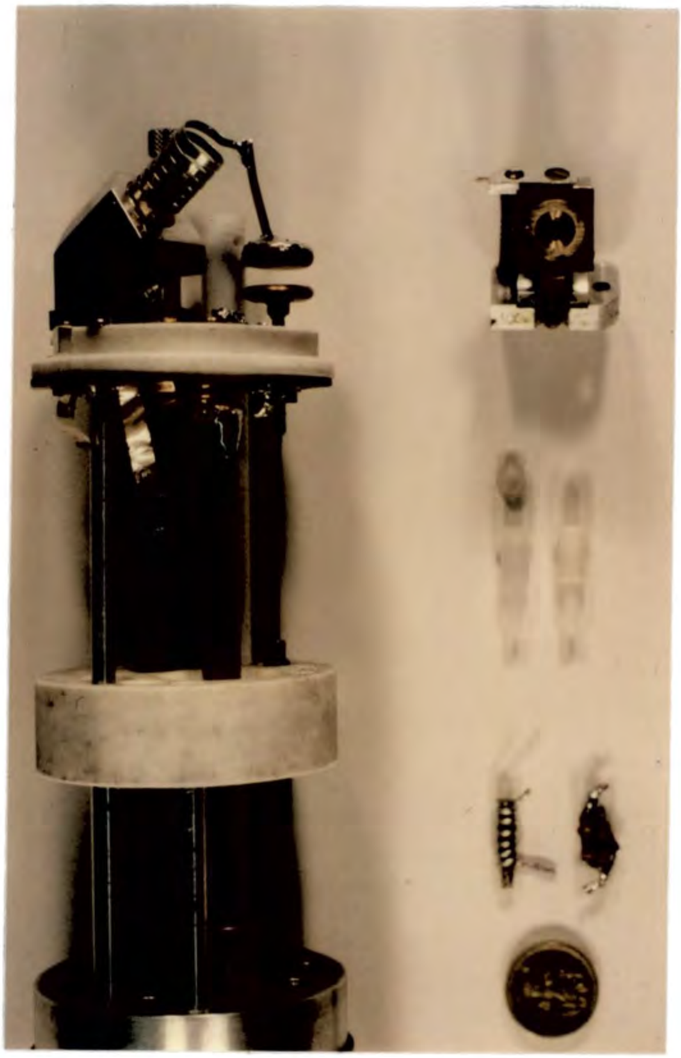

3.3 Pulse Sequences

A variety of different pulse sequences were used to extract the magnetic resonance data presented in this thesis. The purpose of this section is to document those sequences and give comment on their implementation. The sequences have been diagrammatically tabulated in Figure 3.4.

The single pulse and single pulse-decoupled sequences shown in Figure 3.4a and b were part of the standard Library programs available with the CXP spectrometer. The cross-polarization sequence (Figure 3.4c) used spin temperature inversion[11] and flipback[12] to eliminate instrumental artifacts and reduce the recycle time, respectively. The standard Bruker phase-cycling was found to be in error, which necessitated a new program, PESTNMR.PPG, to be written in order to obtain 'true' spin temperature inversion and flipback under quadrature detection conditions.

The multiple pulse sequence which was used in the CRAMPS experiments was coined UNIPAMPS.PPG and is shown in Figure 3.4g.[13] This was a mnemonic for UNIversal Phase Alternating Multiple Pulse Sequence. This sequence will accommodate most symmetrised pulse sequences with the only difference being a spin temperature inversion phase alternation step, which helps to reduce spurious ringing and carrier frequency break through. This sequence will be discussed in more detail in Chapter 4, where the spin response to symmetrised pulse suquences will be covered.

There are several methods of measuring the relaxation properties of nuclei in a solid. The choice of a method is dependent upon the nature of the nuclei being measured. The inversion recovery method[14] (Figure 3.4f) was used for all proton relaxation measurements. This data was subjected to exponential fitting[15] in order to minimize T_1 error. Where relaxation data were desired for quadrupolar nuclei, the composite-π-inversion method[16] (Figure 3.4e) was modified to include decoupling conditions. This sequence was employed to insure broadband inversion of the entire quadrupolar linewidth. The DANTE[17] sequence was used to measure relaxation mechanisms under polarization transfer conditions and is shown in Figure 3.4d. This sequence was implemented with a flipback pulse, but pulse programmer size limitations prevented spin temperature inversion from being employed.

This completes the discussion of the pulse sequences utilized in this thesis.

FIGURE 3.4

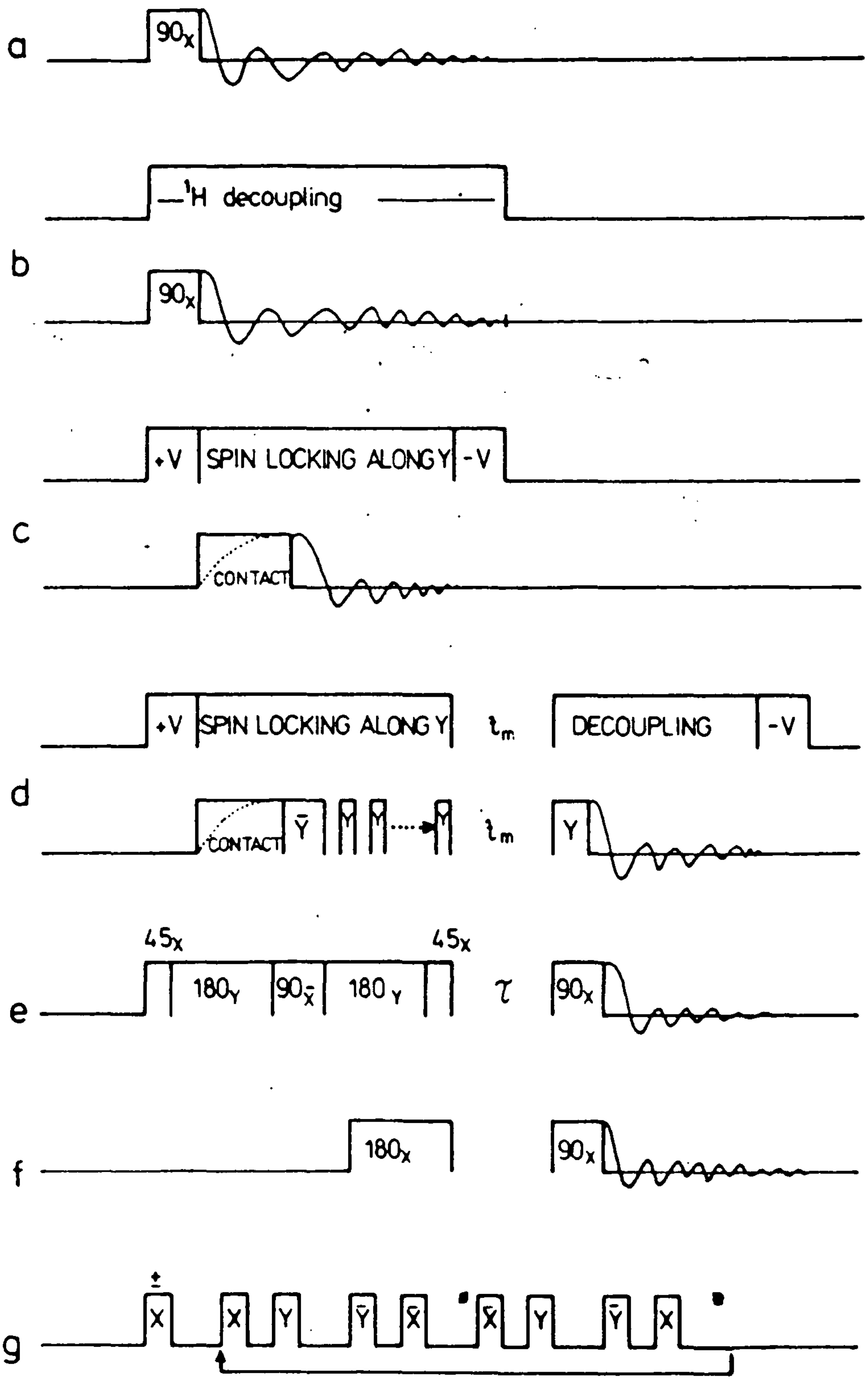
a
90x
—1H decoupling
b
90x
+V
SPIN LOCKING ALONG Y
-V
c
CONTACT
+V
SPIN LOCKING ALONG Y
tm
DECOUPLING
-V
d
CONTACT
Ȳ
Y
Y
Y
tm
Y
45x
45x
e
180Y
90X̄
180Y
τ
90x
f
180x
90x
g
±
X
X
Y
Ȳ
X̄
X̄
Y
Ȳ
X

3.4 Referencing Methods

A variety of nuclei were used in the course of these investigations, as molecular probes from which to gather chemical data using magnetic resonance methods. For each nucleus, referencing standards and nomenclature have been established in the literature. It is the purpose of this section to document the notation employed in this thesis.

3.4.1 Proton and Fluorine-19 Referencing

The problems associated with chemical shift scaling in the CRAMPS experiment will be covered in detail in the following Chapter. It will suffice to state at this point, that because of nonlinear behaviour of scaling information in the CRAMPS experiment, it was prudent to use an internal referencing standard to directly measure the chemical shift.

In the case of ^{1}H CRAMPS, one or two crystals of adamantane (1.74 ppm relative to TMS) could be added to a sample after conditions had been optimised on the 'clean' aliqout. For ^{19}F CRAMPS, a small amount of CaF_2 (-107.7 ppm relative to $CFCl_3$) was added to the sample in the same manner as for ^{1}H CRAMPS.

3.4.2 Silicon-29 Referencing

The silicon-29 chemical shifts were obtained using Q_8M_8 as a secondary reference by replacement. The chemical shift for the most intense peak in the trimethylsilyl (M) region was set at +11.5 ppm[18] relative to the resonance of TMS A consistent relationship has been established between the condensation of a silicon site and the chemical shift.[19] From this a notation has been established which correlates the region of chemical shift to the structural configuration of a nuclear site.[20] The "Q^0 to Q^4" notation will be used in this thesis to indicate sites with 4 hydroxyl groups to sites with none, respectively.

3.4.3 Sodium-23 Referencing

The chemical shift of sodium-23 was referenced relative to Na^+ (aq) at infinite dilution.[21] This gives NaCl (s) a chemical shift of +7.1 ppm, which was used as the most convenient compound to calibrate the spectrometer,under actual operating conditions.

3.4.4 Aluminium-27 Referencing

The chemical shift of aluminium-27 was referenced relative to octahedral Al^{+3} using a 1 M solution of $Al(H_2O)_6{}^{3+}$ (aq). The single absorbance line was set to zero ppm.

3.4.5 Carbon-13 Referencing

The chemical shift of Carbon-13 nuclei were referenced relative to TMS This was done by secondary reference, using adamantane, setting the high frequency absorbance as -38.5 ppm.

3.4.6 Rotation Angle Adjustment

During any of the MAR experiments the angle of the spinning axis of the rotor, relative to the static field, was set to $54^o44'8''$. This was done in a sensitive manner by maximising the spinning sideband pattern resulting from the first-order quadrupolar transitions of Br-79 or I-127. This method has been shown to be accurate within $\pm$ 0.1^o of the angle.[22]

3.5 Materials Studied

The chemicals, compounds and materials used in this thesis originated from a wide variety of sources. They will be listed here, roughly grouped in the 'projects' they formed when the research was carried through. All sample aliquots were studied in the powdered form, and stored in glass vials between analysis.

3.5.1 Silicate Material Sources

A number of different areas in solid state silicate chemistry were investigated through the course of this research. The sources of these compounds are documented in the following text.

The layer silicates are described in Table 3.2. All minerals were subject to powder diffraction analysis in order to check the validity of their assignment. The meta silicates are listed in Table 3.3. Obtaining high quality samples of these types of minerals was difficult. Even 'gem' quality was no assurance of purity, since often it is a paramagnetic inpurity which provides the colour which makes the mineral attractive as a gem-stone.

Table 3.2 Layer Silicate Sources

Silicate	Source	Description
KENYAITE	LDG*	MAGADII LAKE, KENYA
KENYAITE	BM*	OHBM 1971
KENYAITE	CURETON*	MAGADII LAKE, KENYA
MAGADIITE	CURETON	TRINITY COUNTY, CALIFORNIA
MAGADIITE	BM	OHBM 1971, 321, GABON
MAGADIITE	LDG	NATURAL
MAGADIITE	LDG	SYNTHETIC
MAGADIITE	SHELL*	SYNTHETIC NH_4^+
MAGADIITE	SHELL	SYNTHETIC Na^+
OCTOSILICATE	LDG	SYNTHETIC
KANEMITE	LDG	SYNTHETIC (from Philadelphia) Quartz)
MAKATITE	LDG	SYNTHETIC
PRECIPITATED SILICA	LDG	SYNTHETIC

*LDG = Courtesy of Leslie Dent-Glasser, Dept. of Chemistry, Aberdeen University.

*BM = Courtesy of John Fuller, British Museum, Mineralogy.

*Cureton = Cureton Mineralogical Co., Tucson, Arizona.

*Shell = Courtesy of G.R. Hays, Shell Laboratorium, Amsterdam.

Table 3.3 Meta Silicate Sources

Silicate	Source	Description
Ca-metasilicate	LDG	SYNTHETIC
Ba-metasilicate	LDG	SYNTHETIC
Sr-metasilicate	LDG	SYNTHETIC
Na-metasilicate	LDG	SYNTHETIC
α-wollastonite	RFP*	NATURAL (P1 grade)
β-wollastonite	RFP	NATURAL (P4 grade)
enstatite	RFP	NATURAL
apophyllite	CURETON	NATURAL

*RFP = R.F.D. Parkinson & Co., Somerset.

Tables 3.4 describes the silica polymorphs and hydrated silicates studied. All of these samples were mineralogical specimens.

Table 3.4 Silica Polymorphs Sources

Silicate	Source	Description
CHALCEDONY	RFP	SOUTH AFRICA "BLUE LACE AGATE"
CHALCEDONY	RFP	DEVON
CHALCEDONY	RFP	CORNWALL
FLINT	GBL*	KENT
FLINT	RFP	WILTSHIRE
QUARTZ	RFP	Co. DURHAM
OPAL	GBL	HUNGARY
AMETHYST	RFP	ZAMBIA

*GBL = Gregory, Bottley & Lloyd, Mineralogists & Geologists, London

The spray dried silicates are shown in Table 3.5. All of these powders were obtained courtesy of Unilever Research, Port Sunlight.

Table 3.5 Spray dried Silicates

Sample	$SiO_2:Na_2O$ Ratio
PH 45	3.3
PH 46	3.0
PH 47	2.6
PH 48	2.0
PH 50	1.4
PH 50/A	1.4
PH 51	1.0

These systems were produced in an industrial pilot plant by mixing Na_2CO_3 and SiO_2 slurr~~y~~ies, at a given ratio, and aspirating the mixture into a drying tower held at constant humidity. Sample aliquots were taken in the middle of each run and final ratio determined by conventional volumetric analytical analysis.

3.5.2 Crown Ether Sources

The crown-ethers studied in this thesis are described in Table 3.6. The nomenclature and general chemistry has been reviewed in the literature.[23] The synthesis of the Na-18-C-6 complex was completed in this laboratory according to a well established preparation.[24]

Table 3.6 Description of Crown Ethers

Crown Ether	Source
Na-18-C-6	SYNTHETIC
Na-15-C-5	D.P.*
$NaClO_4$.Benzo-15-C-5	FRI**
$NaClO_4$.2Benzo-15-C-5	FRI
***$NaBPh_4$.Benzo-15-C-5	FRI
$NaBPh_4$.2Benzo-15-C-5	FRI
$NaBPh_4$.Benzo15-C-5.EtOH	FRI
NaI.Benzo15-C-5.H_2O	FRI

*D.P. = Courtesy of D. Parker, Dept. of Chemistry, Durham University

**FRI = Courtesy of The Food Research Institute, Norwich

***$NaBPh_4$ = sodium tetraphenylborate

3.5.3 Sodium Borate Sources

The sodium borates are described in Table 3.7. The Borax was commercially available, and used to prepare the Tincalconite according to the literature.[25]

Table 3.7 Description of Sodium Borates

Borate	Formula	Source
Borax	$Na_2B_4O_7.10H_2O$	BDH 30231
Tincalconite	$Na_2B_4O_7.5H_2O$	SYNTHETIC

3.5.4 FLUOROPOLYMER SOURCES

A number of different fluoropolymers and crystalline precursors were studied. The source of these materials and/or their exact composition will not be given, but the samples will be referred to in code throughout the text where they are discussed. Any other crystalline standards were commonly available through commercial suppliers and will be indicated as such.

CHAPTER FOUR

HIGH γ NUCLEI: ^{1}H and ^{19}F CRAMPS DEVELOPMENT

"The true creator is necessity, who is
the mother of invention".
Plato

CHAPTER 4: HIGH γ NUCLEI: PROTON AND FLUORINE-19 CRAMPS DEVELOPMENT

4.1 Brief Literature Evaluation

4.2 Theory of Spin Response

4.3 Experimental Optimisation

4.3.1 Proton Details

4.3.2 Fluorine Details

4.4 Conclusions

Chapter 4: High γ Nuclei: Proton and Fluorine-19 CRAMPS Development

The purpose of this chapter is to discuss the relevant details of performing CRAMPS experiments on solid materials. The proton and fluorine nuclei are treated equivalently throughout this discussion, excepting in Section 4.3 where aspects of experimental design criteria inherently differentiate the two cases. Most applications of the experiment are left to Chapter six, but the limitations and capabilities of the experiment will be demonstrated for both nuclei using relevant examples.

The incentive for the development of these techniques was project-driven, meaning, as the need for data arose in the study of a chemical system the method was developed to deliver the results. This experimentalist approach to the subject will be reflected in the discussion.

4.1 Brief Literature Evaluation

The nature of dipolar broadening and its contribution to the solid state NMR lineshape has been described in Chapter two in the manner used by Pake.[1] The experimental methods demonstrated in that paper realised an order of resolution that allowed NMR to be used extensively as a complimentary technique in the analytical investigation of hydrogen and fluorine bonding in the solid state.[2] The application of 'high resolution' methods began with the demonstration of a ten fold reduction in the fluorine-19 line width of CaF_2 using a magic-angle field rotation experiment.[3] Further resolution was achieved with the development of symmetricized multiple pulse sequences[4] and their combination with magic angle specimen rotation.[5,6]

The CRAMPS experiment has been applied to a variety of organic solids,[7] polymers and coals[8] in low magnetic fields (ca. 1.1 Tesla) giving good resolution of isotropic chemical shift values. Variation of the angle of alignment of rotation axis, relative to the static field, has also shown that the chemical shift anisotropies can be recovered.[9] A further five-fold increase in resolution has been obtained by implementing the CRAMPS experiment at 6.5 Tesla.[10] The advantages of working at higher field have been verified by application to hydrogen bonding studies of organic solids[11] and silicagels.[12] Further efforts have been made, in the course of this research, utilising the fluorine-19 nucleus as a molecular probe in organic solids[13] and fluoropolymers[14] at moderately high field (4.7 Tesla).

The theoretical intricacies of these experiments have been rigorously treated in the literature.[15] The intention in this chapter is to evaluate those aspects of the CRAMPS technique, which have been found to be experimentally critical, in application to difficult chemical systems at moderately high magnetic fields.

4.2 Theory of Spin Response

The key to extracting information from a solid, using magnetic resonance methods, is coherent averaging.[15] The object is to experimentally manipulate selected internal Hamiltonians, such that they average to zero, leaving other desired interactions available for detection and measurement. The manipulation takes the form of an imposed time average of the unwanted interaction. An interaction will experience averaging through an experiment if it is made time dependent relative to the time constant describing the character of the interaction contribution (ie linewidth).

A variety of methods with which the investigator may assert time dependence upon an interaction have been discussed in Chapter two (see Table 2.2). Further, the effect of sample rotation has been treated as a general form of a rotation transformation, and shown to be an averaging manipulation which operates upon the spatial angular coordinates of the internal Hamiltonians. This section will address the method of averaging in spin space using symmetricized multiple pulse sequences.

The most simple way to document the discriminating nature of this technique is to follow the evolution of the internal Hamiltonians through the perturbation period of a specific sequence. The most obvious choice, to be used as an example, is the UNIPAMPS sequence which was utilized for the acquisition of the data presented in this text. This sequence has been described in general in Chapter three.

The symmetricized pulse train we will consider consists of an eight-pulse MREV-8[16] sequence (composed of two WAHUHA[4] sequences placed back to back), with a phase alternation step imposed upon the perparation pulse.

In order to consider the action of any pulse sequence, it is first necessary to define a Hamiltonian describing the nuclear spin system of interest. For our purposes it is sufficient to begin with the truncated Hamiltonian in the rotating frame defined by

$$\hbar\mathcal{H}(t) = \hbar\mathcal{H}_{RF}(t) + \hbar\mathcal{H}_{D} + \hbar\mathcal{H}_{O} + \hbar\mathcal{H}_{E} \qquad (4.1)$$

where

$\hbar\mathcal{H}_{RF}(t)$ = ideal radiofrequency interaction

$$= \hbar\exp\left[-\iota\ \underline{\omega}_1\ \hat{I}_Z\ t_p\right] \qquad (4.1a)$$

$\hbar\mathcal{H}_{D}$ = truncated dipolar Hamiltonian

$$= \sum_{I<S}\sum \frac{\gamma^2\hbar^2}{r^3_{IS}}\left[3\hat{I}_{IZ}\hat{I}_{SZ} - \hat{\underline{I}}_I\cdot\hat{\underline{I}}_S\right] \qquad (4.1b)$$

$\hbar\mathcal{H}_{O}$ = off resonance and chemical shift Hamiltonian

$$= \hbar\sum_{I}\left[\Delta\underline{\omega} + \underline{\omega}_0\underline{\sigma}_{ZI}\right]\hat{I}_{ZI} \qquad (4.1c)$$

$\hbar\mathcal{H}_{E}$ = pulse imperfection Hamiltonian

$= \hbar\sum_{K}\mathcal{H}_K(t)$ where K is a summation over all (4.1d)

imperfections and can describe

$$\left.\begin{array}{lll} \text{phase error} & \hbar\mathcal{H}_K = & \hbar-\underline{\omega}_1\sin\phi_X\hat{I}_Y \\ \\ \text{phase transients} & \hbar\mathcal{H}_K = & \hbar\underline{\omega}_T(t)\hat{I}_Y \\ \\ \text{pulse length error} & \hbar\mathcal{H}_K = & \hbar\dfrac{\delta_X}{t_p}\hat{I}_X \\ \\ \text{rf inhomogeneity} & \hbar\mathcal{H}_K = & \hbar\displaystyle\sum_{\iota}\frac{\epsilon_\iota}{t_p}\hat{I}_X^{\iota} \end{array}\right] \quad \text{for an X pulse}$$

In the above, ϕ_X is the phase of the X pulse, δ_X is the pulse size, ω_T is the rf amplitude orthogonal to the X direction, t_p is the pulse width, and ϵ_ι is the rotation angle error at the ι^{th} nucleus caused by inhomogeneity.

By using 'average Hamiltonian theory'[17] the action of the rf perturbation can be described in an 'interaction' frame where the pulses impose a time modulation on to the other terms of the internal Hamiltonian, over the period of a cycle, t_c. The character of this modulation may be described by a time development operator, U_{rf}, and the response of the remaining internal Hamiltonians may be described by a time independent average Hamiltonian, defined by U_{int}. This may be expanded to consider higher order contributions to the average Hamiltonian[18] such that

$$U_{int}\,(t_c) = \exp\left[-\iota t_c(\bar{\mathcal{H}}^{(0)}_{int} + \bar{\mathcal{H}}^{(1)}_{int} + \bar{\mathcal{H}}^{(2)}_{int})\right] \qquad (4.2)$$

where $\bar{\mathcal{H}}^{(n)}_{int}$ is the average Hamiltonian denoting the n^{th} order of magnitude contribution to the expansion.

The properties of U_{rf} are such that it operates in analagous fashion to the rotation manipulations described in Chapter two. For example, the action of the rf time operator on the dipolar Hamiltonian, imparts a time dependence, giving an averaged dipolar Hamiltonian which can be described as

$$\bar{\mathcal{H}}_D = U_{rf}^{-1} \mathcal{H}_D U_{rf}$$

If $\mathcal{H}_{rf}$ is designed to be cyclic, then the rotating frame and the interaction frame will coincide at each cycle period where $U_{rf}(nt_c) = \pm 1$, if n is the number of whole cycles. This means there is an actual toggling point between the rotating frame of reference and the interaction frame of reference, where the Hamiltonian is common to both time domains. This is an important point, since it is during this toggling window that observation of the Hamiltonian may be made in the rotating frame as in the usual FT NMR experiment. The advantage gained is that during the time where the detector is turned off the Hamiltonian evolves in a time dependent frame of motion as a result of the pulse sequence. When the detector is turned back on during the toggling window it appears that the Hamiltonian has acquired some time averaging (determined by U_{rf}, the pulse train) relative to the time constant defining the rotating frame of reference.

The actual behaviour of the time interaction operators for the MREV-8 sequence is shown in Table 4.1. The symmetry of the sequence is obvious by inspection of the behaviour of the radio frequency interaction U_{rf}.

Table 4.1: The MREV-8 Sequence in the 'toggling' frame of Reference

Operation	$\mathcal{H}_{rf}(t)$	$U_{rf}(t)$	
t	0	1	
P_X	$-\omega_1 I_X$	$\exp[\iota\omega_1 t_1 I_X]$	
t	0	$\exp[\iota\beta I_X]$	
P_Y	$-\omega_1 I_Y$	$\exp[\iota\omega_1 t_2 I_Y]\exp[\iota\beta I_X]$	
t	0	$\exp[\iota\beta I_Y]\exp[\iota\beta I_X]$	
t	0	$\exp[\iota\beta I_Y]\exp[\iota\beta I_X]$	
$P_{\bar{Y}}$	$+\omega_1 I_Y$	$\exp[\iota(\beta-\omega_1 t_3)I_Y]\exp[\iota\beta I_X]$	
t	0	$\exp[\iota\beta I_X]$	
$P_{\bar{X}}$	$+\omega_1 I_X$	$\exp[\iota(\beta-\omega_1 t_4)I_X]$	
t	0	1	
t	0	1	TOGGLE
$P_{\bar{X}}$	$+\omega_1 I_X$	$\exp[-\iota\omega_1 t_5 I_X]$	
t	0	$\exp[-\iota\beta I_X]$	
P_Y	$-\omega_1 I_Y$	$\exp[\iota\omega_1 t_6 I_Y]\exp[-\iota\beta I_X]$	
t	0	$\exp[\iota\beta I_Y]\exp[-\iota\beta I_X]$	
t	0	$\exp[\iota\beta I_Y]\exp[-\iota\beta I_X]$	
$P_{\bar{Y}}$	$+\omega_1 I_Y$	$\exp[\iota(\beta-\omega_1 t_7)I_Y]\exp[-\iota\beta I_X]$	
t	0	$\exp[-\iota\beta I_X]$	
P_X	$-\omega_1 I_X$	$\exp[[-\iota(\beta-\omega_1 t_8)I_X]$	
t	0	1	
t	0	1	TOGGLE

where β is the flip angle and all I are spin operators

Data sampling may only occur coherently where the magnetization has been returned to the rotating frame, denoted by the unity operator in the toggling frame.

It is now possible to consider the evolution of the spin system of interest, $\mathcal{H}_D$ and $\mathcal{H}_O$, through the interaction manipulation. The interaction operator may be treated as a transformation function between the rotating and toggling frames of reference. The evolution of $\mathcal{H}_D$ and $\mathcal{H}_O$ can then be written as

$$\mathcal{H}_D(t) = U_{rf}^{-1}\, \mathcal{H}_D\, U_{rf}(t) \tag{4.3}$$

and similarly

$$\mathcal{H}_O(t) = U_{rf}^{-1}\, \mathcal{H}_O\, U_{rf}(t) \tag{4.4}$$

It has already been stated that U_{rf} is performing a modulation in a cyclic fashion with the time constant t_c. This property is also imparted to $\mathcal{H}_D(t)$ and $\mathcal{H}_O(t)$ through the transformation operation. This means that the spin system evolves with a periodic time dependence imposed by the interaction operator. Since observation is done from the rotating frame, at the toggling windows, the system appears to develop in the absence of any pulse train. The result is an NMR signal which is time averaged over the period of the cycle defined by the interaction frame, $\bar{\mathcal{H}}_{int}(t)$.

In experimental terms, the 'period' of time averaging is defined by the pulse cycle time, t_c. The interaction operator is defined by the symmetricized pulse sequence used. We have assumed during this discussion that $\bar{\mathcal{H}}_{int}(t)$ adequately describes the evolution of the spin system while in the interaction frame of reference. This is only exactly correct if $||t_c\mathcal{H}_{int}|| << 1$. In real terms this accounts for the inversely proportional relationship between cycle time and effective decoupling power. For most applications in this research the dominant part of $\mathcal{H}_{int}$ is the dipolar coupling Hamiltonian $\mathcal{H}_D$. As the absolute magnitude of $\mathcal{H}_D$ increases the cycle time defining the modulation imposed by the pulse sequence must decrease. The sequence itself is designed in order to time average the highest order of expansion of $\bar{\mathcal{H}}_D$ possible, to zero.[19,20] This removes those contribution from the rotating frame of reference leaving other terms untouched.

In an ordinary FT NMR experiment the spin ensemble will oscillate about the offset field in the rotating frame, defined by the larmor frequency. In a multiple pulse experiment the spin ensemble is observed during the toggling window. As has been stated, from the rotating frame, it appears to be moving under some effective Hamiltonian defined by $U_{rf}(t)$. Assuming 'ideal pulse' behaviour, the effective precession of the spin ensemble will be scaled by the character of the pulse sequence. Each sequence will have an 'ideal' scaling factor which is a function of the effective field created by the pulse sequence. For an MREV-8 sequence the frequency scaling is a factor of $\sqrt{2}/3$, which corresponds to a chemical shift compression of two.

The scaling will also vary as a function of frequency offset, $\Delta\omega$. As equation 4.1c evolves under the transformation shown in equation 4.4, the offset term will do so with a different field dependence than that of the larmor term. The simple explanation for this is that spins which are off resonance do not 'follow' the pusle train in an ideal sense. Since the pulses only behave ideally on (or very near to) resonance, those spins which are off resonance experience dephasing of their transverse magnetization, relative to the pulse width. This manifests itself as an increase in linewidth and will be experimentally verified in the next section.

Up to this point discussion has focused upon the MREV-8 sequence without considering the UNIPAMPS sequence fully. In table 4.1 the preparation pulse has been ignored since it plays no direct role in U_{rf}. The average Hamiltonian has been discussed for the pulse cycle defined between toggling windows where data sampling is performed. The preparation pulse positions the magnetization along the Y direction in the rotating frame, perpendicular to the effective field. This places the maximum transverse magnetization where it may respond to the symmetricized pulse train, and effectively determines the flip angle. The implementation of phase alternation on the initialing pulse is completely transparent to the symmetricised pulse sequence. Since the signal will be phase sensitive it will respond to the phase alternation, but any instrumental artifacts such as carrier frequency breakthrough will remain insensitive. By phasing the receiver in step with (but orthogonal to) the preparation pulse it is then possible to subtract the instrumental artifacts from the true signal. This results in a two phase cycle where the signal averages on every second free induction decay and any artifacts cancel. This completes the limited theoretical treatment of the pulse and spin response to multiple pulse sequences.

4.3 Experimental Optimization

Relative to a 'standard' FT NMR single or double resonance experiment, the optimization of a spectrometer for a multiple pulse experiment can be complicated. The advent of flip-angle-compensated cycles such as MREV-8 has greatly reduced the sensitivity of the experiment to misadjustment, but this remains an important concern for optimum resolution. As previously stated with regard to the CRAMPS experiment, the most critical component of the spectrometer, given the current quality of commercially available hardware, is the probe. Assuming that a probe can be configured such that a circuit residing within will deliver sufficiently strong and homogeneous rf power to accommodate the investigations of interest, the critical factor then becomes the perturbing pulse train. For optimum resolution the pulses must be finely tuned for coherent phase, duration, and amplitude relative to each other. This operation has received some attention in the literature in attempts to develop a simple methodical approach to the spectrometer adjustment.[21,22] Specific pulse sequences have been developed as an aid to sensitive adjustment[23], and the relevant tuning criteria have been evaluated.[8,24]

The exact method used to calibrate the CXP-200 spectrometer employed for this research followed closely the application note recommended by the manufacturer.[25] Essentially the method is similar to those documented in the literature, using a recursive application of phase and amplitude sensitive pulse sequences to orthogonalize the X and Y channels of the transmitter, relative to the receiver.

There is very little to add to this procedure except a word of caution; check the calibration against a standard, often. An example of such a check is shown in Figure 4.1. This figure is composed of co-added signal averaged transients of the proton CRAMPS spectra of (Adamantane) at several different offset frequencies. On resonance the single absorption line gives a scaled resolution of 0.2 ppm line width. This calibration check exhibits the $\sqrt{2}/3$ frequency scaling which is theoretically expected for the MREV-8 sequence. The offset effect on T_2, discussed in the previous section, is clearly visible as the offset approaches 4000 Hz. The advantages of the 'UNIPAMPS' sequence are also evident since a flat baseline has been preserved in the frequency domain, even as the signal is moved onto the carrier frequency. This completes the general discussion of setting up the CRAMPS experiment. The details that remain to be commented upon are specific to the nuclei under observation.

4.3.1 Proton Details

The fine tuning of the spectrometer for ^1H CRAMPS was performed on a spherical glass pearl which contained tap water. The pearl was mounted in a rotor and spun slowly in the probe. A reasonable coil would be expected to give an homogeneous line width, upon shimming, of two to five Hz, which was sufficient to continue with the tune-up procedure. The 90^o pulse length was usually set at 2 μs. The cycle time varied between 16 μs to 24 μs depending upon the experiment.

Figure 4.1 : PROTON CRAMPS CALIBRATION

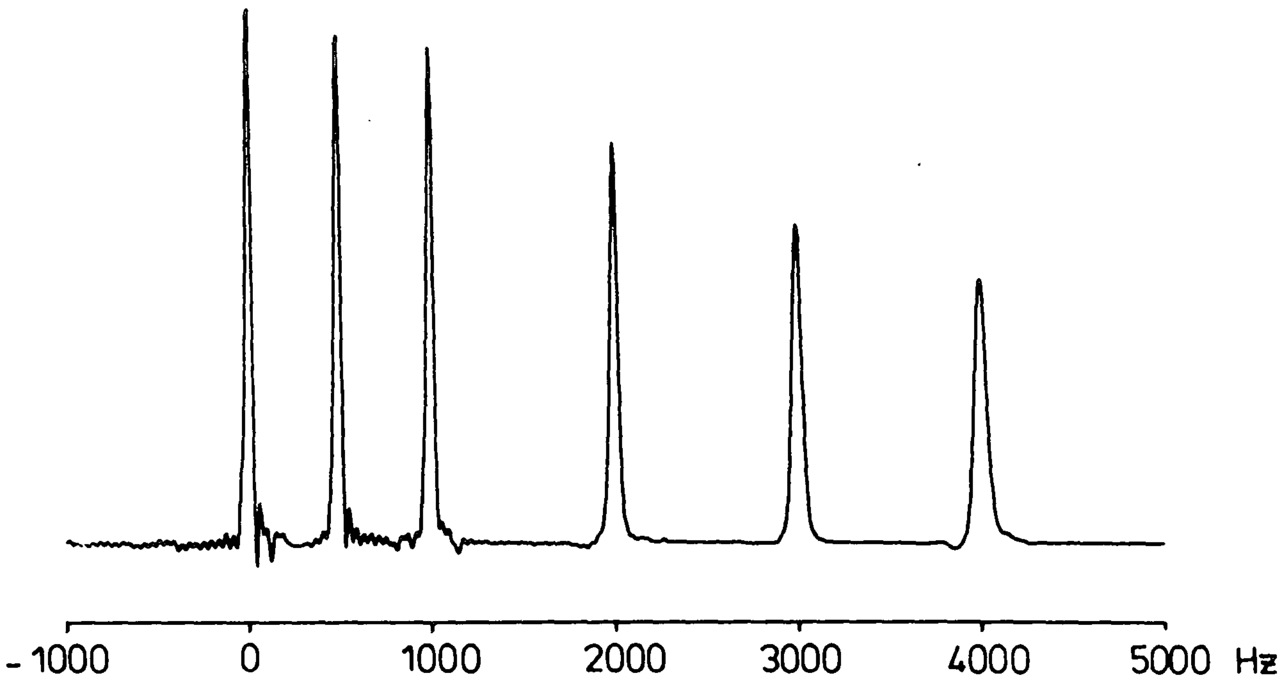

The variable cycle time was implemented by changing the window lengths, moving to a semi-windowless sequence[26] where the widest possible sweep width (shortest cycle time) was wished.

Upon tune-up completion the spectrometer performance was verified by running the scaling sequence shown in Figure 4.1. Adamantane serves as a check against resolution, and as a chemical shift reference, giving a single line at 1.74 ppm with a line width of 0.2 ppm.

Figure 4.2 demonstrates what resolution is possible at 4.7 Tesla using an MREV-8 pulse train. The CRAMPS spectrum of 4,4 dimethybenzophenone is just able to begin resolving the aromatic region. It has been suggested[7] that this splitting reveals a three to one (high frequency to low frequency chemical shift) ratio, indicating that one proton in each aromatic ring receives higher shielding from the carbonyl group. In Figure 4.2*a* the ^{1}H CRAMPS spectrum of 3,5 dimethylbenzoic acid is shown. Benzoic acid and its derivatives[27,28] are known to crystallize as dimers through hydrogen bonding of the -COOH groups. This is reflected in the high frequency shift of the carboxyclic proton. The assignment of nuclei to spectral lines are trivial in these examples, and have been chosen to illustrate the capabilities of the probe and software configured.

What remains to be added at this point are words of caution for which the price of experience has been paid. The BR-24 pulse sequence[20] was never successfully used at short pulse lengths ($\hat{=}$ 2μs) because the high duty cycle caused electrical uncertainty in the probe circuit; it couldn't handle the power consistently.

Figure 4.2 : PROTON CRAMPS RESOLUTION

a) 3,5 dimethyl benzoic acid

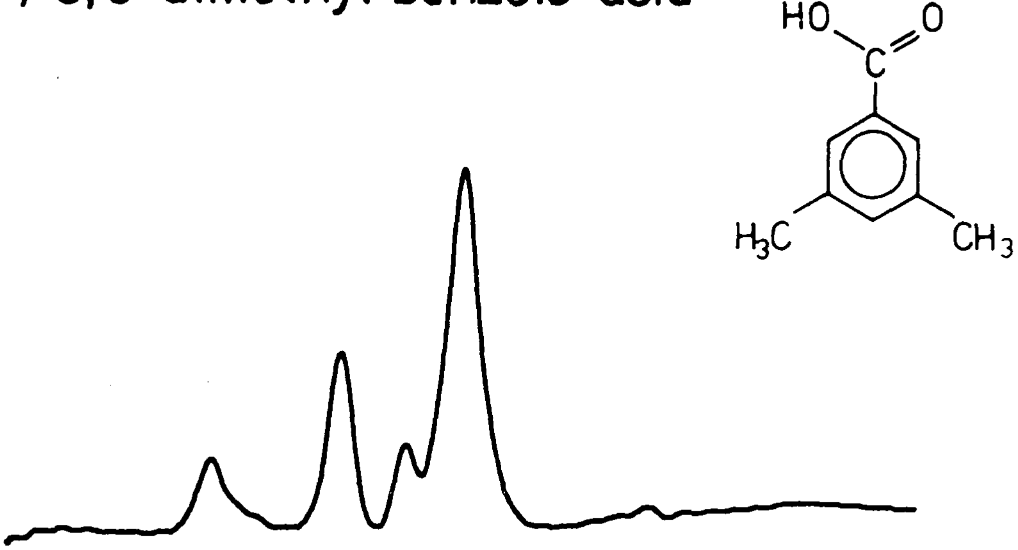

b) 4,4 dimethylbenzophenone

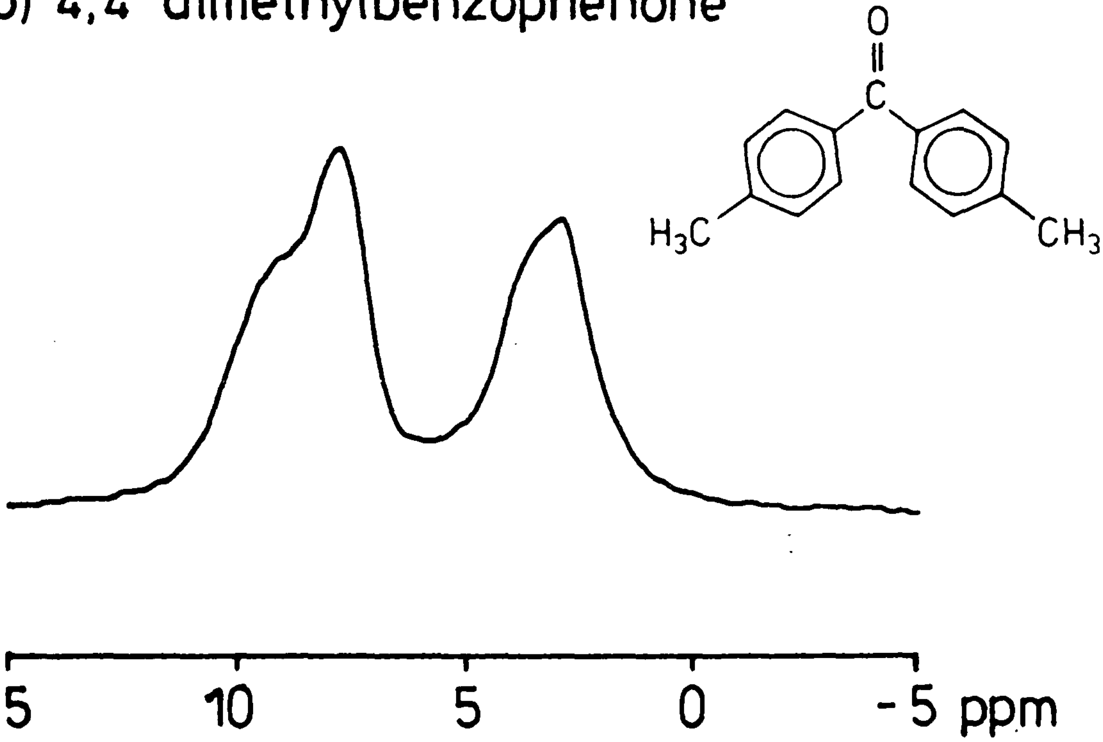

Where large pulse widths were used the cycle time must increase, which consequently sacrifices sweep width, limiting the utility of the experiment.

Bulk succeptibility has been a problem at this field strength, especially in inorganic solids. Any sample which was significantly ionic caused serious problems by detuning the probe coil to the extent that it was no longer within range of the requisite 50 Ohm match. For these samples the probe must be completely retuned in order to obtain any reasonable data. This was not always possible where samples were extremely electrically lossey.

4.3.2 Fluorine-19 Details

The fluorine-19 CRAMPS experiment was set up using perfluorobenzene as a tuning standard. The same tuning procedures were used as those employed for the ^1H CRAMPS experiment. The fluorine-19 nucleus is known to exhibit a very large chemical shift dispersion in the NMR spectrum.[29] This placed a high incentive on using the shortest possible cycle time in an experiment. The semi-windowless limit was found to yield the best results, giving a cycle time of approximately 16 μs. Upon completion of the spectrometer tuning, calibration similar to that shown in Figure 4.1 was performed using CaF_2. In an analogous fashion to Adamantane, CaF_2 serves as a resolution check, and a chemical shift reference, giving a single line at -107.7 ppm relative to $CFCl_3$, approximately 0.4 ppm wide.

An example illustrating the resolving power of the fluorine-19 CRAMPS experiment is shown in Figure 4.3 . The static single pulse spectrum of perfluoroaniline, not shown, is a broad uninformative line approximately 18 kilohertz full width at half height. Application of an UNIPAMPS line narrowing sequence resolves some spectral features. Upon application of magic angle specimen rotation the line breaks up into three central lines and associated sidebands. The spectra obtained in the solid state correlate closely with that measured using solution state NMR[30]. The two peaks at -165.9 and -167.0 ppm correspond to the ortho and meta fluorines respectively. The parafluorine is shifted to lower frequency, which suggests that a greater electron density exists in the para position relative to the ortho and meta positions. The behaviour of pentafluoroaniline under nucleophilic attack supports these observations,[31] since the para position is more succeptible to substitution under these conditions.[32]

Figure 4.3 : PERFLUOROANILINE

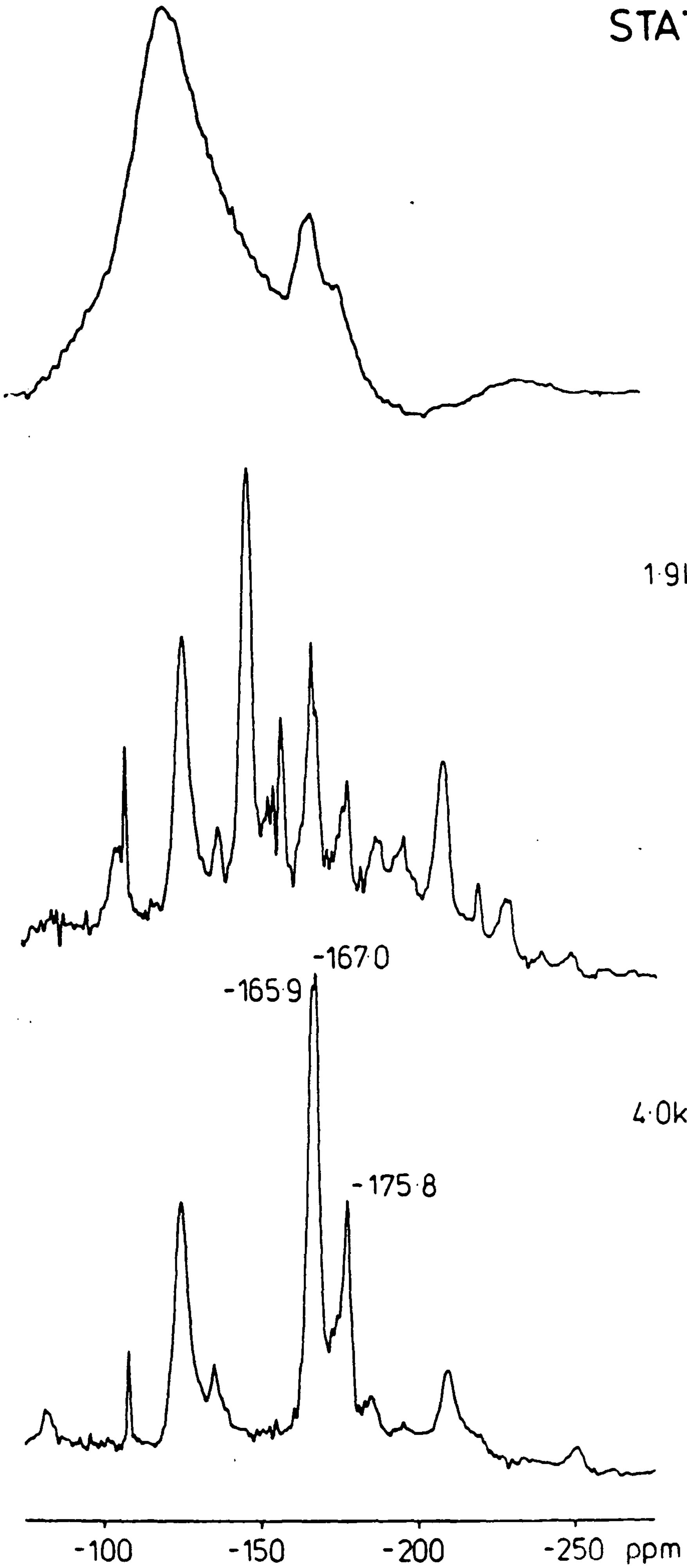

4.4 Conclusions

The purpose of this chapter has been to introduce and discuss the CRAMPS experiment in sufficient rigor that the data presented in this thesis are easily interpretable. Attention has been paid to those experimental criteria which experience has shown to be critical in the successful application of the CRAMPS experiment to difficult chemical systems. Some simple examples have illustrated the utility of the experiment for both ^1H and ^{19}F nuclei. Applications of this experiment will be demonstrated in a variety of chemical systems in Chapter six.

CHAPTER FIVE

QUADRUPOLAR NUCLEI:

^{23}Na single and double resonance experimental development

"Men love to wonder, and that is the seed of our science".
Emerson

CHAPTER 5

QUADRUPOLAR NUCLEI: ^{23}Na single and double methods development

5.1 Introduction

The discovery[1] that a nucleus may possess a magnetic moment and a quadrupole moment led eventually to the investigation of these properties in solids by magnetic resonance techniques.[2] The significance of the phenomena resulting from the nature of quadrupole moments is that they provide insight into the electric fields (as opposed to magnetic fields) operating in a solid.

Recently quadrupolar nuclei have received a great deal of notice in the literature, especially in the area of inorganic solids.[3] Although the theory of NMR of quadrupolar nuclei has been discussed in depth at a very early stage[4], further consideration was necessary to extend the techniques available, particularly with regard to half integer spin quadrupolar nuclei. Attention has focused on the correct determination of the isotropic chemical shift[5,6] requiring the theoretical treatment of contributions to lineshape[7], rotational sidebands[8] and dependency of the lineshape and true chemical shift on the quadrupolar moment and the asymmetry of the EFG.[9] Applications have been successful in demonstrating a correlation between bond angles and corrected chemical shift values[10], where previously the data had failed to exhibit any dependence.[11] Investigation has also examined the coherent excitation of separate transitions, and a two-dimensional (2-D) experiment has been shown to simultaneously separate the chemical shift value from the corresponding quadrupole interaction parameters.[12]

For the purpose of this thesis, interest in quadrupolar nuclei (specifically ^{23}Na) was a consequence of the desire to utilize another molecular probe in the framework of the inorganic solids which were being investigated. It will be shown that in order to obtain quantitatively accurate data from quadrupolar nuclei, careful adjustment of spectrometer conditions is necessary. Even the qualitative interpretation of the 'simple' case of a single pulse spectrum can be complicated, where quadrupolar transitions are involved.

Further extension of investigating techniques has been considered, specifically with the intent to demonstrate the utility of the double resonance experiments when applied to quadrupolar nuclei. This necessitated a search for 'standard' reference compounds from potential candidates whose properties were well known by other analytical methods.

The purpose of this chapter is to document and characterize the response of quadrupolar nuclei, specifically ^{23}Na, to a variety of single and double resonance NMR experiments. Conclusions will be drawn upon the utility of these experiments in investigating the molecular structure of inorganic solids. Applications to 'real' systems will be shown in Chapter 6.

5.2 Extended Theory of Quadrupolar Nuclei

In order to fully consider the investigation of quadrupolar nuclei in solids the theory covered in Chapter 2 must be expanded to treat the quadrupolar interaction in further detail. For the purpose of this thesis this will be limited to lineshape contributions, spin response to excitation, and the polarization transfer experiment.

5.2.1 General Contributions to Absorption Lineshapes

It has been shown in Chapter 2 that fast sample spinning can efficiently average randomly oriented spin-interaction tensors. At this point it is necessary to evaluate the effectiveness of this manipulation in line narrowing in the presence of first and second-order quadrupolar perturbation of the Zeeman interaction.

Beginning with the Hamiltonian;

$$h\mathcal{H} = h\mathcal{H}_Z + h\mathcal{H}_Q + h\mathcal{H}_{CSA} + h\mathcal{H}_D \qquad (5.1)$$

in a strong magnetic field, $\underline{B}_o$, (section 2.43) the last three terms in equation 5.1 can be treated as perturbations on $\mathcal{H}_Z$ assuming

$$|\mathcal{H}_Z| >> |\mathcal{H}_Q|, \quad |\mathcal{H}_{CSA}|, \quad |\mathcal{H}_D| \qquad (5.2)$$

If we also assume that, due to dilution, the dipolar coupling between quadrupolar nuclei is weak, and work under heteronuclear decoupling conditions, the $\mathcal{H}_D$ term can be ignored. In most cases $|\mathcal{H}_Q| >> |\mathcal{H}_{CSA}|$, and we will use this assumption, and that of axial symmetry ($\eta = 0$), to define a truncated Hamiltonian with the field $\underline{B}_o$ parallel to the Z axis such that[13]

$$h\mathcal{H}_{eff} = h\mathcal{H}_Z + h\mathcal{H}_Q \tag{5.3}$$

where

$$h\mathcal{H}_Z = h\ \gamma\ \underline{B}_o\ \hat{\underline{I}}_Z\ (1-\sigma_{iso})$$

$$h\mathcal{H}_Q = \frac{e^2q\ Qh}{4I(2I-1)} \left[\frac{1}{2}\ (3\cos^2\beta-1)(3\hat{I}_Z^2-I(I+1))\right.$$

$$+\ \frac{3}{2}\ \sin\beta\cos\beta\ [\hat{I}_Z(\hat{I}_+ + \hat{I}_-) + \hat{I}_+ + \hat{I}_-)\hat{I}_Z]$$

$$\left. +\ \frac{3}{4}\ \sin^2\beta\ (\hat{I}_+^2 + \hat{I}_-^2)\right]$$

The raising and lowering operators have been used to simplify the notation, where $\hat{I}_\pm = \hat{I}_X \pm i\hat{I}_Y$, and β describes the angle through which the rotation transformation has been performed (about y) to make the z axis of the EFG tensor coincident with $\underline{B}_o$. Second-order perturbation theory can be used to put equation 5.3 in a more easily discernible form[14] where the energy levels can be described by

$$E_m^0 = \hbar \gamma \underline{B}_o m \tag{5.4}$$

$$E_m^1 = \hbar \frac{1}{4} \underline{\omega}_Q (3\cos^2\beta - 1)(m^2 - \frac{1}{3} I (I + 1))$$

$$E_m^2 = \hbar \left[\frac{\underline{\omega}_Q^2}{12\gamma\underline{B}_o}\right] m \left[\frac{3}{2} \cos^2\beta(1-\cos^2\beta)(8m^2-4(I(I+1))+1) + \frac{3}{8} (1-\cos^2\beta)^2(-2m^2+2(I(I+1))-1)\right]$$

The total possible resonance frequencies would then be given by

$$\underline{\omega}_m = \sum_{\alpha=1}^{N} \frac{E_{m-1}^\alpha - E_m^\alpha}{\hbar} = \underline{\omega}_m^0 + \underline{\omega}_m^1 + \underline{\omega}_m^2 \tag{5.5}$$

where

$$\underline{\omega}_m^0 = \underline{\omega}_L = \frac{E_{m-1}^0 - E_m^0}{\hbar} = \gamma \underline{B}_o \hat{\underline{I}}_o$$

$$\underline{\omega}_m^1 = \frac{E_{m-1}^1 - E_m^1}{\hbar} = \underline{\omega}_Q(m - \frac{1}{2}) \frac{3\cos^2\beta - 1}{2}$$

$$\underline{\omega}_m^2 = \frac{E_{m-1}^2 - E_m^2}{\hbar} = \frac{\underline{\omega}_Q^2}{16\underline{\omega}_L} \left[(I(I + 1)) - \frac{3}{4}\right]\left[1 - \cos^2\beta\right]\left[9\cos^2\beta - 1\right]$$

From this it is easy to see that where the higher order terms do not contribute (cubic environment, small eq) there will be a single resonance frequency defined by $\underline{\omega}_L$.

By substitution for m, it is possible to see that for a half integer spin the Zeeman transition will not be affected in first order but there will be satellite lines, from a second order perturbation, (of intensity 3:4:3 for a spin $\frac{3}{2}$ case[15]), and a frequency shift of the quadrupolar transitions. The frequency shift of the higher order transitions are a consequence of the dependence of $\underline{\omega}_m^1$ and $\underline{\omega}_m^2$ on $\underline{\omega}_Q$, effectively a function of the orientation of the EFG with respect to $\underline{B}_o$. In addition it must be considered that a powder is composed of randomly oriented crystallites, where the nuclei have a random distribution of orientations to the static field. This will cause an inhomogeneous broadening of the lines, as a result of the super-position of all the narrow transitions arising from each individual orientation. It is plain to see from equation 5.4 that contributions to the lineshape will also be dependent upon, β, the angle of the principal axis to $\underline{B}_o$. In Chapter two we have already defined the form of dependence of the quadrupolar interaction on β, under rotation in spin coordinate space. This has been investigated in the literature and several 'ideal' values suggested.[16,17] This however may prove of limited utility since in any 'real' samples the contributions from $\mathcal{H}_D$ and $\mathcal{H}_{CSA}$ will be nontrivial, demanding rotation at the 'magic angle' combined with spin-decoupling in order to allow observation of any quadrupolar contribution of interest. For the purposes of this thesis the theory of quadrupolar lineshapes will not be discussed any further than the qualitative state which has been reached at this point.

5.2.2 Response to Transient Excitation

The response of the quadrupolar interaction to transient excitation has been derived and experimentally investigated in the literature.[18,19] Although the nature of this work was confined to the study of quadrupolar relaxation in solids, the relationships developed to calculate the spin response to a perturbing magnetic field can be applied in general to the NMR experiment.[20] Using spin density matrix theory, and the 'fictitious spin' analogy, it is possible to calculate the spin response to rf excitation in the presence of the quadrupolar interaction.[21] The calculation is performed as an average over all possible energy levels. Therefore the ratio of spin density matrices describing the magnetization in each level, as a result of the perturbing pulse, yields the fraction of the pulse perturbing each level. The results for the spin $I = \frac{3}{2}, \frac{5}{2}$ cases are shown in Table 5.1.

The values which result as a consequence of these calculations, are significant with respect to the successful calibration of the rf amplitude in an experiment, where coherent excitation of the multiple quadrupolar transitions is wished. From Table 5.1 it can be seen that the r.f. pulse amplitude, for a half integral quadrupolar nuclei, which gives the maximum response for the central transition, is $(I + \frac{1}{2})^{-1}$ that of the effective amplitude which excites all transitions.

Table 5.1

Spin	Transition	$\frac{\pi}{2}$ pulse length fraction
$\frac{3}{2}$	all	1
	$\pm\frac{3}{2}, \pm\frac{1}{2}$	$\frac{1}{\sqrt{3}} = .578$
	$\frac{1}{2}, -\frac{1}{2}$	$\frac{1}{\sqrt{4}} = .500$
$\frac{5}{2}$	all	1
	$\pm\frac{5}{2}, \pm\frac{3}{2}$	$\frac{1}{\sqrt{5}} = .447$
	$\pm\frac{3}{2}, \pm\frac{1}{2}$	$\frac{1}{\sqrt{8}} = .354$
	$\frac{1}{2}, -\frac{1}{2}$	$\frac{1}{\sqrt{9}} = .333$

For a spin $\frac{3}{2}$ case this means that the pulse width which produces a '90^{o}' pulse for all transitions is producing an '180^{o}' pulse for the central transition. These two cases can be easily recognized experimentally, in a single frequency experiment, using a cubic environment to calibrate the rf field.[22]

However, these calculations have assumed uniform excitation of all transitions. If we wish to consider the case of a powder sample, in a magic angle rotation experiment, this is no longer a safe assumption. In the doubly rotating frame each crystal will possess a different set of tensor components which describe the EFG principal axes system, relative to the spinning frame of reference. The polarization axes will be modulated by the sample rotation, and $\underline{\omega}_Q$ will change with crystal orientation during spinning.[23] This means that where $|\underline{\omega}_{rf}| \ll |\underline{\omega}_Q|$ only the central transition can be perturbed, and where $|\underline{\omega}_{rf}| \gg |\underline{\omega}_Q|$, all transitions are affected including the quadrupolar spin states. Intermediate values of $\underline{\omega}_Q$ produce an aperiodic behaviour of the central transition magnetization. This has important consequences when quantitative intensities are critical. It has been shown that uniform excitation of the central transition can be insured only if the rf pulse is strong ($|\underline{\omega}_{rf}| \gg |\underline{\omega}_{rotor}|$) and the flip angle is small.[23] These criteria may be difficult to meet experimentally, where the quadrupole interaction is large. In this case part of the total line intensity will reside in the spinning side bands which accompany the central line.

5.2.3 Polarization Transfer in Quadrupolar Nuclei

In order to evaluate the role of the quadrupolar interaction under cross-polarization conditions it is necessary to consider a truncated Hamiltonian of the form

$$h\mathcal{H} = h\mathcal{H}_0 + h\mathcal{H}_{1I}(t) + h\mathcal{H}_{1S}(t) + h\mathcal{H}_{QS} + h\mathcal{H}_{II} + h\mathcal{H}_{SS} + h\mathcal{H}_{IS} \tag{5.6}$$

The Zeeman interactions with $\underline{B}_0$ of both the abundant (I) and dilute quadrupolar (S) spins are contained in $\mathcal{H}_0$. The $\mathcal{H}_{1I}$ and $\mathcal{H}_{1S}$ terms relate the coupling of the spins to the radio frequency perturbation. $\mathcal{H}_{II}$, $\mathcal{H}_{SS}$, $\mathcal{H}_{IS}$ terms have their usual meaning (Chapter 2) defining the secular dipolar coupling of the two spin systems. We may treat this Hamiltonian as done previously in section 2.5, and choose the phase of an unitary transformation $\left[(R = \exp[\,-it(\omega_{0I}I_z+\omega_{0S}S_Z)])\right]$ such that the I and S magnetization are aligned on the same axes.[24] We can then have the time independent Hamiltonian in the doubly rotating frame[25] in the form

$$h\mathcal{H}_{rot} = h\mathcal{H}_{1I} + h\mathcal{H}_{1S} + h\mathcal{H}_{QS} + h\mathcal{H}_{II} + h\mathcal{H}_{SS} + h\mathcal{H}_{IS}$$

where

$$h\mathcal{H}_{1I} = -h\,\gamma_I\,\underline{B}_{1I}\sum_{\iota}\hat{\underline{I}}_{\iota X}$$

$$h\mathcal{H}_{1S} = -h\,\gamma_S\underline{B}_{1S}\sum_{\iota}\hat{\underline{S}}_{\iota X}$$

$$\hbar\mathcal{H}_{QS} = \frac{\hbar e^2 qQ}{4S(2S-1)}\left[\left[3\hat{S}_Z^2 - S(S+1) + \frac{1}{2}\eta\,(\hat{S}_X^2 + \hat{S}_Y^2)\right](\cos^2\beta - 1)\right]$$

$$\hbar\mathcal{H}_{IS} = \hbar\gamma_I\gamma_S \sum_{k,q} \hat{I}_{Zk}\,\hat{S}_{Zq}\,\frac{1-3\cos^2\beta_{k,q}}{r_{k,q}^3}$$

$$\hbar\mathcal{H}_{II} = \hbar^2\gamma_I^2 \sum_{j,k} (3\hat{I}_{Zj}\hat{I}_{Zk} - \hat{\underline{I}}_j\cdot\hat{\underline{I}}_k)\left[\frac{1-3\cos^2\beta_{j,k}}{r_{j,k}^3}\right]$$

$$\hbar\mathcal{H}_{SS} = \hbar^2\gamma_S^2 \sum_{p,q} (3\hat{S}_{Zp}\hat{S}_{Zq} - \hat{\underline{S}}_p\cdot\hat{\underline{S}}_q)\left[\frac{1-3\cos^2\beta_{p,q}}{r_{p,q}^3}\right]$$

The validity of the double resonance experiment, applied to quadrupolar nuclei, has been discussed[26] and experimentally verified[27] in the low field case ($|\underline{\omega}_Q| \gg |\underline{\omega}_Z|$). The quadrupolar double resonance experiment can be treated in analogy with the method in section 2.5 except for one condition, namely the coherent adjustment of the matching pulse amplitudes.

The matching condition can be restated[24]

$$\alpha_I\,\gamma_I\,\underline{B}_{1I} = \alpha_S\,\gamma_S\,\underline{B}_{1S} \tag{5.8}$$

where $\alpha_I = 1$ for the NMR case, (pure $\frac{1}{2}$, $-\frac{1}{2}$ transition) or $\alpha = [I(I+1) - m(m-1)]^{\frac{1}{2}}$ for NQR case where $m \longleftrightarrow (m-1)$ defines the quadrupolar levels. We will ignore the second case for pure NQR spectroscopy, and note that a mixed $\pm\frac{1}{2}\,\alpha_I$ to $\pm\frac{3}{2}\,\alpha_S$ transfer is forbidden by the disparate energies between the levels.

The quadrupolar term $\mathcal{H}_{QS}$ has been shown as a separate contribution from $\mathcal{H}_{1S}$ in equation 5.7 in order to emphasize the discriminating properties of the matching condition. The Hartmann-Hahn relationship is rigorously valid only for nuclei with no quadrupolar interactions.[28] This is a consequence of the first resonance constraint which must also operate on the dilute spins (in this case quadrupolar) in the doubly rotating frame: $\hbar\omega_S = \Delta E_S$. In practice this condition is set to observe the central transition resonance at $\gamma_S B_{1S}$, and ω_S is varied through the condition where S and I spins are in thermodynamic contact. Any contributions from quadrupolar terms will oscillate at frequencies large when compared with ω_{1I} and ω_{1S}, and may be ignored.

Inspection of the $\mathcal{H}_{QS}$ term in equation 5.7 confirms that no direct polarization transfer would be expected via this quadrupolar interaction since it is a single species term. Hence it may only couple with $\mathcal{H}_{1S}$ and $\mathcal{H}_{IS}$ directly. Upon coherent application of the perturbing fields, $\mathcal{H}_{1I}$ and $\mathcal{H}_{1S}$, the $\mathcal{H}_{IS}$ term becomes secular and is able to exchange energy with both field terms, completing the polarization transfer pathway.

By choosing a suitable 'standard' compound where the quadrupolar spin has a cubic environment, avoiding any contribution from the non central transitions, it should be possible to observe cross-polarization analogous with the spin $\frac{1}{2}$ case for the dilute species. For this case, all transitions will be excited, and the rate and efficiency of polarization transfer will be a function of the abundant species $T_{1\rho}$, and the ratio of magnetogyric values, as previously stated in section 2.5. This should provide an excellent method of calibrating both rf fields, using the Hartmann-Hahn matching condition as a sensitive measure of the pulse amplitude, for a given field strength.

For the case of non-cubic environment quadrupolar nuclei the situation is more complicated. It has been shown in Chapter 2 that the contributions to the lineshape of a quadrupolar nucleus, in a lower symmetry (less than cubic), are a function of the asymmetry, 'η', and the field gradient, 'eq'. The size and nature of these parameters also affects the relaxation processes which operate at a quadrupolar nuclear site.[29] These same pathways are responsible for polarization transfer during the Hartman-Hahn matching condition created by a cross-polarization contact sequence.

In analogy with the spin $\frac{1}{2}$ case, a variable contact cp experiment will measure the character of the cross relaxation term $\mathcal{H}_{IS}$. But in the case of non-cubic quadrupolar nuclei the $\mathcal{H}_{SS}$ term must be reconsidered to include exchange between the $\pm \frac{1}{2}$ and $\pm \frac{3}{2}$ levels. If level crossing terms[30] are ignored then cross-relaxation to the quadrupolar lineshape should be double component defined by the $\mathcal{H}_{IS}$ and $\mathcal{H}_{SS}$ terms of equation 5.7. The form of the cross-relaxation equation has been measured and found to behave exponentially.[31] This relationship is useful since it may be used to draw conclusions upon the nature of association of the quadrupolar nuclei with the surrounding proton environments. It will be shown that it is also possible to differentiate between the two possible cross-relaxation components using selective experiments.

This completes the theoretical examination of the quadrupolar relationships relevant to the investigations in this thesis. Experimental verification of these principles will complete this chapter.

5.3 Methods Development

In order to coherently perturb and measure any chemical system using magnetic resonance techniques, it is first necessary to carefully calibrate the radio-frequency spectrometer employed, at the resonance frequency of the nuclei of interest. For this purpose 'standard' reference compounds are usually designated which have been well characterised by other spectroscopic methods.[32] With quadrupolar nuclei the matter is further complicated in the presence of higher order transitions, and their effect upon the central transition lineshape and intensity, as a function of pulse length.[12] Where protons are in abundance it is also important to adjust the decoupler field in order to observe the true line width.[33]

The most common procedure used to accomplish this fine tuning of the spectrometer conditions, is to exploit the Hartmann-Hahn relationship. This provides a sensitive measure for the optimization of the pulse length against the double resonance match. The method is simple and obvious provided a suitable matching compound is available.

5.3.1 Candidates for ^{23}Na Cross-Polarization Standards

The criteria for evaluation of a useful matching standard for quadrupolar nuclei are precisely the same as those for a spin $\frac{1}{2}$ nuclei except for one additional constraint: the nuclei should have cubic symmetry. As stated previously this simplifies the transition contributions and essentially allows the nuclei to be treated in an analogous fashion to a spin $\frac{1}{2}$ case.

Several different candidates were investigated as potential ^{23}Na reference standards. The results of these trials were enlightening, even where the systems were not optimal standards, in the surprising sensitivity of the sodium nucleus to changes in the chemical environment. Since all candidates chosen were well characterized systems, this provided an opportunity to document the potential of different experiments to extract information from the solid state using the ^{23}Na nucleus as a molecular probe.

It is important to note that sodium is not bonding covalently to any protons. Assuming an ionic radius of 0.95 Å, it would be reasonable to expect that coupling between protons and Na$^+$ nuclei should be of lesser magnitude than that observed in typical dilute nuclei where covalent bonding character dominates (i.e. ^{13}C-^{1}H systems). It would also be reasonable to expect polarization transfer to be less effective, since it must occur generally over greater distance. Given these expectations suitable matching compounds may be found.

5.3.1.1 Sodium Borohydride $NaBH_4$

The crystal structure of sodium borohydride has shown that the lattice is face centred cubic with four sodium and four boron atoms per unit cell.[34] The dimensions of the ions and the cell size should permit rotation of the BH_4^- ion, and indeed no splitting of the ^{11}B quadrupolar line is seen.[35] This experimental evidence confirms that the Na$^+$ ion possesses local cubic symmetry.

Figure 5.1 shows the results of the sodium-23 spectra of $NaBH_4$ at 4.7 Tesla. Decoupling and MAR have a significant effect on the line widths, but in all cases a

Figure 5.1

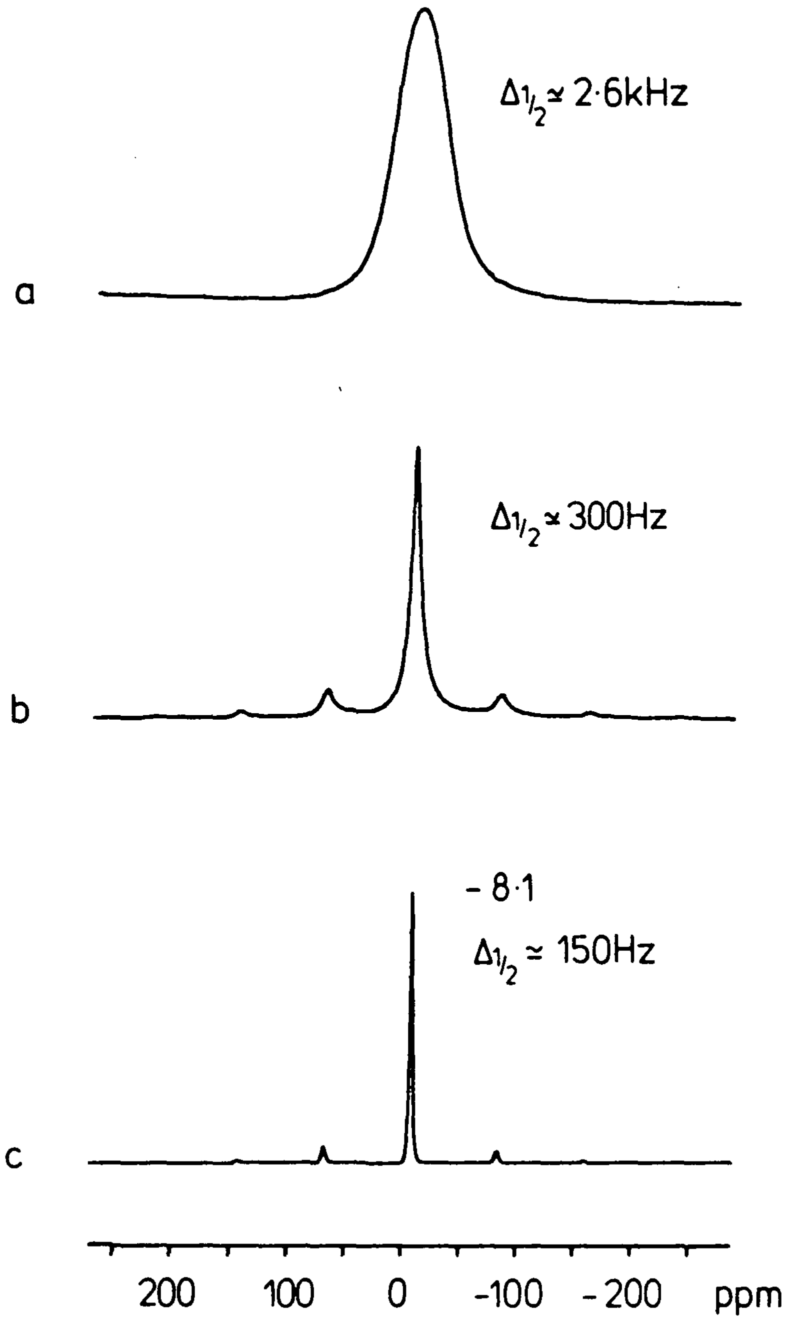

Sodium-23 spectra of Sodium Borohydride
8 transients, 30 s recycle, 4 μs 90° pulse.
- a) static decoupled
- b) MAR (4.0 kHz) coupled
- c) MAR (4.0 kHz) decoupled
- d) CP MAR (4.0 kHz) A.I. comparison

Figure 5.1d

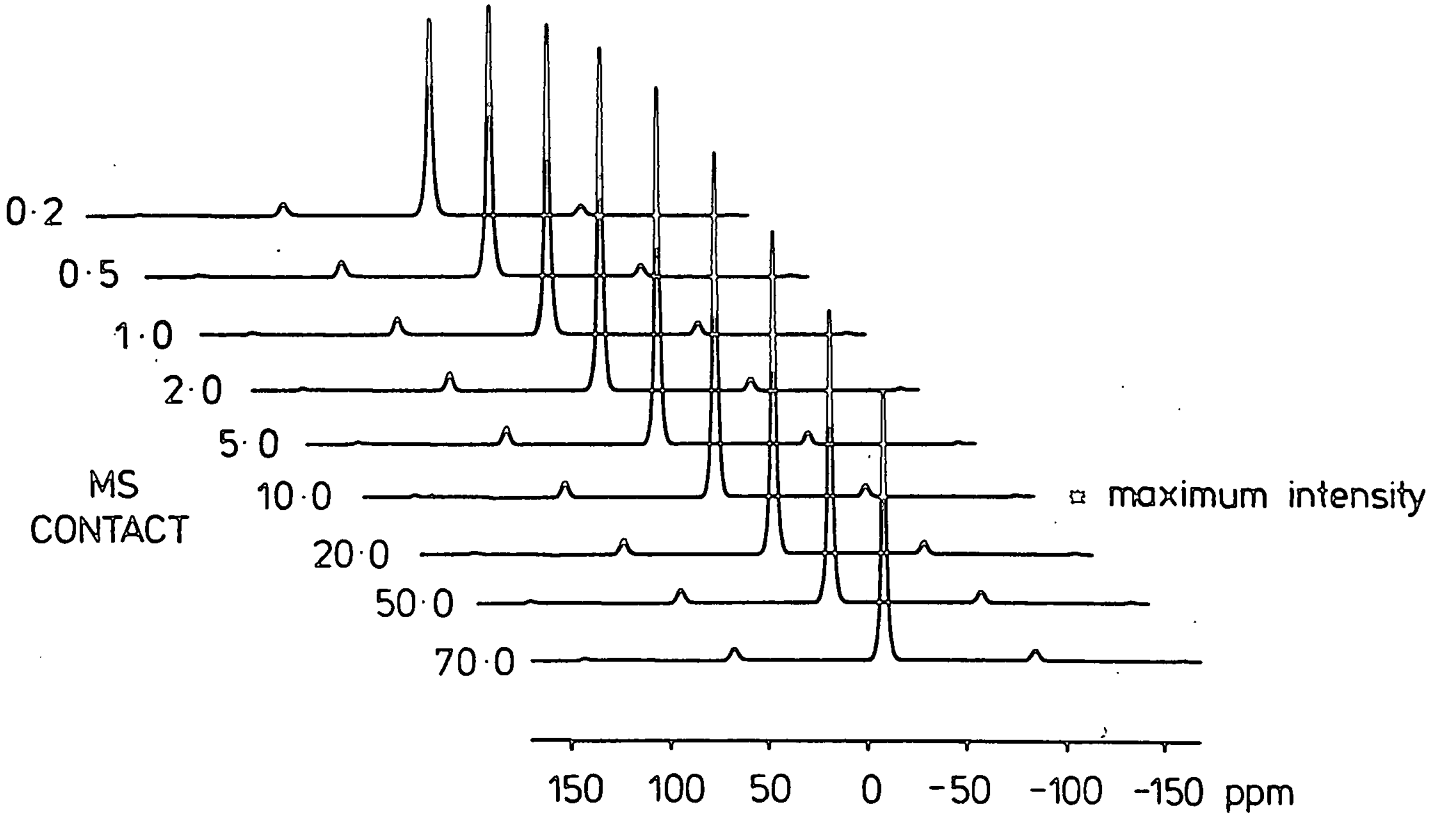
0·2
0·5
1·0
2·0
5·0
10·0
20·0
50·0
70·0
MS
CONTACT
¤ maximum intensity
150
100
50
0
-50
-100
-150
ppm

symmetrical Lorentzian lineshape is observed with rotational echoes producing spinning side bands. At 4.0 kHz, spinning is not fast enough to remove all contributions which result from the quadrupole interaction, but these are small enough such that the lineshape is undistorted and may be regarded as negligible. Therefore this compound may be treated under polarization transfer conditions as a perturbation of the central $\pm \frac{1}{2}$ transition only since the higher order transitions are degenerate. In Figure 5.1d the sodium response to the cross-polarization experiment is shown. The compound cross-polarizes well, indicating a long ^1H $T_{1\rho}$. The rate of cp is slow, which supports the crystal data that indicate the BH_4^- groups may be oscillating. The proton CRAMPS spectrum gives one resonance with a relatively narrow line width (~80 Hz) which also indicates a high degree of motional averaging in the proton environment. This would provide a diffused proton bath from which the Na^+ could draw thermodynamic contact. Optimal contact occurs between 5 and 10 ms, giving enhancement relative to the decoupled experiment of ~1.2:1.0. This poor enhancement can be explained on two accounts, the first being the relatively large distances over which polarization transfer must occur, and secondly the relatively mobile proton bath.

5.3.1.2 γ-Alum: $NaAl(SO_4)_2.12H_2O$

The crystal structure of the γ-Alum has been determined as cubic, with four Al and four Na atoms per unit cell occupying face centred sites.[36] Each metal atom is surrounded by six water molecules with T_h^6 symmetry.[37] The γ-Alum is singular among the alums in the similar distances between the two metal atoms and the coordinating water molecules. This is a consequence of the small ionic radius of Na^+ which causes the $SO_4^=$ to adopt an orientation which allows smaller Na^+-H_2O distances.[38] The Al^{+3}-H_2O distances (1.98 A^o) are of the order of 0.5 A^o shorter than that of Na^+-H_2O (2.45 A^o).

Figure 5.2 and 5.3 show the sodium-23 and aluminium-27 spectra of the γ-Alum, respectively. Both nuclei show significant line narrowing of their spectra upon application of MAR and ^1H decoupling. More significant though, is the observation that with both nuclei the line shape changes as a function of contact time during polarization transfer (5.2d, 5.3d). The most interesting attribute of the variable contact spectra is that there is more than one cross-relaxation component operating on the lineshapes. One component is giving the general trend of the maximum observed at 2 ms with both nuclei. There is also another component which clearly has a different time constant and appears to be changing the quadrupolar contributions to the lineshape.

The fact that both nuclei have maximum cp at ~ 2 ms, despite different Al^{3+}-H_2O, Na-H_2O distances would indicate that polarization transfer is taken from a communal proton bath. ^1H CRAMPS experiments gave a single ^1H chemical shift at 5.1 ppm composed of two components overlapping (broad and narrow). Neither nucleus in the γ-Alum cross-polarizes very efficiently, both giving a negative enhancement ratio of 0.5:1.0. For this reason, and the observed second-order quadrupolar contribution to the central transition lineshape, this compound would make a poor matching standard for either nucleus.

Figure 5.2

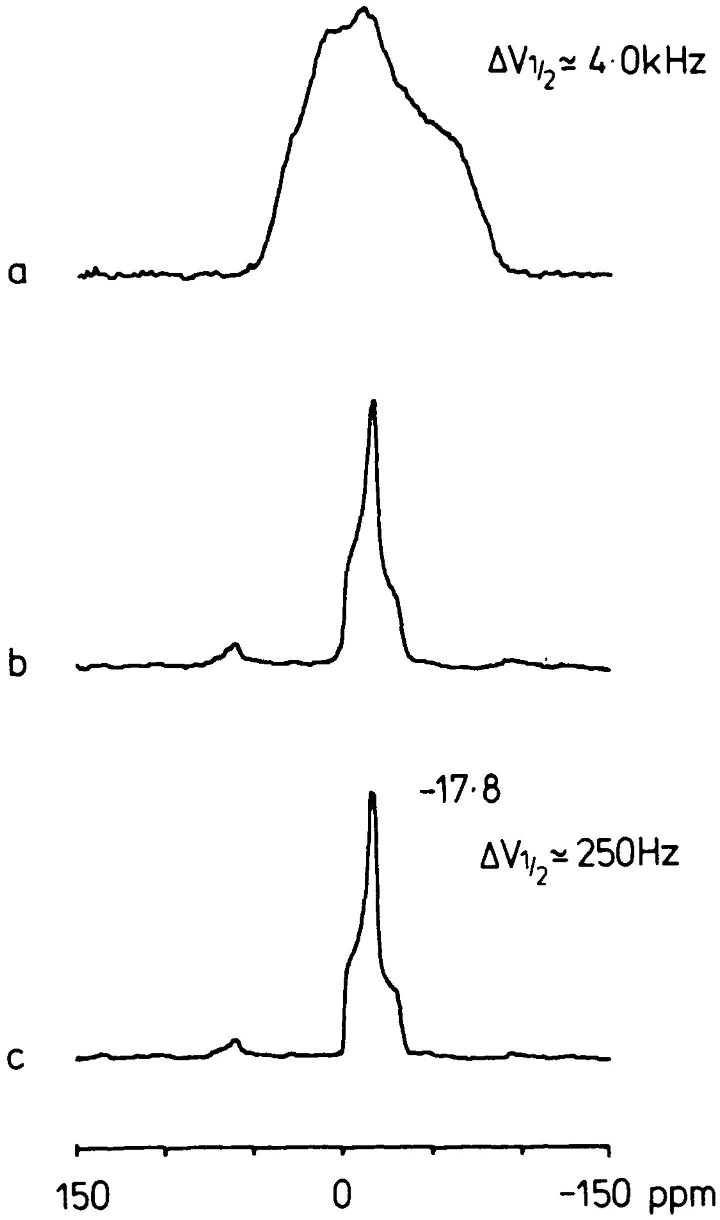

Sodium-23 spectra of γ-Alum
16 transients, 30 s recycle, 2μs t_p

a) static decoupled
b) MAR (4.0 kHz) coupled
c) MAR (4.0 kHz) decoupled
d) CP MAR (4.0 kHz) A.I. comparison

Figure 5.2d

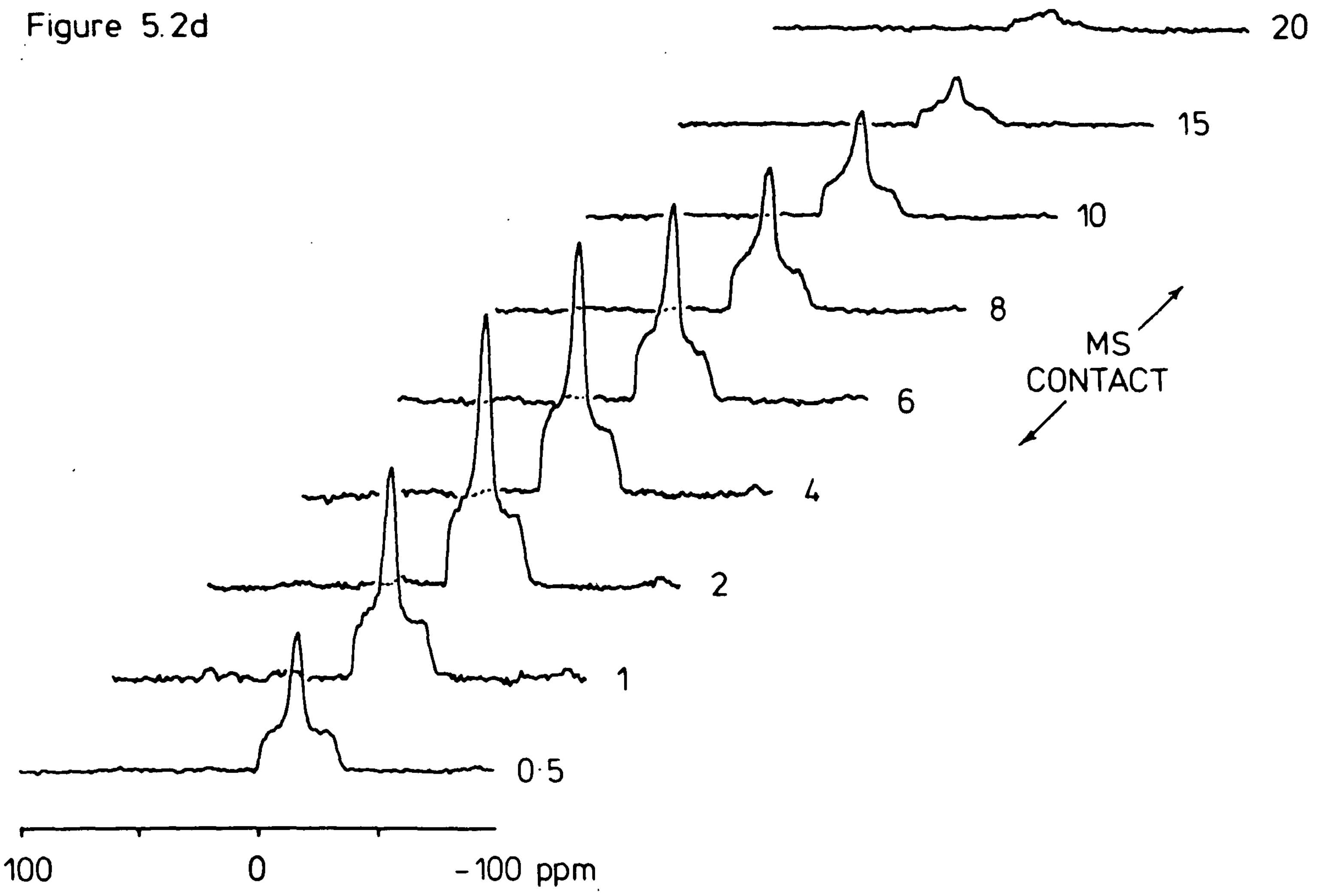

Figure 5.3

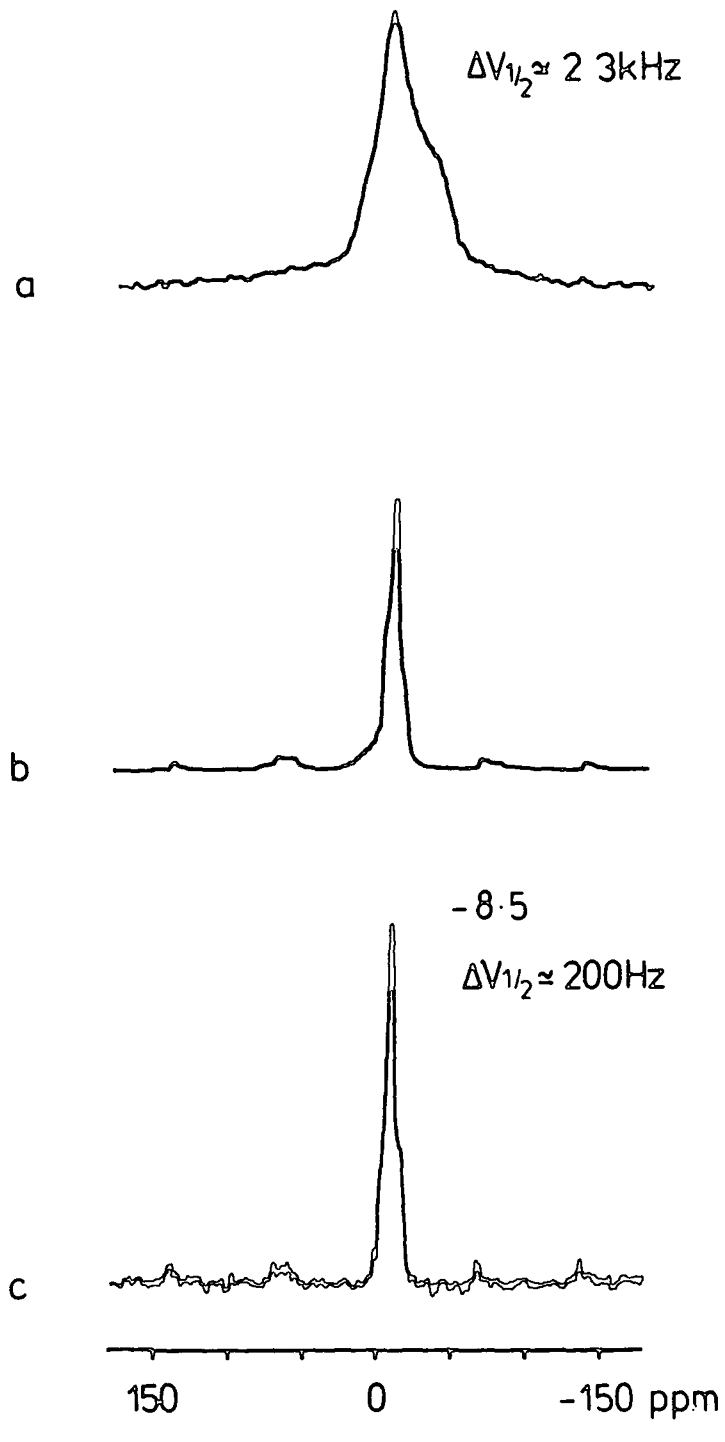

Aluminium-27 spectra of γ-Alum
32 transients, 20 s recycle, 1 μs t_p

a) static^{a} decoupled
b) MAR (3.6 kHz) decoupled
c) CP MAR (3.6 kHz) 2 ms contact
d) CP MAR (3.6 kHz) A.I. comparison

Figure 5.3d

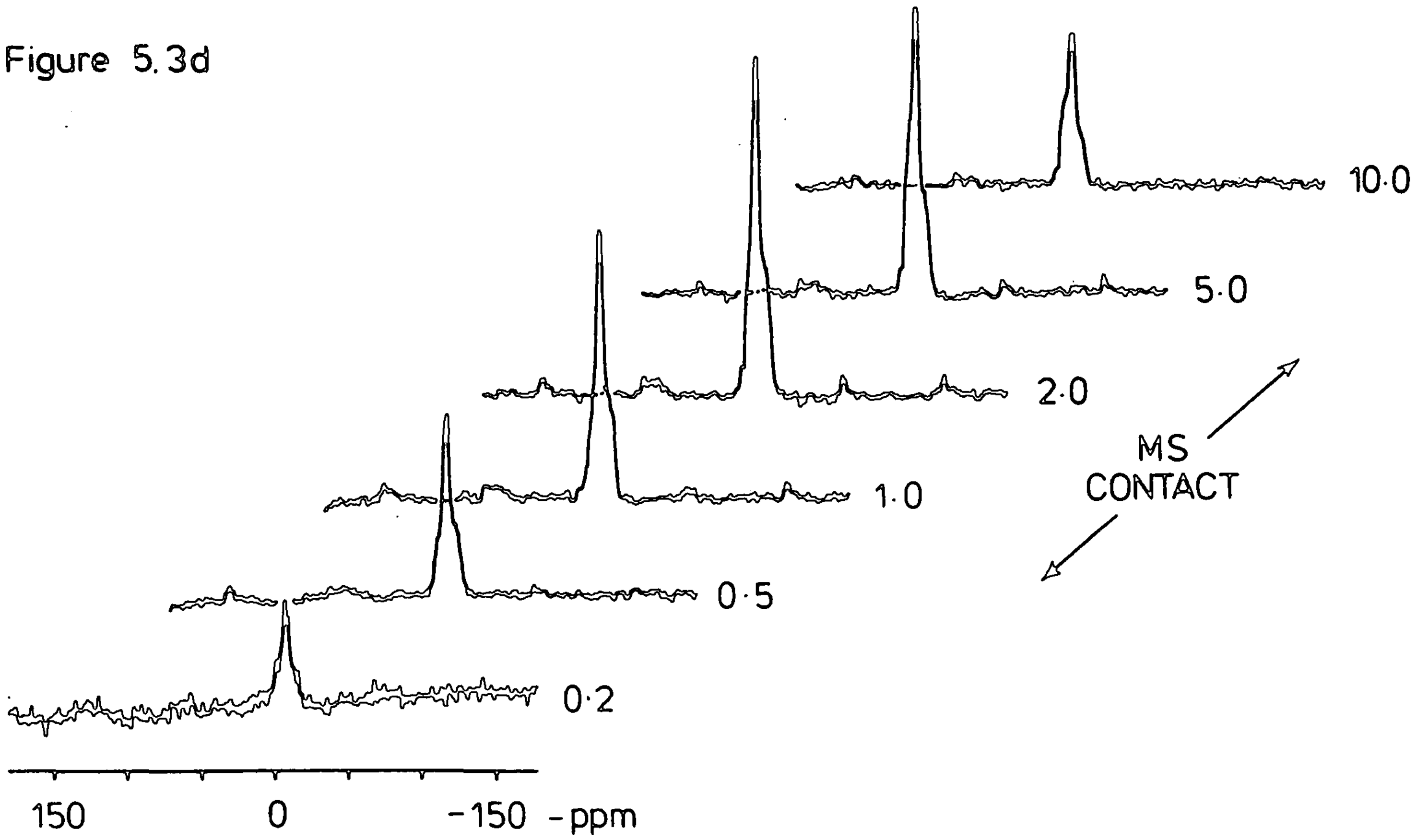

5.3.1.3 Sodium Borates; $Na_2B_4O_7.5H_2O$, $Na_2B_4O_7.10H_2O$

The two sodium borates Tincalconite, $Na_2B_4O_7.5H_2O$, and Borax, $Na_2B_4O_7.10H_2O$, have been used to investigate the behaviour of the quadrupolar sodium-23 nucleus under single and double resonance radiofrequency excitation, and magic angle rotation conditions. Both compounds have been well characterized, the first studies using powder diffraction methods.[39] The original single crystal data[40] have been shown to be of dubious quality. Reliable values have since been reported for both Borax[41,42] and Tincalconite[43] which include the determination of sodium positions in the crystal lattice.

Single crystal NMR studies have also been completed, investigating the boron[44] and sodium[45] sites in both compounds. These data are consistent with the conclusions drawn from crystallographic studies which indicate that both compounds have the same boron-oxygen polyanion structure. This would account for the reversible equilibrium possible between the two structures.[46] The relevant crystallographic properties are shown in Table 5.2.

Table 5.2

	$Na_2B_4O_7.5H_2O$	$Na_2B_4O_7.10H_2O$
STRUCTURAL FORMULA	$Na_2B_4O_5(OH)_4.3H_2O$	$Na_2B_4O_5(OH)_4.8H_2O$
UNIT CELL	Trigonal	Monoclinic
SPACE GROUP	D_3^7(R32)	C_{2h}^6
CELL VOLUME(A^{o3})	765	1475
MOLECULE/UNIT CELL	3	4
INTERAXIAL Na-Na DISTANCE (A^o)	6.97	11.36
SODIUM-23 $\left[\begin{matrix}\text{no. of}\\ \text{atoms)}\end{matrix}\right]$; $\frac{e^2qQ}{h}$; η	(3); +539±2; 0.741±.005	(4); +541±3; 0.449±.015
	(2); +785±2; 0	(4); +849±3; 0.143±.028
	(1); +1299±1; 0	
SODIUM POSITIONS	0,.669,.005 0,0,.005 0,0,.093	$\begin{bmatrix}0,0,0,;0,0,\frac{1}{2}\\ \frac{1}{2},\frac{1}{2},0;\frac{1}{2},\frac{1}{2},\frac{1}{2}\end{bmatrix}$ $\begin{bmatrix}0,.845,\frac{1}{4};0,-.845,\frac{1}{4}\\ \frac{1}{2},.345,\frac{1}{4};\frac{1}{2},-.345,\frac{1}{4}\end{bmatrix}$

From the data contained in the literature it is possible to construct a physical model of the crystalline lattice. Essentially, both compounds consist of a series of alternating chains, lying one on top of the other, along the c direction. One chain is composed of $[B_4O_5(OH)_4]^=$ polyanions which link to each other via hydrogen bonds. The second chain is built of edge sharing $Na^+.6H_2O$ polyhedra. The interaxial distance between chains is controlled by the hydrogen bonding and oxygen sharing between the chains.

In Borax the $Na^+.6H_2O$ polyhedra chains are relatively regular and the polyhedra themselves possess close to octahedral symmetry. Two crystallographically distinct sodium environments have been determined.[47] The argument offered in explanation of the inequivalence was that one polyhedron is a distorted octahedron.[47] This justification is supported by the disparate quadrupole couplings which have been observed.[45] The solid state NMR data shown in Figure 5.4 also indicate that there are two distinct sodium environments. The high frequency environment appears to exhibit a lineshape which is clearly similar to the low frequency absorption, and equal in area. As mentioned in section 5.2.2, where there are quadrupole contributions to the lineshape, coherent quantitative response of the magnetization to excitation is possible only where the pulse is 'short' and 'strong'. Figure 5.5 shows the response of the two sodium environments in borax to increasing pulse length. Proper intensities are observed where the match was set using $NaBH_4$ as the reference standard, with a 2 μs 90^0 pulse.

Figure 5.4

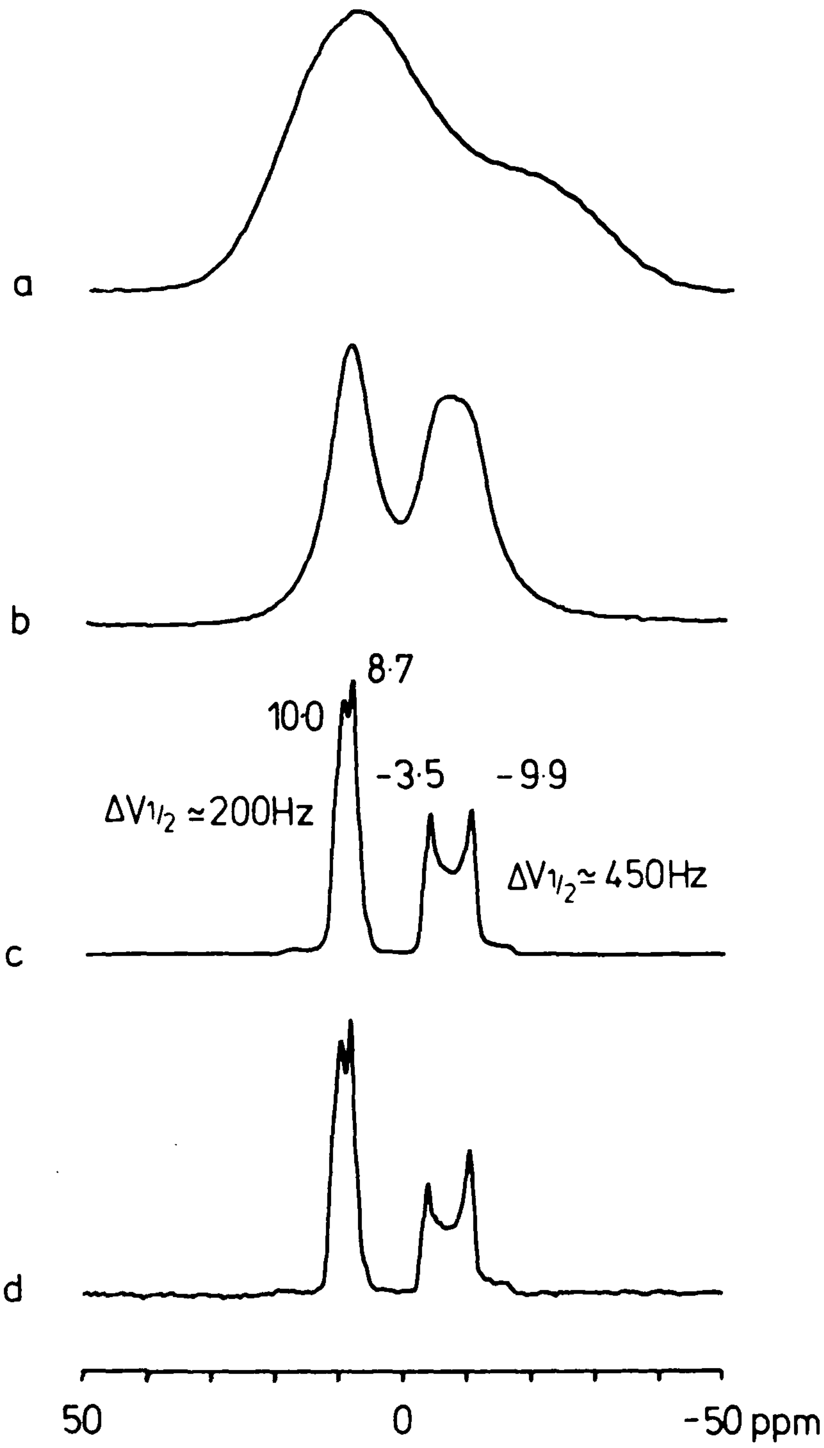

Sodium-23 spectra of Borax
16 transients, 30 s recycle, 2 μs t_p

a) static decoupled
b) MAR (4.0 kHz) coupled
c) MAR (4.0 kHz) decoupled
d) CP MAR (4.0 kHz) 10 ms contact

Figure 5.5

Sodium-23 spectra of Borax; variable t_p
16 transients, 30 s recycle, 2 µs t_p, 4.0 kHz MAR
Response of transverse magnetization to varying pulse length (t_p)

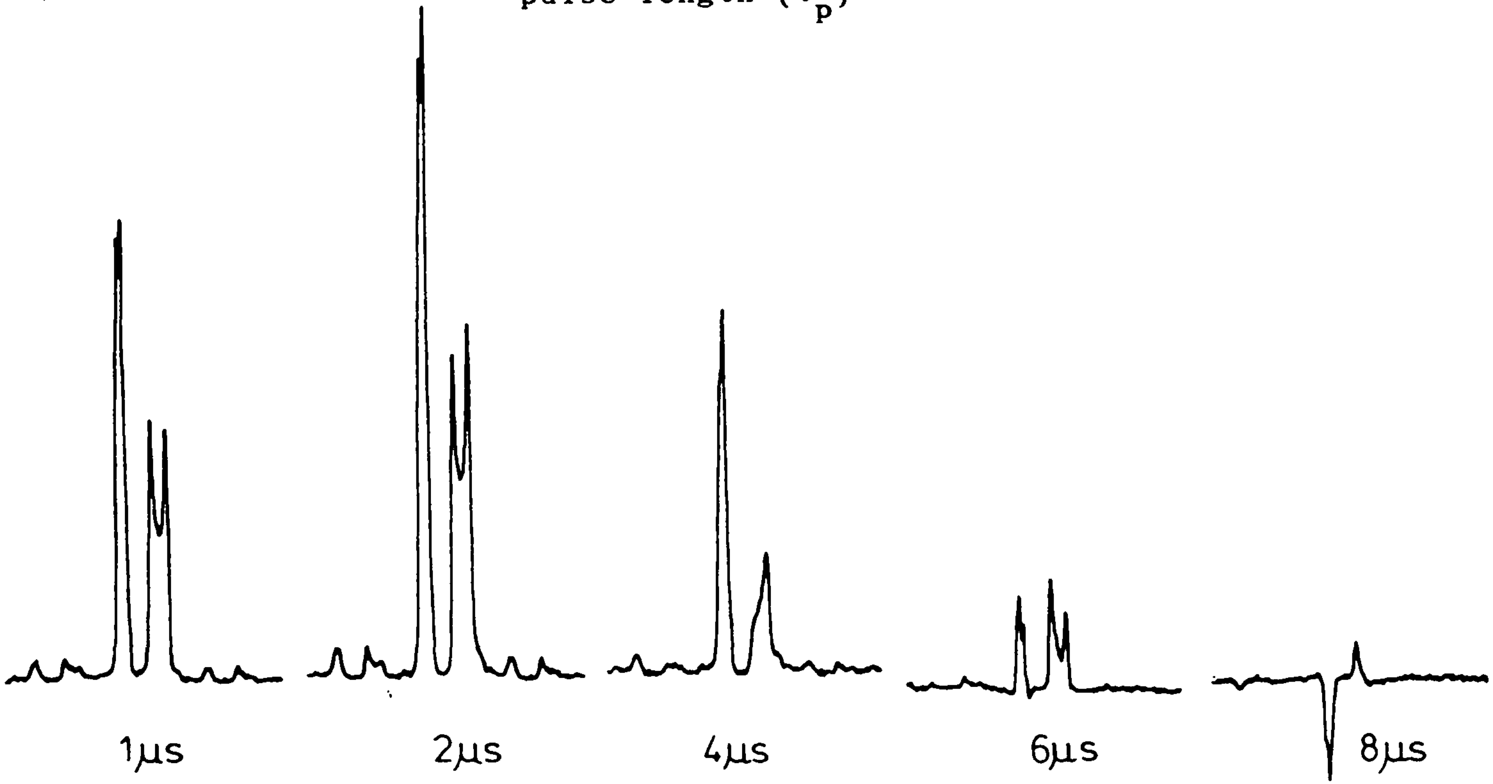

In Figure 5.6 the cross-polarization experiment has been applied to Borax. It is suprising to observe that components of the absorption lineshapes in the two environments respond very differently to the polarization transfer experiment. Both environments cp at approximately the same rate, and exhibit similar $T_{1\rho}$ characteristics, but the high frequency environment appears to cp more efficiently.

The proton CRAMPS spectrum of this compound gives only one relatively broad peak at 4.5 ppm with a slight shoulder evident to high frequency. This experiment fails to differentiate between the three possible proton environments which might be expected, given the two different polyhedra and the borate polyanion. This is not so surprising if one considers that the polyhedra are not severely distorted relative to each other, and the '-OH' population is small (4:16) relative to the water population.

The sodium-23 relaxation data are shown in Figure 5.7. These data were obtained using the composite-π-inversion pulse-decoupled experiment described in Chapter 3. In this experiment a proper $180^{\circ}\pi$ pulse was not achieved, but this does not obscure the observation that both environments relax at approximately the same rate, giving a T_1 of about 0.06 sec^{-1}. However, the results of performing a DANTE sequence yield very different values, as shown in Figure 5.8. The DANTE data indicate that the environments relax with ~ 0.5 sec^{-1} and ~ 0.2 sec^{-1} for the high and low frequency environments respectively. It would appear that the composite π inversion experiment is measuring a different physical process than that of the DANTE sequence.

Figure 5.6

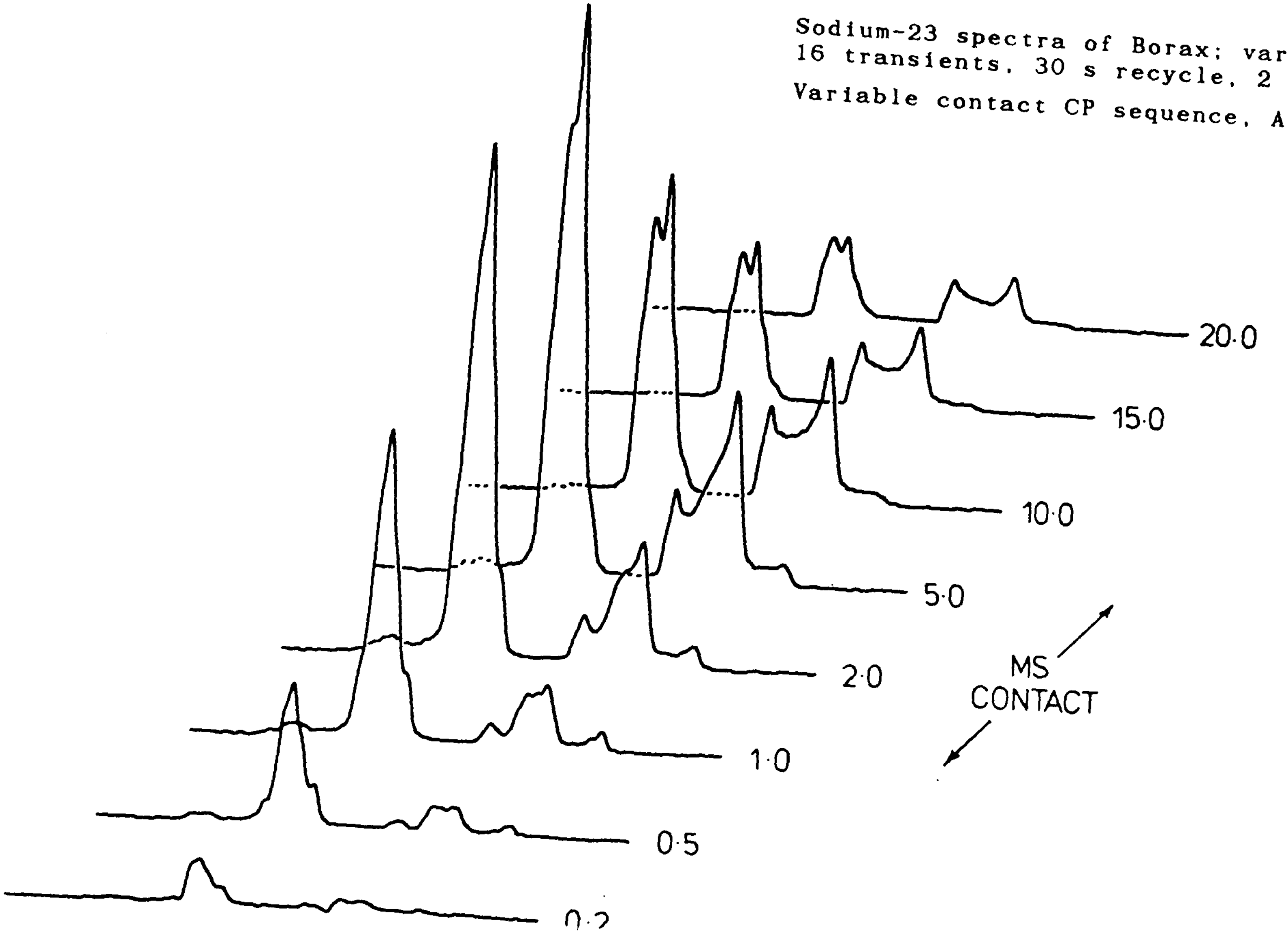

Sodium-23 spectra of Borax; variable CP
16 transients, 30 s recycle, 2 μs t_p, 4.0 kHz MAR
Variable contact CP sequence, A.I. comparison

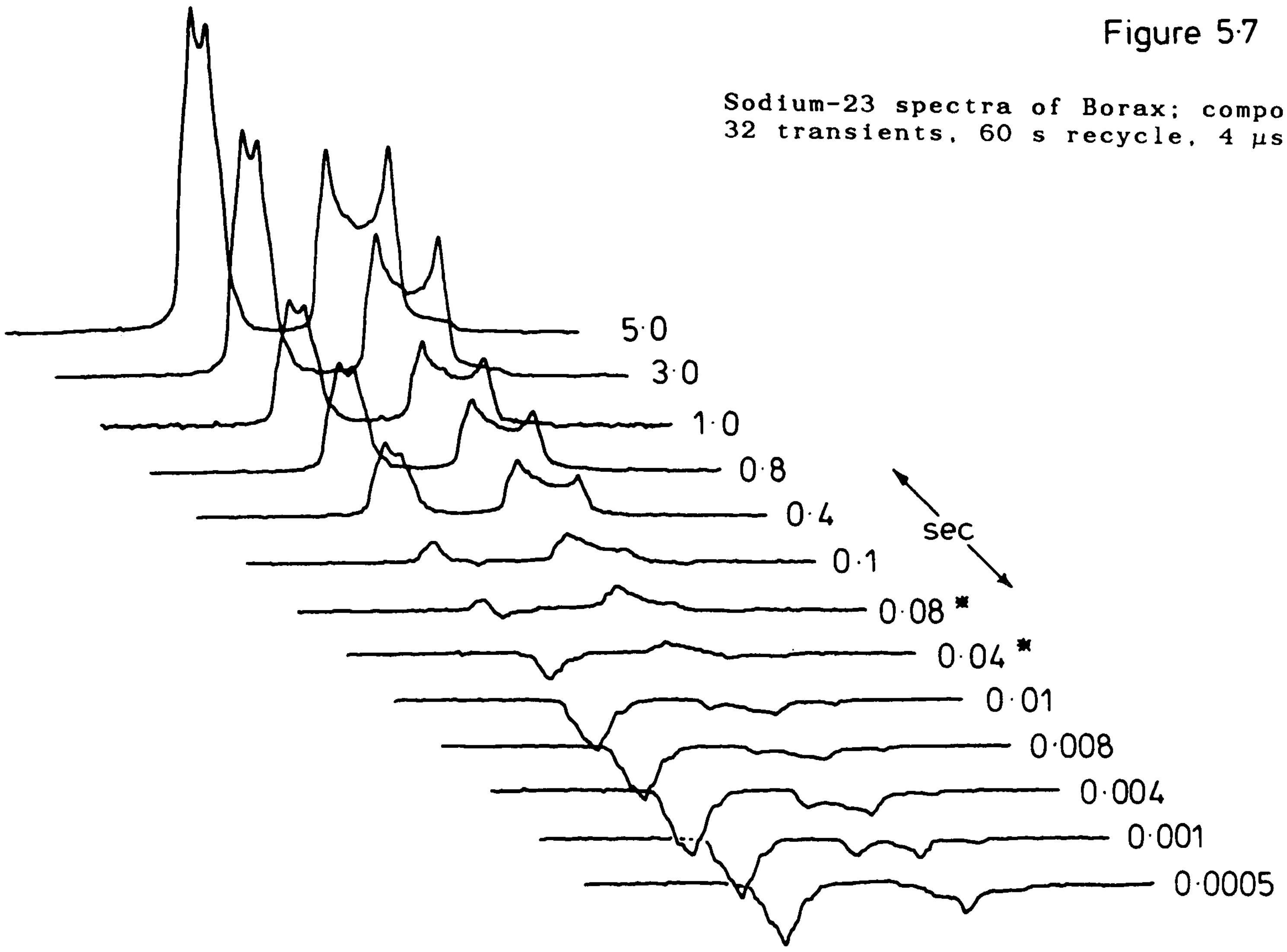

Figure 5·7

Sodium-23 spectra of Borax; composite π inversion
32 transients, 60 s recycle, 4 μs t_p, 4.5 kHz MAR

It is reasonable to postulate that in the DANTE sequence what is observed is the result of two cross-relaxation processess. The first rate we would expect to originate from the T_{IS} terms, measuring the exchange between the $\pm\frac{1}{2}$ transitions of the dilute (quadrupolar) and abundant spins. The second rate which is reasonable to expect, is the thermodynamic recovery of the $\pm\frac{3}{2}$ levels from the spin heating which results as a consequence of the Hartmann-Hahn contact. Both of these terms allow polarization and relaxation transfer mechanisms to occur since they are mutually conserving and secular. The magnitude and character of these terms is dependent upon the quadrupolar coupling and the asymmetry parameter of the sodium environment involved, as shown in equation 5.7. The rate processess involved should exhibit this dependency and it should be possible to design discriminating experiments. No quantitative studies have been made in this thesis since this relationship is only noted in passing in order to explain the differing data observed between the composite π inversion and DANTE experiments.

From these experiments it is possible to make assignments of the sodium environments to the data. The low frequency is observed to cross-polarize less efficiently and relax more quickly (by DANTE) than the high frequency line. This would all seem to indicate that this absorption is a result of the distorted sodium polyhedra which have been postulated from the crystal data. One explanation of the source of distortion noted, would be the intrusion into the sodium.$6H_2O$ polyhedra by oxygen atoms from the $[B_4O_5(OH)_4]^=$

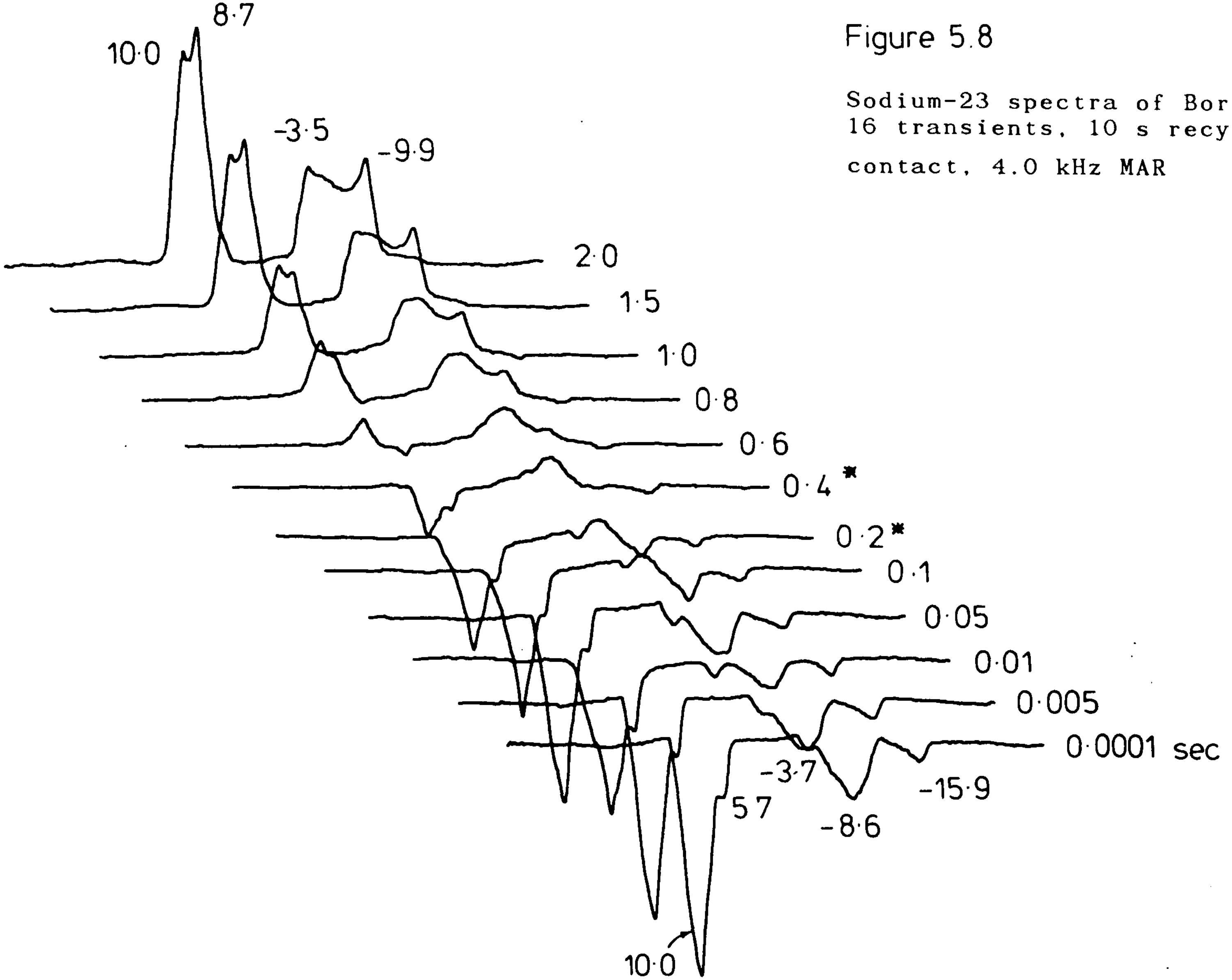

Figure 5.8

Sodium-23 spectra of Borax; DANTE sequence 16 transients, 10 s recycle, 4 μs t_p, 2 ms contact, 4.0 kHz MAR anions. This would create higher shielding and less efficient polarization transfer about the sodium site. A less symmetrical environment would also relax more quickly. The MAR NMR data presented in this chapter support this explanation. It would also seem obvious on this basis to assign the low frequency environment to the sodium which possesses the lower asymmetry and higher quadrupole coupling, reported in the single crystal NMR data.

Equivalent arguments can be made for the high frequency environment. This line cross-polarizes more efficiently and relaxes more slowly, indicative of a more symmetric local environment. The relative deshielding inferred by the chemical shift would also be expected in the undisturbed $Na^+.6H_2O$ octahedron. Given these data it is reasonable to assign this high frequency absorption line to an environment with a lower quadrupole coupling, as determined by the single crystal data.

In Tincalconite, diffraction data have shown that the lesser water content forces distortions of the polyhedra in order to maintain a proper oxygen charge balance.[43] The $[B_4O_5(OH)_4]^=$ polyanion remains the same, so the changes occur in the $Na^+.6H_2O$ polyhedra chains in order to preserve the three dimensional layer structure. The result is closer chain packing and face sharing in the sodium polyhedra, and a further sharing of the'-B-OH' hydroxyl groups in the $Na^+.6H_2O$ polyhedra. This manifests itself crystallographically in the observation of three distinct sodium environments.[43] Within the unit cell, one sodium environment remains a nearly regular octahedron, in another sodium environment the polyhedra are slightly distorted, and a third sodium site sits in polyhedra which share two faces each with other polyhedra, which is quite significantly distorted from the regular octahedron.

The single crystal NMR data indicate that all six sodium nuclei per unit cell must occupy special symmetry related positions in order to be consistent with the three inequivalent sites observed crystallographically. Each position will possess distinct point symmetry which, in a crystal, would be differentiating. In a powder this is not the case, since there can be no special orientations to the field upon which the polarization axes could be placed to distinguish the symmetry restrictions operating upon the site. Previous powder NMR investigations have failed to find more than two unique sites.[48] This was probably because of the overlap of signals from sites with similar quadrupolar coupling tensors. Tentative assignments have been made[45] placing the three sodiums observed with low quadrupole coupling, in the regular octahedron polyhedra determined crystallographically. This means two sodiums reside in slightly distorted polyhedra, and one sodium, with the highest quadrupole coupling, occupies a severely distorted polyhedron. These assignments would naively lead one to expect an NMR MAR spectrum with three absorption lines of intensity 3:2:1, going from high to low frequency respectively.

The single pulse decoupled spectra of Tincalconite are shown in Figure 5.9c. A single line at -5.2 ppm is observed, with what appears to be a shoulder at -0.2 ppm. In Figure 5.10 a variable contact cp stack plot is presented, which indicates the environments cross-polarize inefficiently. The relaxation parameters have been measured by the composite-π-pulse inversion sequence and give a relatively fast relaxation rate of 0.005 sec^{-1} for the entire line. These data imply that all sodium environments in the $.5H_2O$ lattice experience significant shielding (fast relaxation and low frequency chemical shift) which is indictive of a distorted polyhedral environment. The distortion is caused by the intrusion of oxygen atoms from the borate anion, which provide the higher degree of shielding.

These data are quite surprising, given the naive expectations drawn from the single crystal data. It is necessary to investigate this compound at higher field strength in order to obtain any further insight, and Figure 5.11 shows the result. The variable pulse length sequence was run at 7 Tesla with a decoupling field of approximately 30 kHz. This was sufficient to see that the lineshape at this field strength is clearly composed of several components. Unambiguous assignment of these components would be possible using lineshape simulation programs, a facility which was unavailable. However, it is possible to construct a reasonable, qualitative, argument explaining this single chemical shift using the magnetic resonance data obtained.

If the quadrupole coupling data in Table 5.2 areexamined closely it can be seen that three sodium environments possess small quadrupole coupling but a relatively large asymmetry parameter. It is reasonable to assign this environment to the major absorbance line at -5.2 ppm and right handside shoulder, given expected

Figure 5.9

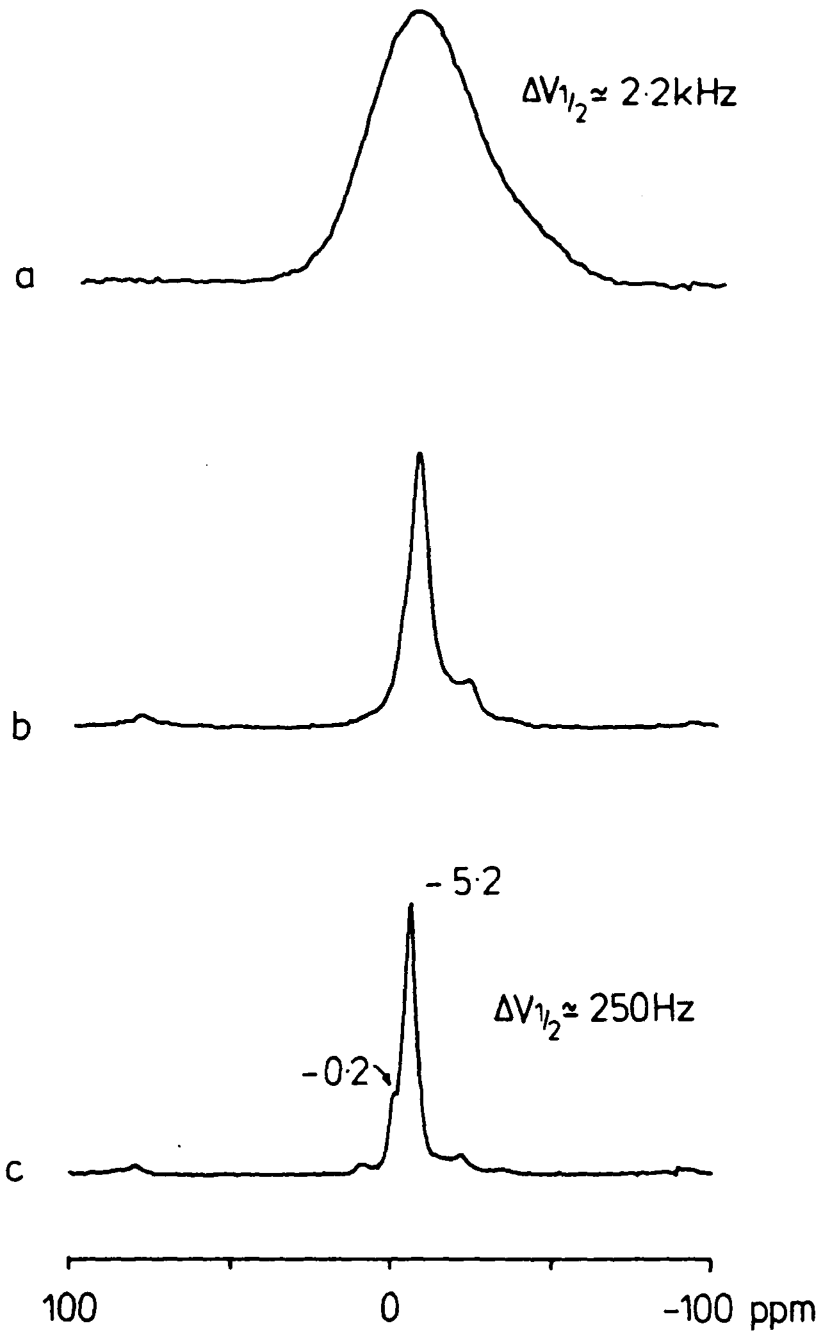

Sodium-23 spectra of Tincalconite
8 transients, 30 s recycle, 2 μs t_p

a) static decoupled
b) MAR (4.5 kHz) coupled
c) MAR (4.5 KHz) decoupled

Figure 5.10

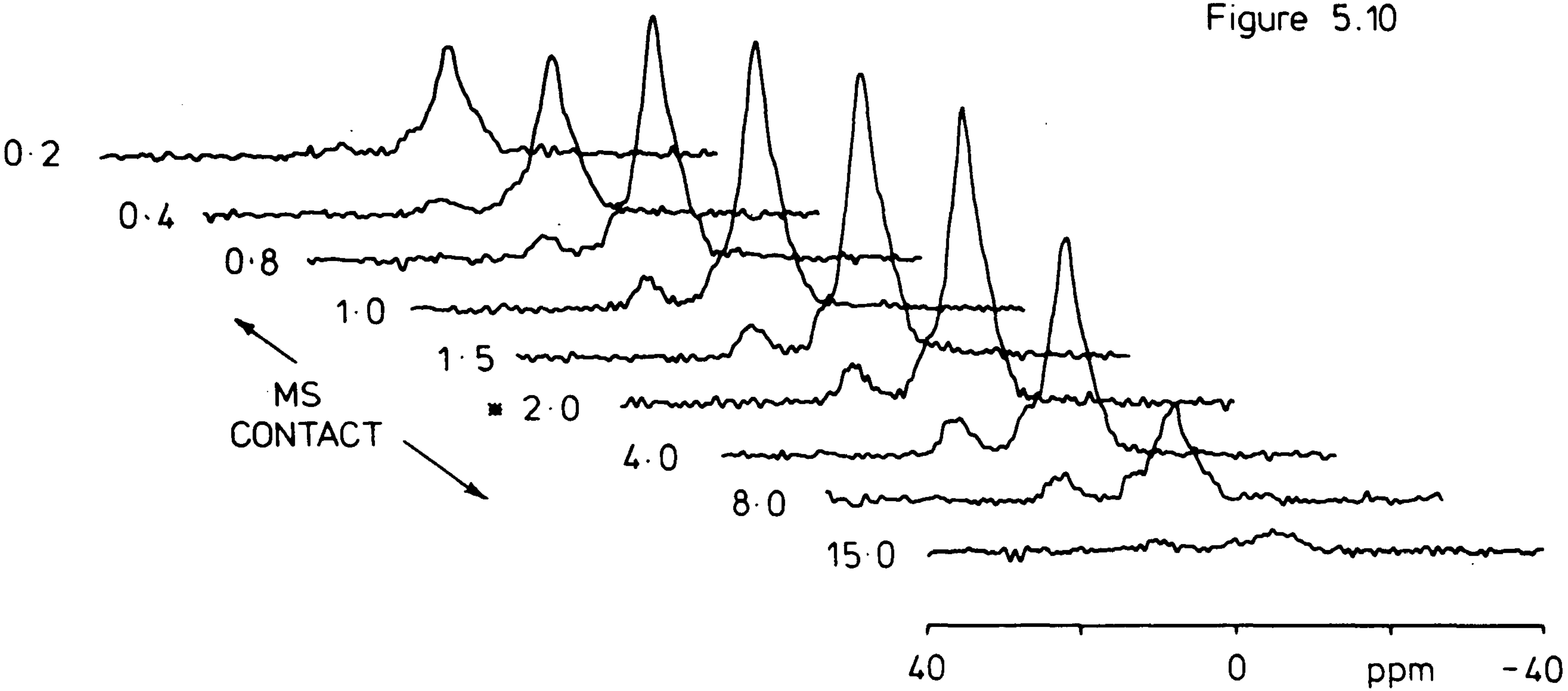

Sodium-23 spectra of Tincalconite; variable CP
16 transients, 10 s recycle, 4 μs t_p

Figure 5.11

Sodium-23 spectra of Tincalconite; variable pulse length response
16 transients, 10 s recycle, MAR 4.0 kHz,
7.0 Tesla

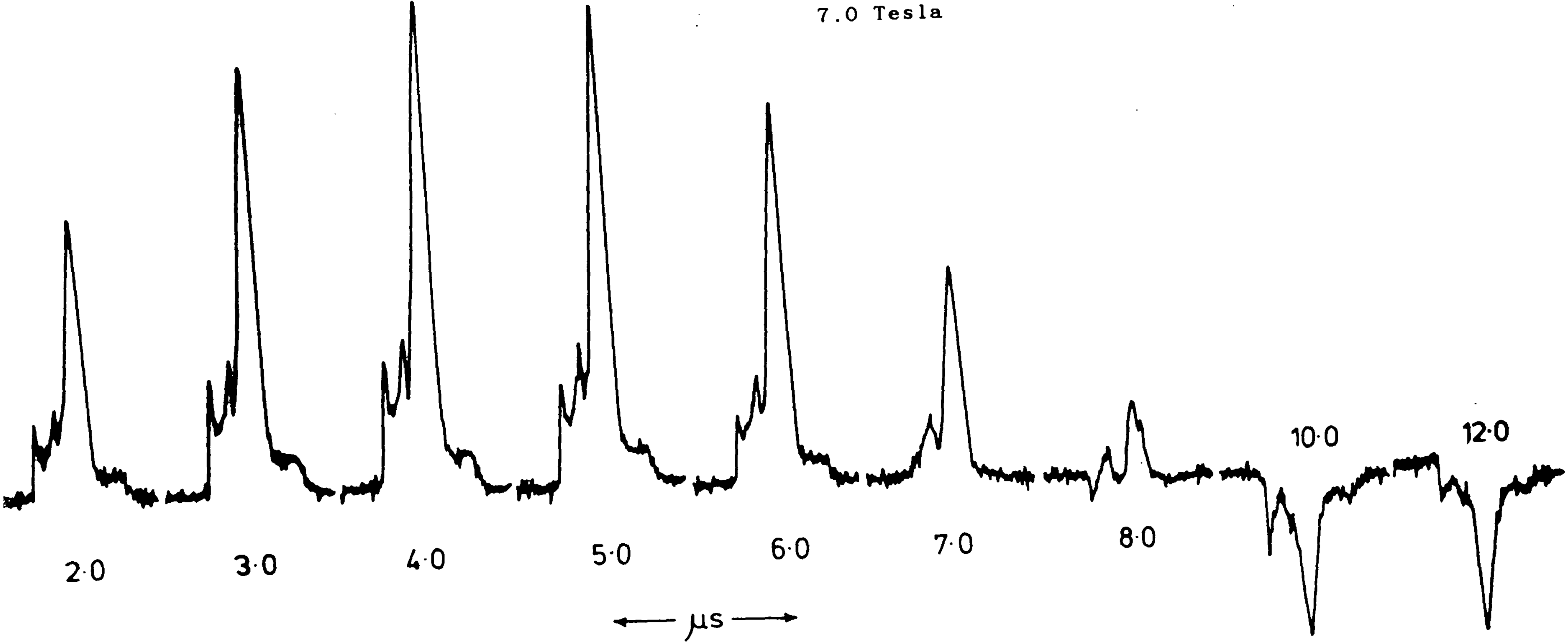

contributions to the lineshape via the asymmetry parameter.[16] The two smaller features at higher frequency obscured by the main line, may originate from the two environments with intermediate quadrupole coupling. The single sodium environment which possesses the largest quadrupole coupling constant may be entirely hidden from view, since a great deal of its intensity will reside in the higher order transition features which are unobserved by virtue of the frequency shifts involved. The fact that the shielding appears to be similar for all environments can be accounted for by considering the reduced interaxial distance. It would be reasonable to expect a significant amount of exchange to occur between the polyhedra given the amount of sharing of oxygen between polyhedra, and the closer proximity. These arguments allow a qualitative explanation of the single resonance lineshape observed for Tincalconite.

5.3.2 Demonstration of Polarization Transfer Selectivity

The purpose of implimenting the cross-polarization experiment has been stated as two fold. The first application, that of setting a Hartmann-Hahn match and calibrating the $\underline{B}_1$ fields has been demonstrated in the preceeding section. Illustration of the selective nature of the polarization transfer pathway can be accomplished using any compound which contains two sodium sites which possess different relationships to the proton environment. The layer silicate kenyaite provides such an example, and the sodium-23 spectra are shown in Figure 5.12. There are two distinct sodium environments, one which exhibits residual quadrupolar contributions in the MAR experiment by the presence of spinning sidebands. The second environment shows a single Lorentzian lineshape. The cross-polarization spectra exhibit a reversal of intensity, which can be interpreted as degree of efficiency of polarization transfer. With this data the high frequency environment can be assigned to sodiums which are bound in the mineral lattice, and the low frequency environment may be assigned to those sodium which reside between layers, in close proximity to the interstitial water molecules. The chemical shifts and consequent shielding arguments support these assignments also. The exact nature of this mineral will be discussed in much greater detail in Chapter 6, but serves here as an eloquent illustration of the power of this experiment as an analytical tool.

Figure 5.12

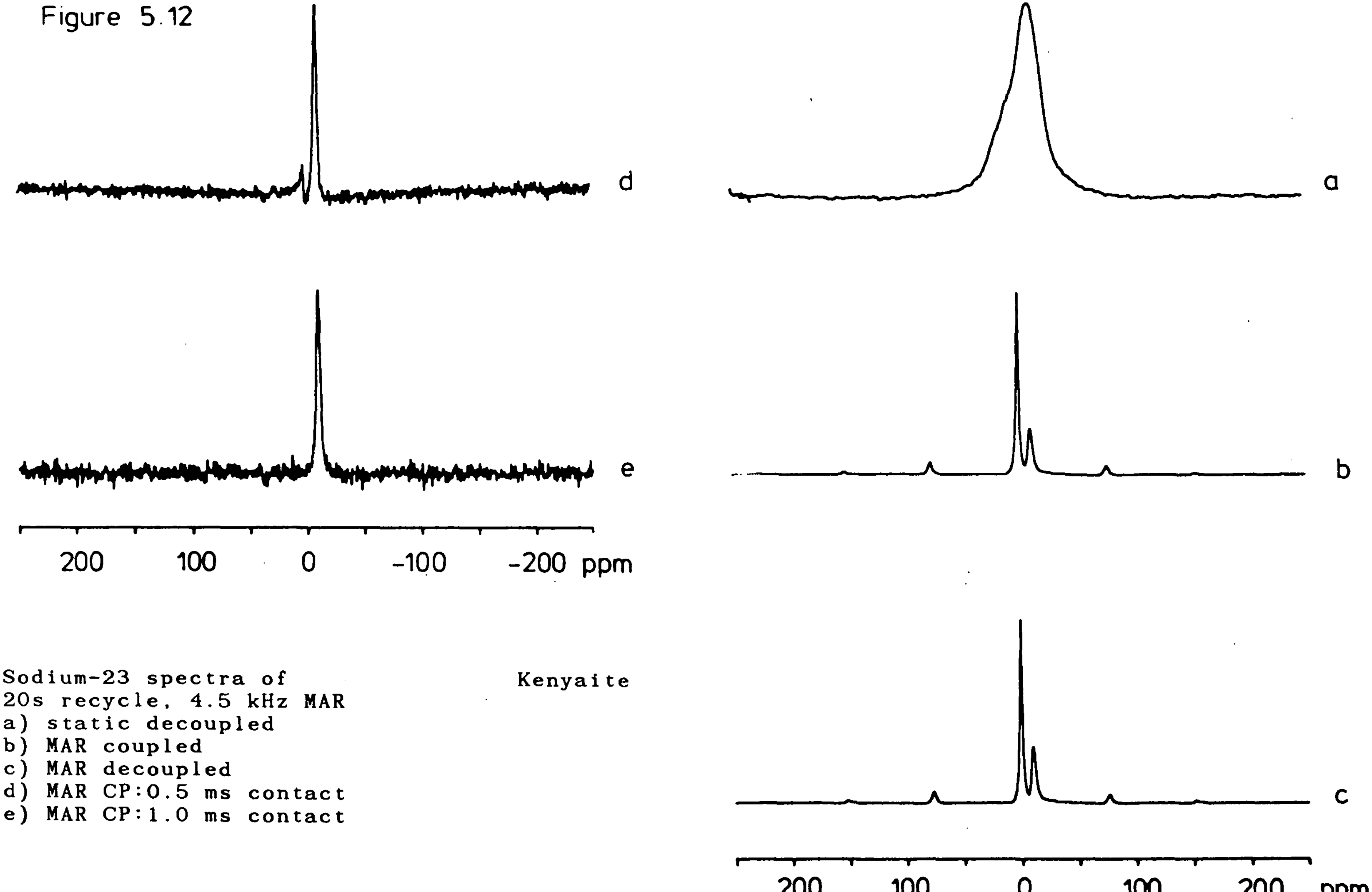

Sodium-23 spectra of Kenyaite
20s recycle, 4.5 kHz MAR
a) static decoupled
b) MAR coupled
c) MAR decoupled
d) MAR CP:0.5 ms contact
e) MAR CP:1.0 ms contact

5.4 Conclusions

The purpose of this chapter has been to document the character of the data which may be extracted from quadrupolar nuclei, when used as molecular probes in solids, by direct observation. The theory of quadrupolar nuclei has been discussed and a variety of magnetic resonance experiments has been demonstrated by application to a number of chemical systems. These investigations have shown that a great deal of information can be obtained using quadrupolar nuclei, but that in order for this data to be sensibly interpreted, the experiment must be performed under rigorously defined conditions. The cross-polarization experiment has been shown to be a sensitive tool for the calibration of the perturbing rf fields, and a suitable reference compound has been demonstrated. The diagnostic capabilities of single and double resonance experiments have also been demonstrated and shown to discriminate between sodium environments.

CHAPTER SIX

APPLICATIONS OF SOLID STATE NMR METHODS

"You can't depend upon your judgement when your imagination is out of focus".
Mark Twain

CHAPTER SIX: Applications of NMR Methods to the study of Chemical Systems in the Solid State

Applications of NMR Methods to the Study of Chemical Systems in the Solid State.

6.0 Introduction

This chapter represents the culmination of the methods developed in previous chapters. The results presented up to this point have been relatively trivial, in a chemical sense, since most systems used as examples have been well characterized by other analytical techniques. The real utility of solid state NMR is evident when previously inaccessible data is obtained, resulting from application of magnetic resonance methods to difficult chemical problems, where conventional techniques have failed.

The results and discussion contained in this chapter cover a diverse range of solid state systems. The original impetus for the majority of the development work presented in earlier chapters, was founded in the investigation of silicates. This is reflected in the relative emphasis placed on the silicate section. The remaining studies illustrate the versatility of solid state NMR when applied to chemical systems of current interest and industrial importance.

Each section is organized such that the compounds investigated within are chemically similar systems. The sections themselves are treated separately since they are chemically unrelated. Corroborative techniques have been used where possible and conclusions drawn upon the complementary nature of the data obtained.

6.1 Solid Silicate Systems

The study of insoluble inorganic silicates, using silicon-29 solid state NMR methods, has shown that the isotropic chemical shift is influenced by ionization of the silicate anion and cation substitution in the silicate lattice, but is determined mainly by the degree of condensation of silicon-oxygen tetrahedra and octahedra which constitute the anion.[1] Further investigations of isotropic chemical shifts[2,4] and chemical shift tensor components[3,4] have shown that the diamagnetic shielding of an SiO_4 tetrahedron is sensitive to the Si-O bond-length. These relationships provide a means to systematically investigate the structural properties of silicates using silicon-29 solid state NMR methods.[5,6]

The sodium atom has also been employed as a molecular probe using the isotropic chemical shift as a sensitive measure of sodium coordination in minerals.[7] The quadrupolar nature of the ^{23}Na nucleus has also been exploited, using conventional relaxation experiments, to determine the nature, and sodium population, of different electric field gradient environments.[8]

The proton environments of industrially important silicates, such as zeolites[9] and silica-gel,[10,11] have been investigated using MAR and CRAMPS NMR experiments. The motivation for these studies has been the direct observation of catalytic sites. However the role of protons, in the form of water and hydroxyl groups, in minerals has been recognised.[12,13] In this section the methods which have been described in the preceding chapters are applied to a variety of solid silicate systems. Conclusions will be drawn upon the data presented within each section.

6.1.1 Metasilicates: Cyclosilicates and Polysilicates

Metasilicates may be defined as a composition of silicon, oxygen, and an alkali cation such that there are less than two moles of basic oxide per mole of silica, and less than four oxygen atoms per silicon atom. The scarcity of oxygen forces a condensed structure, and in the 1:1 ratio silicates considered in this section there are three oxygen atoms to each silicon. This causes the anion tetrahedra to share corners, forming infinite rings or chains which constitute the two subgroups; cyclo- and poly-silicates.[14] The influence of a cation on the silicate anion is well known in the metasilicates.[15] As the cation alters in size the repeating unit (chain or ring) changes in periodicity,[16] orientation,[17] or bond length[18] to accommodate the cation. Within each anion there may also be several polymorphs with varying structures depending upon the nature of the mineral formation[19](i.e. temperature, pressure).

Various data have been reported in the literature but there appears to be inconsistency with nomenclature which can cause confusion concerning which polymorph is being referred to.[20] Before proceeding it is prudent to state which nomenclature will be used for the metasilicates studied in this text.

The crystal structure of Na_2SiO_3 has been solved.[21] It consists of SiO_3 chains with two metasilicate tetrahedra in the repeat unit. Only one phase of sodium metasilicate has been reported, so no ambiguity exists here.

The crystal structure of $BaSiO_3$ has also been investigated. This was also found to be an infinite chain structure, of composition $\infty[Si_2O_6]$, where the barium atoms are irregularly coordinated to eight oxygen, connecting the chains. There has also been a low temperature phase of $BaSiO_3$ reported which forms cyclic anions.[14] This will be referred to as the 'pseudo' phase in analogy with the wollastonite minerals.

There are three polymorphs of $CaSiO_3$. One modification is composed of cyclic trimeric anions ($Si_3O_9^{6-}$) and will be referred to as pseudo-wollastonite.[23] The two remaining modifications are both infinite chains of constitution (Si_2O_6) with two tetrahedra per repeat unit. The difference between the chain polymorphs is found in the packing per unit cell, and these will be referred to as para-wollastonite and wollastonite.[24] The properties of calcium and strontium metasilicates have been investigated using infrared spectroscopy.[25] The strontium metasilicate also exhibits modifications depending upon the nature of its synthesis.[26] Two different modifications have been reported, a cyclic analogue of pseudo wollastonite and a chain structure which is isomorphous with $SrGeO_3$.[26,27]

Enstatite ($MgSiO_3$) has been shown to be composed of single chains with a repeating configuration every two tetrahedra.[28] There are three polymorphs, clino, proto and ortho enstatite which represent subtle changes in the chain conformation.

The NMR data for a number of metasilicates have been reported in the literature, which are shown in Table 6.1.

Table 6.1: Metasilicate chemical shifts (in ppm) reported in the literature

Metasilicate	
Li_2SiO_3	-74.5[a]
Na_2SiO_3	-76.8[a], -78.0[c]
$BaSiO_3$	-80[c]
$Ca_3Si_3O_9$ (pseudo)	-83.5[b]
$Ca_3Si_3O_9$	-87.9;-89.4[e], -88.0[b], -89[c]
$SrSiO_3$	-85[c]
$MgSiO_3$	-82[a], -81;-84[c]

a. ref. 29
b. ref. 30
c. ref. 31
d. ref. 32
e. 2:1 ratio ref. 29

In all cases, excepting pseudo wollastonite, no specification of polymorph or sample history was discussed, assignments were presumably made using the isotropic chemical shift and corroborative analysis is not mentioned. General trends have been noted between the cation properties and the silicon-29 chemical shift.[29] These studies have attempted to correlate the Pauling electrostatic bond strength,[33] between the cation and the silicate anion, with the chemical shift. This relied upon the observation that the Pauling electronegativity increases with the covalent character of the cation-oxygen bond, which has been shown to correlate with the bond strength.[34] In general, the relationship is noteworthy, but in attempts to quantify the correlation there are anomalies between calculated and observed values.[32]

In Table 6.2 the silicon-29 data obtained as a result of this investigation are shown. All values were measured from single pulse, proton decoupled experiments, except apophyllite, which cross polarized exceptionally well. Ring or chain assignments are made as a result of deductions from X-ray powder diffraction spectra.

Table 6.2: Metasilicate Silicon-29 Data at 4.7 Tesla

Metasilicate	δ ppm ($\Delta V\frac{1}{2}$, Hz)	Configuration
Na_2SiO_3 (synthetic)	-76.9 (80)	chain
$BaSiO_3$ (synthetic)	-79.9 (25)	chain
$CaSiO_3$ (synthetic)	-83.6 (30)	ring
$CaSiO_3$ (P1 grade β wollastonite)	-88.4 (220)	chain
$CaSiO_3$ (P4 grade β wollastonite)	-88.3 (300)	chain
$CaSiO_3$ (calcined α wollastonite)	-83.9 (50)	ring
$SrSiO_3$ (synthetic)	-86.9 (80)	ring
$Mg_2Si_2O_6$ (natural)	-81.0, -83.5 (80)	chain
$KCa_4[Si_4O_{10}](F,OH).8H_2O$ (apophyllite)	-93.1 (20)	sheet

where $\Delta V\frac{1}{2}$ refers to the full linewidth at half height in Hz and P1,P4 refers to mineralogical grade.

In Figure 6.1 the data from Tables 6.1 and 6.2 are graphically presented showing the relationship between observed chemical shift and Pauling electronegativity (χ). The superscripts indicate data taken from literature and the corresponding reference given in Table 6.1. The data illustrate a general trend (dotted line) correlating the cation electronegativity with chemical shift as a function of conformation. However, given the naive expectations of the general relationships developed to explain relative condensation and cation effect, one is at a loss to explain the data observed for Ba, Na, and Li cations. In order to fully explain the data in Figure 6.1 it is necessary to consider that cation electronegativity is not the only factor controlling the conformation of silicate chains or rings.[35] It has been shown that size and mean valency of a cation also determine the periodicity of a metasilicate.[15] For example, the reason both ring and chain polymorphs exist is because, given different formation conditions (temperature, pressure), the effective radius of the cation changes, thermodynamically selecting a different configuration.[35b]

Upon close scrutiny it is possible to explain the unusual values for the polysilicate $M_2^+[SiO_3]$. Since there are two monovalent cations, per tetrahedron, equalizing the charge balance of the chains, the chains themselves must stretch in order to accommodate the cations. This decreases the average valence of the cation. Cations such as Li, Na, and Ba can be considered as relatively electropositive, such that their valence electrons spend a

Figure 6.1 : Anhydrous Metasilicate chemical shift vs electronegativity

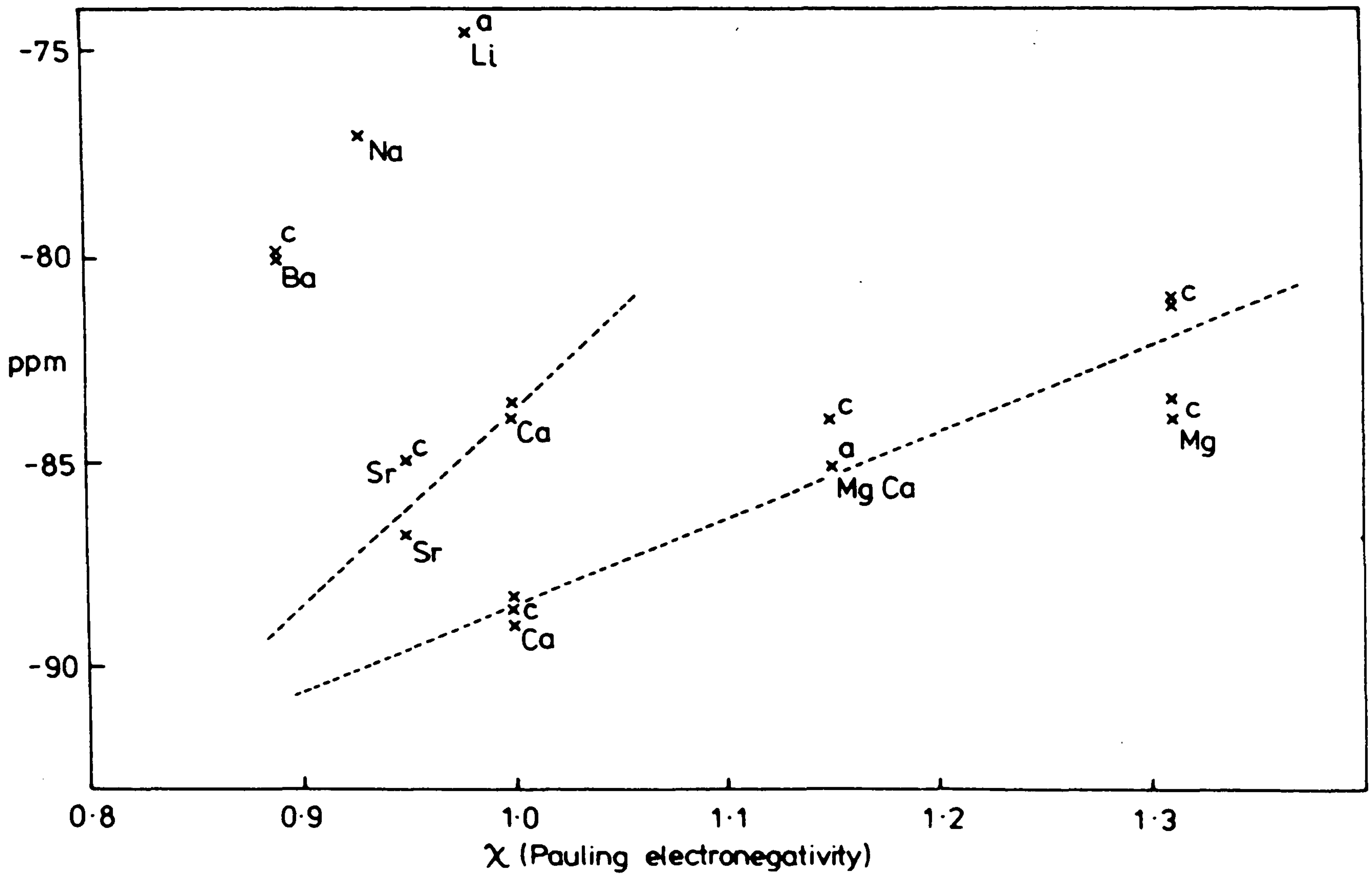

great deal of time on the anion. The Barium cation is known to favour an unusually large variety of polymorphs, which are not observed for other divalent cations, principally because of its large radius[14]. The silicate anions therefore experience a high degree of charge density which further promotes stretching of the chain. The summation of these effects changes the conformation of the chain (bond angle and length) to stabilize the charge balance with the cation. This results, finally, in significantly different shielding of the tetrahedra which constitute the chain, which is reflected in the chemical shift. Thus it is not simply a case of an ordered change in the distribution of valence electrons, as the cation changes, hence the dispersion of data points.

The formation of cyclosilicates is generally less favourable than that of chains. This is because the packing of tetrahedra in the rings is energetically less favourable than the packing available in a chain configuration. However, cyclic anions will form in the presence of highly electronegative cations, or in the case of single ring silicates, in the presence of 'soft' cations such as Na^+, K^+, Ca^{2+}, Sr^{2+}, Ba^{2+}, where the conditions are thermodynamically unfavourable for chains.[36] The large, and relatively nebulous, bonding orbitals which give these cations the trivial classification of 'soft' cause little destabilizing effect, or imposed strain, on the anion to accommodate them in a lattice where the tetrahedra are already closely packed. This explains the existence of the cyclosilicate polymorphs of the single chain metasilicates.

In particular the calcium polymorphs presented in this investigation make a good example. The isotropic chemical shift experiences a 5.0 ppm shift to low frequency upon formation of pseudo-wollastonite. This is a result of deshielding of the silicate anion by the closer proximity of the calcium cation in the close fitting ring lattice. As an aside, this same relationship established between the size, electronegativity, and valency of cations, and the shape of silicate chains also holds for phyllosilicates, where the chains are linked in tetrahedral layers, each tetrahedron sharing three corners. The linking of the chains is accomplished through further condensation of the anion tetrahedra. This in turn changes the identity period of the chain in order to accommodate the cation valence demands. This can be illustrated by considering the mineral apophyllite ($KCa_4[Si_4O_{10}]_2(F,OH).8H_2O$) where the chain periodicity required by the cation is double that needed in wollastonite.[37] The chemical shift of apophyllite is sensitive to the condensation of the tetrahedra, exhibiting a further 5 ppm shift to lower frequency, giving -93.1 ppm. Using silicate nomenclature the wollastonite environment is a Q^2 tetrahedron and the apophyllite contains Q^3 tetrahedra as a consequence of linking to form layers. This demonstrates a change where the cation effect has remained relatively constant but the chemical shift has been sensitive to a change in periodicity of the chain links.

In conclusion, the silicon-29 NMR data have been shown to be sensitive to changing cation effect within the anhydrous metasilicates. It has been shown that ring and chain polymorphs can be differentiated using NMR, and an attempt has been made to explain anomalous chemical shift data. This has resulted in the conclusion that conformation and periodicity are dependent upon many criteria, most importantly thermal history and cation properties, which also change the shielding of the silicate anion.

6.1.2 Sodium Silicate Hydrates

A variety of sodium silicate hydrates have been prepared and characterized in the literature.[38] Single crystal refinements have shown that, unlike the anhydrous sodium silicates (Na_2SiO_3,[39] $\alpha Na_2Si_2O_5$,[40] $\beta Na_2Si_2O_5$[41]) which form chains and sheets through shared tetrahedra corners, the hydrates form isolated anion tetrahedra, which are unlinked through any common oxygen atoms.[42,43,44,45] Further refinement[46a] supports the suggestion[43] that the formulae should be written $Na_2(H_2SiO_4).XH_2O$ to reflect the structure of the silicate anion. The chains are held in place by hydrogen bonding to oxygen atoms coordinated to the sodium cations, which form helical chains of sodium.XH_2O octahedra.

The $Na_2O.SiO_2.H_2O$ system here is of industrial importance. The nature of its origin is such that, apart from the Na_2O/SiO_2 ratio value, little is known of the species present in the final product. The physical properties change drastically over the range of ratios investigated; a 1.0 ratio (1.0R) aliquot appears as a low density blown powder and a 3.3 ratio product resembles an amorphous glass. This diverse density and solubility behaviour made conventional methods of analysis difficult.

Consequently no precise data are known about the water content of the final state, but from the conditions of synthesis it is presumed to remain approximately constant throughout the series. Briefly restating the conditions of manufacture (see Chapter three); these powders have been produced by mixing two aqueous slurries of Na_2O and SiO_2, under pressure, and aspirating the mixture into a constant humidity atmosphere.

The NMR data obtained for these systems are shown in Table 6.3. All spectra were acquired using a single pulse experiment with broad band proton decoupling. All spectra recorded consisted of a single absorbance which exhibited a coherent change in chemical shift as the $Na_2O:SiO_2$ ratio changed. The 3.3 R powder was the only peak to exhibit any fine structure, in the form of weak shoulders in the silicon-29 data, on both sides of the central peak. Some sodium-23 spectra gave weak spinning sidebands. Generally these spectra required a large number of transients and, because of their unkown composition, long recycle delays to ensure even qualitatively accurate data. Neither nuclei were found to cross-polarize to any extent, nor did the cp experiment yield any new data. The proton CRAMPS spectra were broad (~ 300 Hz) and uninformative for all samples. The data shown exhibit definite trends in the chemical shift and linewidth values, for both nuclei, with respect to the ratio.

Table 6.3: Sodium Silicate Hydrate NMR data

Ratio ($Na_2O:SiO_2$)*	Sodium-23 ppm ΔV1/2 (kHz)	Silicon-29 ppm ΔV1/2 (kHz)
3.3R	-34.9 (2.2)	-88.4shldr,-97.0(.2)-107.1shldr
3.0R	-10.9 (2.9)	-93.6(.4)
2.6R	-9.0 (2.4)	-92.4(.3)
2.0R	-7.2 (1.5)ssb	-90.0(.3)
1.4R	-8.1 (1.6)ssb	-86.0(.2)
1.4R	-4.4 (1.4)ssb	-85.1(.2)
1.0R	-1.7 (1.1)ssb	-77.6(.1)

*ratio is % by weight

ssb = spinning sidebands

shldr = as shoulder on main spectral feature

Assuming a constant cation effect, then the silicon-29 chemical shifts can be interpreted as indicating an increase in shielding of the silicon atom as a result of greater condensation of the silicate tetrahedra, as the SiO_2 content increases. The sodium-23 lines are relatively broad and exhibit no evidence of quadrupolar contribution to the lineshape. At low ratio values (high Na_2O) the central line is narrower and accompanied by spinning sidebands. This indicates an increase in anisotropy of the local environment of the sodium atom.

In devising a model to describe the system, given the data obtained, there are several theories, which have been suggested in the literature in the investigation of silicate glasses, which might be considered. The local structure of a silicate glass can be described as a random network,[46b] disordered association of crystallites,[47] or 'discrete ions'.[48] Changes in local structure have been suggested to account for inflection points and correlation trend changes in physical properties of alkali glasses.[49,50] Significantly, this has been correlated with the molecular percentage of Na_2O to SiO_2[51] and found to coincide with values of 33% and 50%, which corresponds roughly to 3R and 1R ratio values in the notation used in Table 6.3. These mole percentage singularities are related to the formation of disilicate ($Na_2Si_2O_5$) and metasilicate (Na_2SiO_3) species respectively.

The spectral line shapes observed in this investigation are uniformly uninformative, except for the 3.3R powder, indicating no differentiation of ordering in local environments. Given the relatively large linewidths it is possible that each ratio powder represents a disordered array of environments which have a roughly Gaussian distribution of shielding environments, dictated by the $Na_2O:SiO_2$ ratio, centered about the average chemical shift. However, the isotropic chemical shift of both nuclei is sensitive to the changing ratio. Furthermore, the values observed are in the range such that the silicon tetrahedra are expected to be in Q^2 and Q^3 environments as the ratio progresses from 1R to 3.3R.

These data indicate that in a high SiO_2 environment (i.e. 3.3R) the silicon atoms are forming a polymeric structure where only one oxygen bond of the silicate tetrahedra is bonding to a sodium atom. In the low SiO_2 powders (i.e. 1.0R) the silicate anion now coordinates two sodium nuclei. The observed increase in anisotropy and deshielding of the sodium nucleus with decreasing ratio value support this explanation.

It is now possible to consider the chemical introduction of sodium into the SiO_2 tetrahedra as completely random: if this is the case then it would be reasonable to expect a statistically random distribution of Q^0, Q^1, Q^2, Q^3, Q^4 silicon environments in a sample, depending upon the stoichiometry of the original slurry.

If the sodium was coordinated to the silicate tetrahedron in an ordered manner, then it would be reasonable to expect a singular distribution of silicon environments centred about unique chemical shift values, as every tetrahedron accepts first one sodium atom, and then two, and so forth as the ratio decreases.

Immediately it is obvious from the NMR data that the second mechanism is not dominating. However, neither is the first mechanism sufficient to explain the data since the distributions are not completely random. The probable reason for the failure of both conventional hypotheses is possibly because of the presence of water. The H_2O molecules may allow the formation of a variety of species of similar condensation which blur the statistical singularities which it would be reasonable to expect in a glassy system.[52,53]

An illustrative example demonstrating the variety of species possible in a system of this type can be found in the sodium metasilicate $Na_2SiO_3.9H_2O$. This compound is known to be unstable[43] and, as commercially available white crystals, contains several of the lesser hydrates and possibly anhydrous species. This is evident upon observing the silicon-29 and sodium-23 NMR data shown in Figures 6.2 and 6.3 respectively. The single pulse decoupled spectrum in 6.2a shows at least six unique silicon environments, which lie in the range of Q^0 to Q^3 species. It is not surprising that the high frequency environment cross-polarizes quite readily in 6.2b, since (from the chemical shift) it probably represents the true $Na_2H_2SiO_4.8H_2O$ octahydrate.[30,43] The sodium-23 spectra shown in Figure 6.3 suggest that there is more than one sodium environment. The single pulse decoupled MAR sodium spectrum in Figure 6.3b also shows significant quadrupolar coupling in the line shape. The sodium-23 cross-polarization spectrum (6.3c) suggests that there are components which are in different thermodynamic contact with the lattice. This is especially easy to see in Figure 6.2d where the cross relaxation rate is significantly different between environments, changing the line shape as a function of contact time. This also suggests the existence of more than one sodium environment in the sample. Attempts to obtain MAR spectra at higher field were unsuccessful because of repeated decomposition of the sample, upon spinning at 3 kHz, in a 7.0 Tesla static field.

In conclusion, both the sodium-23 and silicon-29 chemical shift have been shown to be sensitive to a changing $Na_2O.SiO_2.H_2O$ ratio. The data obtained have allowed conclusions to be drawn upon the character of the species which constitute a disordered amorphous system and the nature of their formation.

Figure 6.2 : Silicon-29 Spectra of $NaSiO_3 \cdot 9H_2O$

Silicon-29 spectra of $Na_2SiO_3 . 9H_2O$

MAR 3.5 kHz, 4 μs 90° pulse
a) MAR decoupled spectrum, 1800 transients
b) MAR cp experiment, 100 transients, 1.0 ms contact
c) Variable contact cp sequence, 100 transients

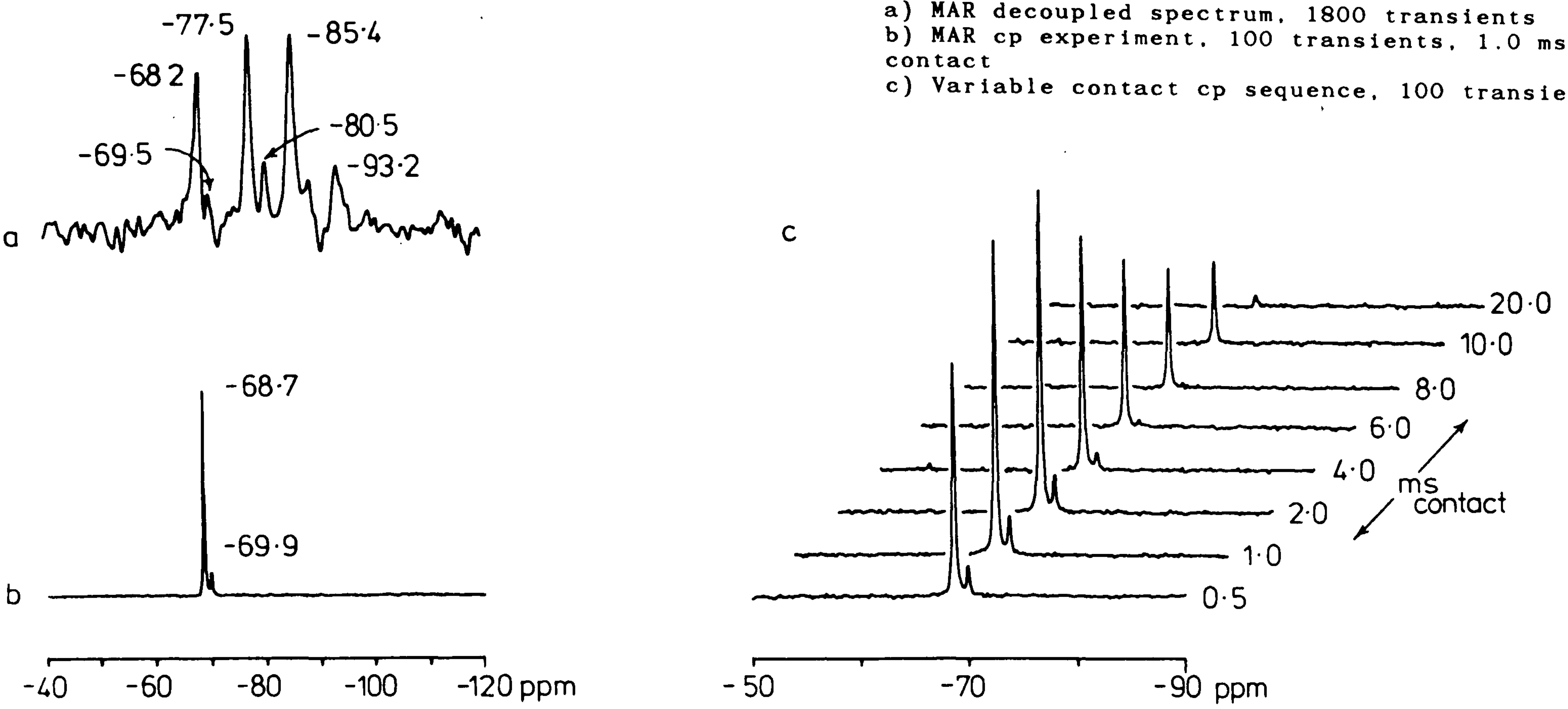

Figure 6.3: Sodium-23 Spectra of $NaSiO_3 \cdot 9H_2O$

Sodium-23 spectra of $Na_2SiO_3.9H_2O$

MAR 3.5 kHz, 2 μs 90° pulse
a) static decoupled, 20 transients
b) MAR decoupled, 20 transients
c) MAR cp decoupled, 20 transients
d) Variable contact cp sequence, 50 transients

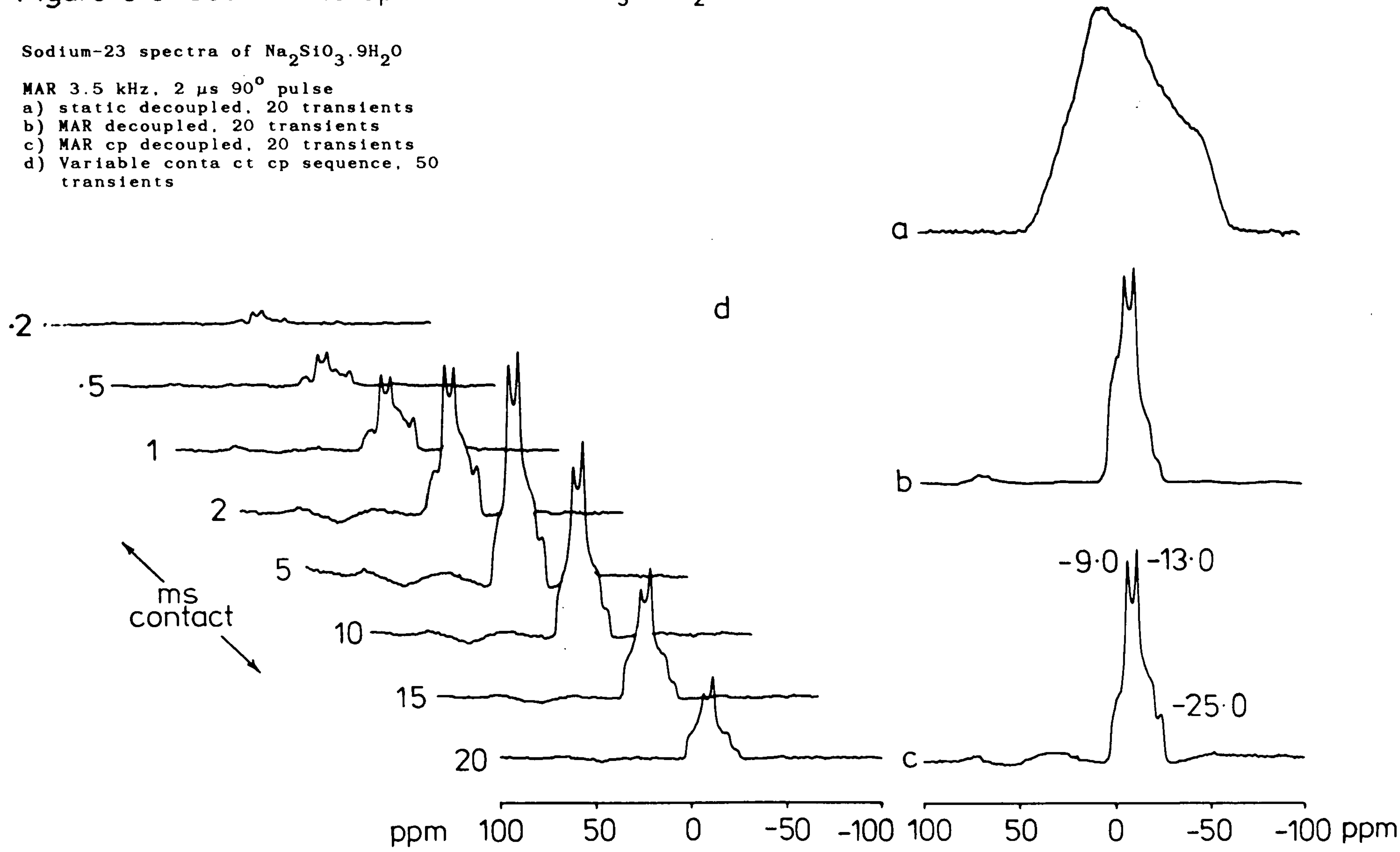

6.1.3 Layered Sodium Phyllosilicate Hydrates

Hydrous sodium silicate minerals have been shown to possess unique ion exchange and intercalation properties.[54,55] It has been suggested that the observed microporous behaviour and reactivity are a result of a lamellar structure.[56,57] Structural characterization has been difficult in all but the simplest of these minerals[58,59,60] because of the lack of single crystals for X-ray determinations. It has been shown[61] that solid state multinuclear NMR can be sensitive to layer thickness, and both inter and intra layer order. In this section further investigations will confirm this and allow construction of a model for the structure of these compounds.

Table 6.4 shows the empirical formulae and basal spacing of the five hydrated sodium silicates which have been characterized in this investigation. In phyllosilicates the layers can be considered as 'regions of equal directedness'[14] in the a,b plane of a lattice. The basal spacing would then be defined as the fundamental repeat distance in the c direction which includes the layer thickness and any interlayer space.

The sample sources have been described in Chapter Three but the number and origin of samples for each mineral are reiterated with appropriate literature reference in Table 6.4.

Table 6.4: Hydrated Sodium Phyllosilicate

Trivial Name	Empirical Formulae	Origins(number)*	Basal Space(d_{001} A°)
MAKATITE	$Na_2O.4SiO_2.5H_2O$	NATURAL[62]	N.A.
		SYNTHETIC[68] (1)	9.0
KANEMITE	$Na_2O.4SiO_2.7H_2O$	NATURAL[63]	10.3
		SYNTHETIC[55] (1)	10.2
OCTOSILICATE	$Na_2O.8SiO_2.9H_2O$	SYNTHETIC[64] (1)	11.1
MAGADIITE	$Na_2O.14SiO_2.10H_2O$	NATURAL[65] (3)	15.5
		SYNTHETIC[66] (3)	13.2
KENYAITE	$Na_2O.22SiO_2.10H_2O$	NATURAL[65] (3)	19.7
		SYNTHETIC[67]	19.5

*The values in parentheses indicate the number of samples of each type which have been characterized in this investigation. The superscript indicates the appropriate reference.

The ordered behaviour of the basal spacing, with respect to the increasing SiO_2 content of a mineral, indicates that this series of compounds represents an unique example of a sequential progression of layer construction. The synthetic relationships between these minerals has been well established,[55] and it has been suggested that the lamina thickening is a consequence of surface hydroxyl group condensation between the silicate layers.[67] In general the data generated in this investigation support this hypothesis, and are shown in Table 6.5. The intensity numbers reported have been normalized to 1.0 for the Q^3 absorbance which is observed in each spectrum.

Table 6.5 Multinuclear Data for Sodium Phyllosilicate Hydrates

	Silicon-29									
	Single Pulse Decoupled						CP (2 ms contact)			
KENYAITE (Nat)L.D.G										
δ ppm	-99.5	-108.2	-110.6	-111.2	-114.0	-118.5	-99.5	--	-111.3	-114.0
($\Delta V\frac{1}{2}$, Hz)	(110)	(90)	(80)	(60)	(90)	(80)				
Intensity	1.0 :	0.54 :	0.57 :	0.33 :	1.2 :	0.09				
KENYAITE (Nat)B.M.										
δ ppm	-99.5			Quartz			-99.5		Quartz	
($\Delta V\frac{1}{2}$, Hz)	(150)			Contaminination					Contaminated	
KENYAITE (Nat)Cureton										
δ ppm	-99.1	-109.5		-111.3	-113.6	118.4	-99.5	-111.3	-114.0	
($\Delta V\frac{1}{2}$, Hz)	(130)			broad						broad
Intensity	1.0			1.9						

Table 6.5 (cont'd) Multinuclear Data for Sodium Phyllosilicate Hydrates

	Silicon-29							
	Single Pulse Decoupled				CP (2 ms contact)			
MAGADIITE (Nat)L.D.G.								
δ ppm	-99.5	-109.6	-111.3	-114.0	-99.5	-109.6	-111.3	-114.0
$(\Delta V_{\frac{1}{2}}, \text{Hz})$	(100)	(90)	(50)	(70)				
Intensity	1.0 :	0.59 :	0.52 :	0.29				
MAGADIITE (Nat)Cureton Trinity Co.								
δ ppm	-99.5	-109.5	-111.3	-114.0	-99.5	-109.5	-111.3	-114.0
$(\Delta V_{\frac{1}{2}}, \text{Hz})$	(90)	(70)	(40)	(60)				
Intensity	1.0 :	0.73 :	0.58 :	0.31				
MAGADIITE (Nat)B.M.								
δ ppm	-99.1	-109.3	-111.3	-113.6	-99.5	-109.5	-111.3	-114.0
$(\Delta V_{\frac{1}{2}}, \text{Hz})$	(120)	(80)	(60)	(90)				
Intensity	1.0 :	0.5 :	0.45 :	0.35				

Table 6.5 (cont'd) Multinuclear Data for Sodium Phyllosilicate Hydrates

	Silicon-29							
	Single Pulse Decoupled				CP (2 ms contact)			
MAGADIITE (Syn)L.D.G.								
δ ppm	-99.5	shldr	-111.3	-114.0	-99.5	shldr	-111.3	-114.0
$(\Delta V_{\frac{1}{2}}$, Hz)	(170)	(50)	(140)	(110)				
Intensity	1.0 :	0.2	1.3 :	0.31				
MAGADIITE (Syn)SHELL								
δ ppm	-99.5	-109.0 shldr	-111.3	-114.0	-99.5	-109 shldr	-111.3	-114.0
$(\Delta V_{\frac{1}{2}}$, Hz)	(105)	(70)	(60)	(40)				
Intensity	1.0	0.4	1.1	0.2				
MAGADIITE NH_4 (Syn)SHELL								
δ ppm	-99.5	-109.0 shldr	-111.3	-114.0	-99.5	-109.9	-111.3	-114.0
$(\Delta V_{\frac{1}{2}}$, Hz)	(70)	(50)	(120)	(45)	broad			
Intensity	1.0	1.0	3.0	1.0				

Table 6.5(cont'd) Multinuclear Data for Sodium Phyllosilicate Hydrates

	Silicon-29					
	Single Pulse Decoupled			CP (2 ms contact)		
OCTOSILICATE (Syn)L.D.G.						
δ ppm	-100.2		-111.3	-99.5		-111.3
($\Delta V_{\frac{1}{2}}$, Hz)	(30)		(25)	(80)		(25)
Intensity	1.0 :		0.9			
KANEMITE (Syn)L.D.G.						
δ ppm	-95.9	-97.8		-95.9	-97.8	
($\Delta V_{\frac{1}{2}}$, Hz)	(100)	(70)		(100)	(70)	
Intensity	1.0 :	0.3		1.0 :	0.3	
MAKATITE (Syn)L.D.G.						
δ ppm	-93.5			-93.5	-95.2	
($\Delta V_{\frac{1}{2}}$, Hz)	(140)			(90)	(70)	
					shldr	
Intensity				1.0	0.2	

Table 6.5(cont'd) Multinuclear Data for Sodium Phyllosilicate Hydrates

	Sodium-23			Proton CRAMPS
	Single Pulse Decoupled		CP (1 ms contact)	
KENYAITE (Nat)L.D.G.				
δ ppm	7.3*ssb	-3.8	-3.8	4.5, 1.5
($\Delta V_{\frac{1}{2}}$, Hz)	(170	(250)	(240 Hz)	
KENYAITE (Nat)B.M.				
δ ppm	7.2ssb	-3.5	-3.5	4.5, 1.0
($\Delta V_{\frac{1}{2}}$, Hz)	(160)	(220)	(220)	
KENYAITE (Nat)Cureton				
δ ppm	7.2ssb	-3.5	-3.6	4.4, 1.3
($\Delta V_{\frac{1}{2}}$, Hz)	(150)	(200)	(200)	

Table 6.5(cont'd) Multinuclear Data for Sodium Phyllosilicate Hydrates

	Sodium-23			Proton CRAMPS
	Single Pulse Decoupled		CP (1 ms contact)	
MAGADIITE (Nat)L.D.G.				
δ ppm	7.1ssb	-3.4	-3.4	4.6, 1.3 shldr
($\Delta V_{\frac{1}{2}}$, Hz)	(160)	(250)	(250)	(800)
MAGADIITE (Nat)Cureton Trinity County				
δ ppm	7.2ssb	-3.4	-3.4	4.5, 1.5 shldr
($\Delta V_{\frac{1}{2}}$, Hz)	(240)	(190)	(200)	(700)
MAGADIITE (Nat)B.M.				
δ ppm		-3.04	-3.0	4.5, 1.5 shldr
($\Delta V_{\frac{1}{2}}$, Hz)		(250)	(200)	(700)

Table 6.5(cont'd) Multinuclear Data for Sodium Phyllosilicate Hydrates

	Sodium-23		Proton CRAMPS
	Single Pulse Decoupled	CP (1 ms contact)	
MAGADIITE (Syn)L.D.G.			
δ ppm	-5.1	-5.1	3.6, 1.0
($\Delta V_{\frac{1}{2}}$, Hz)	(350)	(350)	(600)
MAGADIITE (Syn)SHELL			
δ ppm	-4.1	-4.1	3.7
($\Delta V_{\frac{1}{2}}$, Hz)	(300)	(270)	(200)
MAGADIITE-NH_4 (Syn)SHELL			
δ ppm			5.06
($\Delta V_{\frac{1}{2}}$, Hz)			(240)

Table 6.5(cont'd) Multinuclear Data for Sodium Phyllosilicate Hydrates

	Sodium-23		Proton CRAMPS
	Single Pulse Decoupled	CP (1 ms contact)	
OCTOSILICATE (Syn)L.D.G.			
δ ppm	-3.2	-3.2	3.2
($\Delta V_{\frac{1}{2}}$, Hz)	(320)	(300)	(150)
KANEMITE (Syn)L.D.G.			
δ ppm	-32.8ssb	-12.6	3.7, 1.1 shldr
($\Delta V_{\frac{1}{2}}$, Hz)	(2.7 kHz)	(2.1 kHz)	(1.3 kHz)
MAKATITE (Syn)L.D.G.			
δ ppm	-9.1ssb	-9.1	4.6
($\Delta V_{\frac{1}{2}}$, Hz)	(1.1 kHz)	(1.1 kHz)	(1.1 kHz)

6.1.3.1 Discussion of Makatite and Kanemite Data

The crystal structure of the simplest compound, makatite, has been solved.[69] It has been shown to be a corrugated sheet of rings composed of six SiO_4 tetrahedra. Sodium oxygen polyhedra connect the single layers, sharing edges and corners to preserve overall charge balance. The sheet structure is shown in Figure 6.4. The sheet conformation is severely puckered and exhibits a range of ten degrees in measured bond angles.[69] The silicon-29 spectrum shows a single line in the single pulse decoupled experiment, but also exhibits a shoulder in the cp data. The spectra are shown in Figure 6.4d(b). The chemical shift observed reflects the high degree of pucker, since -93.5 ppm is a relatively high frequency value for a Q^3 environment. As stated, the cp experiment also shows a shoulder to low frequency at -95.2 ppm which can be tentatively assigned to the single silicon which does not bond with an oxygen shared with a sodium polyhedron. The sodium-23 and proton spectra are both relatively broad and unresolved peaks. This probably results from a distribution of shielding environments, and not paramagnetic broadening, since the silicon-29 spectra exhibit relatively narrow linewidths. Reasonable yields of makatite have been obtained[55] starting with $\alpha NaSi_2O_5$. It is instructive to consider the crystal structure[70] of $\alpha NaSi_2O_5$, shown in figure 6.4, which is made of chains connected by a single shared oxygen between the Si_2O_5 anions, which form puckered sheets.

Figure 6.4 Makatite Formation

Comparison of $\alpha Na_2Si_2O_5$ and Makatite Conformation

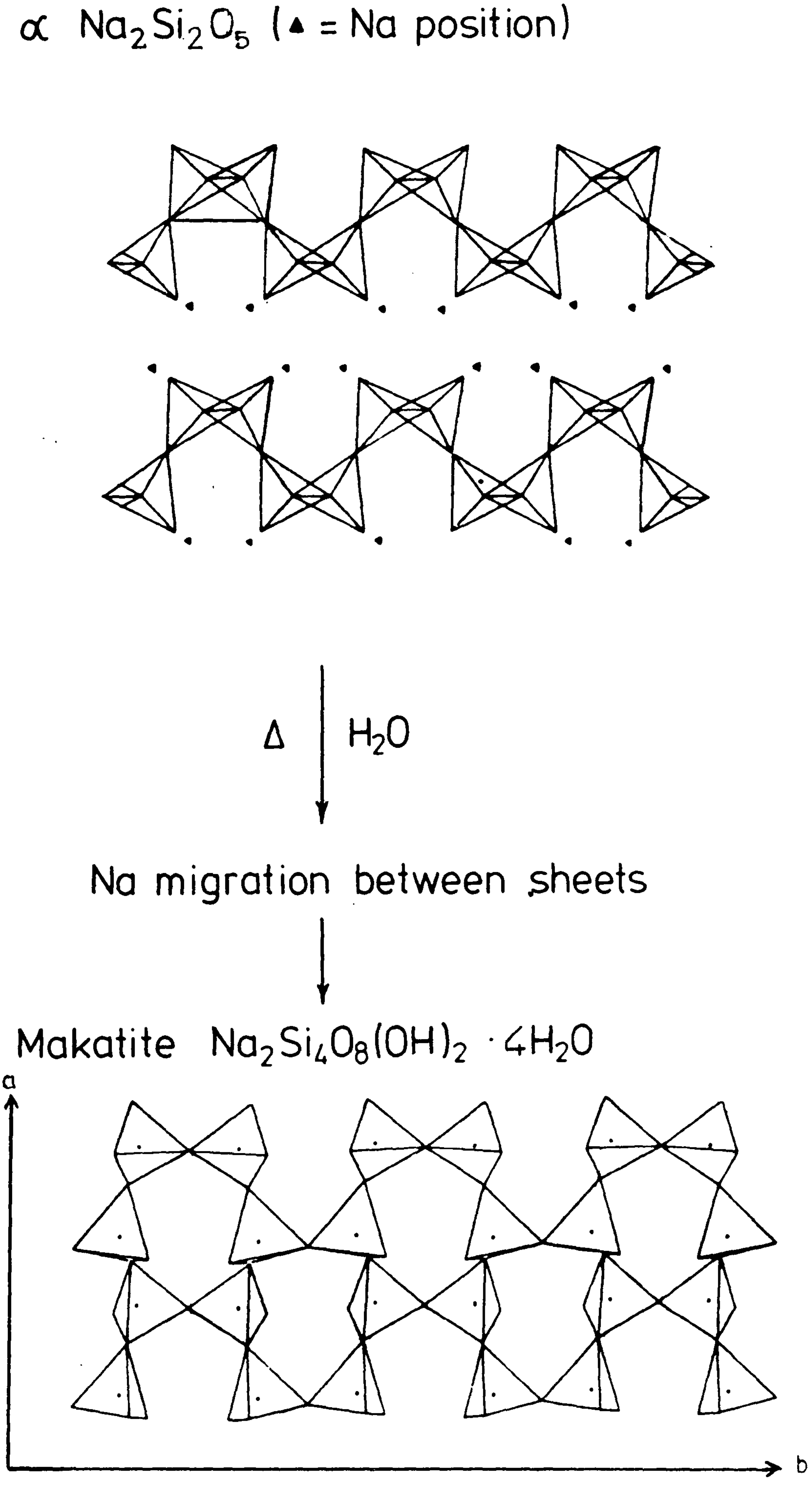

The silicon-29 spectrum was measured and consists of a single peak at -94.6 ppm. Further, the silicon-29 NMR spectrum of $\alpha H_2Si_2O_5$ has been reported. A single resonance is observed with a significant low frequency chemical shift[71] (-98.4 ppm) and also exhibits a shoulder similar to that observed with the data presented here for makatite. This shoulder was attributed to highly condensed regions in the lattice, arising from the silicon tetrahedron which is bonding with shared oxygen between chains.

If the known synthetic relationship between $\alpha Na_2Si_2O_5$ and makatite is considered[55,68] and the crystal structures are compared,[69,70] it is relatively easy to see the probable mechanism of sheet formation in makatite from the chains of $\alpha Na_2Si_2O_5$. Figure 6.4 illustrates how the six membered rings of makatite could be formed from the migration of the sodium ions into the newly formed interlayer channels between the puckered sheets present in makatite. The water, which is known to be synthetically crucial to the layer formation,[14] contributes to the sodium oxygen polyhedra charge balance which control the constraints acting upon the sheet puckering. If more water is available kanemite is formed instead of makatite. The silicon-29 specta for both minerals are shown in Figure 6.4b. Although no single crystal data is available for kanemite, the basal spacing indicates that the layer thickness is changing only slightly. This is probably due to the decreased pucker in the sheets and increased interlayer channel space[55] which results directly from the increased water content. The chemical shift data in Table 6.4 given for kanemite support this explanation, since an

Figure 6.4d Silicon-29 Spectra of Makatite and Kanemite

Silicon-29 Spectra of
a) Maketite MAR 3.2 kHz
b) Kanemite MAR 3.5 kHz
variable transients, 2 ms contact cp

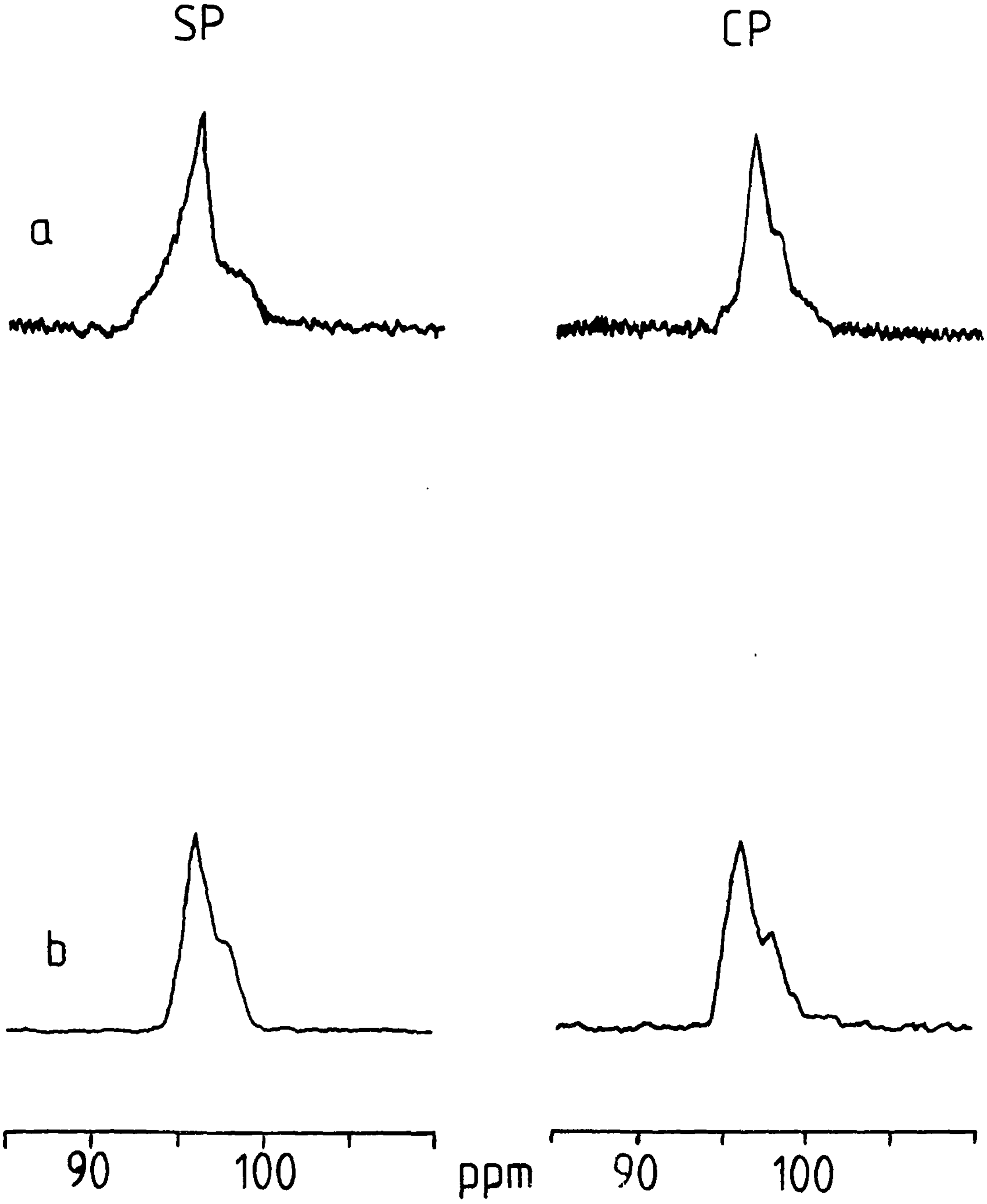

increase in Si-O-Si bond angle (decreased pucker) corresponds to a low frequency shift,[2] and the 3:1 intensity ratio obtained in the silicon-29 data is preserved in the observed silicon environments. This is predicted from the makatite crystal data. The broad and relatively unresolved sodium-23 and proton NMR data for kanemite also probably indicate a relatively disordered environment with a range of chemical shielding of the nuclei, since there is no indication of paramagnetic broadening. The spectra are very similar to that of makatite. A recent NMR study of kanemite and magadiite has failed to report the presence of a shoulder in the silicon-29 spectrum of kanemite,[72] despite the use of higher magnetic fields than employed here. Further, the chemical shifts reported are in disagreement with those observed in this investigation by a difference of 5ppm shift to low frequency. No explanation can be offered for the chemical shift discrepancy but it is possible that the shoulder was not observed because of saturation of the signal. A recycle time of 4 s was used,[72] where experience with the samples in this investigation has shown that this is much too short. No mention is made of proton decoupling which may also explain the single Q^3 environment reported.

The structural formation of makatite and kanemite from simpler sodium silicates has been shown to be a consequence of sheet construction by the condensation and linking of single unbranched chains. It has been suggested that the formation of the more silicious layer silicates is a product of sheet condensation to form the thickened layers postulated from the powder diffraction data.[67] The data presented in Table 6.5 support this hypothesis and give considerable insight into the mechanism of the lamina thickening.

6.1.3.2 Discussion of Octosilicate, Magadiite and Kenyaite Data

Figures 6.5 and 6.6 show the silicon-29 and sodium-23 spectra for representative samples of octosilicate, magadiite and kenyaite. The silicon spectra indicate an increasing amount of Q^4 environment as the SiO_2 content of the empirical formulae increase. This also coincides with increasing differentiation of environments within the Q^4 lattice until eventually, in kenyaite, the cross-polarization data indicate that one Q^4 environment at -108.2 ppm is so far removed from the proton environment that it no longer cross-polarizes. The averaged ratios of Q^3-Q^4 environments indicate a 1:1 relationship for octosilicate, 1:1.5 ratio for magadiite and a 1:2.7 ratio for kenyaite.

If the laminae are assumed to be the simple product of condensation of makatite or kanemite type layers then a simple model can be constructed to correlate the observed NMR intensities with the known formulae stoichiometry. There are actually two ways in which the makatite/kanemite sheets might condense to layers, forming eight and four membered rings or ten membered rings in the process. The projections are shown in Figure 6.7. As an example, the projections shown in Figure 6.7 produce the data for the condensation of two sheets, giving $8SiO_2$ in a repeat unit, and an approximate basal spacing of 14 A^o.

Figure 6.5: Silicon-29 Data for Sodium Polysilicates

a) Kenyaite (L.D.G.) MAR: 3.5 kHz
SP: 200 s recycle   CP: 30 s recycle
500 transients   2000 transients

b) Magadiite (B.M.) MAR: 4.0 kHz
SP: 200 s recycle   CP: 30 s recycle
200 transient   1000 transient

c) Octosilicate (L.D.G.)
SPE: 200 s recycle   CP: 30 s recycle
50 transients   100 transients

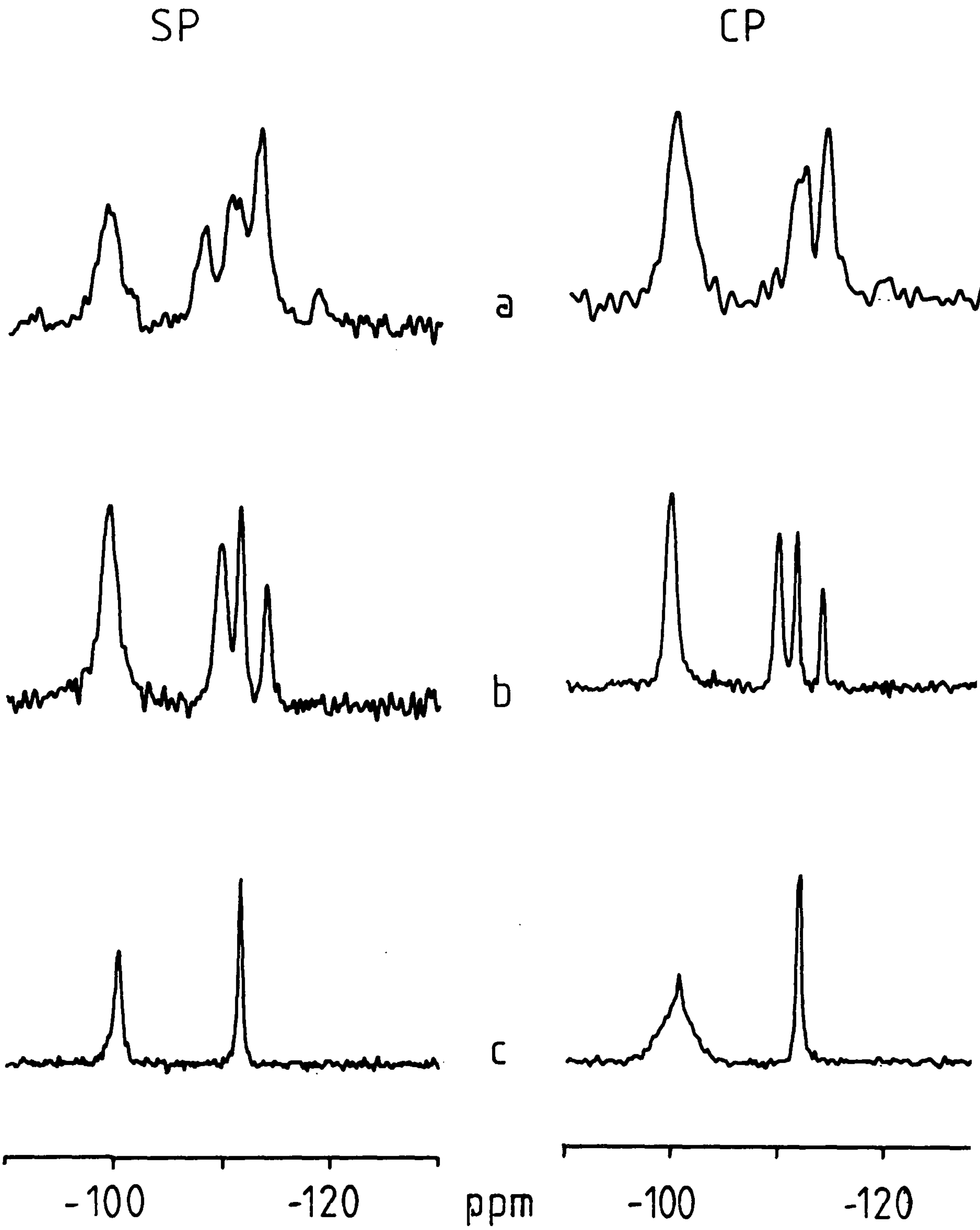

Figure 6.6 : Sodium-23 data for Sodium Polysilicates

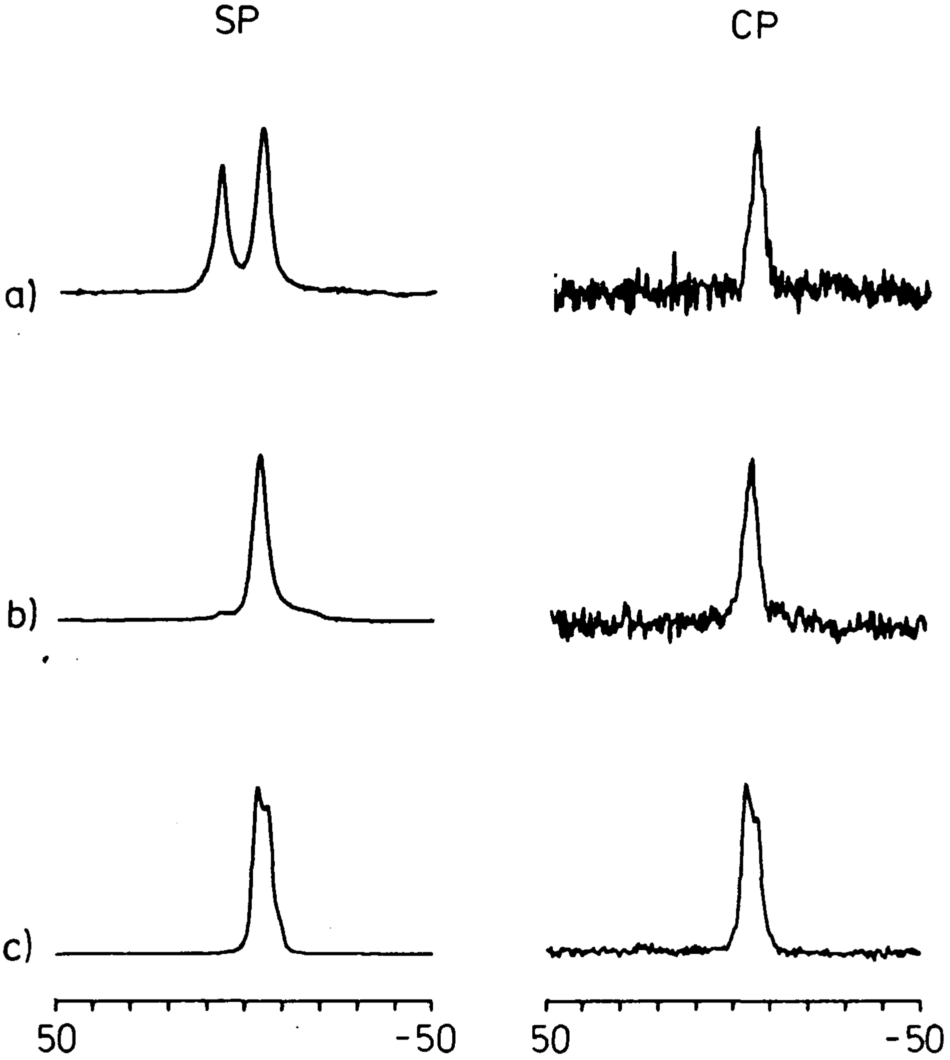

a) Kenyaite (L.D.G.) MAR: 4.0 kHz
SP: 100 s recycle CP: 30 s recycle
100 transients 1000 transients

b) Magadiite (B.M.) MAR: 4.0 kHz
SP: 100 s recycle CP: 30 s recycle
100 transients 1000 transients

c) Octosilicate (L.D.G.) MAR: 4.0 kHz
SP: 100 s recycle CP: 30 s recycle
16 transients 100 transients

Both possible combinations are shown in Figure 6.7, which give $Q^3:Q^4$ intensity ratios of 1:1 and 3:1. A simple formalism may be developed to simplify reference to the eight and four membered ring laminate, and the ten membered ring laminate. The condensation of two layers to form an eight and four membered ring laminate will be refered to as an 'A' laminate, and a 'B' laminate will then refer to a condensation which forms ten membered rings between two layers. This formalism is used in Table 6.6 to simplify reference to the higher numbered hybrid laminates which represent mixed combinations of the basic A and B laminates we have just defined. Table 6.6 shows the calculated ratios for the possible different combinations of laminate formation.

Figure 6.7 : Condensation of Makatite sheets

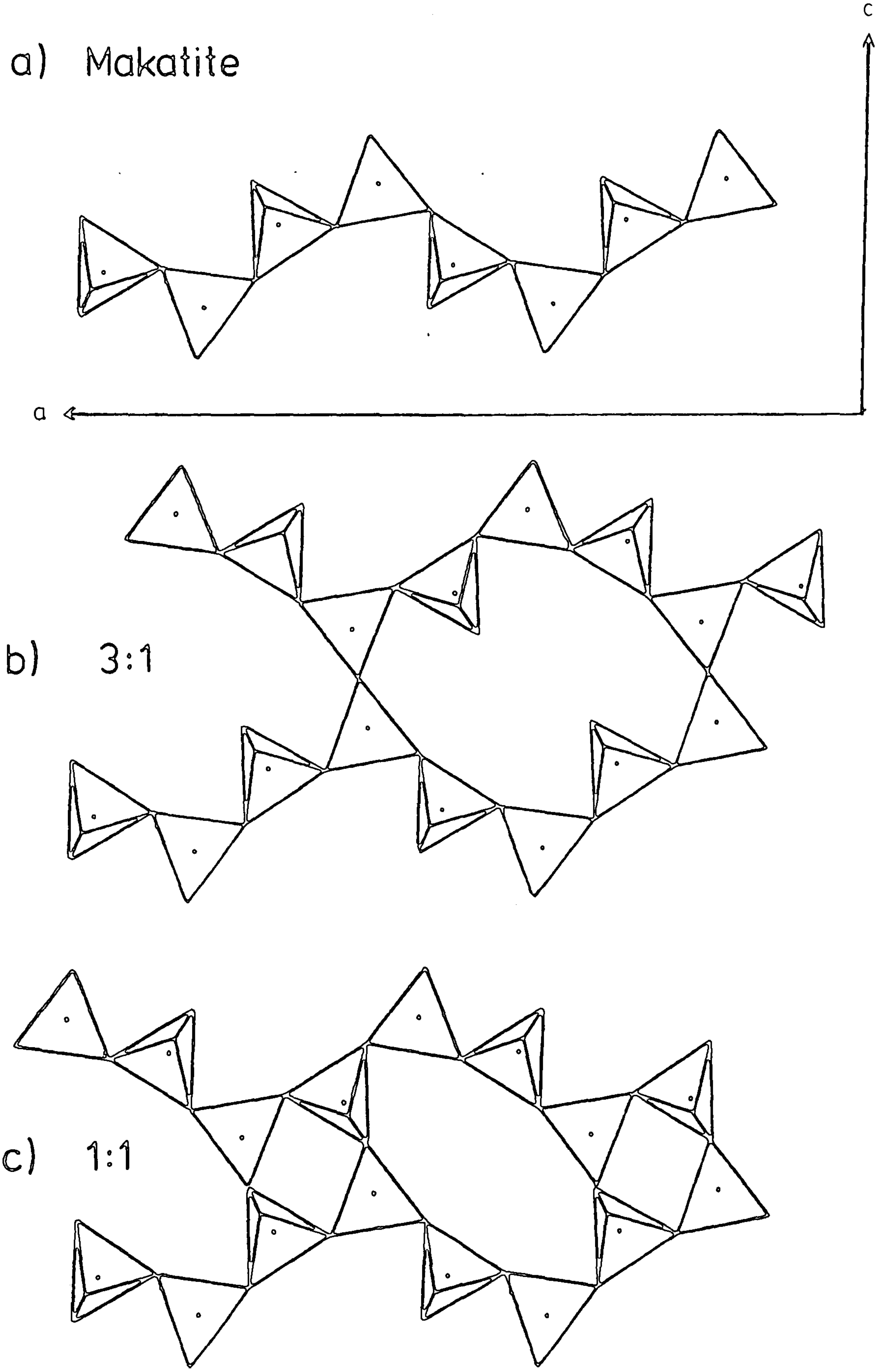

Table 6.6: Calculated $Q_3:Q_4$ Ratio for Hypothetical Condensed Lamina

no. of sheets	no. of SiO_2	Calculated basal Spacing (A^o)	Eight and Four Membered Rings $Q_3:Q_4$	Ten Membered Rings $Q_3:Q_4$	Hybrid Ring Lamina			
6	$24SiO_2$	34 A^o	5A = 1:5	5B = 1.4:1	A+4B 1:1	2A+3B 1:1.4	3A+2B 1:2	4A+1 1:3
5	$20SiO_2$	29 A^o	4A = 1:4	4B = 1.5:1	A+3B 1:1	2A+2B 1:1.5	3A+B 1:2.3	
4	$16SiO_2$	24 A^o	3A = 1:3	3B = 1.6:1	A+2B 1:1	2A+B 1:1.66		
3	$12SiO_2$	19 A^o	2A = 1:2	2B = 2:1	A+B 1:1			
2	$8SiO_2$	14 A^o	A = 1:1	B = 3:1				
1	$4SiO_2$	9 A^o	1:1sheets					

The bottom entry in Table 6.6 of a single sheet giving a 9A^o basal spacing and 1:1 sheets represents a single sheet of makatite or kanemite. The second entry of two condensed sheets has already been described as an example, and both possible combinations illustrated in Figure 6.7. These represent the possible structures for octosilicate. The silicon-29 intensity data indicate that an 'A' laminate is the correct structure, and hence the projection shown in 6.7c is the best fit for the octosilicate data. The calculated basal spacing for octosilicate of 14 A^o is in disagreement with the measured value of 11 A^o. This can be accounted for by the condensation mechanism which would cause a smaller layer thickness by the formation of $(SiO)_3{\equiv}Si\text{-}O\text{-}Si{\equiv}(OSi)_3$ bonds where previously sodium and water had formed hydrogen bonds to the Q^3 units between the sheets.

The cross-polarization spectrum gives a broadened Q^3 environment which probably results from the broadband decoupling of a spin system which is already motionally narrowed. The proton CRAMPS spectrum gives a single peak of 150 Hz full width at half height, which is quite narrow, supporting this explanation. The data presented here for octosilicate refute the suggestion of an octahedral $Si(OH)_6^+$ environment to explain the structure of octosilicate.[64]

The mechanism of sheet condensation requires the diffusion of sodium and water into the newly created interstitial channel.

This phenomenon of ion transport in a mineral has been shown to depend upon three main criteria:[73] 1. anion porosity, 2. electrostatic site energy, and 3. cation radius. Under hydrous conditions sodium is known to diffuse more easily than ^{-}OH and H_3O^+, probably because of the size difference. In the context of the layer structures proposed, as a consequence of makatite/kanemite sheet condensation, the formation of ten membered rings would be less confining than the eight and four membered rings, and promote ion diffusion.

The higher ordered laminates, magadiite and kenyaite are not so obvious in their explanation as was octosilicate. For magadiite the observed average intensity ratio between Q^3:Q^4 environments of 1:1.5 is best fit by a hybrid laminate composed of four sheets condensed in such a fashion that there are two layers composed of eight and four membered rings and one layer of ten membered rings. The structure is shown in Figure 6.8. Close scrutiny of this projection yields the observation that there are three different Q^4 environments, and two different Q^3 environments. The Q^4 tetrahedra have been shaded and cross hatched to indicate the different environments. The correct Q^3:Q^4 ratio of 1:1.5 is preserved, but more importantly a .6:.6:.3 ratio is observed within the Q^4 tetrahedra. This corresponds to two Q^4 tetrahedra which have no contact with Q^3 tetrahedra (marked with lines in Figure 6.8), four Q^4 tetrahedra which share a corner with

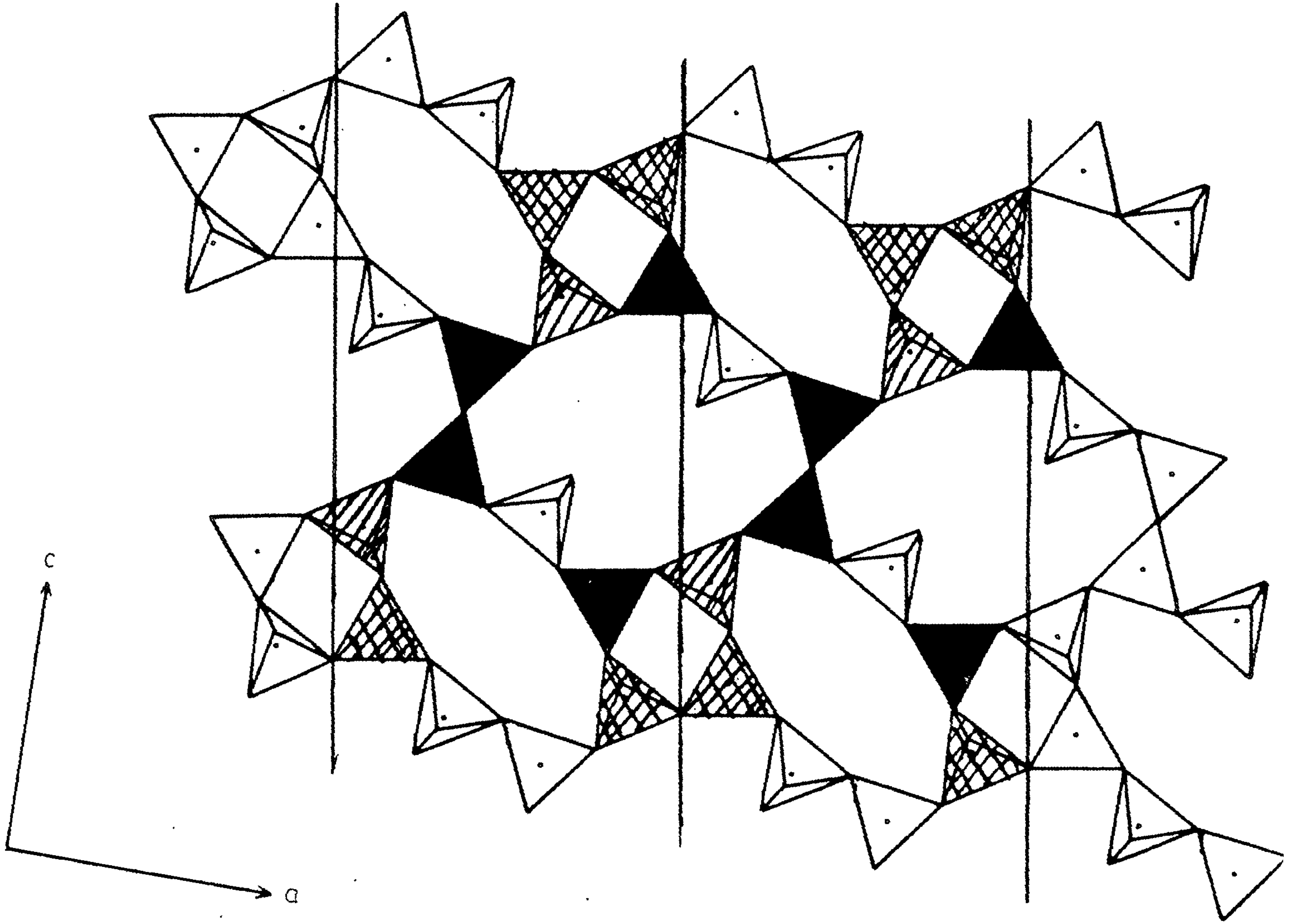

Figure 6.8
Hybrid Laminate
of four sheets

an interlattice Q^3 tetrahedron (entirely shaded), and four Q^4 tetrahedron which share a corner with an interlayer Q^3 tetrahedra (cross hatched).The intensity ratios of the Q^4 sites for this structure correspond extremely well with those observed in the spectral data of Table 6.5, which show three Q^4 peaks. In this structure there would be two types of $(SiO)_3{\equiv}Si{-}OH$ environments in the ratio 2:1,, those internal to the ten membered ring and the interlayer groups. There would also be the possiblity of two sodium environments, again, an interlattice and an interlayer site. The sodium-23 spectra for magadiite do exhibit a second environment at 7.3 ppm in Table 6.5, however it is very small. Figure 6.9a shows the silicon-29 variable contact cp spectra for natural magadiite. At very long contact times a second Q^3 environment at -97.8 ppm becomes visible. This can be assigned to an $(SiO)_3{\equiv}Si{-}O{-}Na^+(H_2O)_x$ environment. Figures 6.9b and c compare the cp and single pulse decoupled spectra respectively. Since the sodium-23 data show only one significant sodium environment for magadiite, it is likely that this results from the sodiums which are associated with Q^3 groups situated in the interlayer space. This indicates that there are at least two different Q^3 environments, one which is most probably a $(SiO_3){\equiv}Si{-}O{-}H$ group, and another which is most likely associated with a sodium atom. The proton CRAMPS spectra shown in Figure 6.10 exhibit the formation of a second proton environment. The chemical shift of 4.5 ppm for the main absorbance indicates that the majority of the protons are placed interstitially having a loose association with the sodium and surface sites which abound there.

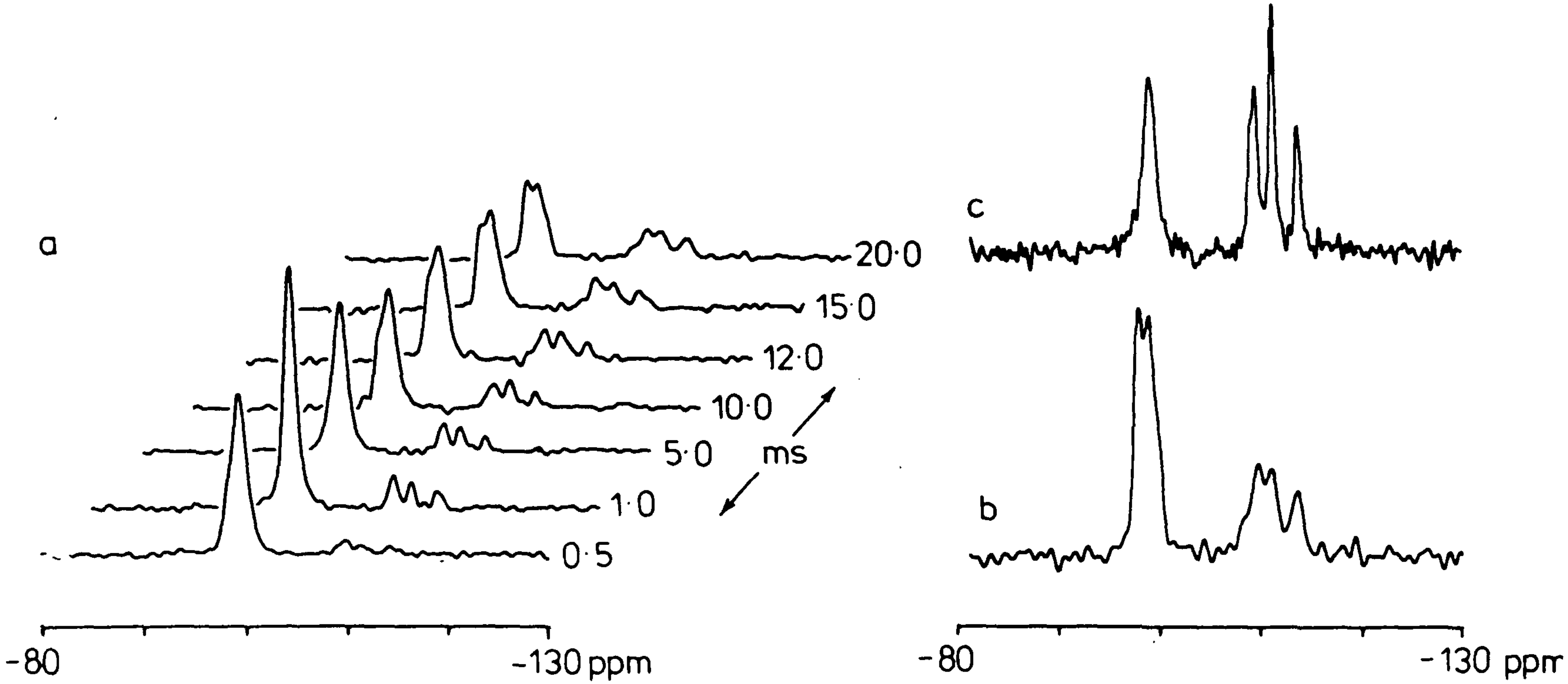

Figure 6.9: Silicon-29 spectra of Magadiite

a) Variable contact cp sequence
30 s recycle 4 kHz MAR
1500 transients

b) cp spectrum at 20 msec contact
30 s recycle 4 kHz
1500 transients

c) Single pulse decoupled spectrum
200 s recycle 4.0 kHz
200 transients

Figure 6.10

Proton CRAMPS Spectra

^{1}H CRAMPS Spectra of Magadiite
100 transients, 20 s recycle,
3 kHz MAR, MREV-8

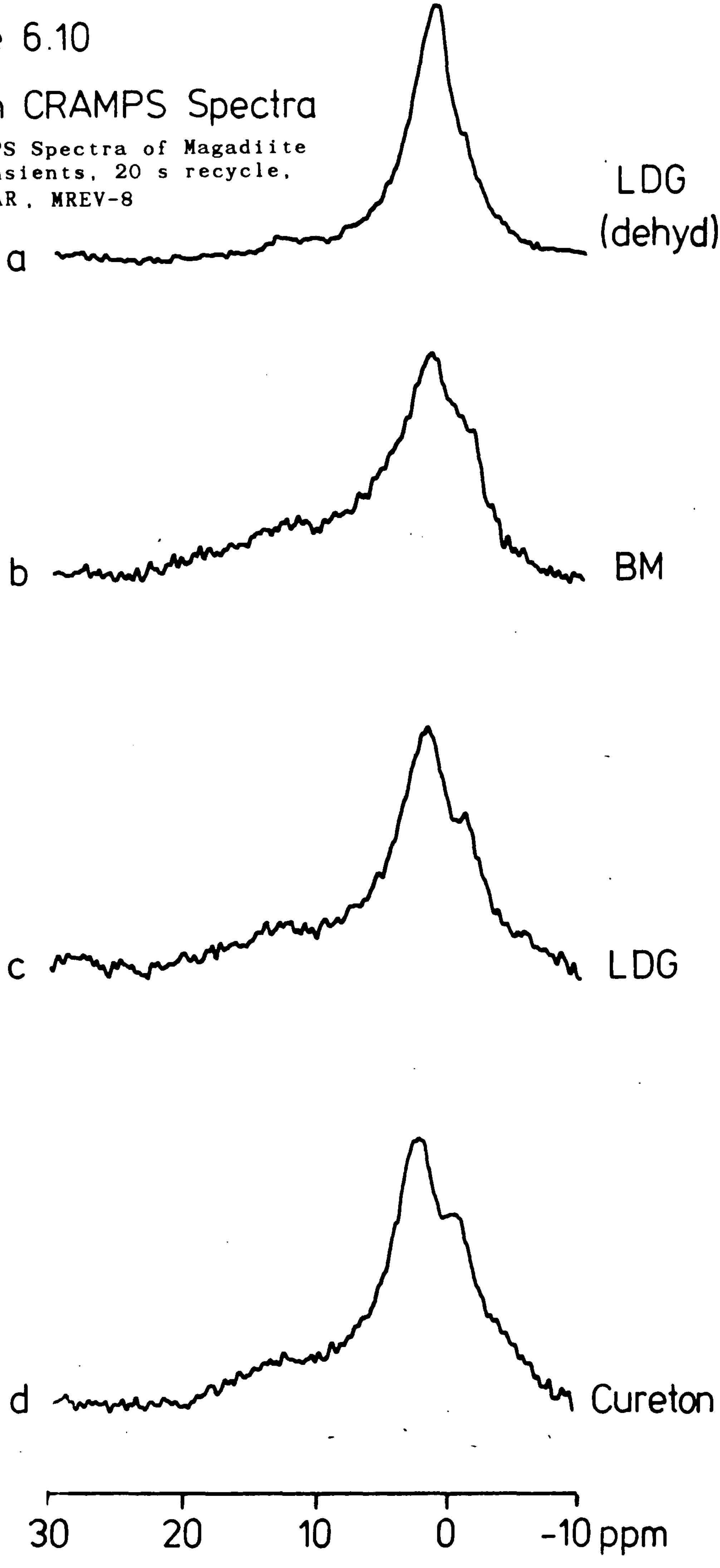

The shoulder at 1.5 ppm may be assigned as Si-OH groups. It is significant that the shoulder remains when magadiite is dehydrated, although much reduced in intensity (Figure 6.10a), since this supports the suggestion that the shoulder indicates the presence of an Si-OH group.

A study of the cross-polarization characteristics was feasible because of the large numbers of high quality samples of magadiite which were obtained. The results are shown in Figure 6.11. As expected the Q^3 environments exhibit a high initial rate of cp and an overall greater efficiency, especially when it is considered that the ratio of $Q^3:Q^4$ is 1:1.5 from the single pulse data. The Q^{3*} data points are the result of the addition of the two intensities of the two Q^3 environments which are observed at long contact times and have been assigned as (O≡Si)O-Na and (O≡Si)O-H groups. The behaviour of the Q^4 data confirms that it cross-polarizes less efficiently and at a slower rate. This is consistent with environments that are not directly bonding to an OH group.

As stated previously the sodium spectra shown in Figure 6.6 also show a small shoulder at 7.0 ppm, which indicates a very small presence of a second sodium environment. Figure 6.12 shows the result of a relaxation study of the sodium nucleus in natural magadiite. The low frequency peak at -3.3 ppm is relaxing much faster than the high frequency shoulder, which would be expected if the low frequency environment originates form an interlayer site, and the high frequency environment arises from sodium which is trapped in the rings in the lattice. Neither peak exhibits any quadrupolar contributions to lineshape.

Figure 6.11: Log(intensity) vs contact time for variable contact cp experiment: Magadiite Data

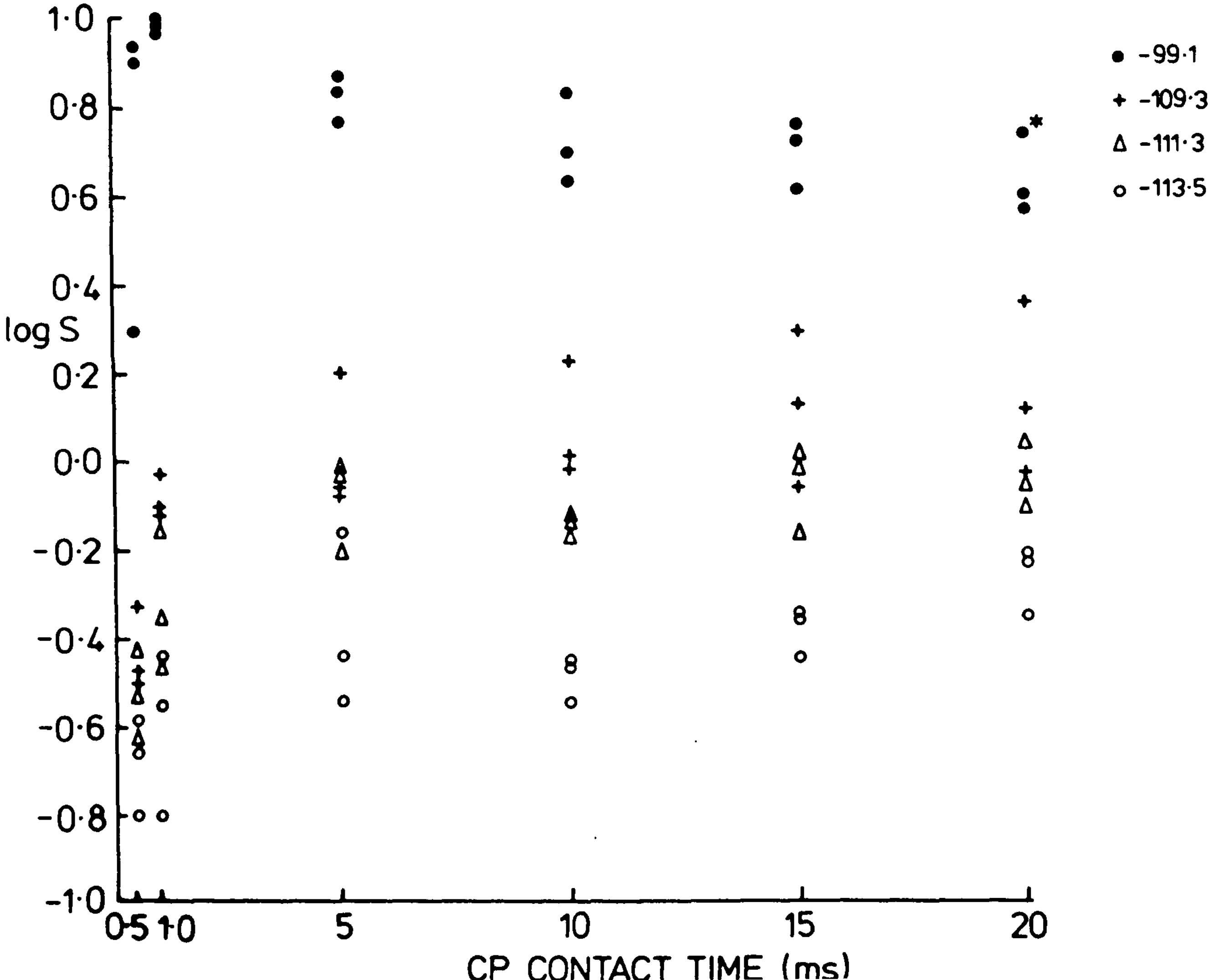

Figure 6.12

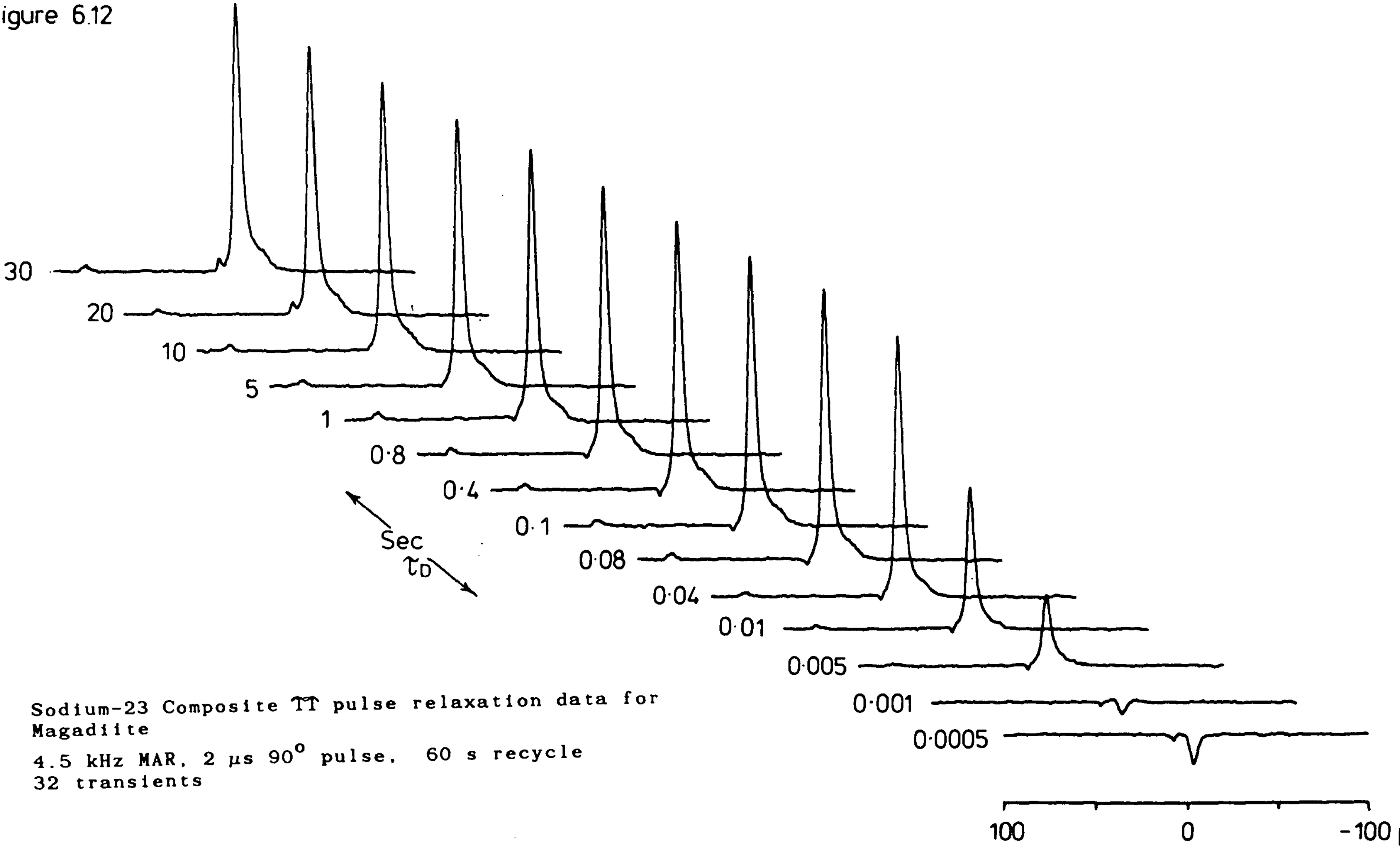

Sodium-23 Composite π pulse relaxation data for Magadiite

4.5 kHz MAR, 2 μs 90° pulse, 60 s recycle
32 transients

This is not surprising since it is likely that each sodium atom is hydrated with water molecules. The sodium cp data in Figure 6.6 also support this assignment since the site would not be expected to cross polarize without close contact with the proton environment.

The observed silicon-29 $Q^3:Q^4$ intensity data for kenyaite can be fitted by a number of the calculated intensity data shown in Table 6.6. The closest comparison exists for the hybrid structures and Figure 6.13 shows the two most likely projections; a five sheet laminate of 3A + B structure and a six sheet laminate of 4A + B structure. The silicon-29 data shown in Figure 6.5 indicate a possible four or five Q^4 environments, with the high frequency Q^4 sites unable to cross polarize efficiently, presumably because of the greater distance of the lattice tetrahedra from the interstitial proton environment. It should be noted that kenyaite did not cross polarize very efficiently relative to magadiite, which also exhibited poor cp efficiency relative to octosilicate. Kenyaite was also observed to cross polarize over a very narrow range between .1 and 5 miliseconds. Since only one kenyaite sample was of sufficient quality to render resolved Q^4 peaks, and this was combined with poor cp characteristics, the variable contact experiment was of limited utility. No new data were observed as a result other than the absence of the site at -108.2 ppm.

The sodium-23 spectra of Figure 6.6 for kenyaite show the appearance of a peak at +7.3 ppm. This new environment exhibits a symmetrical lineshape and spinning sidebands.

Figure 6.13 : Five and Six sheet Laminate Structures

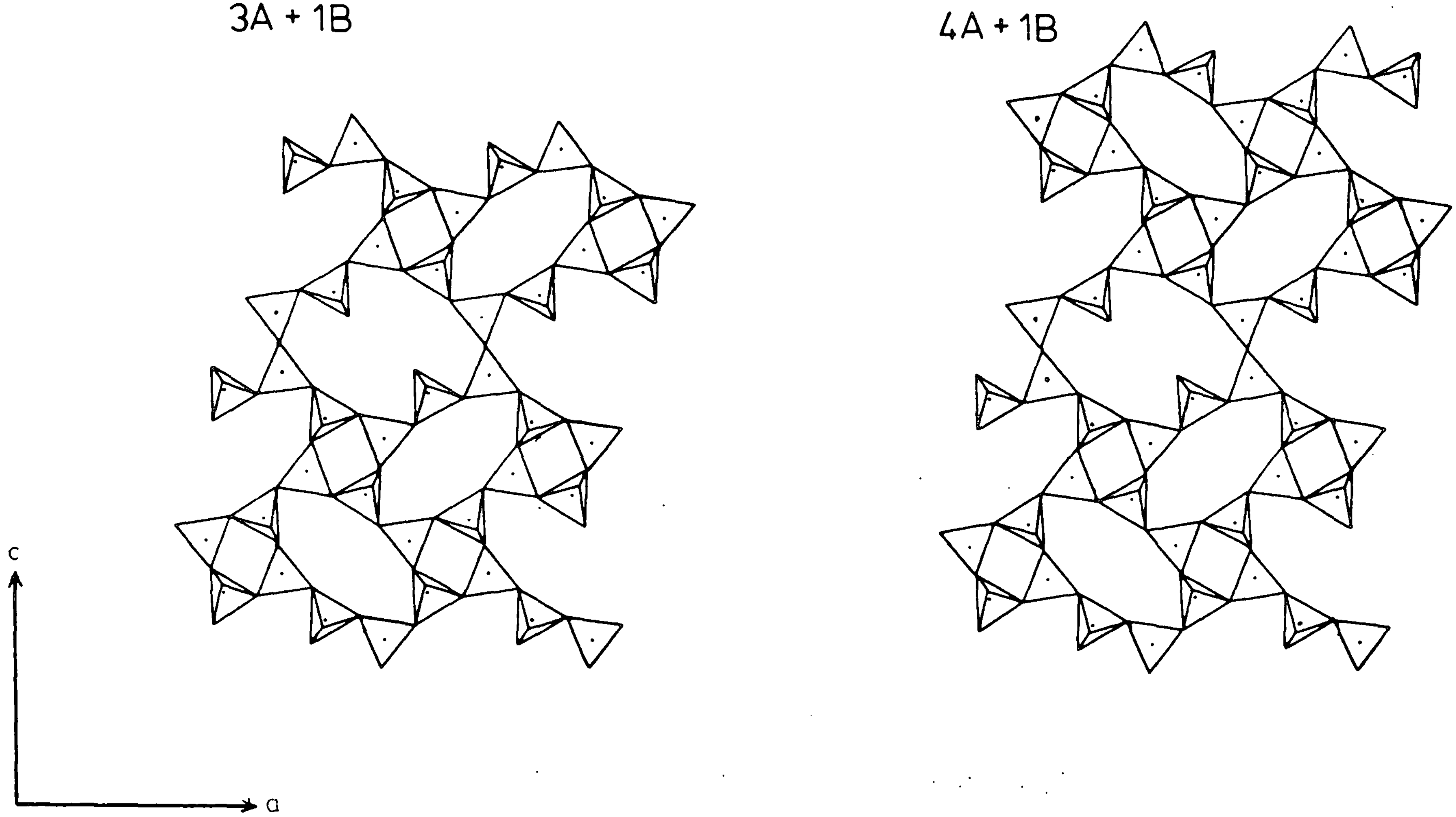

3A + 1B

4A + 1B

The appearance of sidebands indicates that this sodium environment experiences some form of anisotropy in its environment. It is likely that this may be sodium held more rigidly in the lattice, possibly trapped in the eight membered rings and unable to migrate to the interstitial channel. This is supported by the cp data which indicate that this sodium does not cross polarize. If this anisotropic sodium environment was a consequence of an $(SiO)_3{\equiv}Si{-}O{-}Na^+(H_2O)$ interlayer environment it would be reasonable to expect this environment to cross polarize also. The relaxation spectra shown in Figure 6.14 show that the high frequency environment is relaxing very slowly ($T_1 \sim 7$ seconds), while the low frequency environment is relaxing very quickly ($T_1 \sim .001$ seconds). This also supports the assignment of interlattice and interlayer environments for the high and low frequency environments respectively.

The proton CRAMPS data are shown in Figure 6.15. The shoulder observed at 1.5 ppm in the magadiite ^1H CRAMPS spectra has grown into approximately equal proportion with the main absorbance at 4.5 ppm. This would indicate that there is an increasing proportion of surface hydroxyl groups compared to free or lightly bound water. This trend is confirmed by using FTIR to observe the OH stretching region. The data are shown in Figure 6.16 and indicate that magadiite has a high proportion of free -OH to bound -OH groups when compared with kenyaite. This is in good agreement with the ^1H CRAMPS data reported here and recent wide line proton studies on the silicic acid polymorphs of some layered silicates.[74]

Figure 6.14 : Relaxation data for Kengaite

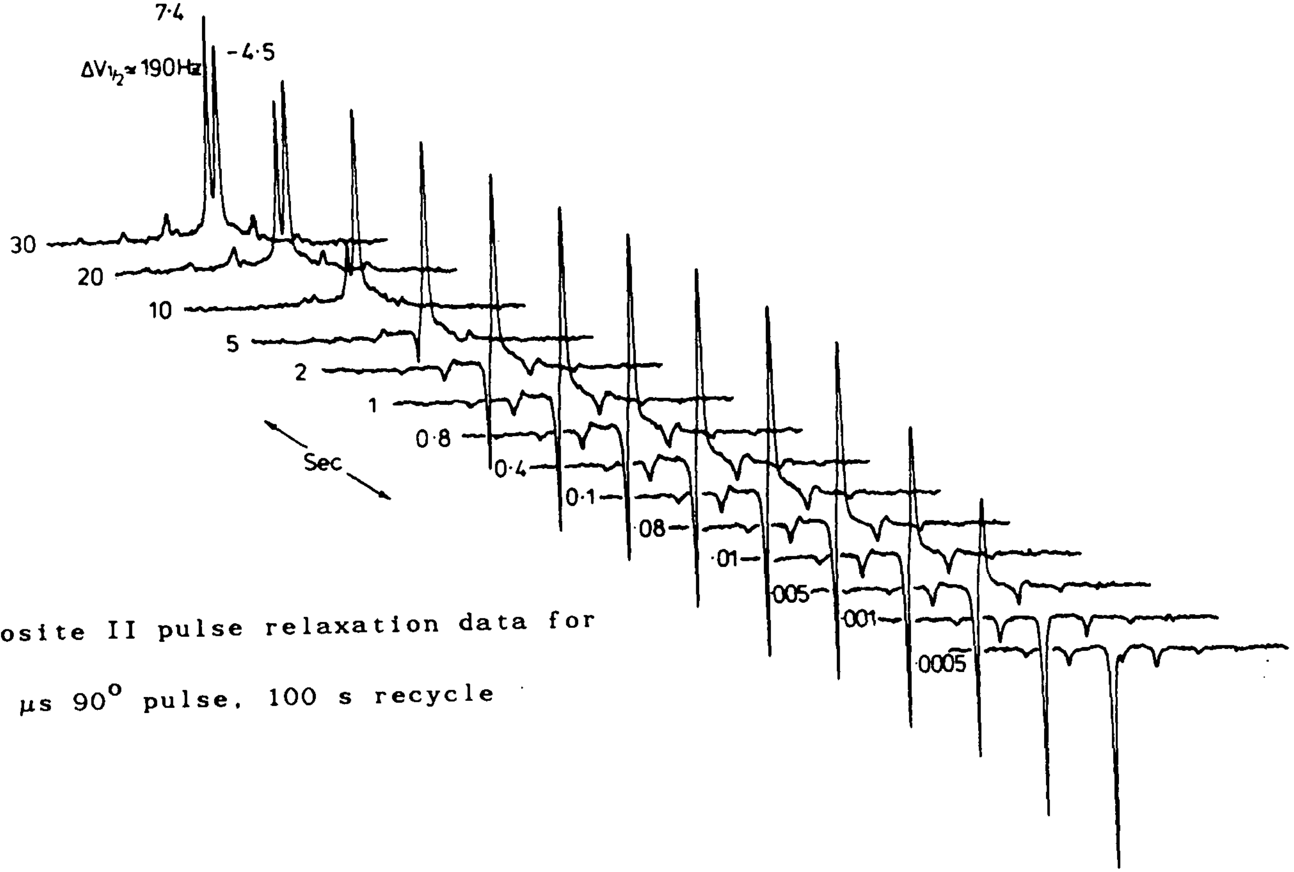

Sodium-23 Composite II pulse relaxation data for Kenyaite

4.5 kHz MAR, 2 μs 90° pulse, 100 s recycle
32 transients

Figure 6.15 Proton CRAMPS Spectra of Kenyaite

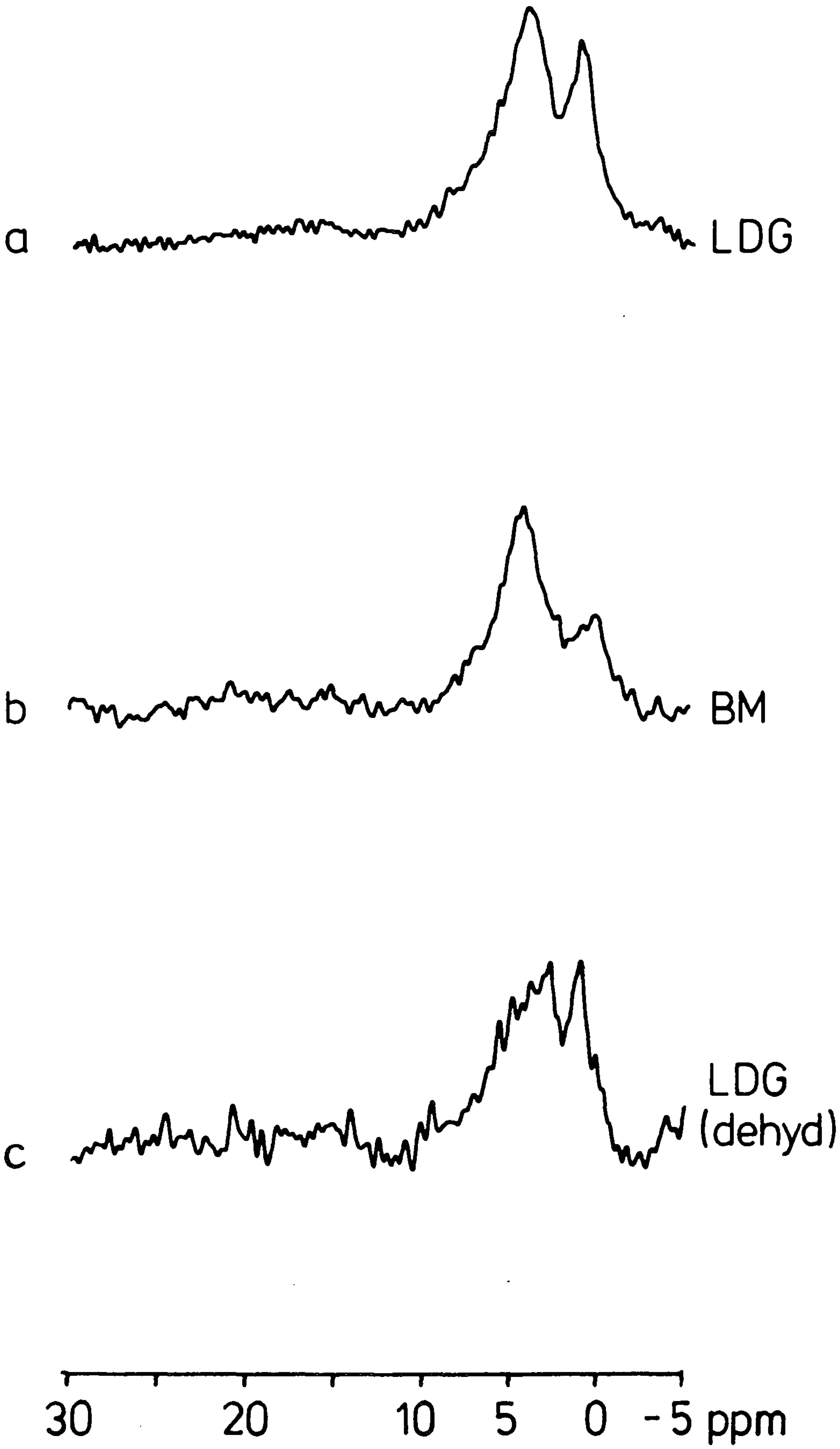

The proton CRAMPS spectra of Figure 6.15c show the effect of dehydration on the proton reservoir. It is known that the interlayer space collapses upon dehydration,[67] probably because the water, which hydrates the interstitial sodium, dictates the interlayer distance through hydrogen bonds. It is significant that upon dehydration there are still two proton environments observed in kenyaite, supporting the two types of hydroxyl groups suggested by the structures in Figure 6.13. It should be noted that the proton CRAMPS spectra were extremely difficult to obtain for kenyaite because of the small amount of water present in any sample ($24SiO_2:10H_2O$).

The data presented for kenyaite indicate that the probable conformation is a hybrid of a ten membered ring layer and eight and four membered ring layers. Further, the basal spacing data make the proposed five sheet structure the more likely choice. These data fit very well with the known synthetic behaviour of kenyaite.[67] The transport of sodium through the layers is confirmed, and explains the eventual formation of quartz as an end product, when the sodium has diffused out of the layers completely.

Recent studies of some of these minerals[72,75] are in disagreement with the data and conclusions presented here. The most obvious explanation of this discrepancy can be found in examination of the recycle delays used in these investigations. It is very likely that the intensity ratios reported, and upon which the conclusions are drawn, are incorrect.

Figure 6.16 : FTIR OF MAGADIITE AND KENYAITE

FTIR data of Magadiite and Kenyaite
Magadiite a) B.M. b) Cureton c) L.D.G.
Kenyaite d) B.M. e) L.D.G.

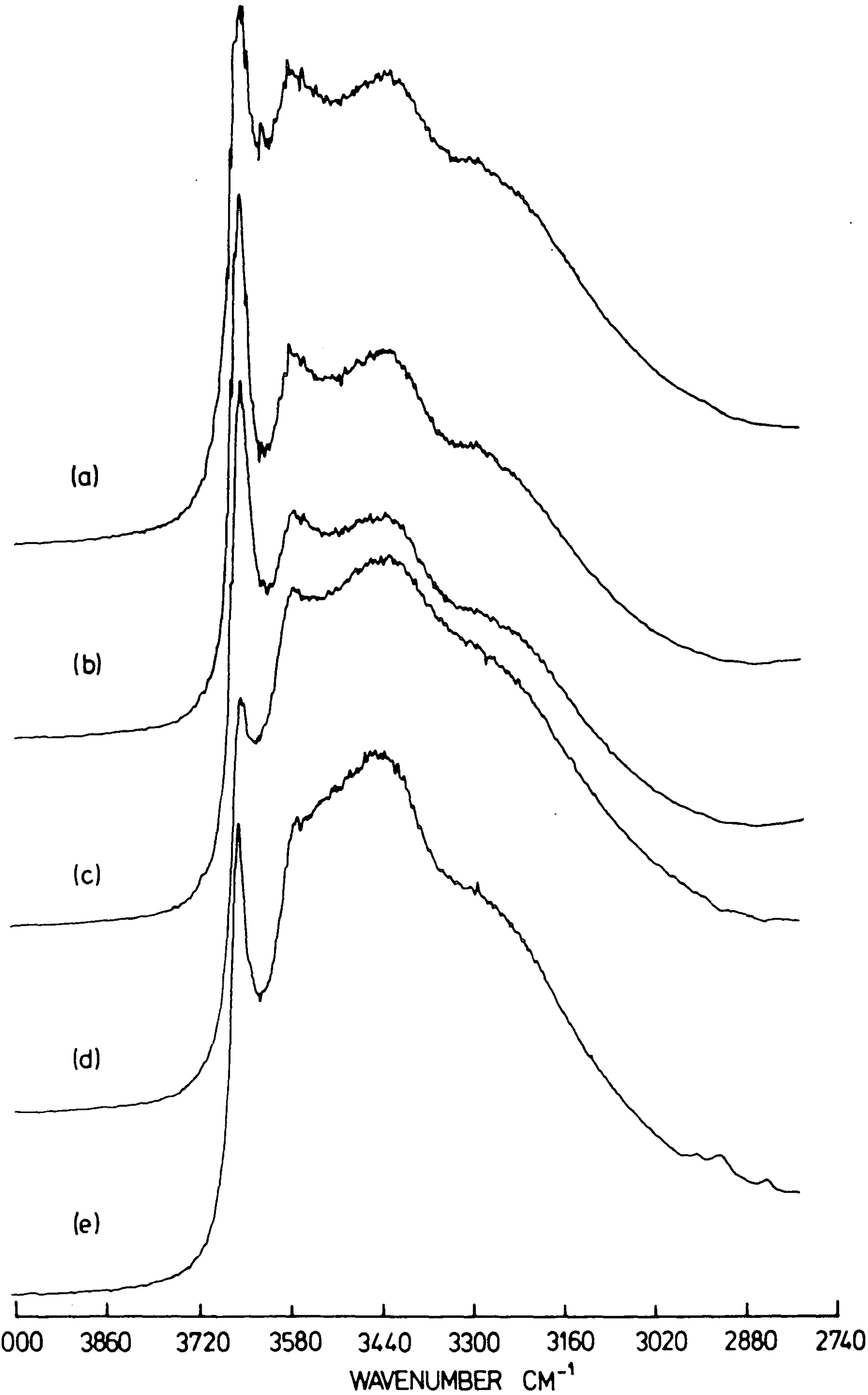

Experience with the samples investigated in this thesis has shown that significant discrepancies can occur with recycle delays below sixty seconds. Given this behaviour it is probable that the spectra reported in the literature suffered from saturation.

6.1.4. Silica Polymorphs

The first high resolution MAR silicon-29 NMR detection of quartz, and differentiation between silica polymorphs, illustrated that this method was sensitive to very small changes in tetrahedra bond angles.[1] This initiated the application of NMR to a diverse range of silica forms; spanning biominerals and grasses,[76] meteorites,[77,78] amorphous minerals,[79] silica gels[80] and vitreous glasses.[81] The result has been the realization of relationships between the isotropic chemical shift (δ) and anion bond angles,[79] bond lengths,[2] and electronegativity.[32]

To date little effort has been made in characterizing the nature of the proton environment, which is known to play an important role in the catalytic[80] and absorbtive[82] nature of silica. This investigation illustrates the utility of ^1H and ^{29}Si NMR methods in application to the characterization of the role of the proton environment in amorphous mineralogical silica. To this end several types of silica minerals were examined with the resulting data shown in Table 6.7.

Table 6.7: NMR data for Silica Polymorphs (all values in ppm)

		Silicon-29 Chemical shift data	
Mineral (source)	^{1}H CRAMPS	$\mathrm{SP}^{*}(\Delta V_{\frac{1}{2}},\mathrm{Hz})$	CP (5 ms contact)
quartz (County Durham)	-	-107.4 (20)	-
amethyst (Zambia)	-	-107.4 (30)	-
opal (Hungary)	-	-105 (750)	-
chalcedony (Devon)	4.8	-107.6 (40)	-99.0,-107.6
chalcedony (Cornwall)	4.9	-107.6 (45)	-99.0.-107.6
agate (South Africa)	5.0	-107.6 (30)	-97.9,-99.5,-101.3,-107.4
flint (Kent)	5.0	-107.6 (60)	-99.0,-107.6
flint (Wiltshire)	5.0	-107.6 (30)	-99.0,-107.6

*single pulse with proton decoupling at 50 kHz

The silicon-29 single pulse chemical shifts observed for quartz and amethyst were in accord with previous reports.[1,79] The proton environments were found to be dilute, to the extent that investigation by ^{1}H NMR was unrealistic, and so it was not surprising to find that both minerals failed to cross polarize to any degree. The sample of opal gave a broad unresolved peak, centred about -105 ppm, and exhibited similar cp and proton characteristics to quartz and amethyst.

The single pulse decoupled silicon-29 data for chalcedony, agate (a variety of chalcedony) and flint, give the characteristic absorbance at -107.6 ppm, indicating a mean bond angle consistent with a quartz-like structure. However, the cp results indicate at least two major environments with significant chemical shift differences. The proton data also indicated that there was a substantial proton environment in the minerals. These preliminary results indicated that flint and chalcedony would serve as suitable candidates for investigation into the behaviour of silica mineral polymorphs using solid state NMR methods.

The precise compositional structures of flint and chalcedony remain a controversy in the mineralogical literature. It was originally postulated that both flint and chalcedony were intimate mixtures of opal and micro-crystalline silica.[83] Investigation by X-ray powder diffraction has established that both contain considerable amounts of quartz[84] estimated at ~ 98% for that of flint, and ~ 90% for chalcedony. Other forms of crystalline silica were found to be absent.[85] One factor which may explain the confusion encountered in attempts to ascertain the precise composition of these minerals, is that of sample inhomegeneity. This is evident in the wide dispersion of data obtained upon examination of a variety of specimens by X-ray diffraction[86] and electron micrographs.[87] Indeed, few properties of these minerals have been found to behave in a consistent manner, making a sound basis for the segregation and distinction of the two minerals difficult. One parameter which at one time appeared reliable was the quantity of water in each mineral, and the state in which it is held interstitially.[82]

The nature of the microcrystalline fraction of the minerals has been well-established. Each contains fan-like arrangements of crystallites[89] providing micropores in which water is situated. Significantly, the size[90] and extent[91] of the pores can be used to differentiate between flint and chalcedony, as shown in Table 6.8. A practical method of distinction based on this difference[92] uses the refractive index of the mineral as the pertinent discriminating criterion.

Table 6.8: Comparison of physical properties of Flint and Chalcedony

	Pore Nature	Pore Diameter ($\times 10^{-6}$ mm)	% H_2O	Refractive Indices
FLINT	Interconnected	~ 140.0	> 1.0	$\alpha = 1.537$ $\gamma = 1.546$
CHALCEDONY	Discrete	~ 10.0	< 1.0	$\alpha = 1.534$ $\gamma = 1.539$

(Note that the diameter of a water molecule is ~ 0.33×10^{-6} mm)

The data presented in the papers mentioned above are doubtless valid, but the explanations appear to be founded upon a possibly fallacious hypothesis, that is the assumption that the water responsible for the observations was present, interstitially, as discrete molecules. However, as a consequence of infra-red investigations[93], it was proposed that the water in chalcedony is chemically bonded to the silica, in the form of surface hydroxyl groups. This contradicts conclusions based on data from thermal analysis[88], but a simple explanation can be proposed. The heating step ($\geq 1000^{o}C$) in the thermal analysis may, in effect, be annealing the pore surface, with the resulting condensation producing the per cent weight-loss values recorded.

In order to establish a more complete understanding of the properties of silica polymorphs, solid state NMR methods have been applied to the study of flint and chalcedony. Response to investigation was uniform, within experimental error, for all samples within each mineral type. For this reason no distinction will be made between the different samples throughout the discussion. The agate, classed as a form of chalcedony, behaved as chalcedony in all measurements except for the cross-polarization spectrum, which shows a distinction of three Q^3 environments. X-ray fluorescence analysis has determined that this may be a result of cation substitution for silicon in the lattice.

The cations detected by analysis were sodium (0.5%) and calcium (0.2%), which have been observed previously as impurities in silica polymorphs.[15] The three Q^3 environments observed for agate presumably represent $(Si\text{-}O)\equiv Si\text{-}O\text{-}M^+, M^{2+}$ formation, where M^+, M^{2+} is either sodium or calcium respectively. The high and low frequency chemical shifts observed in the -97.9 ppm and -101.3 ppm absorbances result from shielding of the silicon tetrahedra by the cations. The precise form of association is difficult to speculate upon, especially for divalent calcium. The absence of a peak at -99.0 ppm in the agate cp data is surprising. It is possible that it sits under the peak at -99.5 ppm or perhaps, if a cation is in proximity to this environment, it experiences shielding which has shifted it 0.5 ppm to lower frequency. This does not affect the proton environments, and so the general discussion for chalcedony is an accurate decription of the properties of agate also.

In Figure 6.17 the static ^1H bandshapes of flint and chalcedony are shown. The bands are both relatively narrow (1.8 kHz and 1.2 kHz respectively), which suggests that the local motion of the relevant protons is occurring at a substantial rate. This motion appears to be sufficient to cause considerable averaging of the proton-proton dipolar interactions.

The partially relaxed spectra (Figure 6.18) show an order of magnitude difference in relaxation rates between protons in the two minerals. This can be considered to be significant.

Figure 6.17: STATIC PROTON SPECTRA

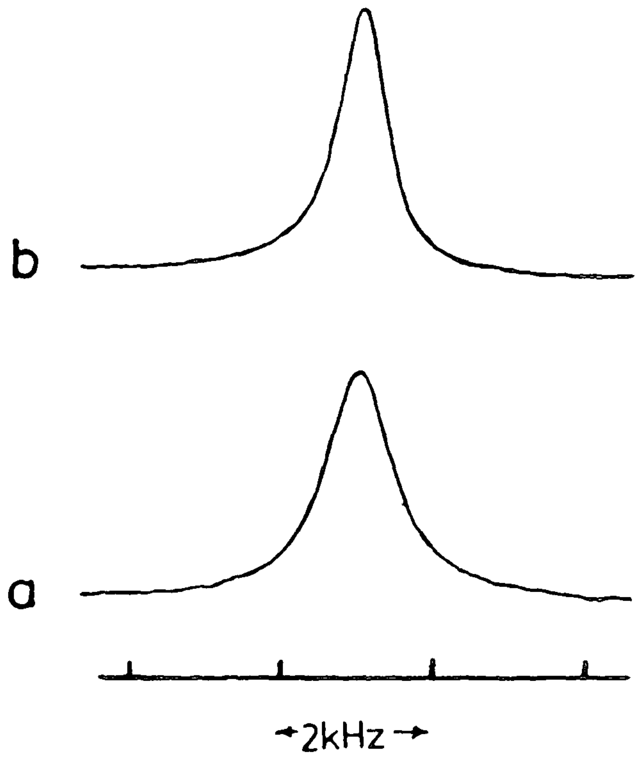

Static proton spectra of a) flint ($\Delta V_{\frac{1}{2}}$ = 1.8 kHz) b) chalecedony ($\Delta V_{\frac{1}{2}}$ = 1.2 kHz)

Figure 6.18 : Proton T_1 Relaxation data

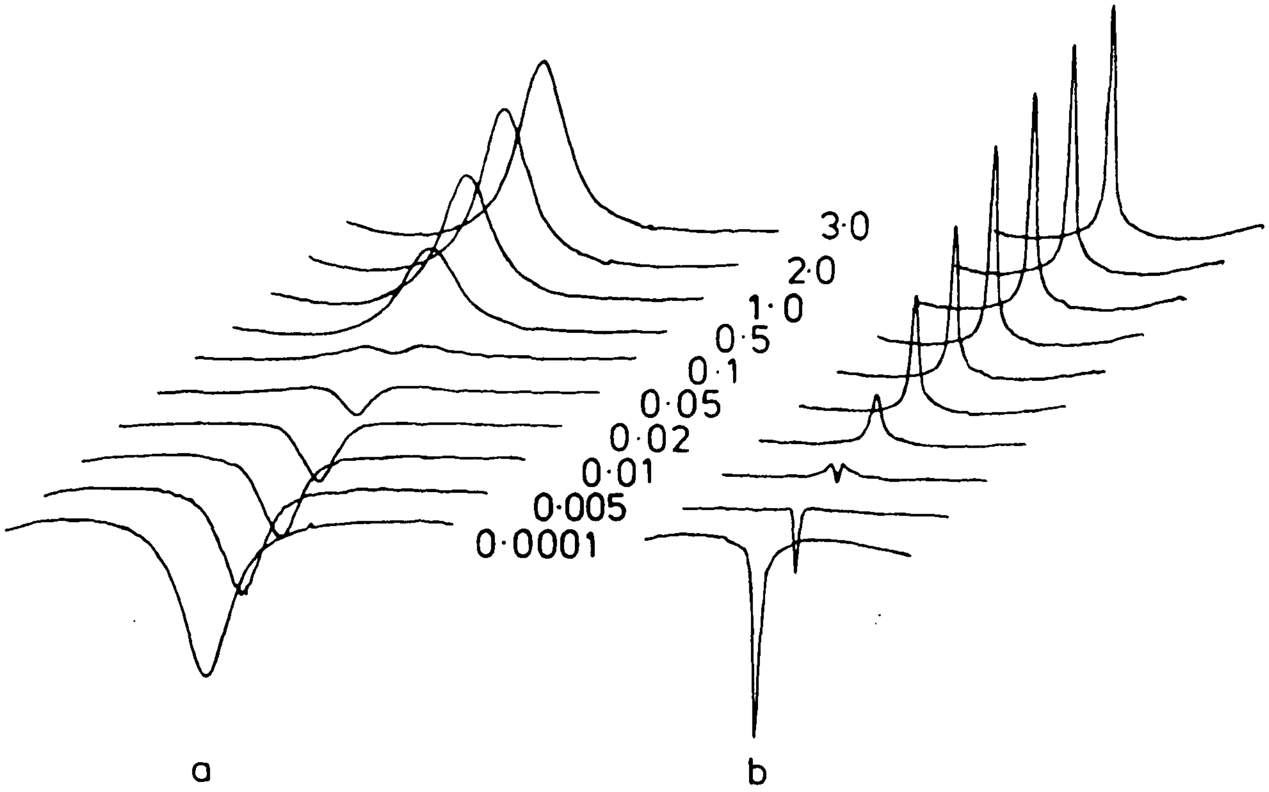

Proton T_1 relaxation data for a) flint (0.15 s) and b) chalcedony (0.01 s). values centred between the spectra are the times, in seconds, for the variable, τ, in a 180-τ-90-observe pulse sequence.

However, close examination of the data has shown that the relaxation behaviour is not single exponential. This is clearly shown in Figure 6.18 where, at intermediate recovery times a relatively sharp peak with a slower recovery is superimposed on a broader, more rapidly relaxing band. Because the experiment measures the bulk properties of the sample, contributions to the effective ^1H reservoir, and hence the numbers generated, may originate from any proton source in the system. In this case we would expect Si-OH and interstitial H_2O to be the major contributors to the relaxation mechanism. The fact that the relaxation behaviour is not simply single exponential supports a hypothesis of two (or more) well-defined proton reservoirs.

It has been well-established that the T_1 for a compound will pass through a minimum as the mobility of the reservoir decreases. Given the narrownesss of the static ^1H bandshape, it is most likely that the T_1 behaviour lies on the high mobility side of the minimum (extreme narrowing case). This would mean that the chalcedony ($T_1 \simeq 0.01s$) contains a less mobile ^1H population than flint ($T_1 \simeq 0.15s$).

In Figure 6.19 the single pulse excitation response of the ^{29}Si nuclei for long recycle times (500s) are shown for chacedony and flint. A single peak is evident at -107.6 ppm, denoting a Q^4 silicon environment. The areas of the peaks for the two minerals are equivalent, indicating an equal number of ^{29}Si nuclei present in the sample, for each mineral, as would be expected.

Figure 6.19 : Silicon-29 data

Absolute intensity comparison of MAR Single Pulse spectra of a) flint ($\Delta V_{\frac{1}{2}} = 60$ Hz, $\delta = -107.6$ ppm), b) chalcedony ($\Delta V_{\frac{1}{2}} = 40$ Hz, $\delta = -107.6$ ppm)

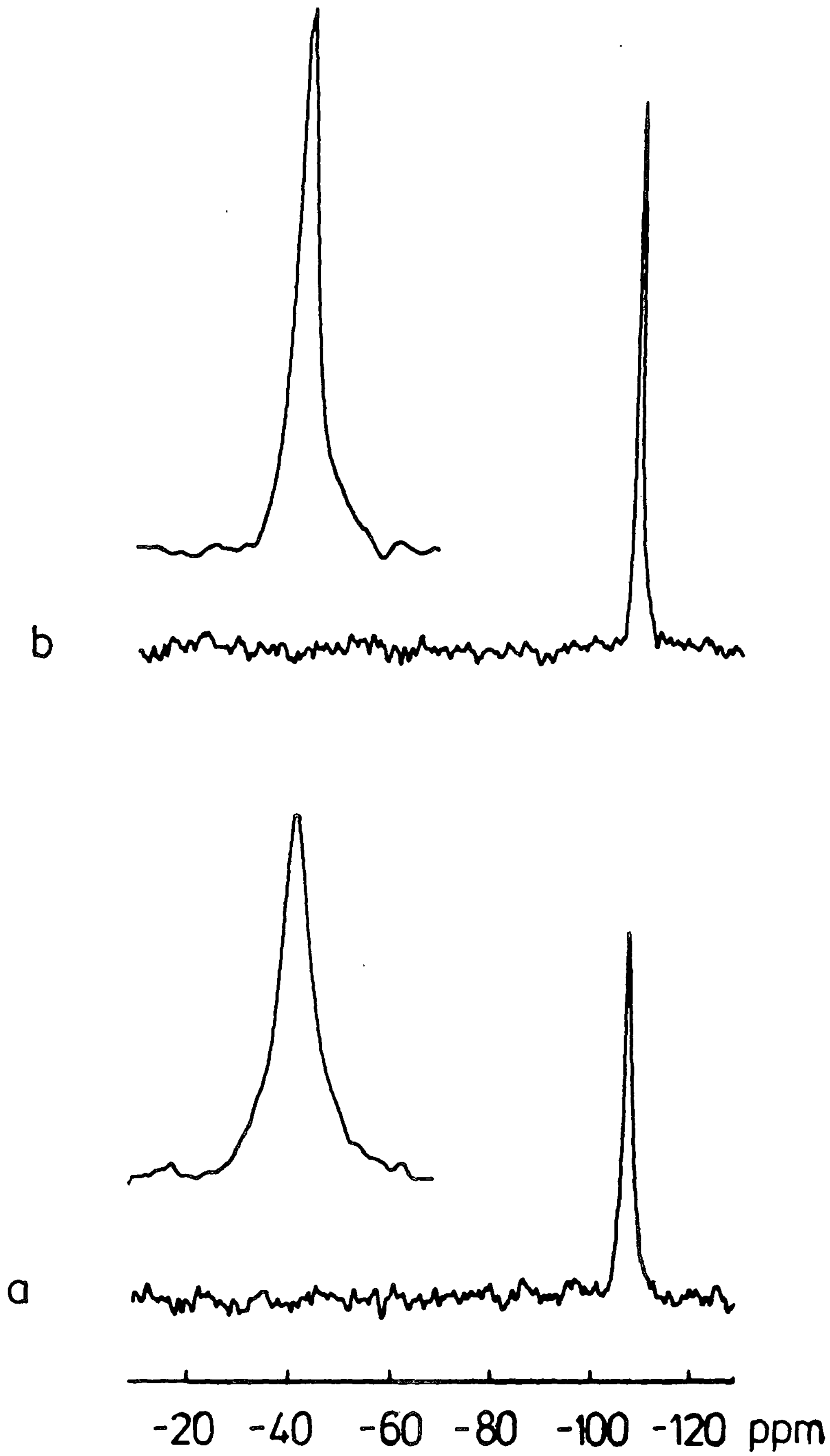

This is important when considered with respect to the response of both minerals to a cross-polarization experiment. The linewidth for flint is, however, approximately 50% greater than for chalcedony, which probably indicates more local order (higher degree of crystallinity) or a lower level of paramagnetic impurity for the latter.

Figure 6.20 shows several significant features resulting from the cp experiment. The most obvious is the appearance of a peak at -99.0 ppm observed for each mineral, which may be assigned to Q^3 silicons in the lattice. The fact that both Q^3 (surface) and Q^4 (lattice) environments are sensitive to cross-polarization indicates there is contact with the ^1H reservoirs for both, though not all Q^4 silicons may contribute to the signal. The data shown in Figure 6.20 are most usefully presented graphically, correlating the signal intensities (logarithmic scale) with the contact time, as shown in Figure 6.21. The rate of cross-polarization depends upon the proximity of protons to the relevant silicon nuclei and on proton mobility. Thus it should be higher for Q^3 sites, than for Q^4 units. However, the magnetization decays via $T_{1\rho}(^1H)$ processes to the lattice. Therefore the signal intensity should move through a maximum, as a function of contact time.

Figure 6.21 demonstrates a higher rate of cross-polarization for the Q^3 environments than for Q^4 in both minerals, with maxima occurring at approximately the same contact time for the former.

Figure 6.20: Silicon-29 cp data

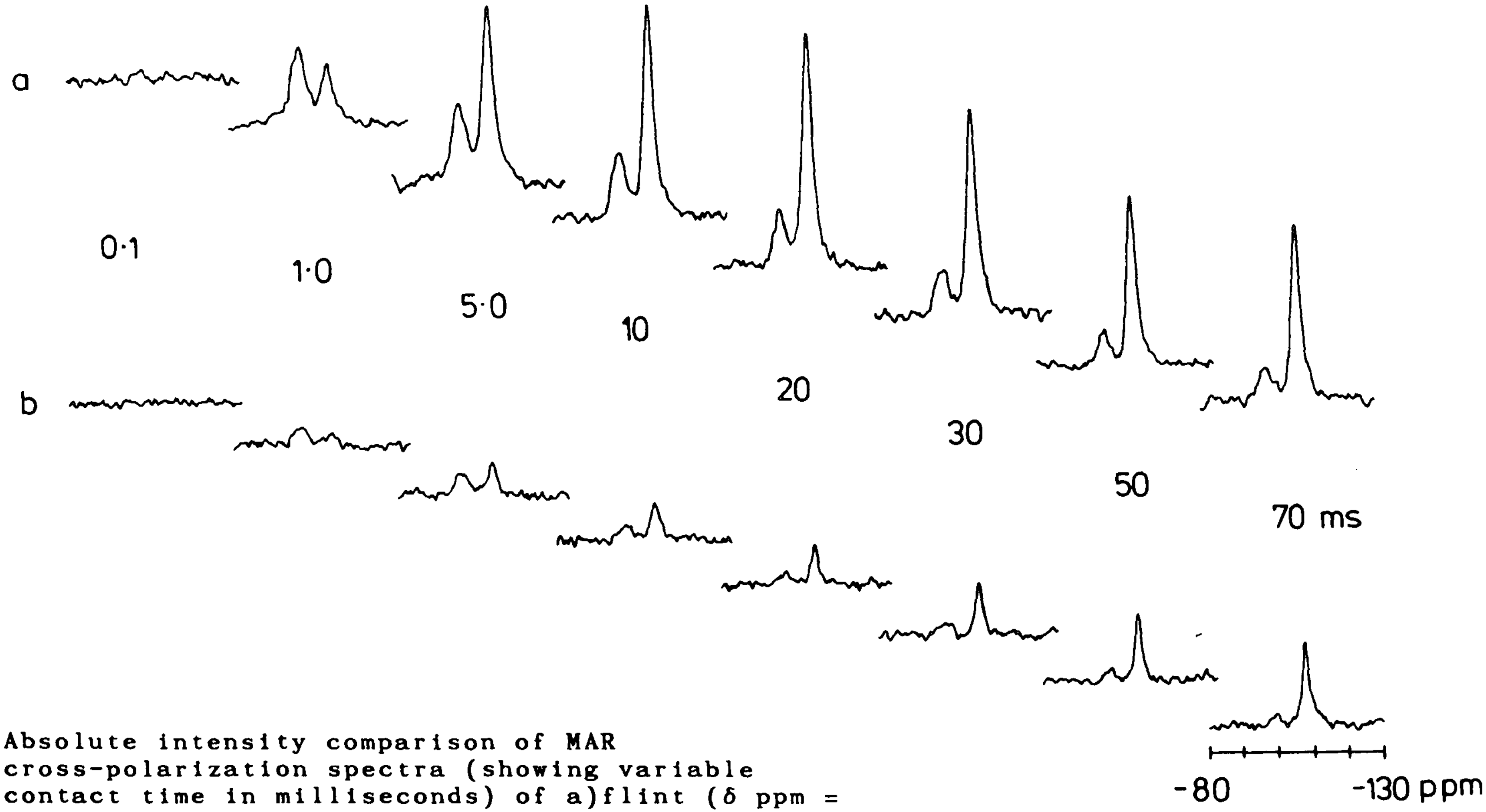

Absolute intensity comparison of MAR cross-polarization spectra (showing variable contact time in milliseconds) of a) flint (δ ppm = -99.0, -107.6), b) chalcedony (δ ppm = -99.0, -107.6)

Figure 6.21: Graphical presentation of cp data

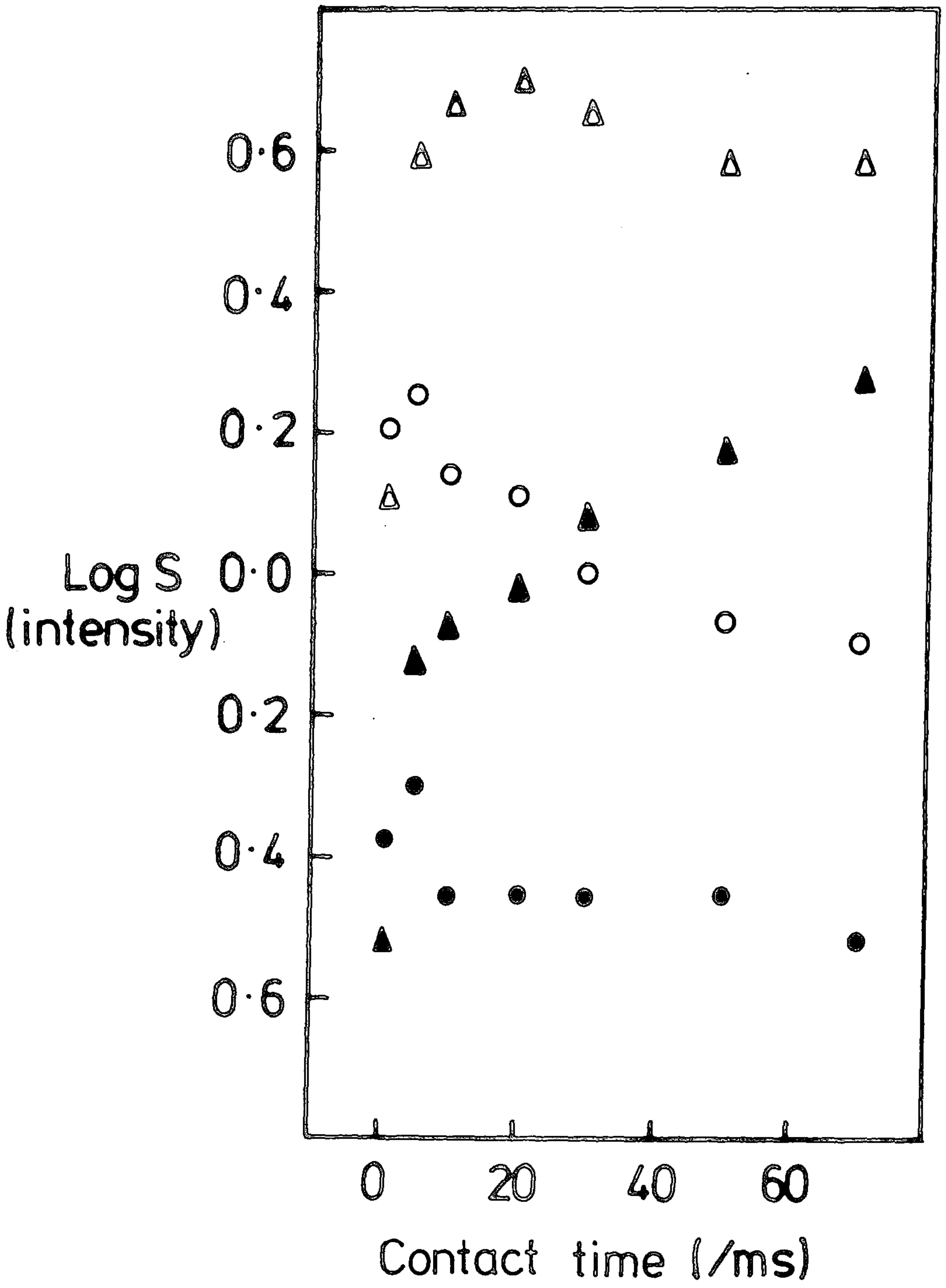

Graphical presentation of cross-polarization data showing logarithmic relationship between the intensity of each silicon environment and contact time.

for flint Q^3-O Q^4-Δ

for chalcedony Q^3-● Q^4-▲

The intensity values were calculated using arbitrary (But convenient) units.

The Q^4 sites are substantially more abundant than the Q^3 silicons and cross polarize only slowly, as expected. It appears that the Q^4 sites for chalcedony do not reach their maximum cp intensities even at 70 ms contact time. The signals for chalcedony Q^3 are sufficiently weak that unambiguous conclusions are difficult to make in this case. It also appears that the slopes at high contact time for the Q^3 and Q^4 sites in flint may differ, suggesting there are differing proton reservoirs involved, with little spin diffusion between them. The implication is that such reservoirs may be surface hydroxyls and water molecules respectively, but lack of spin contact between them is surprising.

The most marked effect demonstrated by Figure 6.21 is that both types of silicon site cross-polarize far less readily for chalcedony than for flint, suggesting that the latter has a greater content of protons or that the protons involved are more rigidly held in the lattice.

The CRAMPS experiment allows direct observation of the proton reservoir(s) in a system. This can be very useful, if the integrity of the reservoir has been preserved. This is not a simple matter. The difficulties involved in measuring water and hydroxyl group content on silica has been documented in the literature. Because of the relatively low populations of protons being measured in the silicon lattice, the physisorption of water (at STP) is sufficient to obscure any information about the real state of the proton reservoir in the system. Flint and chalcedony exhibit such problems, which might be expected, given the relatively large pore radius (Table 6.8).

Figures 6.22 and 6.23 demonstrate what information can be extracted from a difficult mineralogical system using CRAMPS. All spectra shown are quantitatively comparable within their figures.

Contrary to what might be expected from previous investigations[93], Figure 6.22 indicates that the proton populations of these samples of flint and chalcedony are not largely different. It should be noted here that some difficulty has been encountered obtaining consistently reproducible results for ^{1}H CRAMPS spectra of these minerals. Some of the samples examined did support the previous studies, in that differentiating proton populations were observed, with discrete surface hydroxyl and water absorbance peaks. But because of the difficulty in maintaining sample integrity, even under well documented standard conditions of storage (1 M NH_4Cl saturated solution), the samples did change. Shown in Figure 6.22 are the results obtained under these standard conditions.

The obvious linewidth difference observed is real. Even in this state of controlled physisorption we can see that the proton reservoir is more highly mobile in flint compared with chalcedony. Both polymorphs also exhibit a shoulder at 3.9 ppm which we have assigned as Si-OH in origin. The broad baseline, especially evident in chalcedony, may be the result of water protons in the lattice occupying a variety of sites.

Upon dehydration (10 hours, 150°C) both minerals show significantly narrowed linewidths in Figure 6.23, indicating that the disordered proton environment has been removed.

Figure 6.22: Proton CRAMPS Spectra

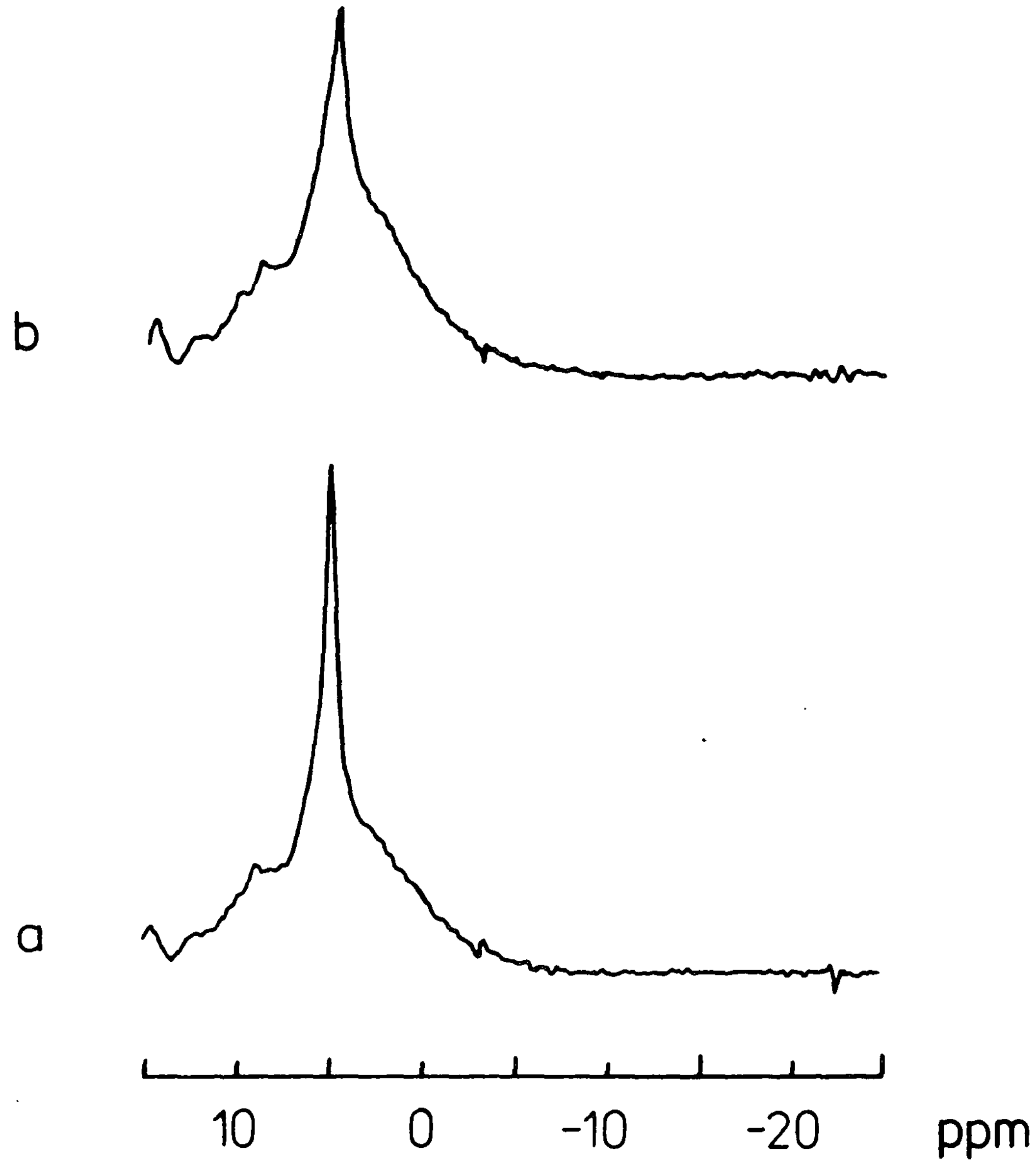

Absolute-intensity comparison of proton CRAMPS spectra for a) flint and b) chalcedony at standard storage conditions.

Figure 6.23: Proton CRAMPS Spectra

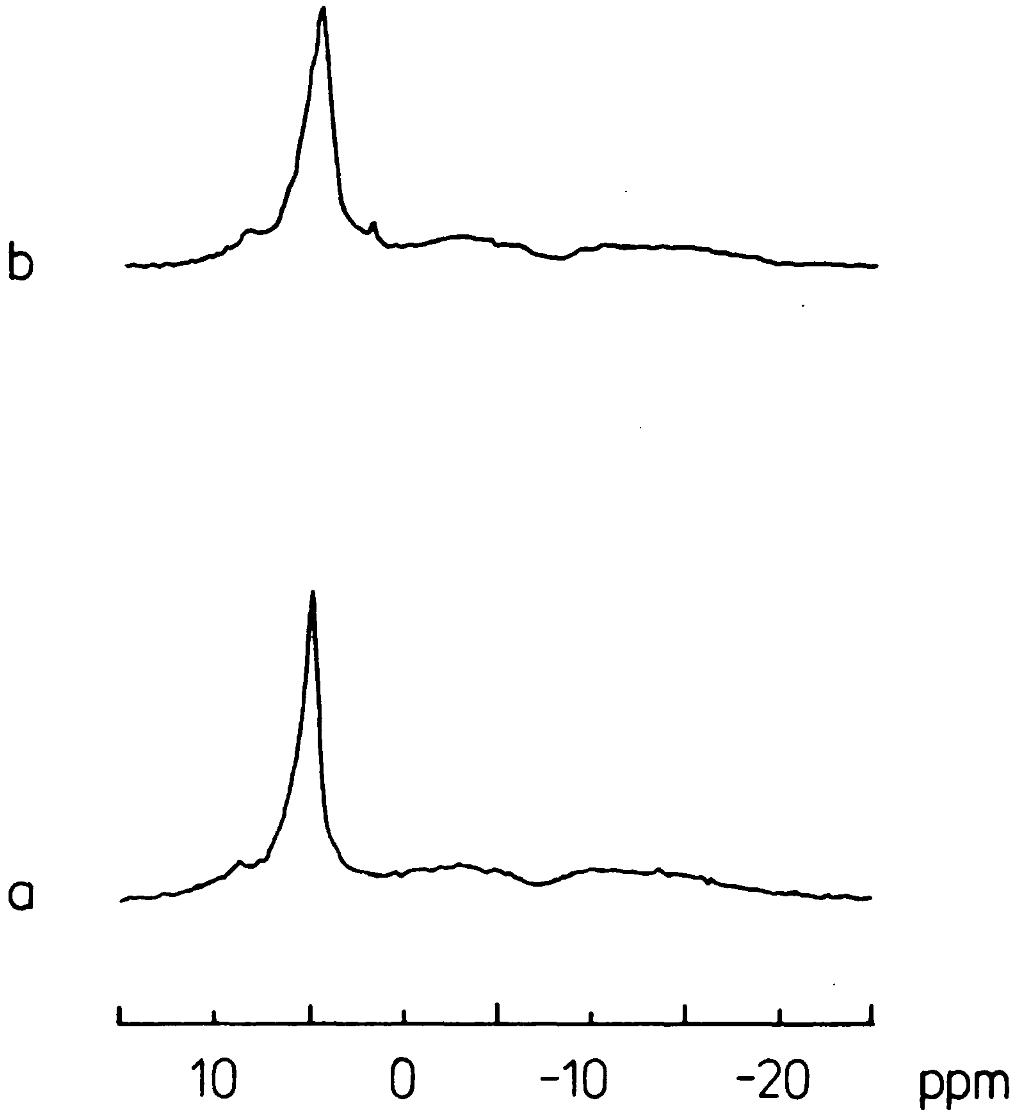

Absolute-intensity comparison of proton CRAMPS spectra for a) flint and b) chalcedony after dehydration.

Further, chalcedony has retained a greater amount of the proton environment than flint. This supports the previous studies suggesting discrete versus connected pore nature, and the relevant size difference (110 vs. 1400 A^o) for chalcedony and flint respectively.

The fact that the Q^4 groups are giving higher intensities at long contact times is in accord with the (r^{-6}) proportionality, since these sites would be removed from direct contact with any proton reservoir. The marked difference between the Q^3 and Q^4 silicon environments in the rate of cross-polarization for both minerals suggests that the Q^3 and Q^4 silicon nuclei are in contact with different proton environments. Moreover, there are considerable differences between Q^3 and Q^4 units in the efficiency of cross-polarization, as indicated by the proportion of the units observed in the cp experiment relative to the SPE spectrum. These observations appear to indicate, perhaps surprisingly, that the two proton reservoirs undergo little mutual spin diffusion. The proton broadline, T_1 and CRAMPS results support the silicon-29 data on this question. The dehydration study confirms that the protons involved in active polarization transfer are a relatively small fraction of the entire proton bath.

From these conclusions it is possible to construct a model to characterize the relationships observed, in order to facilitate our understanding of this complicated mineralogical system. This is shown in Figure 6.24. The Q^3 sites seem to cross-polarize predominantly via a proton population of close proximity and relatively low abundance

(P3H >> P3W), whereas the Q^4 data suggest a proton source of lesser average proximity in this case. Indeed, the slow rate of cross-polarization to Q^4 and the low proportion of Q^4 units observed by cp suggest that Q^4 units are at greatly varying distances from protons, and many are remote from such nuclei, but it may be noted that since the cp source for Q^4 appears to be predominantly different from that for Q^3 it is likely that the former has a much higher abundance (P4W >> P4H). This model describes these silica polymorphs in a simple and adequate fashion that allows differentiation of the two minerals, flint and chalcedony.

Figure 6.24: Model of relationship between proton and silicon environments

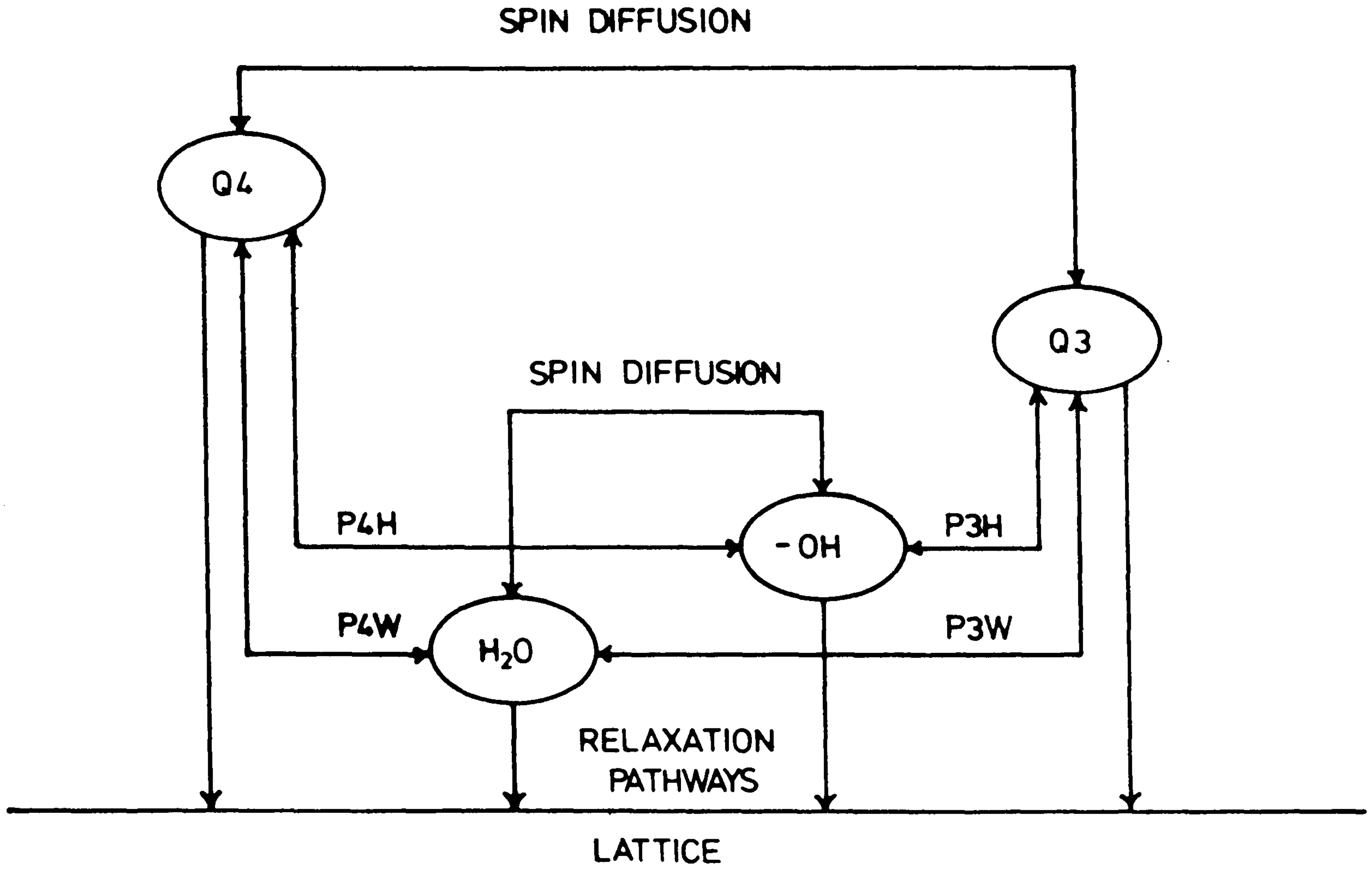

6.2 Macrocyclic Polyether 'Crown' Complexes of Sodium

Since the first report of the isolation and characterization of macrocyclic 'crown' complexes[94] there has been an enthusiastic response to utilize the selective complexation properties these systems have exhibited.[95] Attention has also focused on elucidating the general physical properties[96a] and structures[96b] of these complexes in order to more fully understand the unique behaviour which has been observed.[97] The original characterization[94] had established that a complex forms between the cation portion of an alkali or alkaline earth metal salt and the donor atoms of the polyether ligand, and suggested that the cation was trapped in the cavity formed by the macrocyclic ring. X-ray structure analysis[96b,97] and solution state studies[98] have confirmed that the complex is formed by an ion-dipole interaction between a cation and the negatively charged oxygen atoms of the polyether ring.

The criteria controlling complexation formation and stability have been shown to depend upon the relative sizes of the cavity diameter and the associated cation. This will also be influenced by the type of donor atoms present in the ligand and the charge and electronegativity of the cation. Recent studies have shown that solution state ^{23}Na NMR is sensitive to ion-ligand, ion-ion, and ion-solvent interactions.[99,100] The problem, inherent in the solution state, is to separate the contributions to the NMR signal which are a result of chemical exchange and motional time averaging, from those interactions which are a direct consequence of the ligand-complex structure.

The advantages of working in the solid state have been demonstrated using the ^{13}C nucleus to examine the polyether rings of a variety of crown ether-cation complexes.[101] This allowed conclusions to be drawn upon the ring conformation, but little could be inferred about the nature of the cation bonding, which is of great importance in understanding the complexation mechanism. The most sensitive method should be to observe the cation nucleus itself, if feasible, to deduce the nature of the donor-cation bond. This is possible using NMR because the chemical shift of the cation is a direct measure of the shielding of the nucleus, which reflects the extent of electron penetration of the bonding orbitals. Further, the lineshape will be indicative of local symmetry to the nucleus where quadrupolar nuclei are involved. On this premise a series of crown ether-cation complexes have been examined in the solid state by ^{13}C, ^{23}Na, and ^{1}H CRAMPS NMR. The chemical formulae and cation-oxygen distances are shown in Table 6.9.

This series of compounds present an opportunity to measure the sensitivity of the cation shielding to changing anion and ligand coordination since, in all cases, the cation is sodium. The Na^+ ion in the solution state is believed to bond by accepting electron density into the outermost available orbital, conventionally known as the 3p orbital.[109] As shown in Chaper Five, the sodium chemical shift and lineshape in the solid state are known to be sensitive to these effects. Recent investigations have substantiated this assertion in application to a variety of sodium-ligand complexes of diverse character.[110,111]

Table 6.9: Macrocyclic Polyether Comounds

Complex	cation:ligand ratio	Na^+-O(A^o)	Coordination number	Reference
18-crown-6	——	——	——	106
$18\text{-crown-6}.Na^+.SCN^-.H_2O$	1:1	2.45-2.62	7	103
$15\text{-crown-5}.Na^+.SCN^-$	1:1	NA.	NA.	——
Benzo-15-crown-5	——	——	——	102
$[\text{Benzo-15-crown-5}].Na^+.BPh_4^-$	1:1	NA.	NA.	NA.
$2[\text{Benzo-15-crown-5}].Na^+.BPh_4^-$	2:1	2.49-3.12 $2.48\text{-}3.11^{****}$	5^*	107,105
$[\text{Benzo-15-crown-5}].Na^+.BPh_4^-.CH_3CH_2OH$	1:1	NA.	NA.	107

Table 6.9(cont'd): Macrocyclic Polyether Comounds

Complex	cation:ligand ratio	Na^+-O(A^o)	Coordination number	Reference
[Benzo-15-crown-5] .Na^+.I^-.H_2O	1:1	2.35-2.43	6	104
[Benzo-15-crown-5] .Na^+.CLO_4^-	1:1	2.37-2.63	7^{**}	108,105
2[Benzo-15-crown-5] .Na^+.CLO_4^-	2:1	2.63-2.93	$4\text{-}8^{***}$	108,105

[*] non-symmetric sandwich of Na^+ - exact coordination unclear from structures

[**] 5 coordination to crown ether, 2 from perchlorate

[***] centrosymmetric sandwich(make it a salt beef on rye and I'm yours)of Na^+ - exact coordination unclear from structure

[****] two conformers in unit cell

NA. = Not available in literature.

Table 6.10: Carbon-13 data for Macrocyclic Polyethers

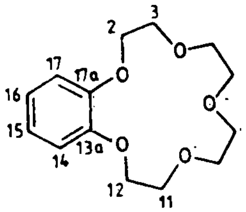

	Aromatic Region						Aliphatic Region			
	17a,13a		15,16		14,17					
18-crown-6										68.7
18-crown-6.Na^+.SCN^-.H_2O										68.7
15-crown-5.Na^+.SCN^-								70.5	70.0	
Benzo-15-crown-5	151.0	150.0	120.8	119.7		111.9	71.4		70.1	68.7
[Benzo-15-crown-5] .Na^+.BPh_4^-	149.2	148.1	126.1	123.9	115.4	112.8				
2 [Benzo-15-crown-5] .Na^+.BPh_4^-	148.7	147.4	126.2	123.0	114.4	113.1				
[Benzo-15-crown-5] .Na^+.BPh_4^-.CH_3CH_2OH	149.0		126.7	124.6	114.9	112.7				

Table 6.10(cont'd): Carbon-13 data for Macrocyclic Polyethers

	Aromatic Region			Aliphatic Region
	17a,13a	15,16	14,17	
$[\text{Benzo-15-crown-5}].\text{Na}^+.\text{I}^-.\text{H}_2\text{O}$	148.0 147.4	126.2 124.4	118.1 115.3	
$[\text{Benzo-15-crown-5}].\text{Na}^+.\text{CLO}_4^-$	147.5	125.4 124.2	115.5	
$2[\text{Benzo-15-crown-5}].\text{Na}^+.\text{CLO}_4^-$	149.4	124.1 123.2	115.4 112.9	

The solid state carbon-13 data for this series of compounds are given in Table 6.10. The Benzo-15-crown-5 ligand is shown in Table 6.10 indicating the numbering of the benzo-crown atoms. The chemical shift values for some of these complexes have been reported in the literature previously[101] demonstrating the increase in structural information accessible using solid state, as opposed to solution state, NMR methods. The assignments in the aromatic region are relatively straightforward, and in accord with the previous study.[101] However, assignment of the aliphatic region is not trivial and, for the purposes of this thesis, not critical to allow interpretation of the cation-ligand, cation-anion relationships under investigation. These data are not discussed in detail here since, as stated, many of these values have been reported and satisfactorily assigned in the literature.[101]

The ^{1}H CRAMPS data are shown in Table 6.11. The associated proton spectra are shown in Figure 6.25 and Figure 6.26. Assignment for the BPh_4^- ligand complexes are trivial, given the intensities shown in Figure 6.25. In Figures 6.25 and 6.26 the numbers under each absorbtion line indicate the number of protons assigned to that peak. No crystal structures have been published in the literature excepting for a report listing the Na^+-O bond distances and cell symmetry for the 2:1 $NaBPh_4$ complex.[105] Without any further data available trivial assignments between aliphatic and aromatic regions correspond very well to that which would be expected from the formula.

Table 6.11: Proton CRAMPS and Sodium-23 NMR data for Macrocyclic Polyether-cation Complexes

	PROTON CRAMPS				SODIUM-23					
	δ ppm				SP with decoupling			CP		
18-crown-6	4.0									
18-crown-6 .Na^+.SCN^-.H_2O	4.3			1.5		-22.1[a]			-22.1[a]	
15-c-5.Na^+.SCN^-			3.9		-9.9			-9.9		
B-15-c-5	6.7	6.1	3.5	1.3shldr						
[B-15-c-5] .Na^+.BPh_4^-	7.2		2.6		-13.0[a]	-26.0[a]		———	———	———
[B-15-c-5] .Na^+.BPh_4^-	7.2		2.6			-41.0[a]	-46.0[a]	———	———	———
[B-15-c-5] .Na^+.BPh_4^- .CH_3CH_2OH	7.3	5.0	3.6	1.3	-14.0	-26.0[a]	-50.0	-16.0[a]	-26.0[a]	-50.0[a]

Table 6.11(cont'd): <u>Proton CRAMPS and Sodium-23 NMR data for Macrocyclic Polyether-cation Complexes</u>

	PROTON CRAMPS	SODIUM-23	
	δ ppm	SP with decoupling	CP
$[\text{B-15-c-5}]$ $.Na^+.I^-.H_2O$	3.9	-14.0^a -25.6^a	-16.0^a -26.0^a -50.0^a
$[\text{B-15-c-5}]$ $.Na^+.ClO_4^-$	7.1 5.8 3.8	-14.0^a -27.0^a	-14.0^a -27.0^a
$2[\text{B-15-c-5}]$ $.Na^+.ClO_4^-$	7.6 6.8 3.8 1.0shldr	-34.9	-34.9

[a] as~~s~~ymetric line shape observed

B-15-c-5 = Benzo-15-crown-5

Figure 6.25: Proton CRAMPS Spectra

16 μs cycle time
30 s recycle delay
32 transients

L = [Benzo-15-crown-5]

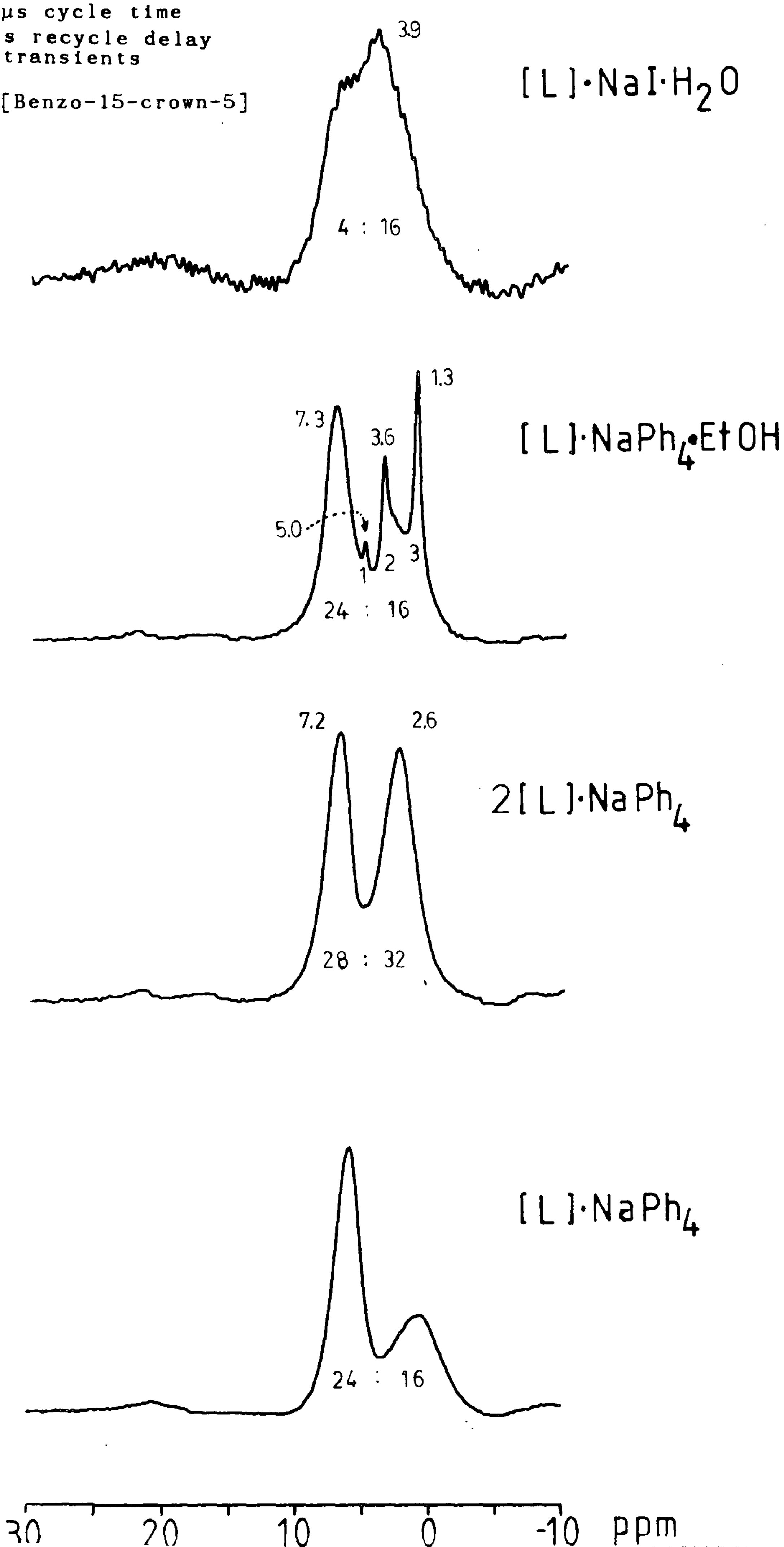

Figure 6.26 : Proton CRAMPS Spectra of 'crown' complexes

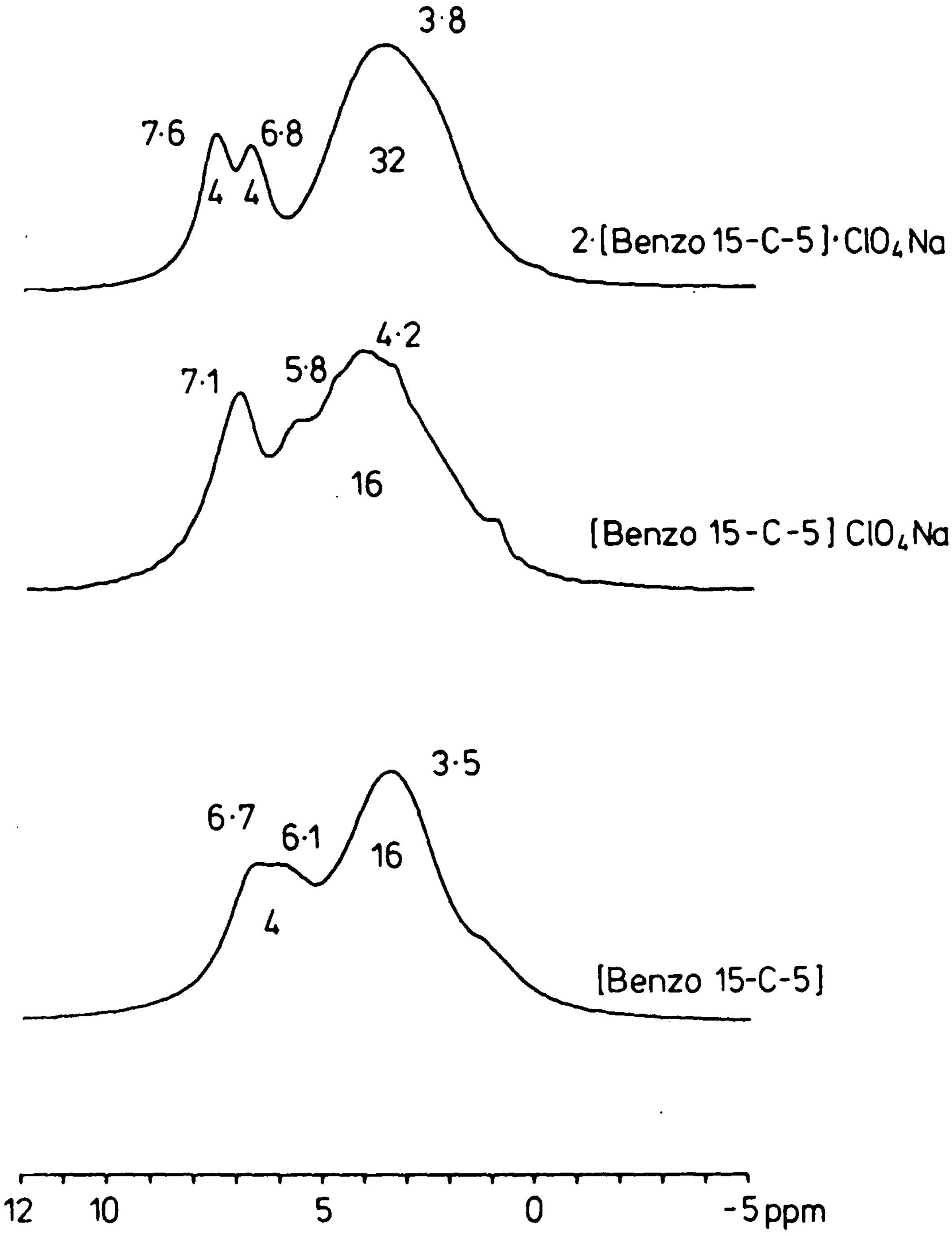

Proton CRAMPS Spectra for 'Crown ether' Complexes 16 μs cycle time. 30 s recycle delay, 32 transients

It is interesting to note the resolution obtained from the .EtOH complex, where it appears the features of the ethanol molecule are visible, superimposed upon the aliphatic region. In contrast, the iodine complex shows broad unresolved features, perhaps as a result of quadrupolar broadening of the aliphatic region. It should be noted here that this sample behaved in an electrically lossy manner, significantly detuning the CRAMPS probe. This made acquisition difficult, and may account in some manner for the poor spectrum obtained.

The proton CRAMPS spectra of the perchlorate complexes are shown along with that of the pure ligand in Figure 6.26. The assignments for the benzo-15-crown-5 polyether and 1:1 perchlorate complex are straightforward. The 2:1 complex is noteworthy because of the differentiation of the aromatic protons. It has been shown that the centrosymmetric sandwich arrangement of the two macrocycles about the sodium atom causes the polycyclic ether to exist as two conformers with different torsion angles about the C(8)-C(9) bond.[105] The reported structures are shown in Figure 6.26b. The crystal structure indicates that this bond is placed such that it is the closest group to the benzene rings of the opposite conformer situated across the sodium sandwich. Thus what is observed is an inter-ligand effect which apparently deshields the protons of one conformer.

The sodium chemical shift data for the polyether-cation complexes have been shown in Table 6.11. The chemical shift values for the uncomplexed salts are given in Table 6.12.

The symmetry at each sodium atom was such that the lineshape exhibited no quadrupolar contribution at 4.7 Tesla.

Table 6.12: Sodium-23 Data for Uncomplexed Salts

	Cell Symmetry	δ (ppm) @ 4.7 Tesla
$NaClO_4$	tetragonal	-20.0
NaSCN	cubic	-2.1
$NaBPh_4$	tetragonal	-51.7
NaI	cubic	-2.0

No presence of unreacted salt was observed in any of the spectra. The sodium-23 chemical shift of -22 ppm for the 18-crown-6.NaSCN complex is the same as has been reported previously in the literature.[110] The higher shielding and asymmetric lineshape, relative to that observed for 15-crown-5.NaSCN, supports the suggestion that the sodium nucleus fits into the 18-crown-6 cavity more deeply, and would thus be more effectively shielded by the electrons from the polyether oxygens.

The sodium-23 spectra for the NaI and $NaBPh_4$ complexes are shown in Figure 6.27. The remarkable similarity between lineshapes and the chemical shifts of the observed singularities supports recent suggestions that the symmetry surrounding the cation is relatively unaffected by the species which is acting as the coordinating anion.[111]

In the absence of crystal data for the EtOH and 1:1 $NaBPh_4$ complexes, their NMR spectra suggest that the sodium cation occupies similar coordination and symmetry environments to those for the iodine complex. The 2:1 complex does exhibit significant shielding, presumably as a result of the reported asymmetric sandwich structure which surrounds the sodium atom with oxygen nuclei. The lineshape also indicates an environment with higher symmetry, which supports the asymmetric sandwich structure conformation. It should be noted that the shielding values for the singularities (-41, -46 ppm) are approaching that observed for the Na^- ion, -61 ppm,[110] which may give some relative measure of the degree of electron density resident on the sodium ion in such a highly shielded sandwich environment.

The sodium-23 spectra for the 1:1 and 2:1 perchlorate complexes are shown in Figures 6.28 and 6.29 respectively. The 1:1 complex gives a lineshape not unlike that observed for the 1:1 $NaBPh_4$ complex. This is again in accord with the observation that the complexing anion does not greatly affect the nature of the cation-ligand structure. The spectra of the 2:1 complex strongly supports the crystal structure assignment of a centrosymmetric sandwich conformation. The lineshape is divested of any asymmetric contributions under both static and MAR conditions, and the chemical shift is indicative of the higher shielding which would be expected for this environment. The ability of the sodium-23 NMR spectrum to elucidate the symmetry of the cation is remarkable in this instance. This illustrates a definitive method of corroborating the proposed site symmetry of the cation.

Figure 6.26b Structure Projections

[Benzo-15-C-5]·NaClO$_4$

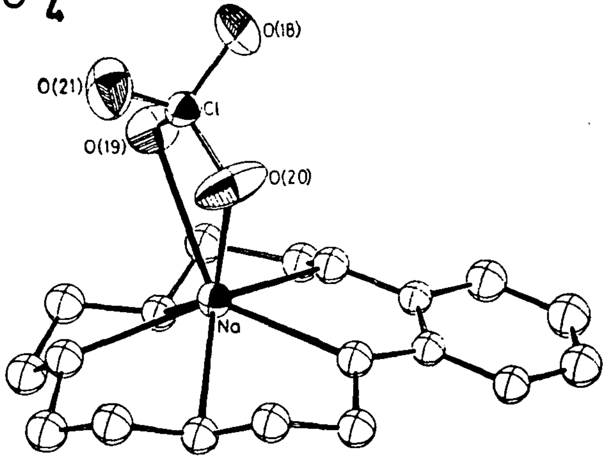

2[Benzo-15-C-5]· NaClO$_4$

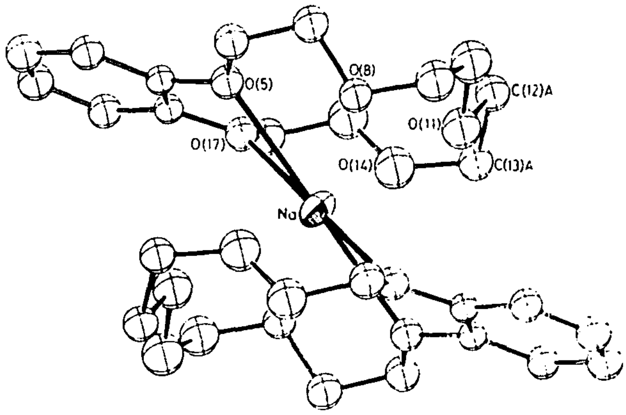

2[Benzo-15-C-5]·NaBPh$_4$

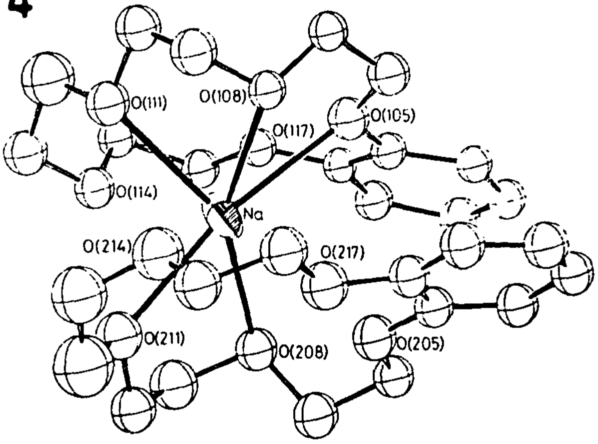

Figure 6.27: Sodium-23 NMR Data for Crown Ethers.
MAR = 4.0 kHz, 2 μs 90° pulse, variable transient totals

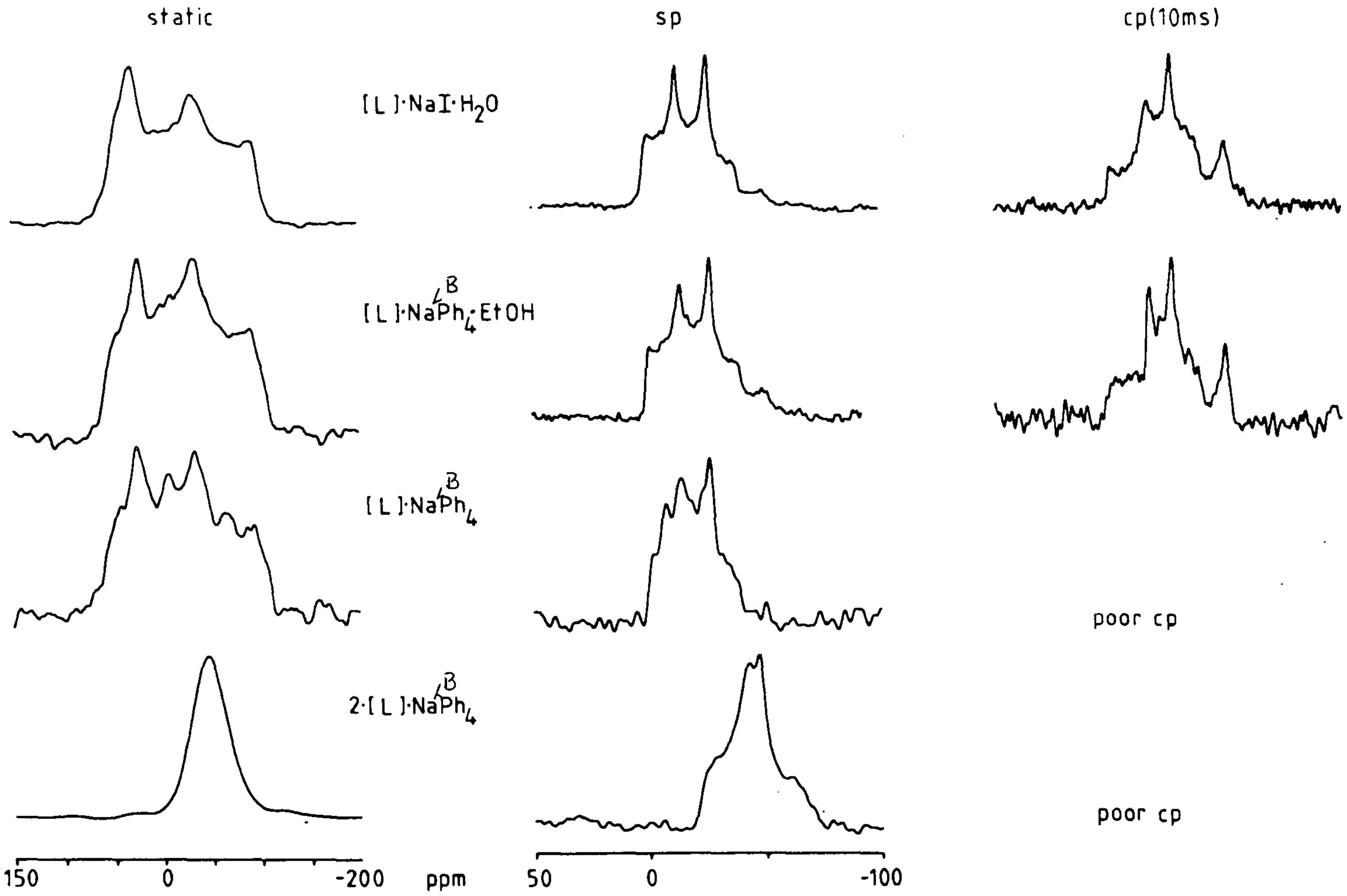

In conclusion, it has been shown that the sodium-23 NMR chemical shift and lineshape are sensitive to electron density changes and symmetry of the local environment inside a macrocyclic crown ether cavity. In the absence of crystal data, correlation can be made between complexes of similar ligands and cations using the NMR data. It has also been shown that the magnetic resonance properties of the sodium cation are relatively insensitive to the coordinating anion. This is perhaps not surprising given the overwhelming presence of shielding electrons available from the polyether ring oxygens, and the associated nuclear bond distances.

Figure 6.28 Sodium-23 Spectra of [Benzo-15-C-5]·NaClO

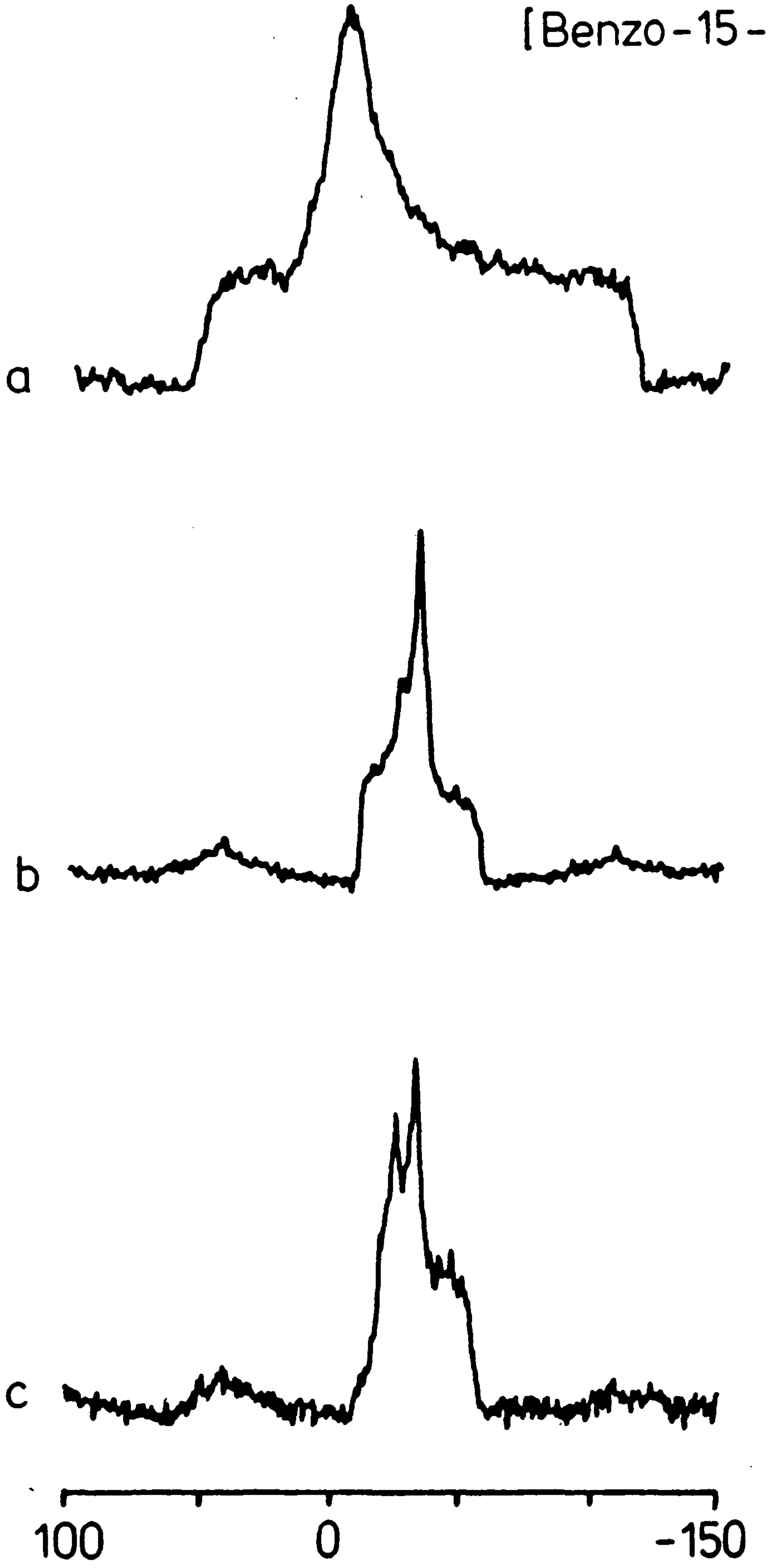

MAR 4.0 kHz, 2 μs 90° pulse, 32 transients
a) static
b) single pulse decoupled
c) cp at 10 ms contact

Figure 6.29: Sodium-23 spectra of 2[Benzo-15-C-5]·$Na{\cdot}ClO_4$

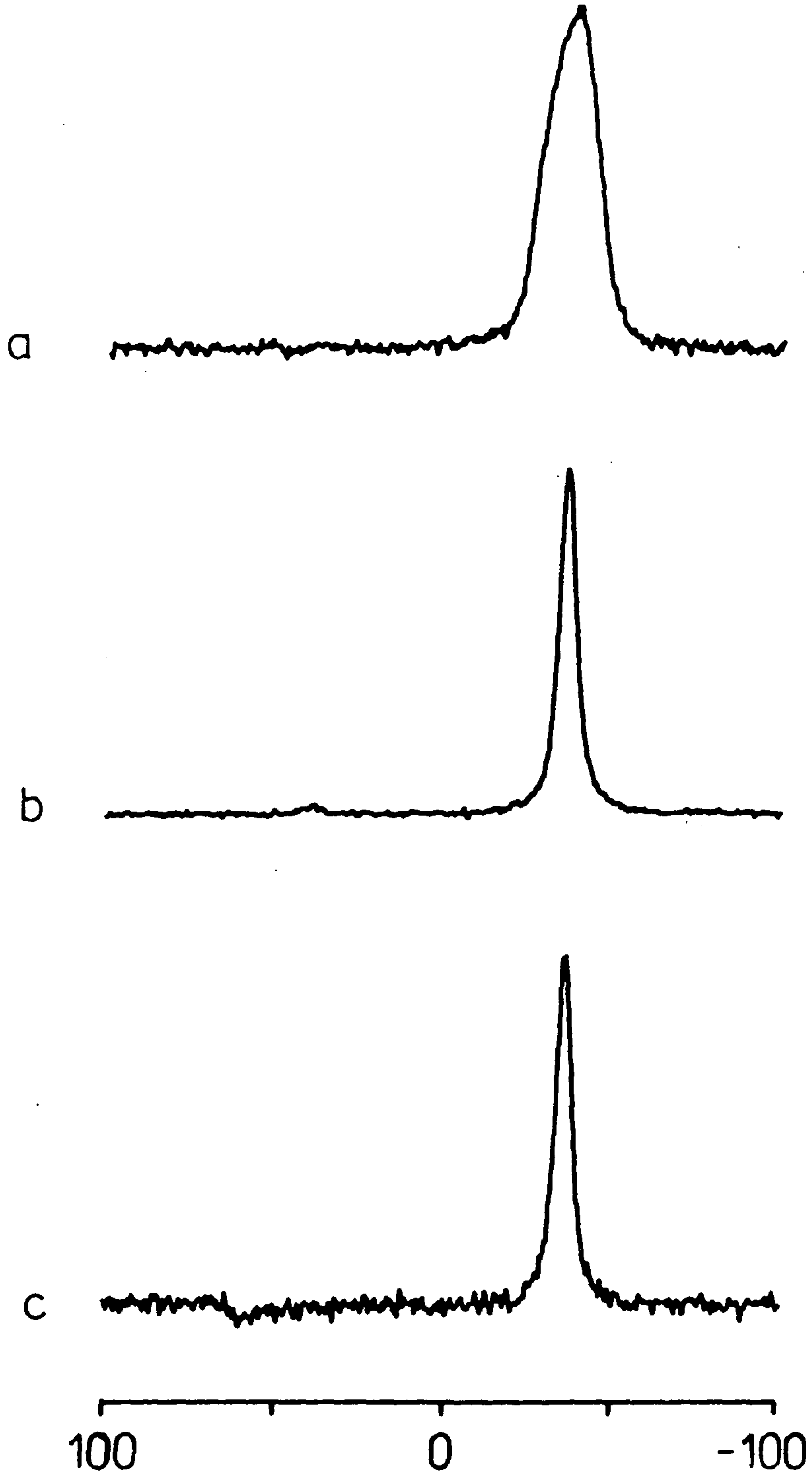

MAR 4.0 kHz, 2 μs 90° pulse, 32 transients

a) static

b) single pulse decoupled

c) cp at 10 ms contact

6.3 Fluoropolymers

High resolution NMR has been widely applied to the investigation of chemical microstructure in protonated and fluorinated polymers.[113] The reason for the remarkable success of solution state NMR, in application to polymers, has been the direct and sensitive correlation between chemically shifted resonances and specific nuclear sites within a polymer. For obvious reasons this has been limited to those polymers possessing a sufficiently low melt viscosity or significant solubility in a suitable solvent.

The investigation of solid polymers was originally restricted to the study of molecular motion by relaxation measurements because of the dominance of spectral features by dipolar interactions. The shortcoming of relaxation data is that they are not specific to different types of motion, although the utility of these experiments has been demonstrated in the determination of amorphous and crystalline state behaviour within protonated[114] and perfluorinated polymers.[115] The development of multiple pulse methods and subsequent application to solid polymers has greatly increased the data available to the polymer chemist.[116] Investigations of fluoropolymers have shown that resolution of chemically shifted environments[117] and determination of shielding tensors[118] are both possible in amorphous polymers. Further studies have shown that if some preferred orientation can be placed upon the polymer, by method of manufacture, then it is possible to measure the orientation of a C-F shielding tensor relative to the molecular axis.[119] It has also been shown that the application of variable temperature methods with multiple pulse decoupling sequences can greatly enhance determination of the nature of the crystallinity and molecular motion in random oriented poly(tetrafluoroethylene) (PTFE).

The MPS and CRAMPS experiments have been discussed theoretically in chapters two and four, and simple examples given. The purpose of this investigation is to demonstrate the further resolution of chemical shift data which can be obtained when the CRAMPS experiment is applied to fluoropolymer systems. The first example which will be considered is that of poly(chlorotrifluoroethylene) (Kel-F). The spectra for 300 mesh Kel-F are shown in Figure 6.30. The multiple pulse static spectrum is shown in 6.30a, exhibiting a non-axially symmetric lineshape. The resolution of two spectral features upon rotation of the sample is shown in 6.30b and 6.30c where the spinning rate has roughly doubled respectively. The inset in 6.30c shows the central features as the spectrum is moved onto resonance, for best resolution. Two absorbtion lines are resolved which exhibit an intensity ratio of 2:1 when the side band intensities are considered. The chemical shift values may be explained if the Kel-F is considered in the staggered conformation shown in the Newman projection in Figure 6.30. In this form the $-CF_2-$fluorine nuclei (labelled b) would experience significant deshielding as a result of proximity to the chlorine nucleus.

Figure 6.30: Fluorine-19 Spectra of Kel-F

16 μs cycle time, 32 transients, 30 s recycle delay

a) Static MPS

b) CRAMPS (MAR 1.5 kHz)

c) CRAMPS (MAR 3.0 kHz)

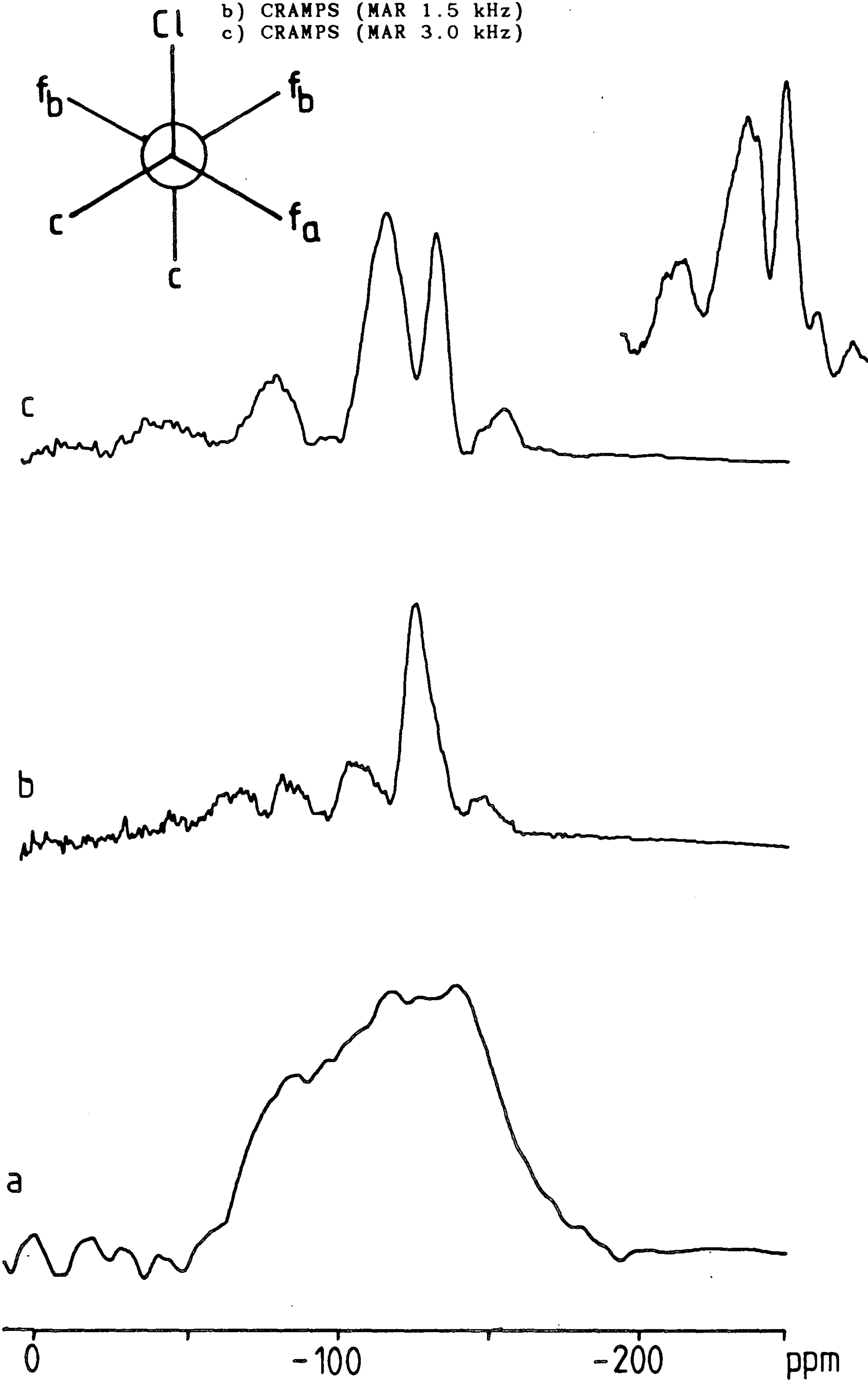

It is not surprising tha the -CF_2- resonance exhibits a spinning sideband pattern, since the chlorine position,relative to the two -F_b nuclei, would also restrict the motion of these nuclei, and impose anisotropy upon their orientation. The -$CClF_a$- fluorine-19 resonance will experience a chemical shift to low frequency as a result of shielding from the increased electron density arising from the chlorine nucleus, through the chlorine-carbon-fluorine bond, but would have no restriction upon its motion or orientation as a result of direct coupling. Given this conformation the chemical shifts of -90 ppm and -120 ppm for the -CF_2- and -CClF- resonance assignments are quite reasonable.

The fluorine-19 solid state nmr spectrum of poly(tetrafluoroethylene) (PTFE) is shown in figure 6.31. PTFE is a long chain polymer which possesses partial orientation when manufactured by an extrusion process. The MPS spectrum is shown in 6.31a, and exhibits an approximately axially symmetric powder pattern. From comparison with lineshape simulations[120a] this spectrum appears to exhibit crystalline character. Upon magic angle rotation, and application of the multiple pulse sequence, two environments are observed at -116.3 and -123.1 ppm. The molecular weight of this polymer is of the order of several tens of thousands, so it is not surprising that no end groups are observed (-C-CF_3 $\delta \simeq -80$ ppm). The region where the peaks are observed is correct for -CF_2- absorbance.

Figure 6.31: Fluorine-19 Spectra of PTFE

16 μs cycle time, 32 transients, 30 s recycle delay

a) static MPS

b) CRAMPS MAR at 3.5 kHz

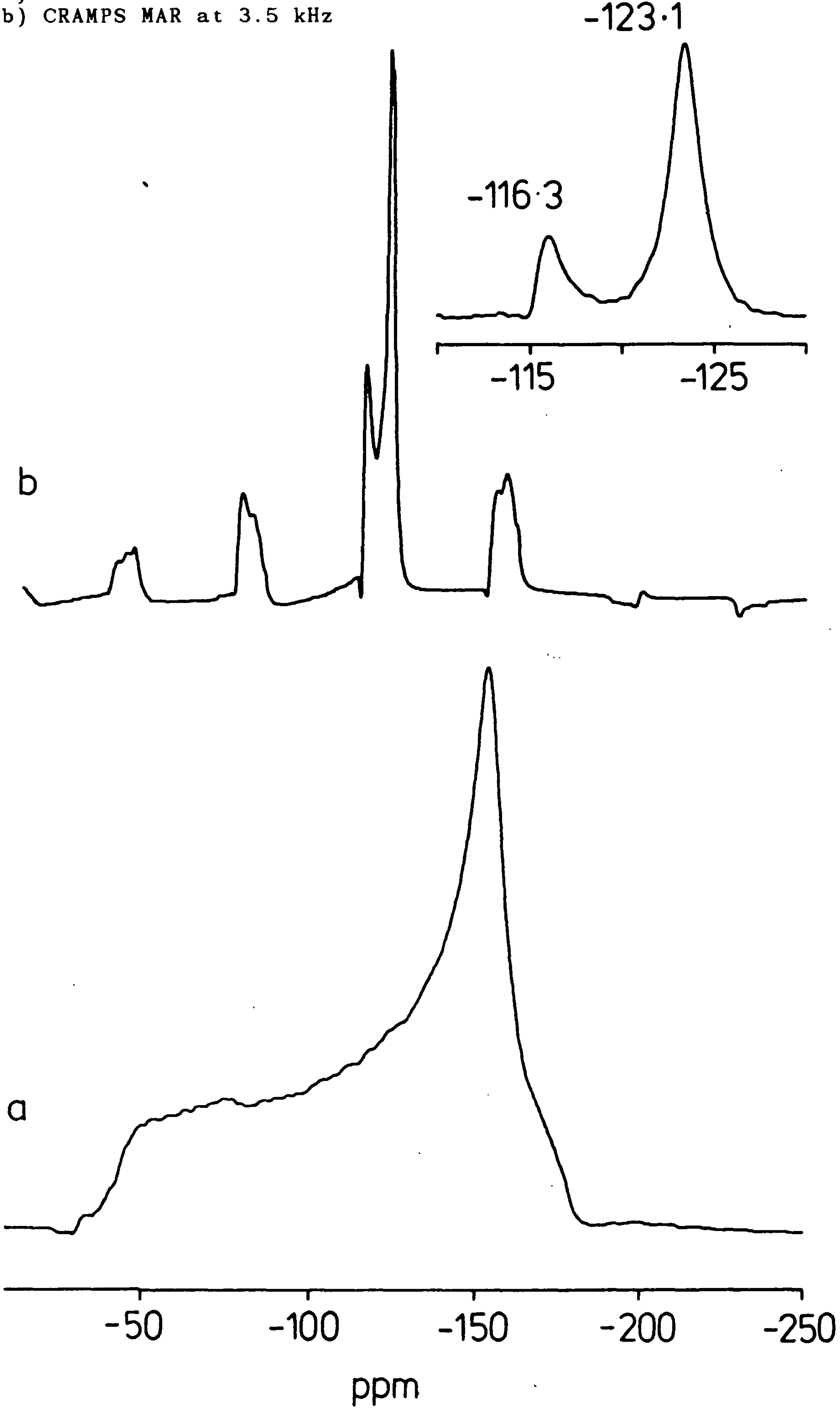

The appearance of two $-CF_2-$ environments is not a result of mixed amorphous and crystalline region $-CF_2-$ groups since it has been shown that this should be easily discernible in the static spectrum,[120] giving a chemical shift difference of approximately 40 ppm between amorphous and crystalline environments.

The differentiation between amorphous and crystalline regions by the MPS experiment can be demonstrated by the copolymerization of PTFE with another perfluorinated monomer. The comonomer used in the following spectra incorporates a bulky side group into the PTFE chain. Figure 6.32 shows the static MPS spectra for the three PTFE copolymers, with the PTFE:comonomer ratio shown. The physical properties of these copolymers change coherently with the ratios. The 23:1 ratio copolymer resembles a gum, similar to that observed with the virgin PTFE. With increasing comonomer content the copolymer becomes a granular amorphous powder. These macroscopic observations suggest that the side groups are destroying any chain alignment which was occurring as a consequence of the manufacturing process. The static fluorine-19 MPS spectra of Figure 6.32 exhibit increasing contributions to the lineshape at high frequency indicating a greater amorphous content to the copolymer constitution.

The CRAMPS spectra for these copolymers are shown in Figure 6.33. What is shown is the central region where the two $-CF_2-$ features are found. No other absorbances were observed in any of the copolymers.

Figure 6.32 : PTFE COPOLYMERS

Fluorine-19 Multiple Pulse Spectra of PTFE Copolymer
16 μs cycle time, 32 transients, 30 s recycle delay

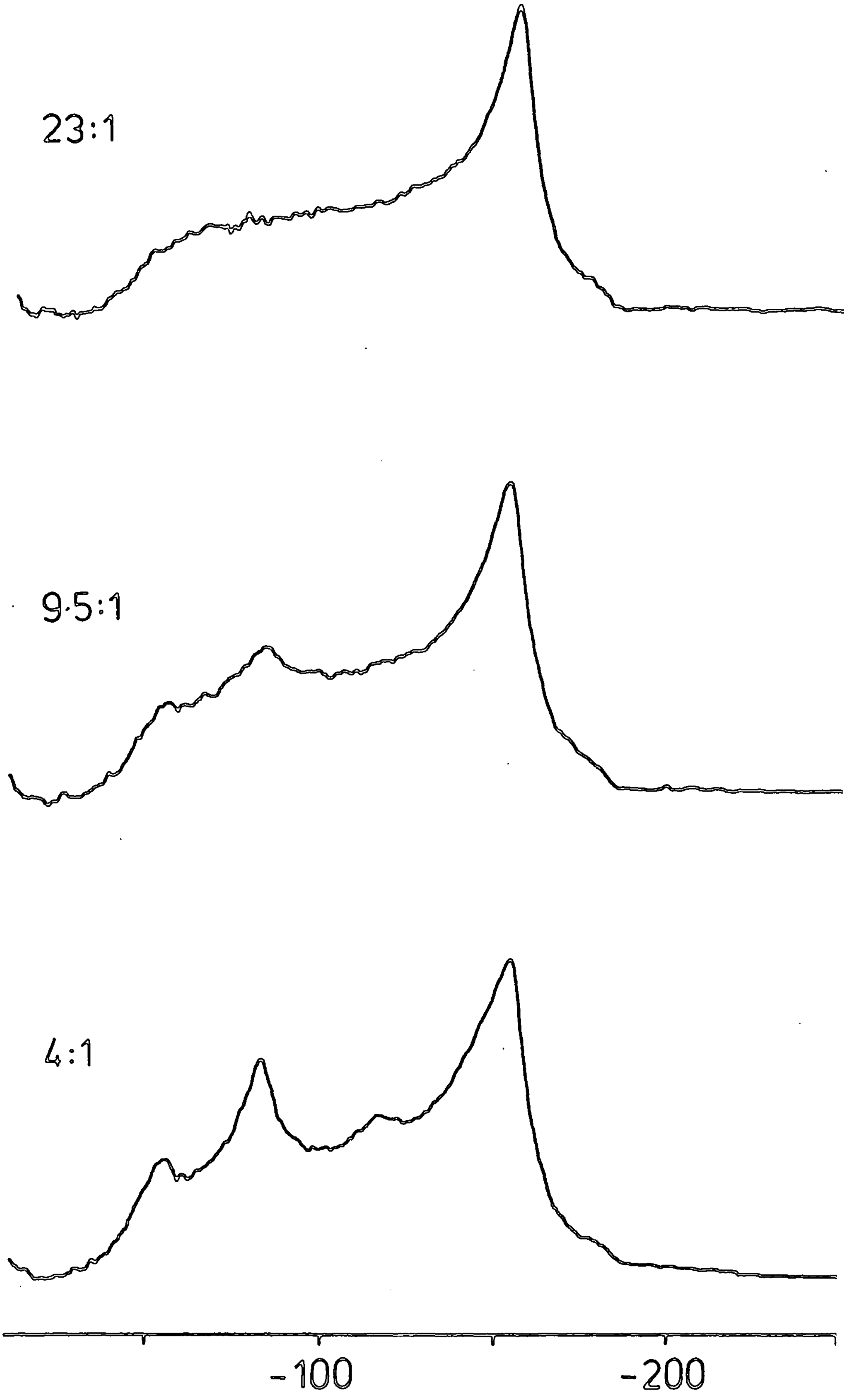

Figure 6.33: Fluorine-19 CRAMPS Spectra of PTFE Copolymers

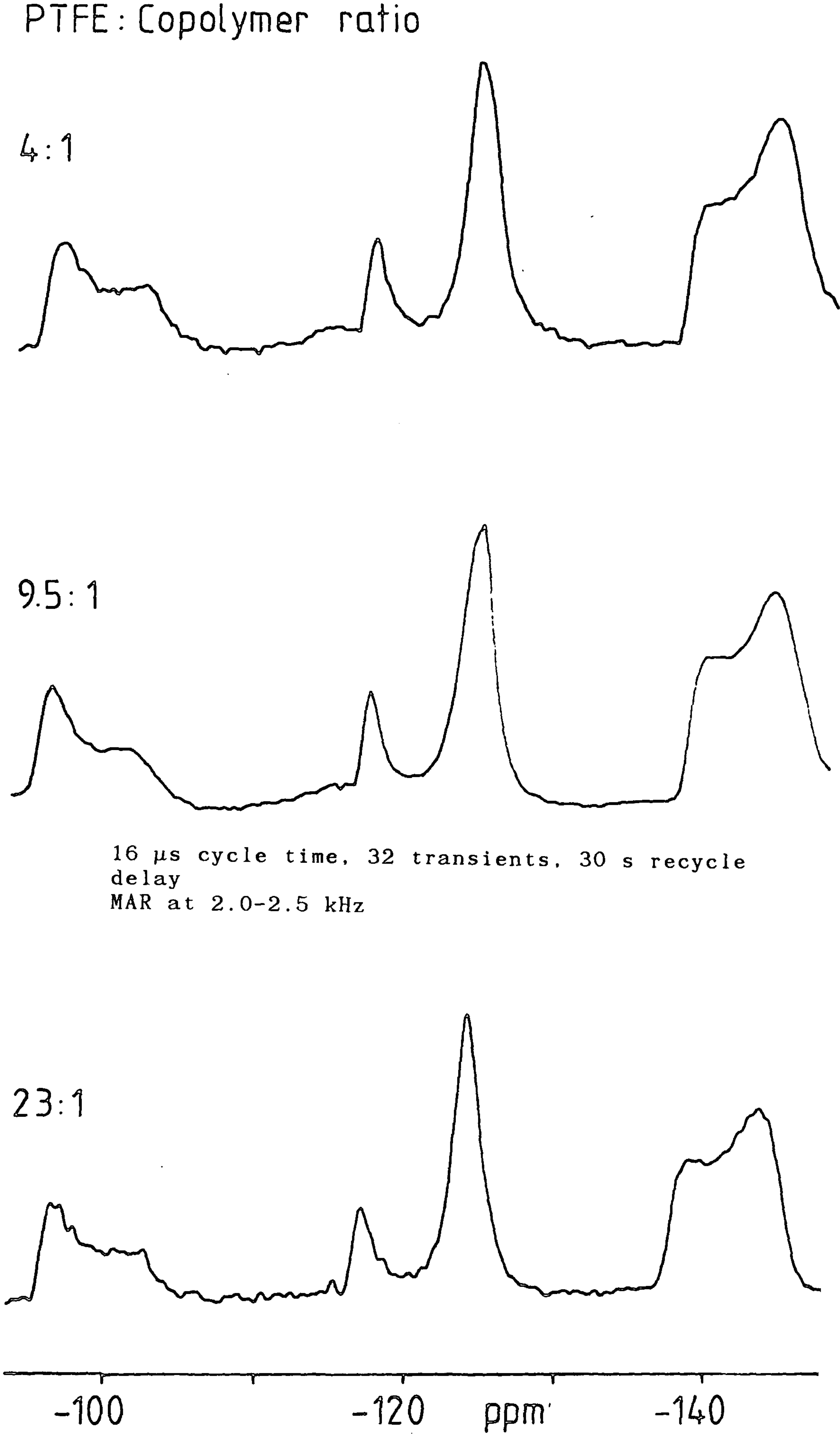

16 μs cycle time, 32 transients, 30 s recycle delay
MAR at 2.0-2.5 kHz

Close scrutiny of the central regions indicates that there is no change in the spectra between the three copolymers, and in fact, comparison with the virgin PTFE (Figure 6.31) shows no difference either. This is perhaps not surprising since the population of -CF- and $-CF_3$ groups present for the given PTFE: comonomer ratios would be very low, making observation difficult. It would seem reasonable to conclude that this is because the CRAMPS spectra presents only the isotropic average of the shielding tensors. The artifacts present in the static spectra of Figure 6.32 represent anisotropic contributions to the lineshape arising from the formation of local regions in the copolymer where the orientation is dictated by the comonomer sidegroups instead of the PTFE chain. This would explain the macroscopic properties observed, and the characteristics of the static spectra. In this example the CRAMPS experiment, when use in conjunction with the static MPS experiment, allows differentiation between anisotropic and local order crystallinity contributions to a polymer's spectral and physical character. It should be noted that no explanation can be offered for the observation of two $-CF_2-$ environments. Perhaps this is a product of the manufacturing process, which aligns the PTFE chains such that there are two $-CF_2-$ environments. Further experiments are necessary in order to answer this question.

In conclusion the fluorine-19 CRAMPS experiment has been shown to be a sensitive method of analysis to differentiate between isotropically different shielding environments. When used in conjunction with the static multiple pulse experiment greater insight can be gained by the different information offered by the two experiments. The examples shown here illustrate, rather graphically, that it is very dangerous to rely on any single method of analysis.

CHAPTER SEVEN

CONCLUSIONS AND SUGGESTIONS OF FUTURE INVESTIGATIONS

"My salad days, when I was green in judgement".
W. Shakespeare

The purpose of the following text is to lend some form of poetic closure to the investigations presented in the body of this thesis. The adage that the measure of a good answer lay in how many new questions arise as a result appears to have been fulfilled here. This is an attempt to briefly address some of those questions in light of the answers presented in this thesis.

In chapters three and four the experimental and theoretical aspects of the CRAMPS experiment have been discussed. The critical criteria for implementing this technique have been presented, and simple examples have been shown which demonstrate the resolution obtained at 4.7 Tesla. In chapter six this method has been applied to a variety of inorganic, organic semi-crystalline, and polymer systems. It has been shown that, as a complimentary method, this experiment can generate data, which is unobtainable by conventional methods of analysis. In all the systems investigated the clear resolution of chemically shifted environments by the CRAMPS method has provided fresh analytical evidence which has been used in support of conclusions drawn upon the structure or behaviour of the systems investigated..

In general, there are some obvious experiments which would be an interesting refinement upon these CRAMPS investigations. For instance, measuring the $T_1, T_{1\rho}$ under multiple pulse decoupling conditions and CRAMPS conditions will allow separation of bulk and site specific relaxation behaviour. Implimenting the windowless pulse sequences mentioned in chapter four is a logical step which will allow an increase in effective decoupling while working at lower power levels. Both these suggestions require a more complex pulse programmer than that which was available for this research.

The experimental hardware might be developed such that variable temperature capabilities are added. This would be widely applicable to the study of molecular motion in catalysis and polymer systems since, in many of these industrial systems, the behaviour over a temperature range is more significant than the behaviour at any single temperature. Further development might be the addition of a second, high frequency, channel to the probe. If approximately 30 db separation can be achieved between the fluorine-19 and proton channels a whole new range of experiments becomes available to the spectroscopist. For example, the investigation of heterogeneous polymer systems becomes possible using a SP, ^{19}F ; MPS, ^{1}H double resonance experiment. Preliminary work has indicated that a $\lambda/4$ rejection line yields better behaviour, for isolating the two channels, in combination with possible inductive/capacitive networks which might be employed. There are a number of obvious configurations which should be explored.

Much of the difficulties encountered with the probe construction, configured for the experiments discussed in this thesis, were involved with reducing spurious signals arising from the materials of construction. Ceramic materials, in particular 'MACOR', seem to offer advantages in this area and exhibit stable thermal properties.

An experimental probe is currently undergoing tests and development.

In chapter five quadrupolar nuclei have been discussed. The nature of the behaviour of the sodium nucleus has been investigated in several well characterized systems. The cross-polarization experiment has been implimented, and the steric selectivity of the experiment exploited to differentiate between sodium environments. This experiment merits development in other quadrupolar nuclei where similar relationships may be used to selectively characterize different nuclear environments. Multiple component cross-relaxation behaviour has been observed during a variable contact cp experiment. Relaxation experiments have shown that this is probably driven by a thermodynamic inequilibrium, between the central and higher order quadrupole transitions, as a consequence of the polarization transfer mechanism. This relationship appears to be a 'high field' analogy to the 'low field', NQR level crossing experiments, which have been discussed by Professor J. Smith (University of London). This would seem to offer a simpler method of measuring exchange between energy levels of a quadrupolar nucleus or information transfer with spin-$\frac{1}{2}$ nuclei, when compared with field cycling NQR. Further theoretical consideration of this phenomenon, and careful experiments, are required to more fully document the nature of this relationship which, in this thesis, is noted only in passing.

Chapter six has illustrated the utility of the methods developed in earlier chapters. Application of solid state NMR to metasilicates has shown that there are anomalies in the correlation between rings and chain polymorphs, and the subsequent silicon-29 chemical shift of the silicate anion. This has been explained in terms of cation size, valence and electronegativity, which dictate the polymorph configuration. Hydrated sodium silicates have also been investigated using silicon-29 and sodium-23 NMR. The results indicate that the sodium-23 chemical shift is sensitive to differences in coordination state. The sodium chemical shift was found to change coherently with the silicon-29 chemical shift and the $Na_2O:SiO_2$ ratio. This indicates that different silicate anion:sodium species are present in the solid. The chemical shifts of both nuclei are observed to alter shielding smoothly, without discrete steps. This suggests that the systems at any one ratio are composed of a weighted distribution of species. The average chemical shift of the distribution is controlled by the stoichiometry of the reaction mixture. It seems likely that this distribution was a result of the presence of water in the system, which allows formation of a variety of hydrated isomorphs, which blur the singularities which would be expected in an anhydrous system. Further variable temperature experiments would indicate the predominant species (by chemical shift assignment) as dehydration occurs.

A series of layer silicates have also been studied. Silicon-29, sodium-23, and proton NMR experiments have produced data which has allowed construction of layer configuration projections. Further studies require extensive synthetic work to investigate the mechanism of layer building and the eventual formation of network silicates. In further investigations network silica polymorphs have been shown to possess at least two proton and silicon environments. The application of an array of solid state NMR methods has allowed construction of a model describing the diffusion proccessess operating in these polymorphs.

Sodium-23 and proton CRAMPS experiments have been applied to a series of crown ethers. The sodium chemical shift and lineshape has been shown to be sensitive to site symmetry and extent of coordination to the polyether ligands. The proton data are diagnostic of the complex constituents, and in one case differentiate between polyether ring conformers. This data allows insight into the insertion mechanism of the crown ether-cation complexation, and indicates that the associated anion is relatively unimportant to the nature of the ligand-cation bond.

The fluoropolymer systems investigated demonstrate what information can be obtained when the CRAMPS experiment is applied to a number of industrially important polymers. Surprisingly two -CF_2- environments have been found in PTFE. Further investigation,focusing about the synthetic procedure, are necessary to establish if this is simply a consequence of the polymers manufacture. The combination of the MPS and CRAMPS experiments provides a method of discerning the nature of contributions observed in a polymer. Further experiments would include variable temperature measurements, and T_1,$T_{1\rho}$ measurements under MPS and CRAMPS conditions.

In conclusion, the Solid State NMR methods developed in this thesis have been applied to a variety of 'difficult' chemical systems. They have been shown to allow conclusions to be drawn upon data which was unaccessible by other methods. This fact alone justifies their development.

- now do you understand?
- no, but I'm confused on a much higher plane.

REFERENCES

CHAPTER 2

1. Stern O., Gerlach W., Ann. Physik., 74, 673 (1924)

2. Van Vleck J.H., Phys. Rev., 74, 1168 (1948)

3. Bloch F., Hansen W.W., Packard M., Phys. Rev., 70, (1946)

4. Proctor W.G., Yu F.C., Phys. Rev., 77, 717 (1950)

5. Mehring M., Principles of High Resolution in N.M.R. in Solids, Springer Verlag, Berlin, 2nd ed., (1983)

6. Ref. 5 page 20.

7 Andrew E.R., Phil. Trans. R. Soc. Lond., A299, 505 (1981)

8. Andrew, E.R., Prog. in N.M.R. Spectroscopy, 8, 1 (1971)

9. Sakurai J.J., Modern Quantum Mechanics, Benjamin Cummings, California, (1985)

10. Poole C.P., Farach H.A., The Theory of Magnetic Resonance, Wiley Interscience, N.Y., (1972)

11. Abragam A., The Principles of Nuclear Magnetism,Oxford Press (1961) page 166

12. See ref. 9 page 163

13. Haeberlen U, High Resolution NMR in Solids Selective Averaging, Advances in Magnetic Resonance, Supplement 1, Academic Press, N.Y. (1976)

14. Bloembergen N., Purcell E.M., Pound R.V., Phys. Rev.,73, 679 (1948)

15. Van Vleck J.H., Phys. Rev., 74, 1168 (1948)

16. See ref. 11 page 104

17. Andrew E.R., Bradbury A., Eades R.G., Nature, 182, 1659 (1958), 183, 1802 (1959)

18. Lowe I.J., Phys. Rev. Lett., 2, 285 (1959)

19. Waugh J.S., Huber L.M., Haeberlen U., Phys. Rev. Lett. 20, 180 (1968)

20. Waugh J.S., Maricq P.M., Cantor R.J., J. Magn. Res., 29, 183 (1978)

21. Ostroff E.D., Waugh J.S., Phys. Rev. Lett., 16, 1097 (1966)

22. Mansfield P., Ware D., Phys. Lett., 22, 133 (1966)

23. See ref. 5, pages 63-127

24. Maricq P.M., Waugh J.S., J. Chem. Phys., 70, 3300 (1979)

25. Herzfeld J., Berger A.J., Chem. Phys., 73, 6021 (1980)

26. Slichter C.P., Principles of Magnetic Resonance,(Harper Row, New York)2nd edition pages 287-290 (1963)

27. Cunningham A.C., Day S.M., Phys. Rev., 152, 287 (1966)

28. Ganapathy S., Schramm S., Oldfield E., J. Chem. Phys., 77(9), 4360 (1982)

29. Das T.P., Hahn E.L., Solid State Physics, Supplement 1, pages 7-26 (1958)

30. Cohen M.H., Reif F., Solid State Physics, 5, 321 (1957)

31. Ref. 11 page 233

32. Oldfield E., Kinsey R.A., Smith K.A., Nichols J.A., Kirkpatrick R.J., J. Magn. Res., 51, 325 (1983)

33. Walker R.D., Gerstein B.C., Phys. Rev. B., 31, 3167 (1985)

34. Abragam A., Chapellier M., Jacquinot J.F., Goldman M., J. Magn. Res., 10(3), 322 (1973)

35. Yannoni C.S., Bleich H.E., J. Chem. Phys., 55, 5406 (1971)

36. Kohl J.E., Semack M.G., White D., J. Chem. Phys., 69(12), 5378 (1978)

37. Zilm K.W., Cohlin R.T., Michl J., Grant D.M., J.A.C.S., 102(22), 6672 (1980)

38. Pines A., Gibby M.S., Waugh J.S., J. Chem. Phys., 59, 569 (1973)

39. Mehring M., Pines A., Rhim W.K., Waugh J.S., J. Chem. Phys., 54, 3239 (1971)

40. Schaefer J., Stejskal E.O., Buchdal R., Macromolecules, 10, 384 (1977)

41. Hartman S.R., Hahn E.L., Phys. Rev., 128, 2042 (1964)

42. Wolf D., Spin-Temperature and Nuclear-Spin Relaxation in Matter: Basic Principles and Applications, Oxford Univ. Press, (1979)

43. MacArthur D.A., Hahn E.L., Walstead R.E., Phys. Rev., 188, 609 (1969)

44. Abragam A., Proctor W.G., Phys. Rev., 109, 1441 (1958)

45. Schumacher R.T., Phys. Rev., 112, 837 (1958)

CHAPTER 3

1. Pulsed N.M.R. Spectrometer CXP Instruction Manual. Bruker Spectrospin Ltd.

2. Hoult D.I., Progress in N.M.R. Spectroscopy, 12, 41 (1978)

3. Roeder S.B., Fukushima E., "Experimental Pulse .M.R., a Nuts and Bolts Approach". Addison-Wesley, London, (1981)

4. Rhim W.K., Elleman D.D., Vaughn R.W., J. Chem. Phys., 59, 3740, (1974)

5. Doty F.D. Ellis P.D., Rev. Sci. Instrum., 52(12), 1868 (1981)

6. Vaughn R.W., Elleman D.D., Stacey L.M., Rhim W.K., Lee J.W., Rev. Sci. Instrum., 43(9), 1356 (1972)

7. Pembleton R.G., Ryan. L.M., Gerstein B.C., Rev. Sci. Instrum., 48(10), 1286 (1977)

8. American Radio Relay League 1985 Handbook, 62 ed. 1985

9. Fry C.G., Iwamiya J.H., Apple T.M., Gerstein B.C., J. Magn. Res., 63, 214 (1985)

10. Gone Fishing

11. Stejskal E.O., Schaefer J., J. Magn. Res., 18, 560 (1975)

12. Haeberlen U., Tegenfeldt N., J. Magn. Res., 36, 453 (1979)

13. Nesbitt G.J., "N.M.R. of Abundant Spins in Solids" N.M.R.D.G. London 1985

14. Vold R., Waugh J., Klein M.P., Phelps D.E., J. Chem. Phys., 48, 3831 (1968)

15. Sass M., Ziessow D., J. Magn. Res. 25, 263 (1977)

16. Tycko R., Schneider E., Pines A., J. Chem. Phys., 81(2), 680 (1984)

17. Caravatti P., Bodenhausen G., Ernst R.R., J. Magn. Res.,55, 88 (1983)

18. Englehardt G., Zeigan D., Hoebbel D., Samoson A., Lippmaa E., Z. Chem., 22, 314 (1982)

19. Lippmaa E., Grimmer A.R., Englehardt G., Magi M., Samoson A., J. Am. Chem. Soc., 102, 4889 (1981)

20. Fechner E., Muller D., Haubenreißer U., Z. Chem., 24, 194 (1984)

21. Templeman G.J., van Geet A.L., J. Am. Chem. Soc., 94, 5578 (1972)

22. Frye J.S., Maciel G.E., J. Magn. Res., 48, 125 (1982)

23. Hilgenfeld R., Saenger W., Topics in Current Chemistry, 101, 1-82 (1981) Springer Verlag.

24. Dale J., Kristiansen P.O., Acta. Chem. Scand., 26, 1471 (1972)

25. Brauer G., Handbook of Preparative Inorganic Chemistry, Vol.1, 2nd ed., Academic Press, 1960

CHAPTER 4

1. Pake G.E., J. Chem. Phys., 1, 327 (1948)
2. Hamilton W.C., Ibers J. A., Hydrogen bonding in Solids, W. A. Benjamin, 1968
3. Lee J.W., Goldberg W.I., Phys Rev., 14, A1261 (1965)
4. Waugh J.S., Huber L.M., Haeberlen U., Phys. Rev. Lett., 20, 180 (1968)
5. Haeberlen U., Waugh J.S., Phys. Rev., 175, 453 (1968)
6. Mehring M., Waugh J.S, Phys. Rev., B5, 3459 (1972)
7. Ryan L.M., Taylor R.E., Paff A.J., Gerstein B.C., J. Chem. Phys. 72(1), 508 (1950)
8. Gerstein B.C., Phil. Trans. R. Soc. Lond., A299, 477 (1981)
9. Taylor R.E., Pembleton R.G., Ryan L.M., Gerstein B.C., J. Chem. Phys. 71, 4541 (1979)
10. Scheler G., Haeberlen U., Rosenberger H., J. Magn. Res., 44, 134 (1981)
11. Rosenberger H., Sonnenberger R., Scheler G., Haubenreisser U., Uhlich T., Fourth Specialized Colloque Ampere, Leipzig, 1979
12. Rosenberger H., Ernst H., Scheler G., Junger I, Sonnenberger R., Z. Phys. Chemie., 263, 846 (1982)
13. Nesbitt G.J., Solid State Investigations of High γ Nuclei: Proton and fluorine-19, Royal Society of chemistry NMR D.G., London, 1985
14. Harris R.K., Jackson P., Nesbitt G.J., Say B.J., Proceedings of the BRSG Meeting, Oxford, 1985
15. Haeberlen U., High Resolution NMR in Solids: Selective Averaging, Academic Press, 1979
16. Mansfield P., J. Phys., C4, 1444 (1971)
17. Haeberlen U., Waugh J.S., Phys. Rev., 175, 453 (1968)
18. Magnus W., Commun. Pure Appl. Maths., 7, 649 (1954)
19. Rhim W.K., Ellemean D.D., Vaughn R.W., J. Chem. Phys., 59(5), 3740, (1973)
20. Burum D.P., Rhim W.K., J. Chem. Phys., 71(2), 9446 (1979)

21. Vaughn R.W., Elleman D.D., Stacey L.M., Rhim W.K., Lee J.W., Rev. Sci. Instrum., 43, 1356 (1972)

22. Garroway A.N., Mansfield P., Stalker D.C., Phys. Rev. B., 11 121 (1975)

23. Haubernreisser U., Schnabel B., J. Magn. Res., 35, 175 (1979)

24. Dohler H., Dohler T., Fenzke D., Ann. der Physik., 233, (1980)

25. Burum D.P., Bruker Application Note BII-1

26. Burum D.P., Linder M., Ernst R.R., J. Magn. Res., 44, 173 (1981)

27. Anca R., Carrera S.M., Bianca S.G., Acta. Cryst., 23, 1010 (1967)

28. Sim G.A., Monteath Robertson J., Goodwin T.H., Acta. Cryst., 8, 157 (1954)

29. Mooney E.F., An Introduction to ^{19}F NMR Spectroscopy, Heyden and Son, 1970

30. Lawrenson I.J., J. Chem. Soc., 1117 (1965)

31. Sheppard W.A., Sharts C.M., Organic Fluorine Chemistry, W.A. Benjamin Inc., New York, 1969

32. Tatlow J.C., Endeavour, 22, 89 (1963)

CHAPTER 5

1. Kellog J.M.B., Rabi I.I., Ramsey N.F., Phys. Rev., 57, 677, (1940)

2. Pound R.V., Phys. Rev., 79, 685 (1950)

3. Fyfe C.A., Gobbi G.C., Hartman J.S., Leninski R.E., O'Brien J.H., J. Magn. Res., 47, 168 (1982)

4. Cohen C.O., Reif F., Solid State Phys., 5, 321 (1957)

5. Behrens H.J., Schnabel B., Physica, 114B, 185 (1982)

6. Freude D., Haase J., Klinowski J., Carpenter T.A.,, Ronikier G., Chem. Phys. Lett., 119(4), 365 (1985)

7. Samoson A., Lippmaa E., Chem. Phys. Lett., 100(3), 205 (1983)

8. Samoson A., Chem. Phys. Lett., 119(1), 29 (1985)

9. a) Samoson A., Kundla E., Lippmaa E., J. Magn. Res., 49,350 (1982)
   b) Kundla E., Samoson A., Lippmaa E., Chem. Phys. Lett., 83(2), 229 (1981)

10. Lippmaa E., Samoson A., Magi M., J. Am. Chem. Soc., 108, 1730 (1986)

11. Nagy J.B., Gabelica Z., Debras G., Derouane E.G., Gilson J.P., Jacobs P.A., Zeolites, 4, 133 (1984)

12. Samoson A., Lippmaa E., Phys. Rev. B., 28(11), 6567 (1983)

13. Abragam A., Principles of Nuclear Magnetism, Oxford University Press, page 233, 1961

14. Volkoff G.M., Can. J. Phys., 31, 820 (1953)

15. Poole C.P., Farach H.A., The Theory of Magnetic Resonance, Wiley Interscience, page 25, 1972

16. Ganapathy S., Schramm S., Oldfield E., J. Chem. Phys., 77(9), 4360 (1982)

17. Walker R.D., Gerstein B.C., Phys. Rev. B., 31, 3167 (1985)

18. Weber M.J., Hahn E.L., Phys. Rev., 120, 365 (1960)

19. Bloom M., Hahn E.L., Herzog B., Phys. Rev., 97, 1699 (1955)

20. Abragam see Ref 1. page 257

21. Schmidt V.H., Ampere Int. Sum. Schl. II, Yugoslavia, 1971

22. Cunnungham A.C., Day S.M., Phys. Rev. 152, 287 (1966)

23. Samoson A., Lippmaa E., Phys. Rev. B., 28(11) 6567 (1983)

24. Hartman S.R., Hahn E.L., Phys. Rev., 128, 2042 (1962)

25. Lurie F.M., Slichter C.P., Phys. Rev., 133, A1108 (1964)

26. Ramsey N.F., Pound R.V., Phys. Rev., 81, 278 (1951)

27. Redfield A.G., Phys. Rev. 130, 589 (1963)

28. Blinc R., Adv. Nuc. Quad. Res., 2, 71 (1975)

29. Becker K.D., Z. Naturforsch., 37A, 697-705 (1982)

30. Edmonds D.T., Phys. Rep., 29C, 233 (1977)

31. McArthur D.A., Hahn E.L., Walstead R., Phys. Rev., 188, 609 (1969)

32. Harris R.K., Mann B.E., N.M.R. and the Periodic Table, Academic Press, 1978

33. Ellaboudy A., Dye J.L., J. Magn. Res., 66, 491 (1986)

34. Soldate A.M., J. Am. Chem. Soc., 69, 987 (1947)

35. Bray P.J., Silver A.H., Bull. Am. Phys. Soc., 1(2), 323 (1956)

36. Strukturbericht III, 456, 1933-1935

37. Haussubl S., Zeit. fur. Kris., 116, 371 (1961)

38. Lipson H., Proc. Roy. Soc.(London), A151, 347 (1935)

39. Minder W., Z. Krist., 92A, 301 (1935)

40. Structure Reports vol 11, 429-432 (1947)

41. Wyckoff R.W.G., Crystal Structures, Vol. 3, 2nd ed., Interscience Publishers, 864-867 (1965)

42. Giese R.F., Can. Mineral., 9(4), 573 (1968)

43. Giacovazzo C., Menchetti S., Scordari F., Amer. Miner. 58, 523 (1973)

44. Cuthbert J.D., Petch H.E., J. Chem. Phys., 38, 1912 (1963)

45. Cuthbert J.D., Petch H.E., J. Chem. Phys., 39, 1247 (1963)

46. Christ C.L., Garrels R.M., Amer. J. Sci., 257, 516 (1959)

47. Morimoto N., Structure Reports, 20, 376 (1956)

48. Dharmatti S.S., Iyer S.A., Vijayaraghavan R., J. Phys. Soc. Japan, 17, 1736 (1962)

CHAPTER 6

1. Lippmaa E., Magi M., Samoson A., Engelhardt G., Grimmer A.R., J. Am. Chem. Soc., 102, 4889 (1980)

2. Grimmer A.R., Radeglia R., Chem. Phys. Lett., 106(4), 262 (1980)

3. Grimmer A.R., Peter R., Fechner E., Molgedy G., Chem. Phys. Lett., 77(2), 331 (1981)

4. Kirkpatrick R.J., Oldfield E., Smith K.A., Henderson D.M., Amer. Miner., 68, 1206 (1983)

5 Thomas J.M. Klinowski J., Adv. in Catalysis, 33, 200 (1985) and references contained within

6. Carpenter M.A., Materials Science Forum, 7, 19 (1986)

7a. Kirkpatrick R.J., Kinsey R.A., Smith K.A., Henderson D.M., Oldfield E., Amer. Miner., 70, 106 (1985)

7b. Yang W.H., Kirkpatrick R.J., Henderson D.M., Amer. Miner., 71, 712 (1986)

8. Basler W., Colloids and Surfaces, 12, 59 (1984)

9. Scholle K.F.M.G.J., Veeman W.S., Post J.G., van Hooff J.H.C., Zeolites, 3,20 (1983)

10. Nondek L., J. Chromatog., 238, 264 (1982)

11. Rosenberger H., Ernst H., Scheler G., Junger I., Sonnenberger R., Z. Phys. Chemie., Leipzig, 263, 846 (1982)

12. Griggs D., Geophys. J., 14, 19 (1967)

13. Burnham C.W., Davis N.F., Am. J. Sci., 270, 54 (1971)

14. Liebau F., Structural Chemistry of Silicates, Springer-Verleg, New York (1985)

15. Liebau F., Handbook of Geochemistry, Springer-Verleg, New York (1972)

16. Prewitt C.T., Peacor D.R., Amer. Miner., 49 1527 (1964)

17. Burnham C.W., Science, 154, 513 (1966)

18. Takeuchi Y., Yamanaka T., Amer. Miner., 61, 229 (1976)

19. Deotter C., Handbuch der Mineralchemie, II(1), 446, Verlag von Theodor Steinkopff, Dresden and Leipzig (1918)

20. Harris R.K., Newman R.H., Org. Mag. Res., 9(7), 426 (1977)

21. McDonald W.S., Cruikshank D.W.J., Acta Cryst., 22, 37 (1967)

22. Große H.P., Tillmanns E., Cryst. Struct. Comm., 3, 603 (1974)

23. Vincent M.G., Jeffery J.W., Acta. Cryst., A35, 938 (1979)

24. Yamanaka T., Mori H., Acta. Cryst., B37, 1010 (1981)

25. Machida K., Adachi G., Shiokawa J., Bull. Chem. Soc. Jpn., 55, 2854 (1982)

26. Moir G.K., Gard S.A., Glasser F.P., Zeit. fur Kryst., 114 437 (1975)

27. Dornberger-Schiff K., Soviet Physics: Crystallography, 6, 694 (1962)

28. Sasaki S., Takeuchi Y., Fujino K., Akimoto S.I., Z. Krystallogr., 158, 279 (1982)

29. Magi M., Lippmaa E., Samoson A., Engelhardt G., Grimmer A.R., J. Phys. Chem., 88, 1518 (1984)

30. Lippmaa E., Magi M., Samoson A., Engelhardt G., Grimmer A.R., J. Am. Chem. Soc., 102, 4889 (1980)

31. Smith K.A., Kirkpatrick R.J., Oldfield E., Henderson D.M., Amer. Miner., 68, 1206 (1983)

32. James N., Oldfield E., J. Am. Chem. Soc., 107, 6769 (1985)

33. Pauling L., The Nature of the Chemical Bond, Cornell Univ. Press, Ithica (1960)

34. Brown I.D., Shannon R.D., Acta Crystallogr., A29, 266 (1973)

35a. Liebau F., 'Structure and Bonding in Crystals', M. O'Keefe, A. Naurotski(eds.), vol II, Academic Press, London 1971 (1981)

35b. Parker S.C., Catlow C.R.A., Cormack A.N., Acta Cryst., B40, 200 (1984)

36. Refence 14, pages 191-206

37a. Prince E., Amer. Miner., 56, 1243 (1971)

37b. Chao G.Y., Amer. Miner., 56, 1235 (1971)

38. Lange H., von Stakelberg M., Z. Anorg. Chem., 256, 273 (1948)

39. Grand A., Piz M.M., Acta Cryst., 5, 837 (1952)

40a. Liebau F., Acta Cryst., 14, 395 (1961)

40b. Pant A.K., Cruikshank D.W.J., Acta Cryst., B24, 13 (1968)

41. Grand A., Bull. Soc. franc. Miner. Crist., 77, 775 (1954)

42. Jamieson P.B., Dent-Glasser L.S., Acta Cryst., 20, 688 (1966)

43. Jamieson P.B., Dent-Glasser L.S., Acta Cryst., 20, 373 (1966)

44. Jamieson P.B., Dent-Glasser L.S., Acta Cryst., 22, 507 (1967)

45. von Jost K.H., Acta Cryst., 21, 583 (1966)

46a. Williams P.P., Dent-Glasser L.S., Acta Cryst., B27, 2269 (1971)

46b. Warren B.B., Loring A.D., J. Am. Chem. Soc., 18, 269 (1935)

47. Randall J.T., Rooksby H.P., Cooper B.S., Z. Krist., 75, 196 (1930)

48. Backris M., Tomlinson J.W., White J.I., J. Chem. Soc. Faraday Trans., 52, 299 (1956)

49. Seddon E., Tippet E.J., Turner W.E.S., J. Soc. Glass Tech., 16(2), 450 (1932)

50. Preston E., Turner W.E.S., J. Soc. Glass Tech., 16(2), 331 (1932)

51. Huggins M.L., J. Opt. Soc. of America, 30, 420 (1940)

52. de Jong B.H.W.S., Schramm C.M., Parziale V.E., Geochim. et Cosmochim. Acta, 48, 2619 (1984)

53. Grimmer A.R., Magi M., Hahnert M., Stode H., Samoson A., Wieker W., Lippmaa E., Phys. & Chem. of Glass., 25(4), 105 (1984)

54a. Lagaly G., Beneke K., Weiss A., Amer. Miner., 60, 642 (1975)

54b. Lagaly G., Beneke K., Weiss A., Amer. Miner., 60, 650 (1975)

54c. Lagaly G., Adv. Colloid. Interf. Sci., 11, 105 (1979)

55. Beneke K., Lagaly G., Amer. Miner., 62, 763 (1977)

56. Brindley G.W., Amer. Miner., 54, 1583 (1969)

57. McAtee J.L., House R., Eugster H.P., Amer. Miner., 53, 2061 (1968)

58. von Jost K.H. Hilmer W., Acta Cryst., 21, 583 (1966)

59a. Jamieson P.B., Dent-Glasser L.S., Acta Cryst., 20, 373 (1966)

59b. Jamieson P.B., Dent-Glasser L.S., Acta Cryst., 20, 688 (1966)

59c. Jamieson P.B., Dent-Glasser L.S., Acta Cryst., 20, 507 (1967)

60. Williams P.P., Dent-Glasser L.S., Acta Cryst., B27, 2269 (1979)

61. Harris R.K., Nesbitt G.J., Roy. Soc. Seventh Int. Meeting on NMR Spec. Cambridge (1984)

62. Sheppard R.A., Gude A.J., Hay R.L., Amer. Miner., 55, 358 (1970)

63. Johan Z., Maglione G.F., Bull. Soc. Fr. Minerl. Crystallogr., 95, 371 (1972)

64. Iler R.K., J. Colloid. Sci., 19, 648 (1964)

65. Eugster H.P., Science, 157, 1177 (1967)

66. McCulloch L., J. Am. Chem. Soc., 74, 2453 (1952)

67. Beneke K., Lagaly G., Amer. Miner., 68, 818 (1983)

68. Hay R.L., Contrib. Mineral. Petrology, 17, 255 (1968)

69. Annehed H., Falth L., Lincoln F.J., Z. Krist., 159, 211 (1982)

70. Liebau F., Acta Cryst., 14, 395 (1961)

71a. Heidemann D., Grimmer A.R., Hubert C., Starke P., Magi M., Z. Anorg. Allg. Chem., 528, 22 (1985)

71b. Heidemann D., Grimmer A.R., Hubert C., Starke P., Magi M., Z. Anorg, Allg. Chem., 528, 35 (1985)

72. Pinnavaia T.J., Johnson I.D., Lipsicas M., J. Solid State Chem., 63, 118 (1986)

73. Dowty E., Amer. Miner., 65, 174 (1980)

74. Sanz J., Rojo M., Ruiz-Hitzky E., Serrastosa J.M., Revue du Chimie Minerale, 20, 807 (1983)

75. Schweiger W., Heidemann D., Bergk K.H., Revue de Chimie. Minerale, 22, 639 (1985)

76. Mann S., Perry C.C., Williams R.J.P., Fyfe C.A., Gobbi G.C., Kennedy G.J., J. Chem. Soc. Chem. Commun., 168 (1983)

77. Yang W.H., Kirkpatrick R.J., Vergo N., Mettone J., Emilsson T.I., Oldfield E., Meteorites, 21(1), 117 (1986)

78. Thomas J.M., Ganzalez-Calbent J.M., Fyfe C.A., Gobbi G.C., Nicol M., Geophysical Res Lett., 10(1) 91 (1983)

79. Smith J.V., Blackwell C.S., Nature, 303, 223 (1983)

80. Maciel G.E., Sindorf D.W., J. Am. Chem. Soc., 102 (1980)

81. Dupree R., Pettifer R.F., Nature, 308, 523 (1984)

82. Morrow B.A., Cody I.A., Lee L.S.M., J. Phys., 80, 2761 (1976)

83. Hill W., Proc. Geol. Assoc., 22 61 (1911)

84. Washburn E.W., Navias L., J. Am. Ceram. Soc., 5, 565 (1922)

85. Weymouth J.H., Williamson W.O., Miner. Mag., 29, 573 (1951)

86. Jensen A.T., Wohlk C.J., Drenck K., Andersen E.K., Dan. Nat. Inst. Build. Res. Acad. Tech. Sci. Progress Report D1, Copenhagen (1957)

87. Robertson R.H.S., Meldau R., Ber. Dent. Keram. Ges., 29, 27 (1952)

88. Shephard W., Flint: its origins, properties and uses, 32, Faber and Faber (1972)

89. White J.F., Corwin J.F., Amer. Miner., 46 112 (1961)

90. Clarke R.R., Antiquity IX, 33, 38 (1935)

91. Folk R.L., Weaver C.E., Am. J. Sci., 250, 498 (1952)

92. Midgely H.G., Geol. Mag., 138, 179 (1951)

93. Pelto C.R., Am. J. Sci., 254, 32 (1956)

94. Demco D.E., Tegenfeldt J., Waugh J.S., Phys. Rev. B., 11, 4133 (1975)

95. Pederson C.J., J. Am. Chem. Soc., 89, 7017 (1967)

96a. Lehn J.M., Structure and Bonding, 16, 1 (1973) Springer Verlag

96b. Lehn J.M., Structure and Bonding, 16, 71 (1973) Springer Verlag

97a. Weber E., Angew. Chem., 219, 19 (1979)

97b. Hiraoka M., Crown Compounds, their characterization and applications, Elsevier (1982)

98. Midgely D., Quant. Rev., 849 (1975)

99. Strasser B.O., Hellenga K., Popov A.I., J. Am. Chem. Soc., 107, 789 (1985)

100. Phillips R.C., Khazaeli S., Dye J.L., J. Phys. Chem., 89, 606 (1985)

101. Belton P.S., Tanner S.F., Wright K.M., Payne M.P. Trater M.R., Wingfield J.N., J. Chem. Soc. Perkin Trans. II, 1307 (1985)

102. Hanson I.R., Acta Cryst., B34, 1026 (1978)

103. Dobler M., Dunitz J.D., Seiler A.P., Acta Cryst., B30, 2741 (1974)

104. Bush M.A., Truter M.R., J. Chem. Soc. Perkin Trans. II, 341 (1972)

105. Owen J.D., J. Chem. Soc. Dalton Trans., 1066 (1980)

106. Dunitz J.D., Sei ler P., Acta Cryst., B30, 2739 (1974)

107. Parsons D.G., Truter M.R., Wingfield J.N., Inorg. Chimica. Acta., 14, 45 (1975)

108. Parsons D.G., Wingfield J.N., Inorg. Chimica. Acta., 17, L25 (1976)

109. Bloor E.G., Kidd R.G., Can. J. Chem. 46, 3425 (1968)

110. Ellaboudy A., Dye J.L., Saito H., J. Mag. Res., 66 491 (1986)

111. Tabeta R., Aida M., Saito H., Bull. Chem. Soc. Jpn., 59, 1957 (1986)

112. Hilgenfeld R., Saenger W., Topics in Current Chemistry, 101, 1-82 (1982) Springer Verlag, Berlin

113. Koenig J.L., "Chemical Microstructure of Polymer Chains", Wiley-Interscience, New York (1980)

114. Kenwright A.M., Packer K.J., Say B.M., J. Mag. Reson., 69, 426 (1980) and references contained therein

115. McCall D.W., Douglas D.C., Falcone D.R., J. Phys. Chem., 71(4), 998 (1967)

116. Haeberlen U., High Resolution NMR in Solids: Selective Averagiing, Academic Press (1976) and references containd therein

117. Ellet D., Haeberlen U., Waugh J.S., Polymer Lett,. 7, 71 (1969)

118. Mehring M., Griffin R.G., Waugh J.S., J. Chem. Phys., 55(2), 746 (1971)

119. Garroway A.N., Stalker D.C., Mansfield P., Polymer, 16, 161 (1975)

120a. Vega A.J., English A.D., Macromolecules, 13, 1635 (1980)

120b. English A.D. Garza O.T., Macromolecules, 12(2), 351 (1979)

120c. English A.D., Vega A.J., Macromolecules, 12(2), 353 (1979)

APPENDIX

RESEARCH COLLOQIUA, SEMINARS, LECTURES AND CONFERENCES

APPENDIX

RESEARCH COLLOQIUA, SEMINARS, LECTURES AND CONFERENCES

The Board of Studies in Chemistry requires that each postgraduate research thesis contains an appendix, listing:

(A) all research colloquia, research seminars and lectures arranged by the Department of Chemistry during the period of the author's residence as a postgraduate student;

(B) Lectures organised by Durham University Chemical Society;

(C) all research conferences attended and papers presented by the author during the period when research for the thesis was carried out;

(D) details of the postgraduate induction course.

(A) LECTURES ORGANISED BY DURHAM UNIVERSITY - 1984-1986

19.9.84	Dr. C. Brown (IBM, California), "New Superbase reactions with organic compounds".
21.9.84	Dr. H.W. Gibson (Signal UOP, Illinois), "Isomerization of Polyacetylene".
19.10.84	Dr. A. Germain (Languedoc, Montpellier), "Anodic Oxidation of Perfluoro Organic Compounds in Perfluoroalkane Sulphonic Acids".
*24.10.84	Prof. R.K. Harris (Durham), "N.M.R. of Solid Polymers"
28.10.84	Dr R. Snaith (Strathclyde), "Exploring Lithium Chemistry: Novel Structures, Bonding, and Reagents"
7.11.84	Prof. W.W. Porterfield (Hampden-Sydney College, USA), "There is no Borane Chemistry (only Geometry)"

*7.11.84	Dr. H.S. Munro (Durham), "New Information from ESCA Data"
21.11.84	Mr. N. Everall (Durham), Picosecond Pulsed Laser Raman Spectroscopy"
*27.11.84	Dr. W.J. Feast (Durham), " A Plain Man's Guide to Polymeric Organic Metals"
28.11.84	Dr. T.A. Stephenson (Edinburgh), "Some recent Studies in Platinum Metal Chemistry"
12.12.84	Dr. K.B. Dillon (Durham), "^{31}P NMR Studies of some Anionic Phosphorus Complexes"
11. 1.85	Emeritus Prof. H. Suchitzky (Salford), "Fruitful Fissions of Benzofuroxanes and Isobenzimidazoles (umpolung of *o*-phenylenediamine)"
13. 2.85	Dr. G.W.J. Fleet (Oxford), "Synthesis of some Alkaloids from Carbohydrate"
19. 2.85	Dr. D.J. Mincher (Durham), "Stereoselective Syntheses of Some Novel Anthracyclinones Related to the Anti-cancer Drug Adriamycin and to the Steffimycin Antibiotics"
27. 2.85	Dr. R.E. Mulvey (Durham), "Some Unusual Lithium Complexes"
6. 3.85	Dr. P.J. Kocienski (Leeds), "Some Synthetic Applications of Silicon-Mediated Annulation Reactions"
7. 3.85	Dr. P.J. Rodgers (I.C.I. plc Agricultural Division, Billingham), "Industrial Polymers from Bacteria"
*12. 3.85	Prof. K.J. Packer (B.P. Ltd./East Anglia) "NMR Investigations of the Structure of Solid Polymers"
*14. 3.85	Prof. A.R. Katritzky F.R.S. (Florida), "Some Adventures in Heterocyclic Chemistry"
20. 3.85	Dr. M. Poliakoff (Nottingham), "New Methods for Detecting Organometallic Intermediates in Solution"
28. 3.85	Prof. H. Ringsdorf (Mainz), "Polymeric Liposomes as Models for Biomembranes and Cells"
24. 4.85	Dr. M.C. Grossel (Bedford College, London) "Hydroxypyridine Dyes - Bleachable One-Dimensional Metals?"

25. 4.85 Major S.A. Shackelford (U.S. Air Force)
"*In Situ* Mechanistic Studies on Condensed Phase Thermochemical Reaction Processes: Deuterium Isotope Effects in HMX Decomposition, Explosives and Combustion"

1. 5.85 Dr. D. Parker (I.C.I plc, Petrochemical and Plastics Division, Wilton)
"Applications of Radioisotopes in Industrial Research"

*7. 5.85 Prof. G.E. Coates (formerly of Wyoming, U.S.A.)
"Chemical Education in England and America: Successes and Deficiencies"

8. 5.85 Prof. D. Tuck (Windsor, Ontario), "Lower Oxidation State Chemistry of Indium"

8. 5.85 Prof. G. Williams (U.C.W., Aberwystwyth)
"Liquid Crystalline Polymers"

*9. 5.85 Prof. R.K. Harris (Durham),
"Chemistry in a Spin: Nuclear Magnetic Resonance"

14. 5.85 Prof. J. Passmore (New Brunswick, U.S.A.), "The Synthesis and Characterisation of some Novel Selenium-Iodine Cations, aided by 77-Se NMR Spectroscopy"

15. 5.85 Dr. J.E. Packer (Auckland, New Zealand)
"Studies of Free Radical Reactions in Aqueous Solution Using Ionising Radiation"

*17. 5.85 Prof. I.D. Brown (McMaster University, Canada)
"Bond Valence as a Model for Inorganic Chemistry"

21. 5.85 Dr. D.L.H. Williams (Durham)
"Chemistry in Colour"

22. 5.85 Dr. M. Hudlicky (Blacksburg, U.S.A.)
Preferential Elimination of Hydrogen Fluoride from Vicinal Bromofluorocompounds"

22. 5.85 Dr. R. Grimmett (Otago, New Zealand)
"Some Aspects of Nucleophilic Substitution in Imidazoles"

*4. 6.85 Dr. P.S. Belton (Food Research Institute, Norwich)
"Analytical Photoacoustic Spectroscopy"

*13. 6.85 Dr. D. Woolins (Imperial College, London)
"Metal - Sulphur - Nitrogen Complexes"

14. 6.85	Prof. Z. Rappoport (Hebrew University, Jerusalem) "The Rich Mechanistic World of Nucleophilic Vinylic Substitution"
*19. 6.85	Dr. T.N. Mitchell (Dortmund), "Some Synthetic and NMR-Spectroscopic Studies of Organotin Compounds"
26. 6.85	Prof. G. Shaw (Bradford), "Synthetic Studies on Imidazole Nucleosides and the Anitbiotic Coformycin"
12. 7.85	Dr. K. Laali (Hydrocarbon Research Institute, University of Southern California, U.S.A.) "Recent Developments in Superacid Chemistry and Mechanistic Considerations in Electrophilic Aromatic Substitutions: A Progress Report"
13. 9.85	Dr. V.S. Parmar (Delhi), "Enzyme Assisted ERC Synthesis"
17.10.85	Dr. C.J. Ludman (Durham), "Some Thermochemical Aspects of Explosions"
30.10.85	Dr. S.N. Whittleton (Durham), "An Investigation of a Reaction Window"
5.11.85	Prof. M.J. O'Donnell (Indiana-Purdue Univeristy, U.S.A.), "New Methodology for the Synthesis of Amino Acids"
20.11.85	Dr. J.A.H. McBride (Sunderland Polytechnic) "A Heterocyclic Tour on a Distorted Tricycle - Biphenylene"
28.11.85	Prof. D.J. Waddington (York), "Resources for the Chemistry Teacher"
15. 1.86	Prof. N. Sheppard (East Anglia), "Vibrational and Spectroscopic Determinations of the Structures of Molecules Chemisorbed on Metal Surfaces"
23. 1.86	Prof. Sir Jack Lewis (Cambridge), "Some More Recent Aspects in the Cluster Chemistry of Ruthenium and Osmium Carbonyls"
29. 1.86	Dr. J.H. Clark (York), "Novel Fluoride Ion Reagents"
*12. 2.86	Dr. J. Yarwood (Durham), "The Structure of Water in Liquid Crystals"
*12. 2.86	Dr. O.S. Tee (Concordia University, Montreal, Canada), "Bromination of Phenols"
19. 2.86	Prof. G. Procter (Salford), "Approaches to the Synthesis of Some Natural Products"

*26. 2.86 Ms. C. Till (Durham), "ESCA and Optical Emission Studies of the Plasma Polymerisation of Perfluoroaromatics"

5. 3.86 Dr. D. Hathway (Durham), "Herbicide Selectivity"

5. 3.86 Dr. M. Schroder (Edinburgh), "Studies on Macrocyclic Compounds"

12. 3.86 Dr. J.M. Brown (Oxford), "Chelate Control in Homogeneous Catalysis"

14. 5.86 Dr. P.R.R. Langridge-Smith (Edinburgh) "Naked Metal Clusters - Synthesis, Characterisation, and Chemistry"

*9. 6.86 Prof. R. Schmutzler (Braunschweig, W. Germany) "Mixed Valence Diphosphorus Compounds"

23. 6.86 Prof. R.E. Wilde (Texas Technical University, U.S.A.), "Molecular Dynamic Processes from Vibrational Bandshapes"

* Indicates colloquia attended by the author.

(B) LECTURES ORGANISED BY DURHAM UNIVERSITY CHEMICAL SOCIETY DURING THE PERIOD 1983-1986

18.10.84	Dr. N. Logan (nottingham), "N_2O_4 and Rocket Fuels".
*24.10.85	Dr. J. Dewing (UMIST), "Zeolites - Small Holes, Big Opportunities"
31.10.85	Dr. P. Timms (Bristol), "Some Chemistry of Fireworks"
7.11.85	Prof. G. Ertl (Munich, W. Germany), "Heterogeneous Catalysis"
14.11.85	Dr. S.G. Davies (Oxford), "Chirality Control and Molecular Recognition"
21.11.85	Prof. K.H. Jack (Newcastle), "Chemistry of Si-Al-O-N Engineering Ceramics"
28.11.85	Dr. B.A.J. Clark (Kodak Ltd.), "Chemistry and Principles of Colour Photography"
30. 1.86	Dr. N.J. Phillips (Loughborough), "Laser Holography"
13. 2.86	Prof. R. Grigg (Queen's, Belfast), "Thermal Generation of 1,3-Dipoles"
20. 2.86	Dr. C.J.F. Barnard (Johnson Matthey Group) "Platinum Anti-Cancer Drug Development"
27. 2.86	Prof. R.K. Harris (Durham), "The Magic of Solid State NMR"
*6. 3.86	Dr. B. Iddon (Salford), "The Magic of Chemistry"

(C) RESEARCH CONFERENCES ATTENDED (* indicates Poster presentation, + indicates a lecture)

*1. "MAR Multinuclear Magnetic Resonance Study of Order in Silicate Minerals." Royal Society of Chemistry Seventh International Meeting on NMR. Cambridge, July 1985.

+2. "NMR of Abundant Spins in Solids: Proton and Fluorine." Royal Society of Chemistry NMR Discussion Group.

3. "Solid-State Tin-119 NMR Spectroscopy: The First Observations of (Tin-119, Tin-117) Coupling Constants." R.K. Harris, T.N. Mitchell, G.J. Nesbitt, Magnetic Resonance in Chemistry, Vol. 23, No. 12, 1080, 1985.

*4. Procedings of the BRSG Meeting, Oxford, 1985. R.K. Harris, P. Jackson, G.J. Nesbitt, B.J. Say,

(D) FIRST YEAR INDUCTION COURSE, OCTOBER 1984

This course consists of a series of one hour lectures on the services available in the department.

1. Departmental Organisation
2. Safety matters
3. Electrical appliances and infrared spectroscopy
4. Chromatography and Microanalysis
5. Atomic absorptiometry and inorganic analysis
6. Library facilities
7. Mass spectroscopy
8. Nuclear Magnetic resonance spectroscopy
9. Glassblowing technique.